

Scaling Dispersion Processes in Surcharged Manholes

Shing-Tak Douglas Lau

VOL 2

This thesis is submitted in partial fulfilment of the requirements for
the Degree of Doctor of Philosophy

University of Sheffield
Department of Civil and Structural Engineering

December 2007

5 Laboratory Experiment – Flow Field Visualisation

5.1 Introduction

This chapter describes the flow field visualisation experiments undertaken in the scale manhole system; and the associated analysis to acquire flow field measurements from the recorded images. The purpose of this laboratory work is to collect flow field information relating to the structure for the validation of the computational fluid dynamics (CFD) manhole models.

Visualisation of flow structures within manholes began with Guymer *et al.* (1998). In the study, the laser induced fluorescence (LIF) technique was used to investigate the internal flow structures of a 390 mm internal diameter (ID) manhole. Two-dimensional tracer images on the vertical plane at the pipe centreline were recorded and those images qualitatively described the flow dynamics occurring in the manhole system (Figure 5.1). Further attempt was made by Guymer *et al.* (1998) to determine spatial and temporal concentration distributions of a solute travelling through the manhole using the same non-intrusive measurement technique. However, the work proved unsuccessful because of insufficient laser power (300 mW) to provide good resolution of the solute concentration (Guymer *et al.*, 1998).

In the present flow field visualisation experiments, two non-intrusive visualisation techniques, laser induced fluorescence (LIF) and particle image velocimetry (PIV), were adopted to obtain flow field data in the scale manhole model for the validation of the CFD models. The LIF technique provided qualitative visualisation of the flow structure and general interpretation of the solute mixing dynamics throughout the manhole. Quantitative flow measurements were generated using the PIV measurement technique. PIV is novel in manhole research. The outcomes from this work provide insights into the hydraulic and solute transport characteristics within the structure and could potentially be used to verify the approach based on submerged jet theory for the prediction of energy loss in surcharged manholes (Bo Pedersen and Mark, 1990).

LIF could also be used for the measurements of spatial and temporal dye concentration distributions associated with a solute travelling through the manhole chamber. This measurement technique could be employed in conjunction with fluorometers to provide additional insights into the internal mixing process within the manhole chamber. The fluorometric data presented in Chapter 4 could only represent the overall mixing behaviour of the structure but do not provide any detail regarding the internal mixing mechanism. In the flow field visualisation experiments, an additional LIF study was conducted to measure solute concentration using fluorometers and the LIF technique simultaneously. However, it is

important to note that the purpose of the study is to suggest a workable experimental methodology for the parallel measurements of dye concentration. It is not intended to provide quantitative CFD validation data.

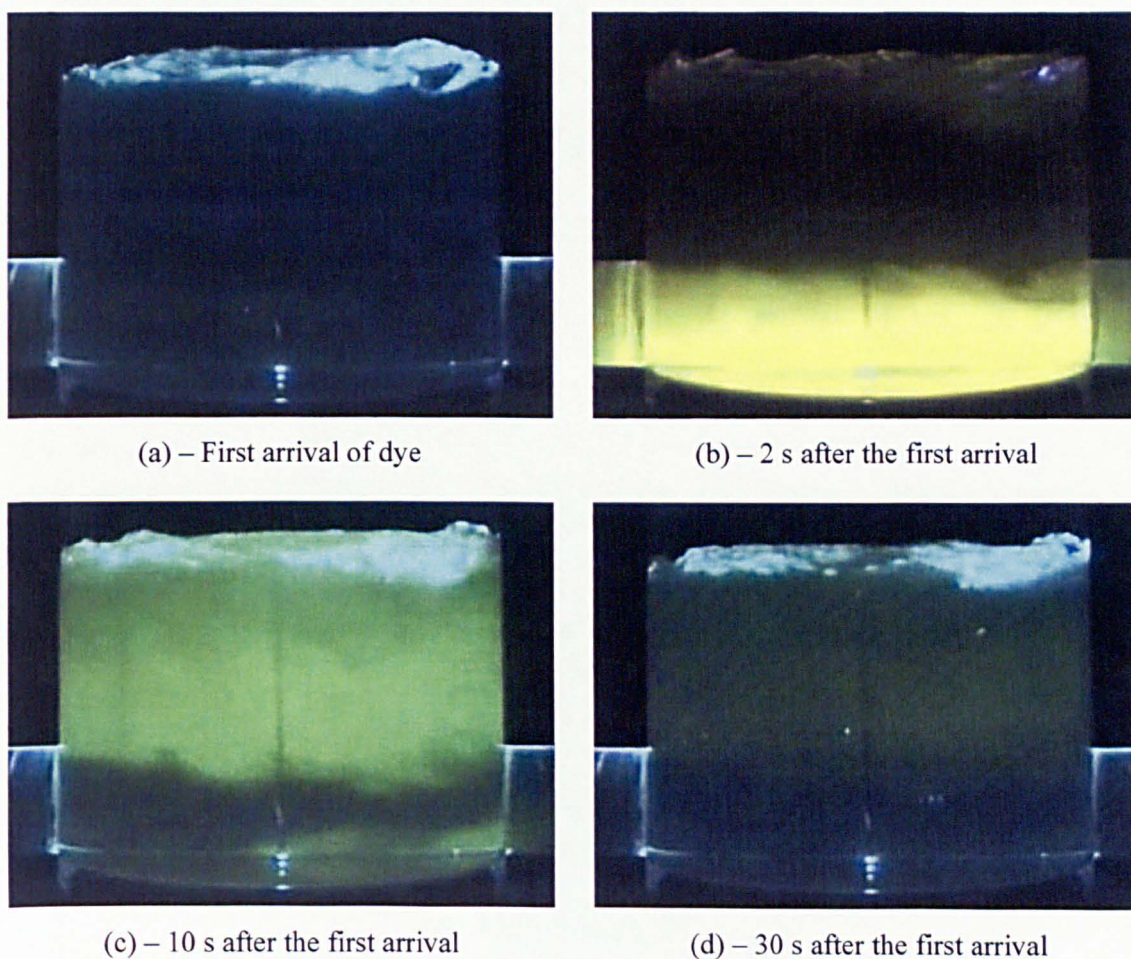


Figure 5.1 – Variations in solute concentration within the 390 mm ID manhole with time ($Q = 1.5$ l/s; Surge = 150 mm; Flow from left to right) (after Guymer *et al.*, 1998)

The flow field visualisation experiments were undertaken collaboratively with the School of Engineering at the University of Warwick. A ‘state-of-the-art’ high speed camera was utilised for flow field image recording. The laboratory experiments examined the flow field on five planes throughout the manhole under two contrasting hydraulic conditions, pre- and post-threshold. These are intended to provide a comprehensive picture of the three-dimensional flow field within the structure. The general laboratory arrangement for the two visualisation techniques is discussed in Section 5.2. The specific laboratory set-up for the LIF experiments is presented in Section 5.3. Section 5.4 discusses the feasibility study of the parallel dye measurements. Section 5.5 describes the PIV experiments and the associated analysis; and the chapter is concluded in Section 5.6.

5.2 Laboratory System

5.2.1 Selection of Hydraulic Conditions

In Chapter 4, it has been shown that for the full range of discharge and surcharge conditions considered, two hydraulic regimes could be identified: pre- and post-threshold. Within each of the two hydraulic regimes, the cumulative temporal concentration profiles were found to form a ‘family’, with the curve shape being essentially independent of either surcharge or discharge (Figure 4.33 and Figure 4.35). This observation suggests that the flow structure within the same hydraulic regime should be comparable, or otherwise the distribution curves would have appeared in different shapes.

Due to limited availability of the image acquisition equipment, it was not possible to investigate the entire range of hydraulic conditions that had been considered in the dye tracing study. Consideration was therefore given to one pre-threshold and one post-threshold hydraulic conditions, assuming that each would represent the characteristics of the flow for their corresponding regime. In terms of CFD validation, two detailed studies, one in each hydraulic regime, would be adequate to demonstrate the validity of the CFD simulations of the manhole. The two hydraulic conditions considered were a mid-point from the pre-threshold depth range (Surcharge ratio, i.e. surcharge over the pipe ID, S , of 1.17) and a mid-point from the post-threshold dataset ($S = 3.27$), both at a discharge of 0.35 l/s, which was a mid-point from the discharge range. Table 5.1 summarises the details of the hydraulic conditions considered.

Flow Field Visualisation Study			
Hydraulic Condition	Hydraulic Regime	Surcharge Ratio (-)	Discharge (l/s)
1	Pre-threshold	1.17	0.35
2	Post-threshold	3.27	0.35

Table 5.1 – Hydraulic conditions considered in the flow field visualisation study

5.2.2 Areas of Interest

In total five two-dimensional planes, comprising three vertical and two horizontal, through the flow field were studied in the scale manhole. The position of the planes is shown in Figure 5.2. The central vertical plane (CVP) is positioned at the centreline of the inlet and outlet pipes. The left vertical plane (LVP) and right vertical plane (RVP) are located at the quarter points (54.5 mm from the pipe centreline) of the circle parallel to the pipe axis. The horizontal plane at the pipe centreline is the central horizontal plane (CHP); and the mid-surcharge horizontal plane

(MSHP) is positioned equidistant from the pipe soffit and the free surface. Note that the position of the MSHP varies with surcharge depth.

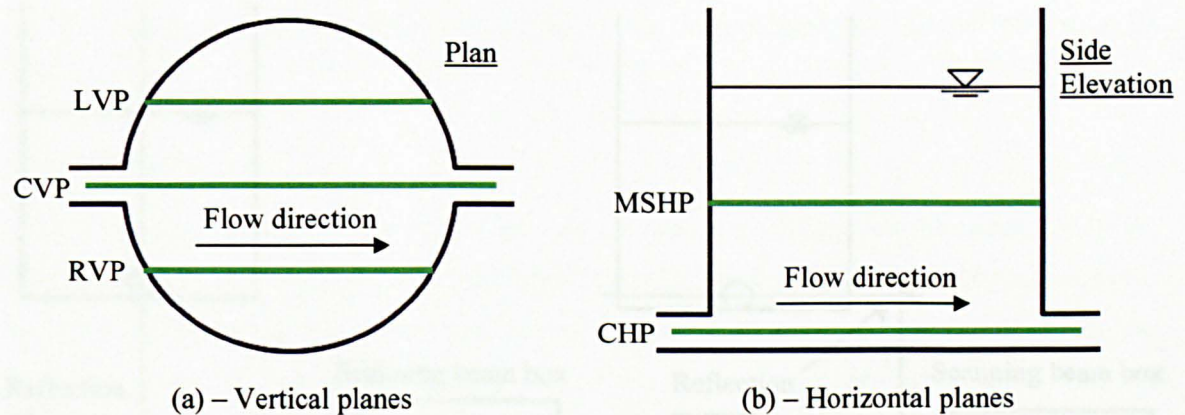


Figure 5.2 –Planes of investigation

5.2.3 Laboratory Configuration

5.2.3.1 General Arrangement for Flow Visualisation Using Light Sheet

The laser induced fluorescence (LIF) and particle image velocimetry (PIV) experiments employed common equipment for manhole illumination and image acquisition. An Argon ion laser with a maximum possible output of 10 W, coupled with a scanning beam box, was used to generate a scanning light sheet. The pseudo light sheet was then directed to the areas of interest using front surface mirrors. Figure 5.3 shows the arrangements for the generation of the vertical and horizontal light sheets in the circular manhole. A 45° angled mirror mounted on a movable slide underneath the manhole was used to produce the vertical light sheets. For the horizontal planes, a pair of front surface mirrors was used to direct the light sheet from the scanning beam box to the designated areas.

To allow the passage of light, the circular manhole was made of clear Perspex. The light sheet was subjected to refraction when passing across the circular Perspex from air to water. To avoid this, the manhole was seated inside a rectangular water-filled box, or water jacket. The front and back side of the water jacket were constructed of clear Perspex to allow light to pass through (Figure 5.4).

A high speed CMOS camera (FASTCAM-X 1024 PCI, Photron), positioned opposite the scanning beam box and perpendicular to the pipe flow direction, was adopted to capture the high velocity flow in the manhole (maximum velocity approached 1 m/s). The camera was held in place by a Manfrotto Magic Arm which was securely clamped on a steel rail bolted onto a concrete base (Figure 5.4). Flow field images on the horizontal planes were taken via a 45°

angled front surface mirror placed directly underneath the manhole. This was because the space under the manhole was insufficient for the camera lens to focus on the horizontal planes.

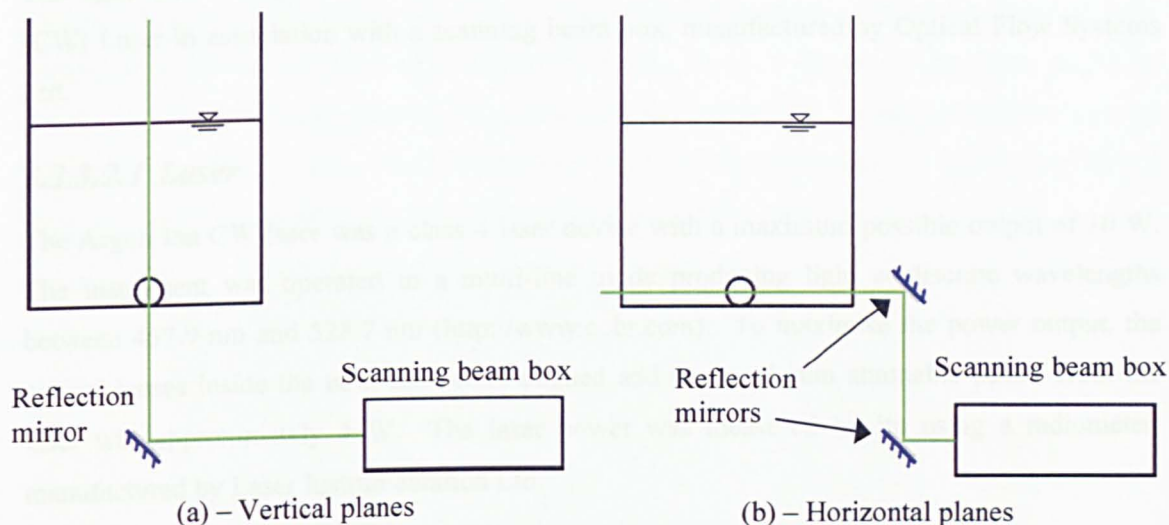


Figure 5.3 –Laboratory arrangement for the light sheet generation

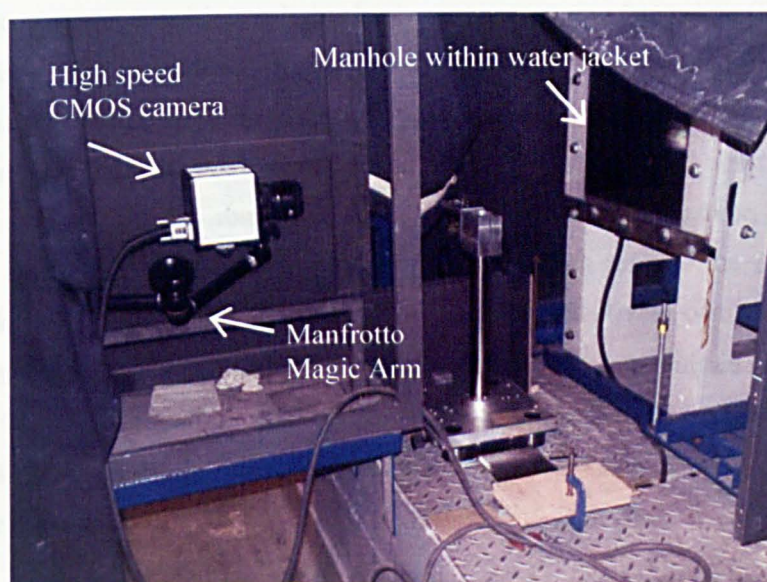


Figure 5.4 – The high speed CMOS camera and the Manfrotto Magic Arm

Since the laser employed for the experiments was a class 4 classification, the entire rig was fully enclosed with blackout boards and blackout materials for health and safety reasons. This measure also prevented external light intrusion.

The following sub-sections describe the light sheet generation system and the image acquisition equipment in detail.

5.2.3.2 Light Sheet Generation

The light sheet was generated by a Coherent Innova 70 Series Argon Ion Continuous Wave (CW) Laser in association with a scanning beam box, manufactured by Optical Flow Systems Ltd.

5.2.3.2.1 Laser

The Argon ion CW laser was a class 4 laser device with a maximum possible output of 10 W. The instrument was operated in a multi-line mode producing light at discrete wavelengths between 457.9 nm and 528.7 nm (<http://www.cohr.com>). To maximise the power output, the optical lenses inside the laser tube were aligned and the maximum attainable power from the laser was approximately 4 W. The laser power was measured in-situ using a radiometer, manufactured by Laser Instrumentation Ltd.

5.2.3.2.2 Scanning Beam Box

The laser beam was converted into a light sheet using a scanning beam box (Figure 5.5). This device comprises a flat reflection mirror, a rotating octagonal mirror and a parabolic mirror to produce a pseudo illumination plane at variable scanning rates. The flat reflection mirror directs the laser beam onto the octagonal mirror which is centred at the focal point of the parabolic mirror. As a result of the rotational motion of the octagonal mirror, the laser beam progressively scans through the entire parabolic mirror which reflects the laser beam into a parallel pseudo light sheet. Since the illumination sheet is effectively composed of a series of laser beams, its intensity should be identical to that of the laser beam emitted from the laser tube (Gray *et al.*, 1991). The scanning beam box generates a light sheet 500 mm wide and the rate of scanning could be adjusted between 66.7 Hz and 2,000 Hz, i.e. the number of scans on the parabolic mirror per second.

The laser system produced a light beam of approximately 2.5 mm diameter with a divergence of 0.5 mrad* (Coherent). Because of the inherent divergence, the beam progressively expanded in its radial direction. Once the beam/light sheet reached the areas of interest, the beam diameter increased to approximately 3 mm, measured by graph paper. Variations of the laser sheet thickness along the investigated planes were estimated based on the divergence value for the 514.5 nm primary beam emitted from the laser. The result indicated that the change in thickness is 0.055 mm ($= 218 \times \tan(0.5 \text{ mrad})$), which is negligible.

* Divergence was measured for a primary beam of wavelength of 514.5 nm at the head of the laser tube

It might be possible to collimate the diverging light beam by placing a pair of collimating lenses in the scanning beam box, resulting in a thinner and parallel light sheet. The collimating lenses comprise a convex lens and a concave lens. The distance between the two lenses determines the thickness of the light sheet (Optical Flow Systems, 1994). However, the laser might be positioned too close to the scanning beam box, and the collimating lenses could not reduce the thickness to less than 3 mm. The minimum thickness of the beam with the lenses fitted in the box was 5 mm. For this reason, they were not used during the experiments.

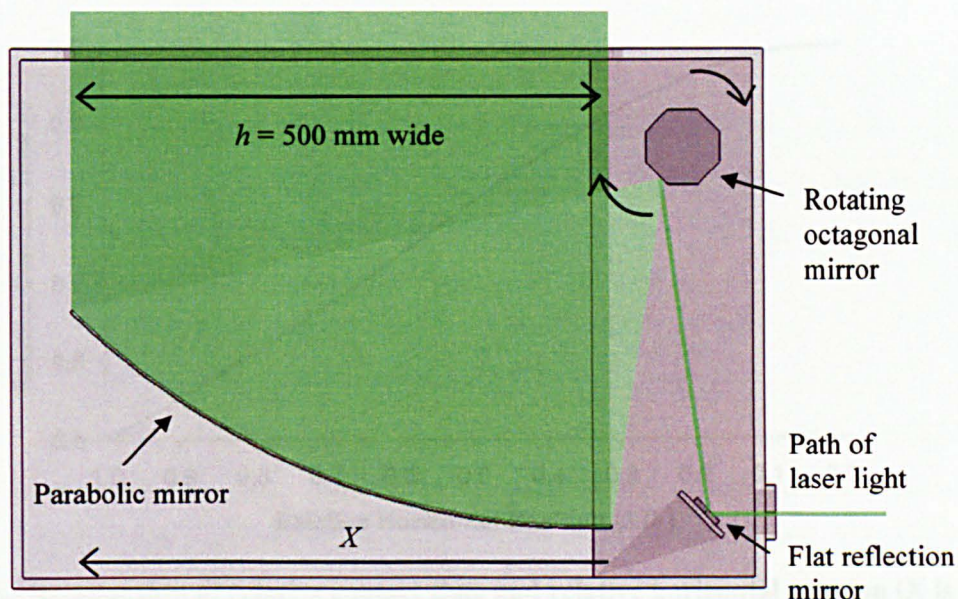


Figure 5.5 – Scanning beam box

Gray *et al.* (1991) claimed that for PIV applications, the scanning beam illumination method is superior to the conventional light sheet generation method, which uses cylindrical lenses or prisms for beam expansion into a sheet. This is because the former method would generate a light sheet with higher intensity, which benefits high speed flow field measurement. Non-uniform intensity along the width of the illumination plane exists when either illumination method is applied. For the scanning beam box, the non-uniformity is caused by the geometrical shape of the parabolic mirror, which led to a change in transitional speed of the beam and hence a variable beam contact time along the mirror (Guymer and Harry, 1996). The maximum relative difference in the contact time, or intensity, along the illumination plane (500 mm) is two-fold and occurs between the mirror ends (Figure 5.6). Since the areas of interest were 218 mm wide and the width of the light sheet was 500 mm, the scanning beam box was positioned so that variations of light intensity along the illumination plane were minimal. Figure 5.7 shows the variations of grey scale value (GSV) along the pipe central axis on the central vertical plane (CVP). The GSVs were measured in constant Rhodamine 6G

concentration conditions and therefore the variations indicate the relative change in the intensity over the plane. The results suggest that the maximum variations appear to approximate to 15 %. It may also be noticed that the GSVs drop at either side of the manhole. This might be explained by the effects of the circular Perspex surface being thicker in the light path direction approaching the inlet and outlet, creating further light intensity attenuation. Despite having the non-uniform intensity along the illumination plane, the LIF and PIV flow field results did not appear to be influenced by this set-up limitation.

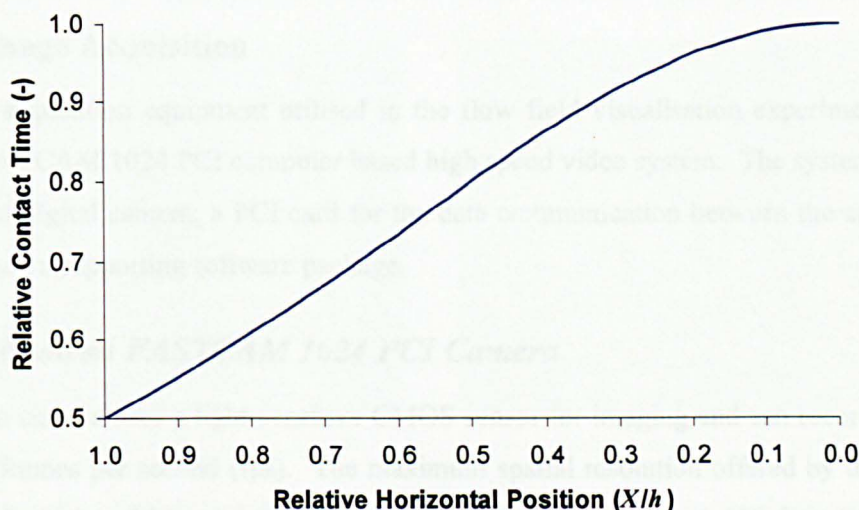


Figure 5.6 – Relationship of relative contact time and relative horizontal position (X is the horizontal position with respect to the mirror end closer to the octagonal mirror and h is the width of the entire illumination plane) (after Guymer and Harry, 1996)

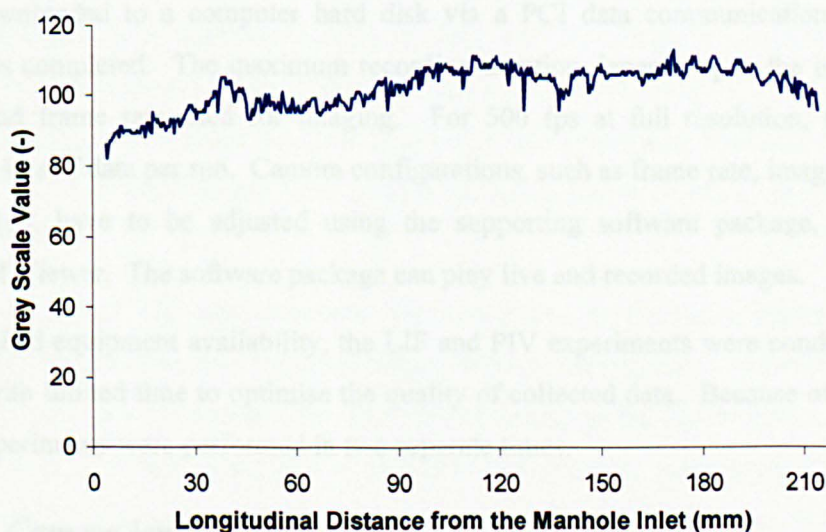


Figure 5.7 – Variations in grey scale value along the pipe central axis on the CVP

5.2.3.2.3 Alignment

The reflection mirrors had to be aligned when the light sheet position was changed. Due to health and safety considerations, this was performed at reduced laser power (400 mW) in association with a OD3 neutral density filter. The filter was attached to the head of the laser tube and reduced the intensity of the beam by 1,000 times. Under these conditions (intensity smaller than 1 mW), it was safe to have access to the enclosed areas without wearing protective eyewear (BS EN 60825-1:1994).

5.2.3.3 Image Acquisition

The image acquisition equipment utilised in the flow field visualisation experiments was the Photron FASTCAM 1024 PCI computer based high speed video system. The system comprises a high speed digital camera; a PCI card for the data communication between the camera and a computer; and a supporting software package.

5.2.3.3.1 Photron FASTCAM 1024 PCI Camera

The Photron camera uses a light-sensitive CMOS sensor for imaging and can record images up to 100,000 frames per second (fps). The maximum spatial resolution offered by the camera is 1024 x 1024 pixels x 8 bits and this spatial resolution supports up to 1,000 fps. Beyond 1,000 fps, the spatial resolution of an image reduces as frame rate increases.

The camera employed has an internal buffer storage of 4GB, which allows a maximum of 3,080 images at 1 million pixels resolution to be taken per run. Temporary files saved in the buffer can be downloaded to a computer hard disk via a PCI data communication card once the recording is completed. The maximum recording duration depends upon the image resolution required and frame rate used for imaging. For 500 fps at full resolution, the camera can generate 6.16 s of data per run. Camera configurations, such as frame rate, image resolution and shutter speed, have to be adjusted using the supporting software package, called Photron FASTCAM Viewer. The software package can play live and recorded images.

Due to limited equipment availability, the LIF and PIV experiments were conducted on a tight schedule with limited time to optimise the quality of collected data. Because of this constraint, the two experiments were performed in two separate times.

5.2.3.3.2 Camera lenses

Two camera lenses were employed in the LIF and PIV experiments. In the LIF study, the camera was attached to a Micro-Nikkor 55 mm f/2.8 manual focus lens. In the later PIV

experiments, this was replaced by a large aperture camera lens (AF Nikkor 50 mm f/1.4D). The f/1.4 lens allowed more light through its aperture and made a significant improvement in the contrast ratio of the particles to the background when high frame rates were used. Figure 5.8 provides a comparison of the PIV images taken by the two camera lenses framing at 500 fps. Particles can hardly be observed in Figure 5.8a, which shows a noticeable difference in terms of PIV image quality compared to Figure 5.8b. An additional benefit of using the 50 mm focal length lens is that it has a distortion-free feature (<http://nikonimaging.com>), implying that the PIV images should not require correction for lens distortion in the image post-processing.

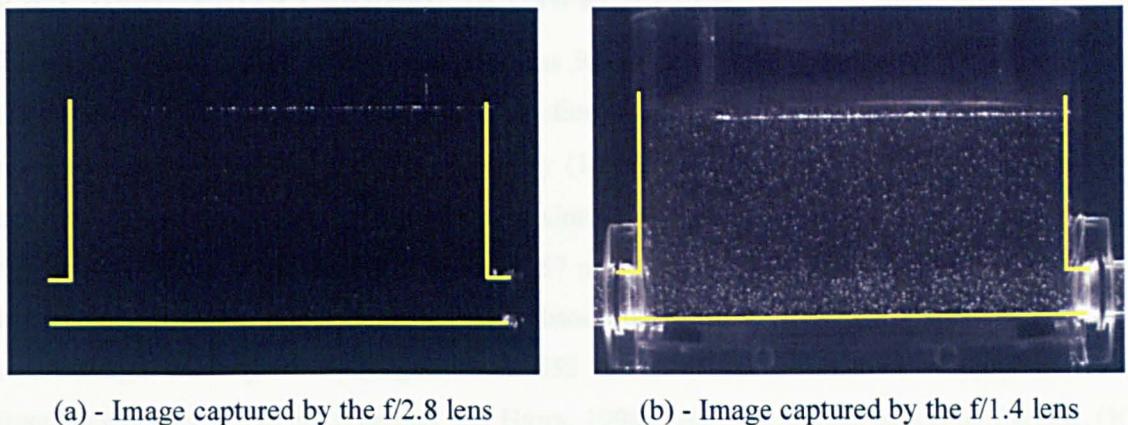


Figure 5.8 – Comparison of the PIV images taken by the two camera lenses at 500 fps

5.3 Laser Induced Fluorescence Experiment

The aims of the laser induced fluorescence (LIF) experiments are to collect qualitative flow field images that describe the flow structures throughout the scale manhole for the validation of the computational fluid dynamics (CFD) models; and to provide a cross-reference for the detailed flow measurements obtained from particle image velocimetry (PIV). In the study, five two-dimensional planes through the flow field under two contrasting hydraulic conditions were examined. The LIF experiments were carried out using the technique developed by Guymer and Harry (1996).

An additional set of LIF measurements was undertaken to determine spatial and temporal concentration distributions of a solute travelling through the manhole. Fluorometers were also employed in the work to correlate the LIF measurements to the fluorometric data. This is a feasibility study intended to suggest a workable experimental methodology for the parallel measurements. As a result, only the central vertical plane (CVP) under the post-threshold conditions was considered in the study. Note that the results from this work do not provide additional flow field data for validating the CFD models.

The principle by which LIF works is that a fluorescent substance is made to emit light of a longer wavelength than that of the excitation source. The Argon ion CW laser in conjunction with the scanning beam box was used to provide a light source with the appropriate range of excitation wavelengths. The flow field was revealed when the fluorescent dye that passively followed the carrier fluid flow was lit by the illumination plane. A filter was fitted to the camera to eliminate light other than the fluorescence, thereby improving the quality of the images.

5.3.1 Selection of Fluorescent Dye and Filter

The dye chosen for the LIF experiments was Rhodamine 6G. It is a red organic dye that fluoresces to yellow after excitation. Selection of the fluorescent dye was based on the recommendation given by Guymer and Harry (1996). The dye absorbs light of wavelengths between 460 nm and 550 nm and has a maximum excitation frequency at 530 nm. As the Argon ion laser operates in a band between 457 nm and 528.7 nm (Coherent), almost 100 % of laser power falls into the Rhodamine 6G's absorption spectrum. Excited Rhodamine 6G dye releases light of longer wavelengths, from 555 nm to 640 nm, and the maximum emission frequency occurs at 590 nm (Guymer and Harry, 1996). An optical long-pass filter (Schott, OG 550) was attached to the camera to eliminate the laser light reflected by the free water surface and the Perspex. The optical characteristics of Rhodamine 6G and the camera filter are presented in Figure 5.9.

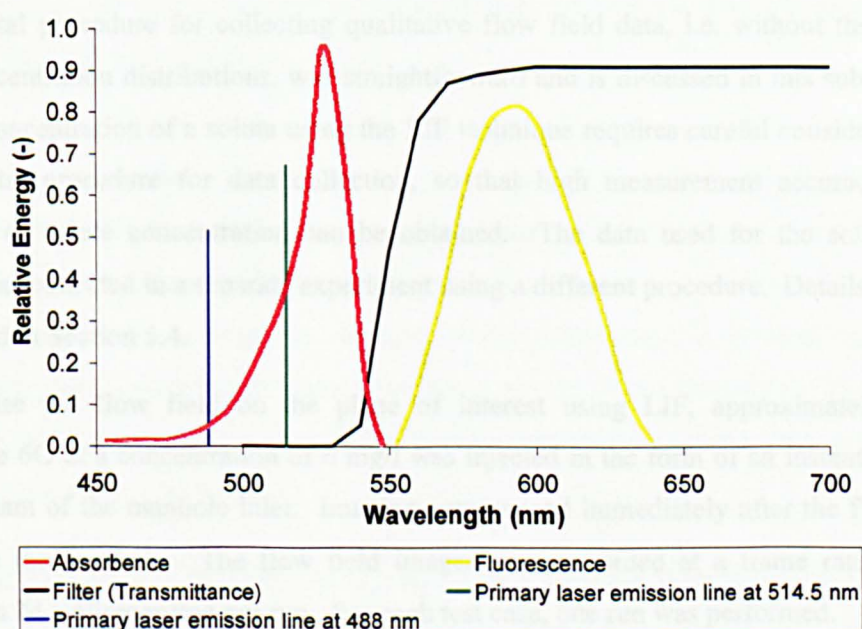


Figure 5.9 – Optical characteristics of Rhodamine 6G and camera filter (after Guymer and Harry, 1996)

Figure 5.10 highlights the effects of the long pass filter on the resultant LIF images. The image taken with the filter (Figure 5.10a) shows that the laser light reflected by the oscillating free surface is removed, and that the dye near the free surface is shown clearer than that in Figure 5.10b. Note that the two images shown in Figure 5.10 were recorded in different test runs.

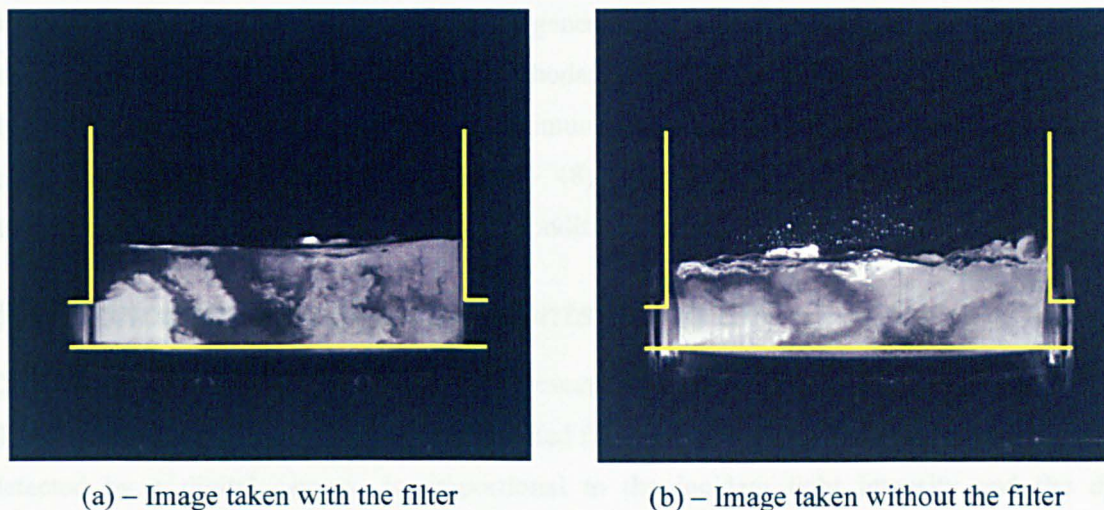


Figure 5.10 – Effects of the optical filter on LIF images (Flow from left to right)

5.3.2 Experimental Procedure for the LIF Experiments

Due to limited availability of the high speed image acquisition system, the LIF experiments were scheduled over only four days. Ten flow visualisation studies were undertaken, in which five flow planes under two surcharge conditions (pre- and post-threshold) were considered. The experimental procedure for collecting qualitative flow field data, i.e. without the analysis of solute concentration distributions, was straightforward and is discussed in this sub-section. To quantify concentration of a solute using the LIF technique requires careful consideration of the experimental procedure for data collection, so that high measurement accuracy and good resolution of solute concentration can be obtained. The data used for the solute transport analysis was collected in a separate experiment using a different procedure. Details of this work are covered in Section 5.4.

To visualise the flow field on the plane of interest using LIF, approximately 25 ml of Rhodamine 6G at a concentration of 6 mg/l was injected in the form of an instantaneous pulse 4 m upstream of the manhole inlet. Imaging commenced immediately after the first arrival of the dye in the manhole. The flow field images were recorded at a frame rate of 125 fps, resulting in 24 s of recording per run. For each test case, one run was performed.

In order not to obstruct the view of the flow field, the water level follower was not operated during the image recording. The surcharge depth was therefore measured before and after a test

to confirm that the average water level did not vary throughout the test. For each water depth measurement, the data was logged for 2 minutes and was analysed using the methodology presented in Section 3.4.3.

In the LIF experiments, the laser power was set at the highest achievable and stable power, which was 3.65 W, and the light sheet was generated at a scanning rate of 2000 Hz (i.e. the highest scanning rate). For the amount of Rhodamine 6G concentration injected (6 mg/l), the dye on the illumination plane obtained a maximum grey scale value (GSV) of 240, providing a good contrast with the background (GSV \sim 48). The LIF flow field images for the five illumination planes under the two surcharge conditions are presented in Section 5.5.4.4.4.

5.4 Concentration Measurements using LIF

Determination of the concentration of a fluorescent dye using LIF is based on the principle of fluorescence: the emission intensity of an excited fluorescent dye, and hence the brightness level detected by a digital camera, is proportional to the incident light intensity and the dye concentration (Chen and Jirka, 1999). Temporal and spatial concentration distributions of a fluorescent tracer in a flow can, therefore, be obtained from the GSV of the raw LIF images via calibration. This measurement approach, hereafter called quantitative LIF analysis, has an advantage over the measurement technique using fluorometer. It provides highly resolved spatial measurements of the dye concentration, gaining insights into the solute transport characteristics over an area of interest (Crimaldi and Koseff, 2001). These results could also be applied to assist with solute transport model validation, for example the CFD species transport model and the ADE transient storage model.

This additional LIF work is a feasibility study aimed at developing a methodology for measuring dye concentration simultaneously using the LIF technique and fluorometers. The benefits of the parallel measurements are to gain a greater understanding in the solute transport process by correlating the spatial concentration distributions over a two-dimensional flow plane to the characteristics of the upstream and downstream profiles; and to create an opportunity for cross-checking the concentration values measured by the two approaches. The experiment considered the central vertical plane (CVP) under the post-threshold hydraulic conditions (Hydraulic condition 2 in Table 5.1).

5.4.1 Laboratory Configuration for the Parallel Measurements

The laboratory arrangements and apparatus employed for the parallel measurements were the same as described in Chapter 3 and Section 5.3.1. No additional equipment was required for the collection of the new LIF dataset. Similarly, the fluorometers were not specifically modified for

the use of Rhodamine 6G as the tracer. Because Rhodamine 6G and Rhodamine WT have similar spectra such that the original emission and excitation filters inside the fluorometer were also fit to use (Solis, 2006; also see Section 3.3.4). To minimise light intrusion into the fluorometers, the illumination light sheet was confined within the manhole excluding the inlet and outlet pipe sections. A schematic diagram of the laboratory configuration is shown in Figure 5.11.

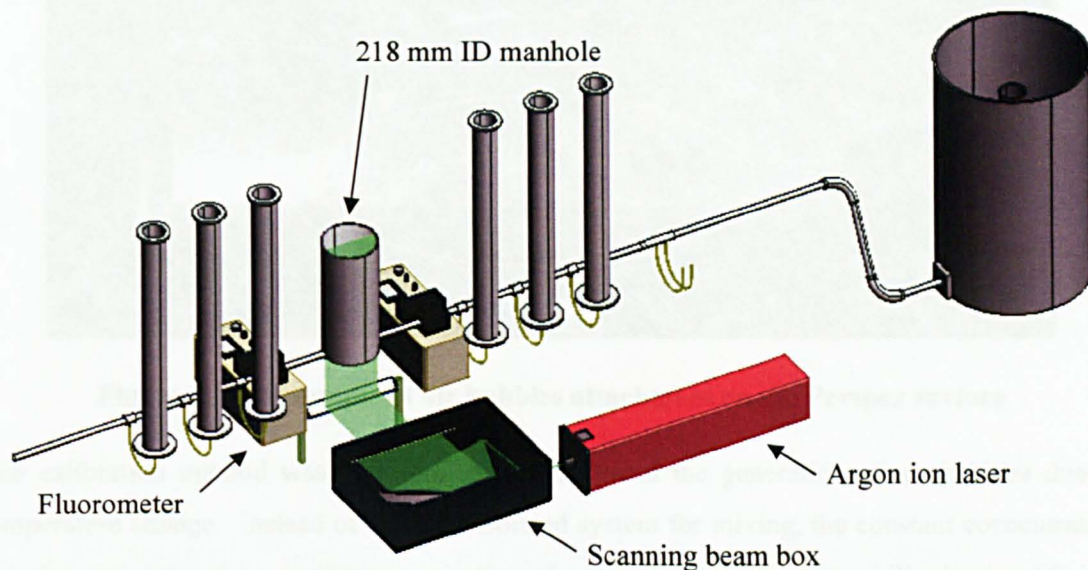


Figure 5.11 –Laboratory configuration for the parallel measurements

5.4.2 LIF and Fluorometer Calibration

The concentration of Rhodamine 6G was determined from the LIF images and fluorometric data by means of calibration. Since the calibration procedure for the two measurement approaches was similar, the two calibrations were undertaken simultaneously. The LIF calibration was to derive a transfer function that correlates the brightness level, i.e. grey scale value (GSV), in a LIF image to a known concentration of Rhodamine 6G; and similarly in the fluorometer calibration.

5.4.2.1 Calibration Procedure

The procedure for the parallel calibrations initially followed the method used in Section 3.3.4. A known concentration solution was added to a known volume of water in a small isolated closed system bypassing the header tank and the sump. Measurement was recorded when the solute became fully mixed. However, as the isolated system could only contain a maximum of 40 litres of water, the solution was heated up rapidly by the Water Puppy pump which caused significant amounts of air bubbles to be released. These bubbles attached to the Perspex surface

and blocked the plane of investigation from being clearly seen (Figure 5.12). Note that the released air bubbles was only a problem to the LIF measurements, the fluorimeters were not affected.

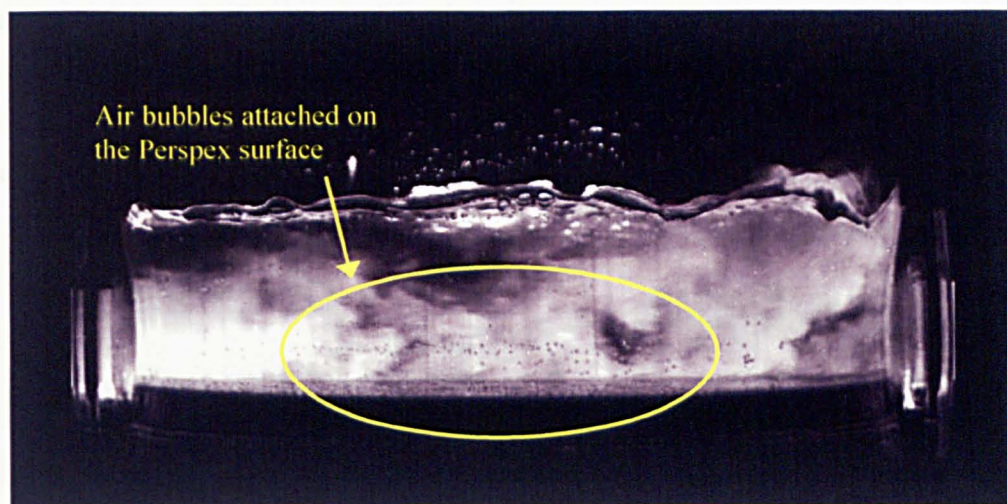


Figure 5.12 – Example of air bubbles attachment on the Perspex surface

The calibration method was therefore revised to avoid the generation of air bubbles due to temperature change. Instead of using an isolated system for mixing, the constant concentration solution was created by continuous injection of a known concentration of Rhodamine 6G into the flow supplied by the constant header tank. As there was a large volume of water stored in the head tank system, this maintained the mixed solution in the test section at constantly room temperature.

Throughout the calibration, the flowrate through the system was regulated to 0.35 l/s and the continuous injection of Rhodamine 6G was made 4 m upstream of the upstream monitoring station pumping at 0.0086 l/s. At this pumping rate, the change in the total flowrate through the experimental section was negligible. The concentration of Rhodamine 6G within the manhole could be estimated once fully mixed conditions had been established, given that the concentration of the source, pumping rate and the flowrate are known:

$$\text{Concentration of the solution in the test section (g/l)} = \frac{\text{Concentration of the source (g/l)} \times \text{Peristaltic pump rate (l/s)}}{\text{Flowrate through the system (l/s)} + \text{Peristaltic pump rate (l/s)}}$$

5.1

For each concentration calibration, the dye solution was injected continuously for 10 minutes. It took approximately 8 minutes to reach fully mixed conditions (e.g. Figure 5.13). The logging of the fluorometric data began at 1 minute prior to the dye injection and ended at 1 minute after

the concentration level returned to background. The data used for the fluorometer calibration was obtained by averaging 30 s of concentration measurements on the profile plateau within the fully mixed regime (Figure 5.13). For the LIF calibration data, a few images were recorded before the injection for background level measurements; once the concentration plateau had been established, 1,250 images recorded at 125 fps, equivalent to 10 seconds of image recording, were captured. Note that the camera settings used in the calibration and in the actual test were the same.

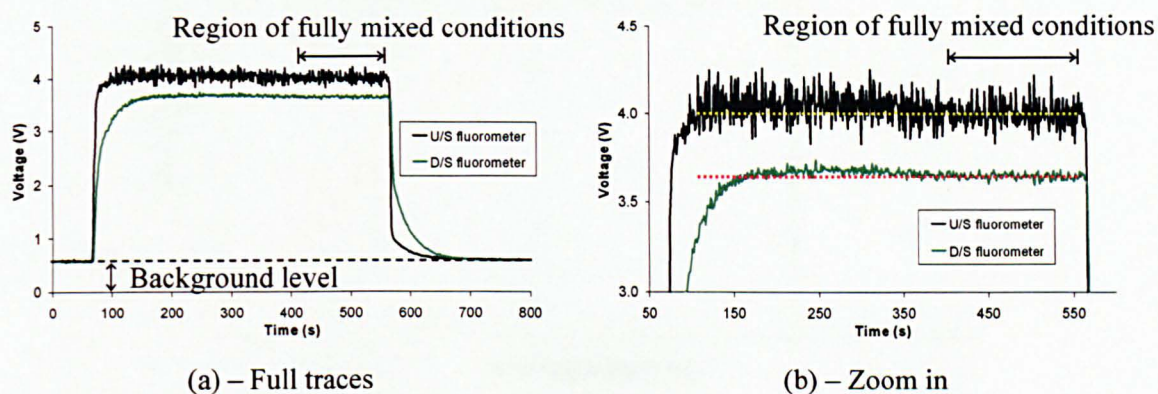


Figure 5.13 – Example of fluorometer data for calibration

5.4.2.2 Range of Concentrations Used in the Parallel Experiments

The LIF technique and fluorometer both measure concentration of a fluorescent dye based on the principle of fluorescence: the emission intensity of an excited fluorescent dye is proportional to the incident light intensity and the dye concentration. However, this relationship holds true only in a certain range of concentrations. This is because when the concentration is too high, the excited fluorescent dye is more inclined to relax via radiationless collision rather than by fluorescence (Walker, 1987), resulting in a phenomenon called concentration quenching. In the extreme scenario of concentration quenching, the fluorescence intensity does not increase with concentration but decreases with further concentration increases. Under quenching conditions, the correct dye concentration cannot be determined from the fluorescence intensity as the intensity could correspond to two different dye concentrations, a higher and lower concentration (Figure 5.14). An additional effect of high concentration to LIF is that the light to cause excitation would be attenuated or blocked by the high concentration of the dye, leading to a reduction in the light intensity along the excitation path (Crimaldi and Koseff, 2001). This effect may not be a concern if the light attenuation by the dye is constant in time and space, for example in a fully mixed solution. This is because the effect could be corrected using theoretical formula (Chen and Jirka, 1999) or a pixel-by-pixel calibration. However, if the light attenuation varies temporally and spatially, for instance when a pulse of fluorescent dye

travelling through an illumination plane in the scale manhole, it is not possible to correct this effect. Without correction the concentration measurements will be erroneous. As a result, the range of dye concentrations used in this LIF experiments had to be carefully determined to avoid light attenuation by high concentration.

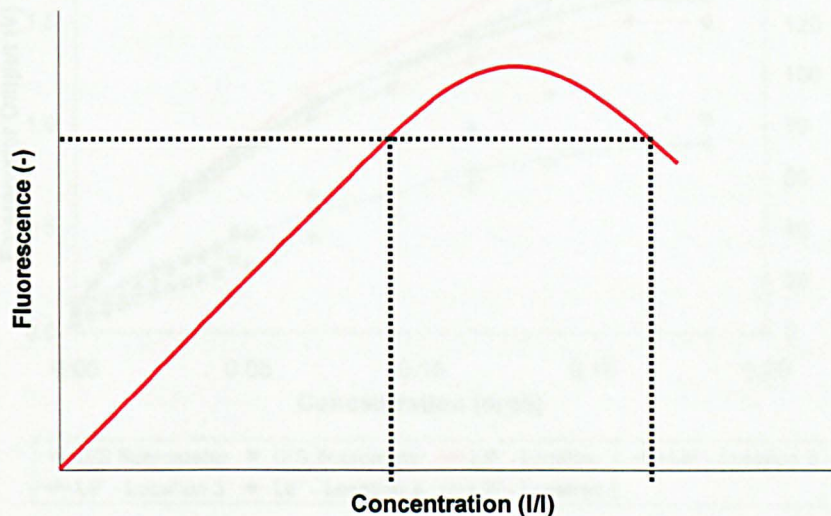


Figure 5.14 – Example of concentration quenching

The range of Rhodamine 6G concentrations that could be used in the LIF experiments for the quantitative LIF analysis was investigated. Due to limited availability of the high speed image acquisition system, this study was carried out using a different image recording device, SONY HD camcorder, prior to the arrival of the high speed camera. The study followed the calibration procedure described in Section 5.4.2.1 and examined a range of concentrations between 0.0 mg/l to 0.5 mg/l. Figure 5.15 shows the results of the study. For the LIF measurements, five pixels at different positions were selected for the study (Figure 5.16). If there was no attenuation, then locations in the same vertical plane should produce the same levels of light intensity. Some variations between horizontal locations are anticipated as a result of inconsistencies along the light sheet (Figure 5.7) and possible interference from defects on the manhole surface. Location 1 and location 3 are vertically aligned with location 2 and location 4 respectively to investigate the effects of light attenuation. For each known concentration, the GSV was obtained by averaging 5 s of image recording framed at 30 fps; whereas the output signal of the fluorometers was the time average reading of 30 s at the concentration plateau (Figure 5.13). It can be noticed that although the GSV detected by the camcorder appears to increase with concentration up to 0.15 mg/l, the effects of the light attenuation become significant when the concentration increases above 0.05 mg/l (Location 1 vs Location 2; Location 3 vs Location 4); the reduction in the intensity is greater than 5 % from this concentration point onwards. In contrast, the fluorometers provide a good linear response to

concentration up to 0.2 mg/l. From these, it is concluded that a concentration of 0.05 mg/l forms the upper concentration limit that could be used in the parallel experiments.

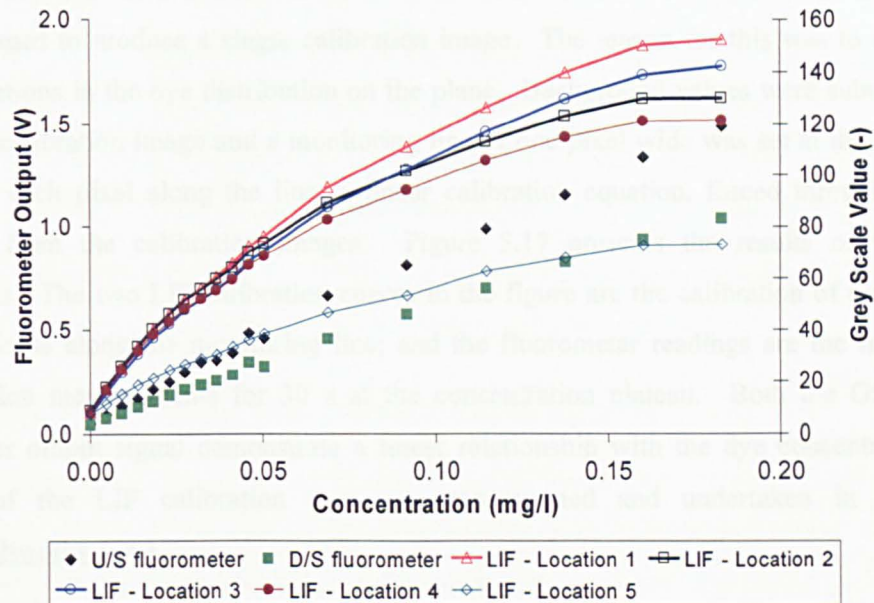


Figure 5.15 – Grey scale value and fluorometer output with respect to dye concentration (LIF images captured by the SONY HD camcorder)

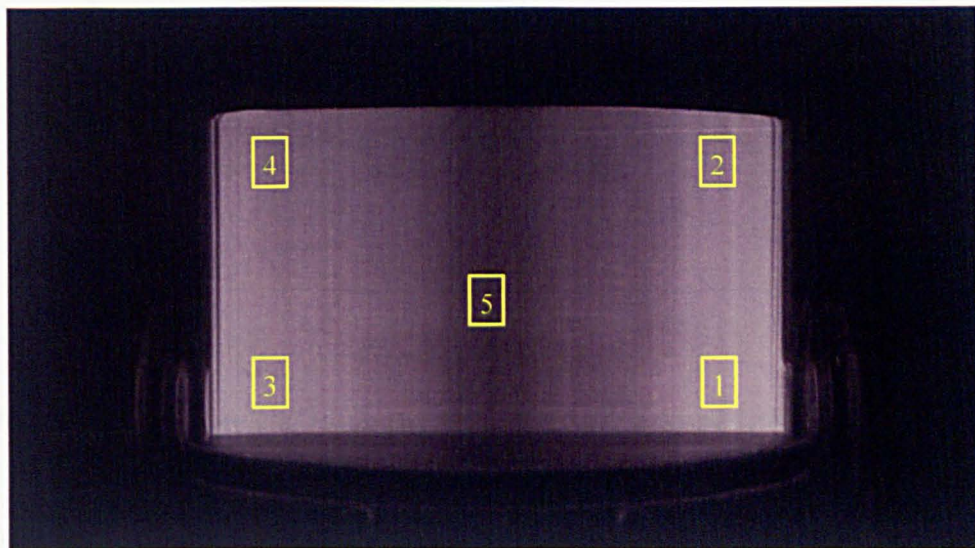


Figure 5.16 – The five monitoring pixels on the CVP (corresponding to Figure 5.15)

5.4.2.3 LIF Calibration Data Analysis

In the ideal situation where the light intensity throughout the illumination plane is uniform, the LIF calibration for the plane can be represented by a single pixel calibration. However, since the light sheet created by the scanning beam box had a non-uniform intensity profile (Figure

5.7), the calibration was undertaken on a column by column basis, i.e. one calibration equation for each column, given that there was no/insignificant light attenuation by high dye concentration. For each of the calibration concentration, 10 s of images recorded at 125 fps were averaged to produce a single calibration image. The reason for this was to remove any small variations in the dye distribution on the plane. Background values were subtracted from the single calibration image and a monitoring line of one pixel wide was set at the central pipe axis. For each pixel along the line, a linear calibration equation, forced through zero, was estimated from the calibration images. Figure 5.17 presents the results of the parallel calibrations. The two LIF calibration curves in the figure are the calibration of two randomly selected pixels along the monitoring line; and the fluorometer readings are the time average concentration measurements for 30 s at the concentration plateau. Both the GSV and the fluorometer output signal demonstrate a linear relationship with the dye concentration. The analysis of the LIF calibration data was programmed and undertaken in MATLAB[®] (www.mathworks.com).

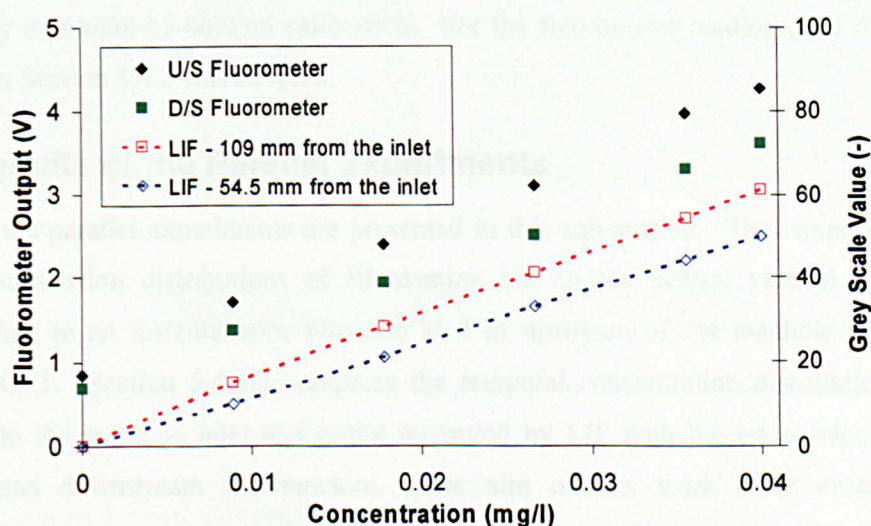


Figure 5.17 – Example of calibrations for fluorometers and LIF images (LIF images captured by the high speed camera)

5.4.3 Experimental Procedure for the Quantitative LIF Analysis

A new set of LIF data for the quantitative LIF analysis was collected based on the procedure described in Section 5.3.2. The tracer measurement was undertaken immediately after the calibrations. Approximately 25 ml of the dilute Rhodamine 6G solution (~ 1.6 mg/L) was injected instantaneously 4 m upstream of the upstream monitoring station. The LIF imaging commenced immediately after the first arrival of the dye in the manhole. A frame rate of 125 fps with a shutter speed of 1/125 s was employed, yielding 24 s of image recording per run.

For the fluorometric data, the data was logged from 1 minute prior to the dye injection and ended 1 minute later after the solute concentration at the downstream measurement position had returned to background levels. In this study, one experimental run was performed.

Temperature has a substantial influence on the fluorescent dye properties. The water temperature was monitored throughout the experiments on a regular basis. However, it was observed that the water temperature in the sump maintained a constant value of 19 °C. Therefore, the data collected did not require temperature correction (see Section 3.3.4).

The laser power was set at 3.65 W (the highest achievable and stable power) and the light sheet was generated by a scanning rate of 2000 Hz (the fastest scanning rate).

5.4.4 Data Analysis of the Parallel Experiments

Data post-processing is required to determine concentrations from the measurements collected in the parallel experiments. The LIF images were first passed through a background removal process, which involved a simple subtraction from the images of the background levels; and followed by a column-by-column calibration. For the fluorometer readings, the data analysis described in Section 3.4.2 was adopted.

5.4.5 Results of the Parallel Experiments

Results of the parallel experiments are presented in this sub-section. The temporally varying spatial concentration distributions of Rhodamine 6G on the central vertical plane (CVP) corresponding to an instantaneous injection at 4 m upstream of the manhole are shown in Section 5.4.5.1. Section 5.4.5.2 compares the temporal concentration distributions in close proximity to the manhole inlet and outlet measured by LIF with the traces recorded by the upstream and downstream fluorometers. The aim of this work is to cross-check the concentration measurements made by the two techniques.

5.4.5.1 Spatial Concentration Distributions

Figure 5.18a-d present the instantaneous spatial concentration distributions within the manhole at 1 s intervals after the first arrival of the dye on the CVP under the post-threshold conditions. It can be observed that a jet is formed underneath the storage in the manhole chamber, carrying the passive solute straight through the manhole. Because of the straight through flow, only a small amount of the solute is dispersed into the storage. This observation suggests the same conclusion as in the tracer results presented in Section 4.4.2.2, that most of the solute short-circuited the manhole without experiencing any mixing with the storage in the chamber.

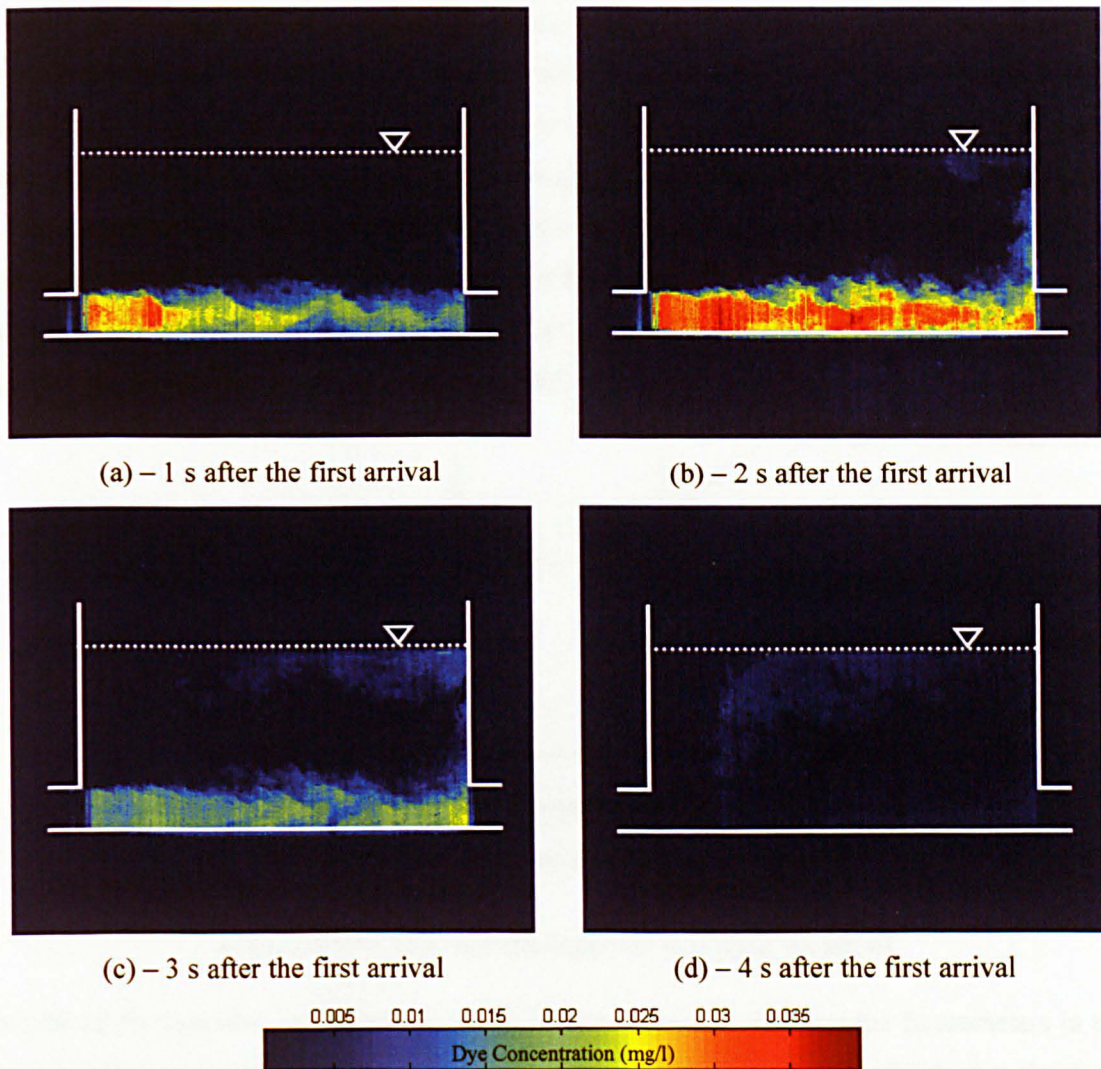


Figure 5.18 – Spatial concentration distributions within the manhole at different times with respect to the first arrival of dye (Flow from left to right)

5.4.5.2 Tracer Profiles Measured by LIF and Fluorometer

To compare the temporal concentration profiles obtained from the LIF measurements to the fluorometric data, two LIF sampling positions were set within the manhole in close proximity to the inlet and outlet (Figure 5.19). The LIF sampling station was represented by a vertical line of a pipe diameter length and one pixel wide. The average GSV along the line was assumed to represent the cross sectional average concentration at the manhole inlet or outlet. Note that the LIF and the fluorometer sampling locations do not overlap.

The upstream LIF sampling station should reveal a similar tracer profile to the corresponding fluorometer, representing the average concentration distribution for the pipe cross sectional area. This is because the flow conditions at the upstream fluorometer were fully developed and between the fluorometer and the LIF transect was a one-dimensional fully-mixed pipe flow.

There might be expected to be differences between the two downstream profiles because of the three-dimensional flow effects in the manhole (see Section 5.5.4.4.4). However, any discrepancy would be expected to occur on the tail of the temporal distribution which corresponds to the solute released from the storage volume. The earlier short-circuiting section of the profiles should remain comparable as the straight through flow is an approximation of one-dimensional fully mixed flow. Note that the longitudinal dispersion effects due to the upstream and downstream delivery pipe on the profiles should be negligible due to the short pipe length (approximately 259 mm on each side).

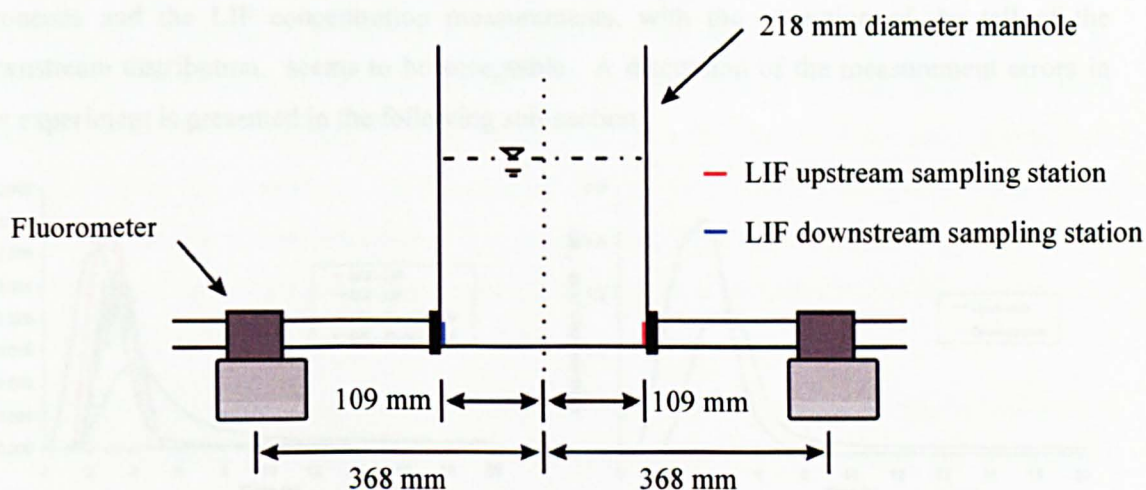


Figure 5.19 – LIF and fluorometer sampling locations

Results of the temporal concentration distribution measured by LIF and the fluorometers in the present LIF experiment are shown in Figure 5.20a. The comparison suggests that there are significant differences between the two sets of profiles. The upstream distribution of the fluorometric data obtains a marginally lower peak and a wider profile in comparison to its counterpart; a long trailing tail is also evident in the fluorometric data whereas this is not observed in the LIF profile. There is greater disagreement between the two measured downstream distributions. The fluorometric downstream profile obtains a much lower peak magnitude, only half of the LIF distribution, and the profile shape considerably differs from that obtained from LIF; the former distribution appears to be skewed and characterised by an exponentially decaying tail, whereas the latter shows an approximately Gaussian shaped distribution with no tail.

Figure 5.20b shows the traces collected in the independent tracer test at similar surcharge and discharge conditions to the LIF experiment (Chapter 3). It was expected that the fluorometric traces recorded in the two experiments would be similar in shape because their shape of the upstream concentration profiles are comparable. However, comparison of the fluorometric

concentration profiles in Figure 5.20a and Figure 5.20b shows significant deviations. For example, the peak reduction ratio of the traces approximates to 60 % in the LIF experiment, whilst it is around 35 % in the counterpart; the concentration after the peak reduces relatively gradually in Figure 5.20a but it drops sharply after the peak concentration in Figure 5.20b. Similarity in terms of the peak reduction ratio can be observed between the LIF distributions and the traces in the independent tracer study, though there is disagreement on the trailing tail between the two downstream profiles. From these comparisons, it is concluded that the fluorometric temporal concentration profiles collected in the current experiment appears to be erroneous and the LIF concentration measurements, with the exception of the tail of the downstream distribution, seems to be acceptable. A discussion of the measurement errors in this experiment is presented in the following sub-section.

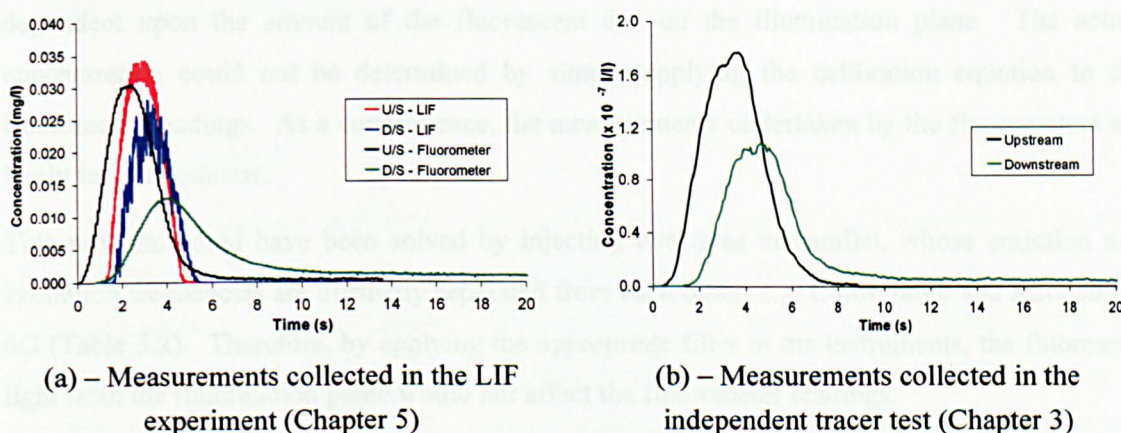


Figure 5.20 – Comparison of the temporal concentration profiles measured in the LIF experiments and the independent tracer test

5.4.6 Discussion of the Quantitative LIF Analysis

In Figure 5.20, the comparison of the temporal concentration distributions measured by LIF and the fluorometers shows significant disagreement in the shape of the profiles. These discrepancies would not be expected as explained in the previous sub-section. An investigation to the causes of the measurement errors has been conducted and two major problems associated with the experimental set-up and procedure applied in the parallel experiments were discovered.

5.4.6.1 Light Intrusion into the Fluorometers

One possible explanation can be offered to the measurement discrepancies is that the fluorescent light in the manhole affected the fluorometers, however, in different fashions during the calibration and during the experimental run. Throughout the parallel experiments, there were two major light sources contributing to the final fluorometer readings; they were the fluorescent

light from the dye inside the manhole and the concentration of the fluorescent dye at the sampling location. In normal applications of the fluorometer, the dye concentration is the only contributing element.

The light intrusion pattern introduced by the excited dye in the manhole was different during the calibration and experiment. Throughout the calibration, data was collected once the dye had been thoroughly mixed within the manhole chamber. The intensity of the light intrusion remained constant during the data collection and the effect of such was directly proportional to the concentration measuring at the fluorometer sampling positions. Therefore, the voltage reading of the fluorometers is directly proportional to concentration in Figure 5.17. However, when a pulse of Rhodamine 6G was injected into the test section, the light intrusion pattern changed and became a function of time. This is because the degree of the light intrusion is dependent upon the amount of the fluorescent dye on the illumination plane. The actual concentration could not be determined by simply applying the calibration equation to the fluorometer readings. As a consequence, the measurements undertaken by the fluorometers are likely to be erroneous.

This problem could have been solved by injecting two dyes in parallel, whose emission and excitation frequencies are distinctly separated from each other, e.g. Chlorophyll and Rhodamine 6G (Table 5.2). Therefore, by applying the appropriate filter in the instruments, the fluoresced light from the illumination plane would not affect the fluorometer readings.

Fluorescent Materials	Begin (nm)	Peak (nm)	End (nm)
<i>Chlorophyll – Fluorometer</i>			
Absorption	200	418	450
Emission	630	670	800
<i>Rhodamine 6G – LIF</i>			
Absorption	460	530	550
Emission	555	590	640

Table 5.2 – Optical characteristics of Chlorophyll (after Du *et al.*, 1998) and Rhodamine 6G (after Guymer and Harry, 1996)

5.4.6.2 Low GSV Resolution

To avoid the effects of light attenuation by high concentration of Rhodamine 6G, a range of low concentrations, between 0.00 mg/l and 0.04 mg/l, was considered in the parallel experiments. However, with the equipment and camera settings used, the system provided a GSV dynamic range of approximately 50, while the full scale is 255. This dynamic range might be too narrow

for low concentration measurements and therefore the LIF profiles shown in Figure 5.20 failed to describe low concentrations, which might have been expected at the recession tail. The failure in measuring low concentrations also resulted in an incomplete picture of the flow field on the CVP in Figure 5.18a-d. The flow field within the dead zone above the jet is not clearly revealed by the fluorescent dye.

There are a number of ways which could improve the GSV resolution for the concentration range considered. However, due to limited availability of the camera, it was not possible to test these methods listed below:

1. Reduce the frame rate and the shutter speed so that the level of light received by a camera can be increased;
2. Use a large aperture lens;
3. Increase laser power.

5.4.7 Conclusion

A parallel measurement technique using LIF and fluorimeters was adopted to quantify concentrations of a solute travelling through the manhole. This work was a feasibility study aimed to provide a workable experimental methodology for the parallel measurements. In this study, consideration of the flow plane was given to the central vertical plane (CVP) at the post-threshold conditions. The results from the LIF measurements successfully showed the temporal and spatial concentration distributions on the CVP. However, the work proved unsuccessful in the fluorometric measurements because of the influence of the fluorescence from the illumination plane. Due to limited availability of the camera, it was not possible to re-run the experiments with the improved methodology suggested in this chapter. Note that this set of experimental LIF was not used to verify the PIV evaluated data.

5.5 Particle Image Velocimetry Experiment

Detailed flow measurements within the manhole were achieved using the particle image velocimetry (PIV) technique. The aims of the work are to quantify the flow characteristics within the scale manhole and provide quantitative flow measurements to assist with a detailed validation of CFD manhole simulations. The PIV technique has the potential to produce instantaneous and time average velocity, turbulent kinetic energy and turbulent intensity information for the planes of investigation. However, the work focuses on the time average velocity for the five illumination planes under the pre- and post-threshold hydraulic conditions.

The PIV experiments were undertaken using the general arrangement described in Section 5.2. PIV data was collected when the seeding particles were continuously injected into the experimental section acting as the tracer. These particles followed the motion of the carrier fluid travelling through the manhole. The position of the seeding particle was revealed by scattering the light on the illumination plane and the instantaneous position was recorded by the high speed camera. Instantaneous velocity was determined by measuring the particle displacement between successive frames and dividing the displacement by the frame rate. The flow calculation was performed in a PIV analysis software, called DaVis FlowMaster version 7.1 by LaVision. The data analysis was carried out by the School of Engineering at the University of Warwick.

5.5.1 Recording Technique

Single frame/multi-exposure PIV and multi-frame/single exposure PIV are the two main branches in PIV recording mode. The major difference between the two is single frame/multi-exposure recording does not provide information on their temporal order of the illumination pulse producing directional ambiguity in the particle displacement (Raffel *et al.*, 1998). Single frame/multi-exposure PIV was commonly used in early PIV work, particularly when high speed digital camera was not available. This is because using this recording technique the temporal resolution of the flow field is reliant on the laser pulse speed rather than the mechanical framing limit of the image recording device.

In these PIV experiments, the multi-frame/single exposure recording technique was employed. To trace the seeding particles in the high velocity regions inside the manhole (the fastest velocity approximated to 1 m/s) and keep the particles in plane between successive frames, a frame rate of 250 fps or above was used.

5.5.2 Seeding Particles

PIV relies on seeding particles suspended in the flow to provide velocity information of the carrier fluid (Melling, 1997). The accuracy of the measurements is dictated by the ability of these particles to follow the instantaneous motion of the fluid flow. To truly reveal the flow characteristics, the particles must be of similar density to that of the carrier fluid and very small size.

In the PIV experiments, Polyamid Seeding Particles (PSP), supplied and recommended by DANTEC for water flow applications, were chosen as the tracer. These particles are white fine 'Polyamid 12' polymers and slightly denser than water ($1,030 \text{ kg/m}^3$). Their shape is non-spherical but round giving a reflective index of 1.5. The PSP used in the experiments had a mean diameter of $50 \mu\text{m}$ with a size distribution from $30 \mu\text{m}$ to $70 \mu\text{m}$. In the PIV images, the particle was seen as a point with a diameter of approximately 2 pixels. According to Raffel *et al.* (1998), this particle image size is the optimum size for digital PIV evaluation to minimise measurement uncertainty (root mean square random error) and the 'peak locking' effect. The peak locking effect is the error introduced in the analysis by rounding particle image displacement to the nearest integer value (Raffel *et al.*, 1998).

5.5.3 Experimental Procedure for the PIV Experiments

The flow field on the five illumination planes, two horizontal and three vertical, under the two hydraulic conditions was investigated in the PIV experiments. The experimental procedure adopted was similar to the procedure described in Section 5.3.2. The major challenge in this work was to adjust the illumination and imaging acquisition systems so that the seeding particles remained in-plane between successive images and no particle streaking appeared in the images.

The seeding particles, PSP, were prepared in a solution containing water and a very small amount of methanol prior to injection into the experimental section. The reason for adding methanol into the solution is to break down the surface tension on the particles preventing particle flocculation and hence improving particle distributions on the flow plane. During the experiments, the pre-mixed solution was continuously injected into the system 4 m upstream of the manhole inlet.

The camera began to record PIV images once the manhole had been fully mixed with medium density of seeding particles on the illumination plane: spatial particle distribution about 10 particles per $10 \times 10 \text{ mm}^2$ and each particle had a diameter of approximately 2 pixels. Two frame rates, which are 250 and 500 fsp giving 12 s and 6 s PIV data per run, were used to

capture the particle displacement on the planes. For the central vertical plane (CVP) and central horizontal plane (CHP), the higher frame rate was employed to keep particles with out-of-plane velocity component on the light sheet between successive images. In order to prevent streaking of particles in the PIV images, the scanning rate of the light sheet generator was adjusted to the same speed as the frame rate, achieving one camera exposure per light sheet scan. For each of the test cases, the measurements were repeated three times. Table 5.3 summarizes the recording configurations used in the PIV experiments. The laser was maintained at 3.65 W and the water level was checked before and after a test.

Plane of Interest	Frame Rate (fps) and Scanning Rate (Hz)	PIV Data per run (s)
Central vertical plane (CVP)	500	6
Left vertical plane (LVP)	250	12
Right vertical plane (RVP)	250	12
Central horizontal plane (CHP)	500	6
Mid surcharge horizontal plane (MSHP)	250	12

Table 5.3 – Summary of recording configurations for the PIV experiment

5.5.4 Particle Image Velocimetry Analysis

To evaluate the flow field using the PIV technique, the plane of investigation is divided into a number of sub-areas, called interrogation areas/windows. In each of the interrogation areas, a local displacement vector is determined from the mean particle displacement of the window between consecutive images. Taking into account the frame rate and the *magnification at imaging* enables the velocity vector for the interrogation window to be determined, and repetition of this process for each of the interrogation areas yields a map of velocity vectors describing the flow characteristics of the investigation plane. The *magnification at image* is defined as the ratio of the physical size of an object to the object size as it appears in the image.

The mean particle displacement within an interrogation area can be determined using manual particle tracking, called particle tracking velocimetry (PTV) analysis, when the tracer particle density on the investigated plane is low (Raffel *et al.*, 2002). However, for medium particle density which is normally seen in PIV, this analysis becomes impractical to use as there are too many particles to track over a series of PIV images. Statistical approaches (auto- and cross-correlation) are therefore used in the evaluation of the mean particle displacement. Since these statistical approaches comprise convoluted mathematical algorithms and iterative computations, the calculation is usually performed with the aid of a computer in association with a PIV analysis software package. For the data collected in the PIV experiments, the analysis was

performed using a software package, called DaVis FlowMaster version 7.1 by LaVision (LaVision, 2006). The data analysis was carried out by the School of Engineering at the University of Warwick.

The PIV analysis comprised three sequential stages:

1. Pre-processing - Manipulate the PIV images for best image quality
2. Evaluation - Estimate the particle displacement vectors on the plane of interest
3. Post-processing - Examine the accuracy of the estimated displacement vectors and post-process spurious vectors

5.5.4.1 PIV Pre-Processing

The PIV data required minimal pre-processing. A mask was applied to the physical boundary of the manhole so that any data outside the mask was not processed in the analysis. There were two purposes for applying the mask: it removed any redundant vectors outside the region of interest; and it reduced the computational time by reducing the number of data points had to be analysed. The masking was performed in DaVis FlowMaster version 7.1.

5.5.4.2 PIV Evaluation

Since the PIV images were recorded using the multi-frame/single exposure recording technique, the evaluation was performed using the cross-correlation function (Raffel *et al.*, 2002). This function can be regarded as a pattern-matching routine (Schlicke, 2001). It estimates the particle displacement of an interrogation window between successive images by determining the displacement to shift the window in the second image to best overlap the pattern of intensity of the same window in the first image (Figure 5.21). By calculating the physical displacement from the pixel displacement and dividing it by the frame rate, an instantaneous velocity for the fluid within the interrogation window can be obtained.

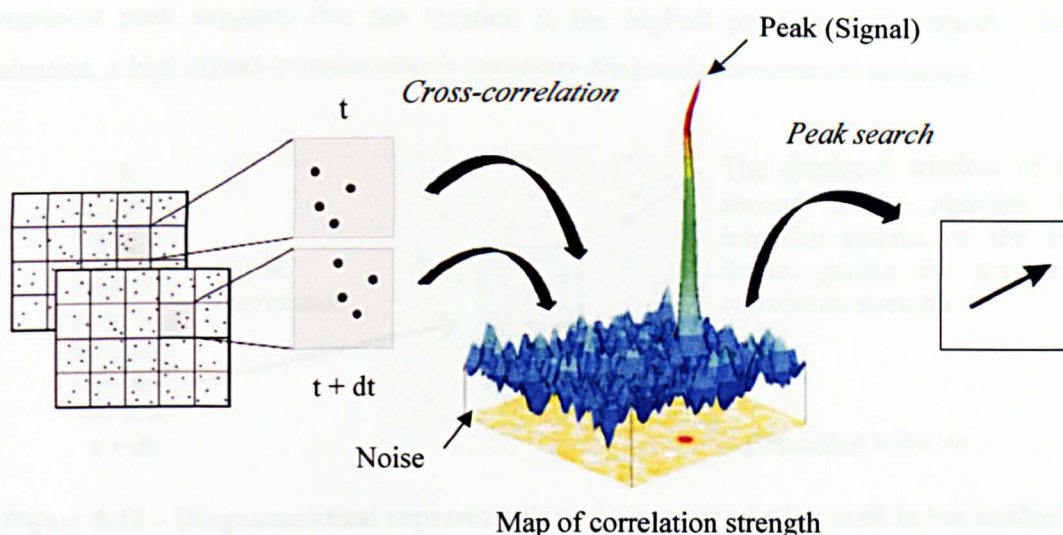


Figure 5.21 – Evaluation of PIV using cross-correlation (after LaVision, 2006)

5.5.4.2.1 Correlation Functions in PIV Analysis

The equation of the cross-correlation function used in the PIV analysis is shown in Equation 5.2. It is the standard cyclic fast Fourier transform (FFT)-based algorithm that calculates a cyclic correlation of the interrogation window. The cyclic correlation means that the correlation is computed as if the interrogation window of the subsequent frame with a size of $N \times N$ is repeated in all directions (LaVision, 2006). Figure 5.22 diagrammatically explains the cross-correlation function. Note that the FFT-based algorithm is only the similar form of the mathematical true correlation, of which requires tedious calculation process.

$$S(dx, dy) = \sum_{x=0}^{x < N} \sum_{y=0}^{y < N} I_1(x, y) I_2(x + dx, y + dy) \quad 5.2$$

where:

- dx, dy are in the range of $\pm 0.5N$ and $\pm 0.5N$ respectively
- I_1, I_2 is the GSV/image intensity of the 1st and 2nd interrogation window
- N is the size of the interrogation window
- $S(dx, dy)$ is the correlation strength at a displacement of dx, dy

In the completion of the calculation, Equation 5.2 generates a map of the correlation strength for the range of displacement dx and dy . The pixel displacement is determined by the location of the highest peak on the correlation map (Figure 5.21). In a good correlation, the map comprises some random/noisy peaks with a relatively low magnitude (noise) and a prominent peak with a significantly higher magnitude (signal). The low peaks indicate an inappropriate displacement such that the pattern of the intensity between the two frames does not match. Conversely, the

prominent peak suggests that the location is the highest possible displacement. In PIV evaluation, a high signal-to-noise ratio is necessary for good measurement accuracy.

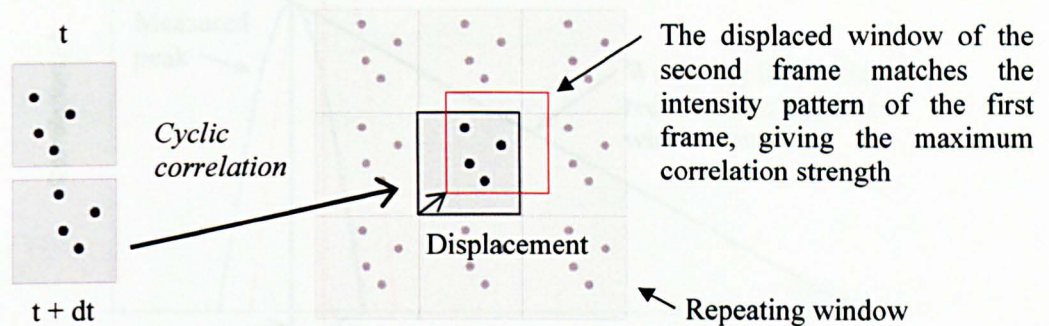


Figure 5.22 – Diagrammatical representation of cross-correlation used in the analysis

As a result of the cyclic correlation, the FFT-based cross-correlation algorithm offers a quicker computation speed, 50 times faster (LaVision, 2006), than the original correlation function. However, there is a disadvantage associated with the algorithm. The periodic arrangement of a finite sized input data, shown in Figure 5.22, in the algorithm introduces a weighting of the correlation, with a maximum value of 1 for zero displacement and linearly decreasing towards 0 for a displacement equal to the interrogation window size. This is because when the actual displacement increases, less data within the window is actually correlated and contributes to the correlation strength. As a result, the analysis inherently tends to bias towards a smaller displacement due to the weighting factor (Figure 5.23); and the accuracy of the measurements is likely to reduce as the actual displacement increases due to the reduction in the correlation strength for the correct displacement. As a rule of thumb, the FFT-based function should be used when the actual displacement is less than about 1/3 of the interrogation window size to ensure a high signal to noise ratio (LaVision, 2006). Alternatively, a correlation coefficient or an advanced correlation technique called the *window shifting approach* can be adopted to reduce/eliminate the effects of the weighting. Details of the former approach can be founded in Raffel *et al.* (1998) and the latter analytical approach, which was considered in the analysis, is discussed in Section 5.5.4.2.2.

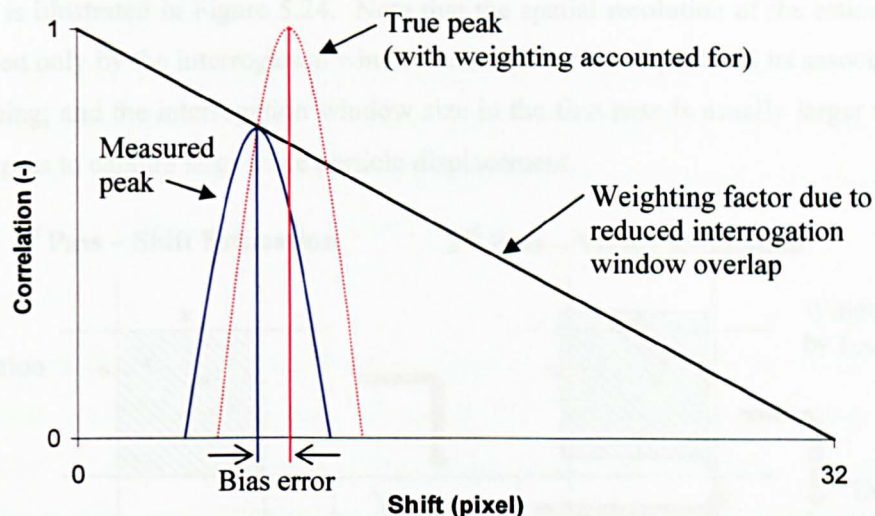


Figure 5.23 – Bias error introduced in the calculation of the cross-correlation using FFT (after Raffel *et al.*, 1998)

5.5.4.2.2 Window Shifting Approach

The *window shifting approach* was adopted to improve the measurement accuracy of the PIV data analysis. This works by shifting the interrogation window position based on a reference vector during vector calculations so that more data can be correlated resulting in a higher correlation strength and hence a higher accuracy. The prominent peak is ideally located near the centre of the ‘displaced’ correlation plane; therefore a weighting value approaching 1 can be obtained. An additional benefit of this *window shifting approach* is that a smaller interrogation area could be used, increasing the spatial resolution of the flow measurement while the measurement of the mean particle pixel displacement for each interrogation window maintains a similar level of accuracy to that of a larger window (LaVision, 2006).

In the PIV software, there are two ways to set up the reference vector in the *window shifting approach*. The reference vector can be obtained by assigning an arbitrary value and the vector will be used globally for the area of interest throughout the entire PIV data. Alternatively, the vector can be determined from a reference vector field, estimated by a ‘first pass’ FFT-based cross-correlation of the corresponding successive frames. In this approach, called *adaptive multi-pass*, the interrogation window shift may vary across the investigation area and throughout the data depending upon the instantaneous flow field. In theory, this technique should provide more realistic reference vectors, as it accounts for the spatial and temporal flow variations in the PIV data.

The *adaptive multi-pass* analysis was used in the PIV analysis to improve the accuracy of the PIV evaluations. A graphical explanation of the *adaptive multi-pass* technique for cross-

correlation is illustrated in Figure 5.24. Note that the spatial resolution of the estimated vector is determined only by the interrogation window size in the second pass and its associated degree of overlapping; and the interrogation window size in the first pass is usually larger than that in the second pass to capture large scale particle displacement.

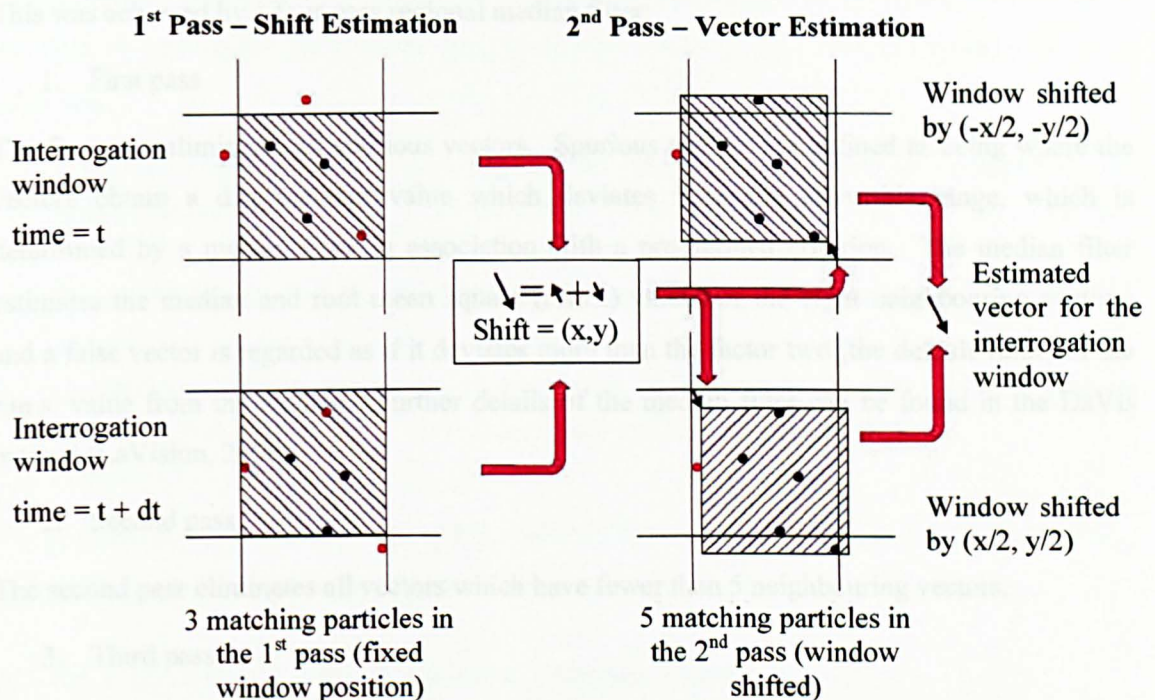


Figure 5.24 – Adaptive multi-pass technique in cross-correlation (after LaVision, 2006)

5.5.4.2.3 Size of Interrogation Window

A decreasing interrogation window size approach was adopted in the *adaptive multi-pass* cross-correlation. A larger window was defined in the first pass to ensure that the large scale particle displacement in the high velocity zone, such as the core of the jet, could be resolved; whilst the smaller window was used to increase the spatial resolution of the measurements and to capture the smaller scale fluid motions. The size chosen for the *adaptive multi-pass* analysis varied slightly over the case study. Typically, a 32 x 32 window size with a 50 % overlap was used in the first pass and a 12 x 12 window size with 25 % overlap in the second pass. This setting was used for a flow with a maximum pixel displacement of between 8 and 15 pixels. The physical dimensions of the interrogation window in the second pass varied from 2.4 x 2.4 mm² to 3.7 x 3.7 mm². Note that the window size in the second pass (8 x 8 pixels² or 12 x 12 pixels²) was the smallest optimum size compromising the size of the particle in the image (2 pixel diameter), quality of the correlation strength and the spatial resolution of the measurements.

5.5.4.3 Post-Processing

By default, the DaVis PIV analysis software performed validation, or post-processing, for every estimated reference and instantaneous vector field. The validation was to ensure that the evaluated vector fields do not contain any spurious displacement vectors for subsequent analysis. This was achieved by a four pass regional median filter:

1. First pass

The first pass eliminates all spurious vectors. Spurious vectors are defined as being where the vectors obtain a displacement value which deviates from the allowable range, which is determined by a median filter in association with a pre-defined criterion. The median filter estimates the median and root mean square (r.m.s.) values of the eight neighbouring vectors; and a false vector is regarded as if it deviates more than the factor two (the default value) of the r.m.s. value from the median. Further details of the median filter can be found in the DaVis manual (LaVision, 2006).

2. Second pass

The second pass eliminates all vectors which have fewer than 5 neighbouring vectors.

3. Third pass

Once the bad vectors are removed, the empty spaces are filled up with interpolated vectors (new) as many as possible. The criterion for filling in is the same median filter as for the removal in the first pass. The interpolated vectors have to be encompassed in the range of the factor three (the default setting) of the r.m.s. value from the median calculated from the existing neighbour vectors using the median filter; or otherwise they will be eliminated. The interpolated vector is estimated by averaging at least two existing neighbouring vectors.

4. Final pass

Same as the second pass, the final pass eliminates all vectors which have less than 5 neighbouring vectors.

Once the four pass regional median filter had completed, the evaluated vector field was smoothed by a 3 x 3 smoothing filter to reduce noise (LaVision, 2006). The filter filled the remaining and former empty spaces with an average of all non-zero neighbour vectors.

5.5.4.4 PIV Validation

PIV data validation was performed to examine the fidelity of the PIV measurements. Since the aim of the experiment is to obtain time average velocity for the five illumination planes within

the scale manhole model, the validation focuses only on this dataset although data for other flow variables, such as the instantaneous velocity, turbulent kinetic energy and turbulent intensity, is also available. Without flow data from other velocity measurement technique such as laser doppler anemometry, the verification of the PIV data was based on validation of the pipe flow measurements, cross-reference to the LIF images and comparisons of the measured velocity at the lines of intersection between the vertical and horizontal planes. The purposes of the three tasks are:

1. Validation of pipe flow measurements - Verify the velocity estimations by comparing the discharge values calculated from the PIV data and measured by the Venturi meter
2. Cross-reference to the LIF images - Validate the flow pattern estimated by the PIV technique
3. Comparisons of the measured velocity at the lines of intersection - Examine the consistency of the PIV measurements for the vertical and horizontal planes

The present study employed one set of 6 s data for the validation exercise and the justification for this is discussed in the following sub-section.

5.5.4.4.1 Recording Time for a Time Average Flow Solution

Despite the fact that the PIV experiments were carried out under a steady state hydraulic condition, i.e. constant flowrate and surcharge, temporal variations of the flow field due to the turbulent motions of the jet were observed in the manhole. In order to obtain a 'true' mean flow field from the temporally varying fluid flow using the PIV technique, the data recording time has to be sufficiently long so as to capture all possible large and small scale fluid motions. To ensure the PIV data obtained for the scale manhole is representative of the mean flow field, a sensitivity study of the variations of the flow field averaged from different length of data was undertaken.

The study considered the PIV results of the horizontal plane at the pipe centreline (CHP) under the pre- and post-threshold conditions for the investigation. This plane was chosen because the recording time per run was the shortest (6 s) compared to the other non-central planes (Table 5.3); and the flow field on the CHP had more temporal fluctuations than the others, as the CHP sliced through the centre of the turbulent jet and the recirculation besides the jet. For each surcharge condition, three flow field solutions, which are the 6 s, 12 s and 18 s average data, were compared. Due to limited buffer size of the high speed camera, the 12 s and 18 s time average results were generated by averaging the data of two and three repeat runs. Note that there was a time interval of approximately 5 minutes between repeat experiments.

The time average flow fields for the CHP at the pre- and post-threshold conditions generated from 6 s, 12 s and 18 s of PIV data are presented in Figure 5.25 and Figure 5.26. For each surcharge case, three contour plots are shown:

1. Figure 5.25a and Figure 5.26a present the superposition of the longitudinal velocity contours for the three time average results; the flooded contours associated with the solid black lines represents the 6 s average data (randomly selected); the dashed lines and the 'dash-dot-dot' lines correspond to the 12 s and 18 s average results respectively.
2. Figure 5.25b and Figure 5.26b shows the difference between the 18 s and 6 s average solutions (Equation 5.3).
3. Figure 5.25c and Figure 5.26c shows the difference between the 18 s and 12 s average results (Equation 5.3).

Difference = 18 s average data – 6 s or 12 s average results

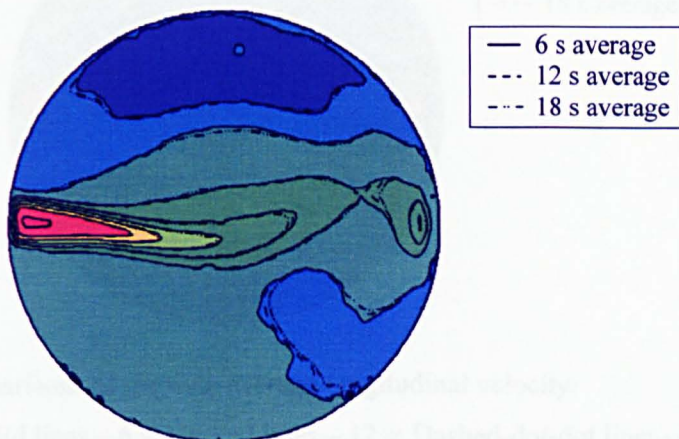
5.3

Comparisons of the time average results for the same surcharge condition reveal almost unnoticeable variations between the data (Figure 5.25a and Figure 5.26a). The difference between the 18 s average results and two time average results appears to vary in a range of ± 0.05 m/s over the plane (Figure 5.25b-c and Figure 5.26b-c). These velocity variations are equivalent to a particle displacement of ± 0.33 pixels. Small flow fluctuations and errors in sub-pixel estimation in the PIV cross-correlation analysis might have contributed to the insignificant velocity differences. It is clear that there are smaller variations between the 12 s and the 18 s average data than between the 6 s and 18 s average results. However, due to limited availability of the PIV software, a 6 s average PIV data has been accepted to be an acceptable time average flow field solution for CFD validation. Therefore, only one set of 6 s data is used to compare with the CFD results in Chapter 6.

In Figure 5.25a and Figure 5.26a, there are regions close to the manhole inlet and outlet where the estimated velocities appear to be implausible. For example, in Figure 5.25a, a large velocity gradient (accelerating) can be noticed immediately after the manhole inlet, where a relatively flat gradient (constant velocity) in the longitudinal direction would have been expected (Abramovich, 1963). Measurement errors are discussed in the following sub-section.

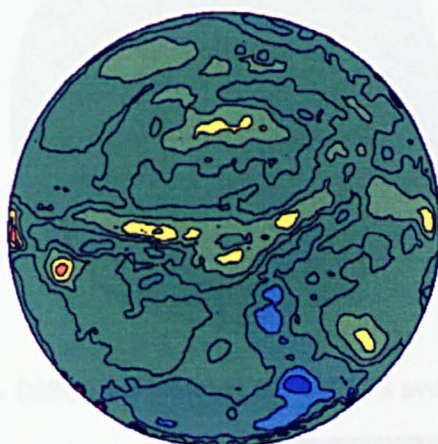
Turbulence data, such as turbulent kinetic energy, Reynolds stresses and turbulent intensity, is also available from the PIV evaluation. However, comparisons of the repeat test results (6 s average) showed inconsistencies in the profiles (e.g. Figure 5.27), suggesting that these measurements are not reliable. The turbulence data is not used for the CFD validation in Chapter 6 because of this reason. It is also thought that to acquire a 'true' time average

turbulence field more than 18 s of PIV data might be required. However, there was insignificant PIV data to prove this.



(a) – Comparisons of the time average longitudinal velocity:

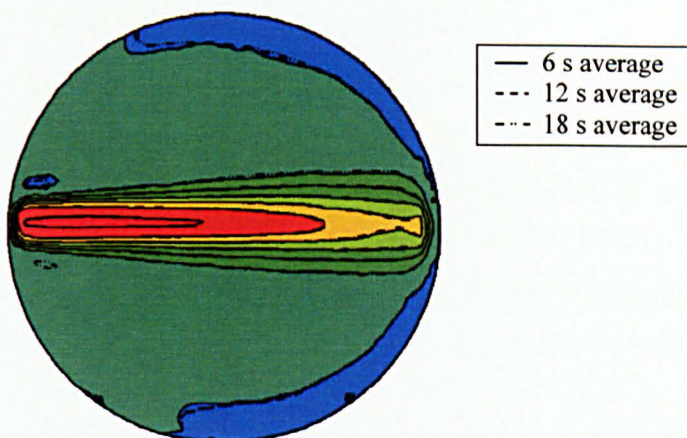
Colour contours with solid lines – 6 s; Dashed lines – 12 s; Dash-dot-dot lines – 18 s



(b) - Difference between 6 s and 18 s average (c) - Difference between 12 s and 18 s average

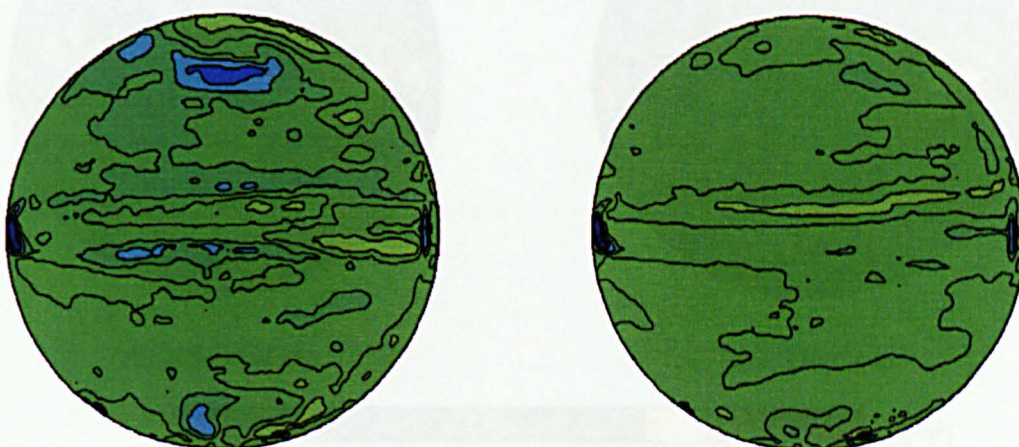


Figure 5.25 – Comparisons of the time average longitudinal velocity for the CHP under the pre-threshold conditions (Flow from left to right)



(a) – Comparisons of the time average longitudinal velocity:

Colour contours with solid lines – 6 s; Dashed lines – 12 s; Dashed-dot-dot lines – 18 s



(b) - Difference between 6 s and 18 s average (c) - Difference between 12 s and 18 s average



Figure 5.26 – Comparisons of the time average longitudinal velocity for the CHP under the post-threshold conditions (Flow from left to right)

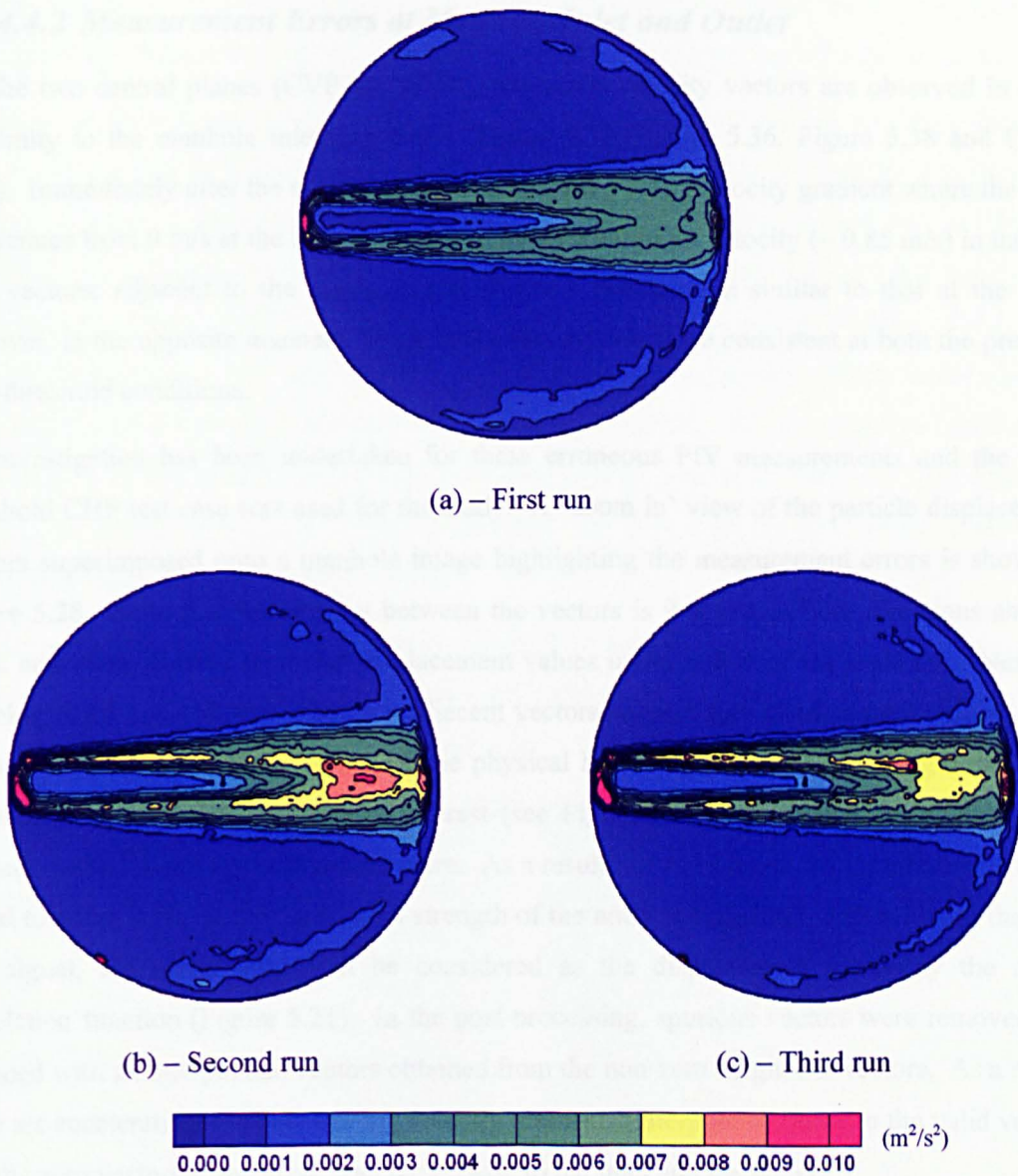


Figure 5.27 – Comparisons of the turbulent kinetic energy for the CHP under the post-threshold conditions between repeat tests (Flow from left to right)

5.5.4.4.2 Measurement Errors at Manhole Inlet and Outlet

On the two central planes (CVP and CHP), erroneous velocity vectors are observed in close proximity to the manhole inlet and outlet (Figure 5.33, Figure 5.36, Figure 5.38 and Figure 5.41). Immediately after the manhole entrance, there is a steep velocity gradient where the fluid accelerates from 0 m/s at the inlet boundary to the maximum jet velocity (~ 0.85 m/s) in three to four vectors; adjacent to the manhole exit shows a deceleration similar to that at the inlet, however, in the opposite manner. These measurement errors are consistent at both the pre- and post-threshold conditions.

An investigation has been undertaken for these erroneous PIV measurements and the post-threshold CHP test case was used for the study. A 'zoom in' view of the particle displacement vectors superimposed onto a manhole image highlighting the measurement errors is shown in Figure 5.28. Note that the spacing between the vectors is 9 pixels in both directions and the black and white vectors represent displacement values under and over the scale bar. Near the chamber entry and exit, the boundary adjacent vectors suggest low displacement values. This might be explained by the presence of the physical boundary (the wall and flange), in that it attenuated the light into the area of interest (see Figure 5.7) and reduced the contrast ratio between particles and the background there. As a result, the correlation map might obtain a low signal to noise ratio. If the correlation strength of the noise is significant and is higher than the real signal, the noise spike will be considered as the displacement vector by the cross-correlation function (Figure 5.21). In the post-processing, spurious vectors were removed and replaced with an interpolated vectors obtained from the non-zero neighbour vectors. As a result, there are accelerating and decelerating velocity gradients, interpolated between the valid vectors and the zero vectors at the mask boundary, close to the inlet and the outlet.

The inlet and outlet boundaries affect a number of vectors downstream (inlet) and upstream (outlet) within the manhole leading to a velocity gradient in these regions (Figure 5.28). The number of affected vectors was estimated by applying four rectangular masks of the same size placed at different longitudinal positions close to the inlet. The masks were progressively shifted away from the inlet by one vector spacing (9 pixels) each time, except the two masks closest to the inlet between which had a distance of two vector spacing (18 pixels) (Figure 5.29). A small rectangular mask, instead of a full size mask for the CHP, was used to reduce computational time. For each of the masks applied, 6 s of PIV data was analysed and the longitudinal velocity along the pipe centreline was extracted from the evaluation. Figure 5.30 compares the derived centreline velocity profiles. The comparison suggests that these profiles have no noticeable difference after approximately 15 mm from the inlet; while there are

variations between 0 mm and 15 mm, implying that this region is affected by the inlet boundary. This study also implies that the velocity gradient is not a function of the position of the mask.

A similar study was not considered for the outlet due to limited availability of the software. However, the extent of the boundary effects should be similar to that at inlet. This was inferred by comparing the longitudinal distance of the two velocity slopes in Figure 5.44a and the fact that the manhole is symmetrical about the manhole vertical centreline. Figure 5.44a presents the longitudinal velocity profiles at the pipe centreline for the two central planes at the post-threshold conditions (CVP and CHP). The inlet and outlet boundary effects under the pre-threshold conditions should be comparable to the post-threshold. This is suggested based on the comparisons of the longitudinal distance of the velocity gradients under the two hydraulic regimes in Figure 5.43a and Figure 5.44a; and the fact that the two experiments were undertaken using the same manhole model.

For the purposes of CFD validation, the manhole PIV measurements closer than 15 mm to the inlet and outlet boundaries should not be used. This distance has taken into account of the measurement errors close to the inlet and outlet.

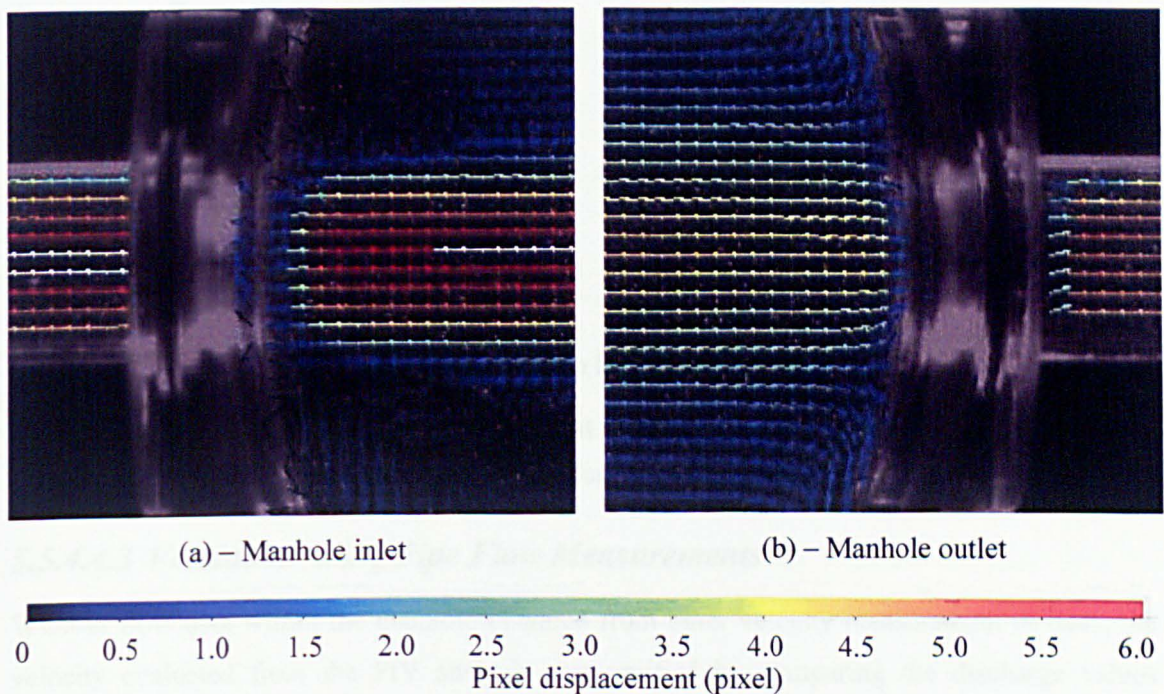
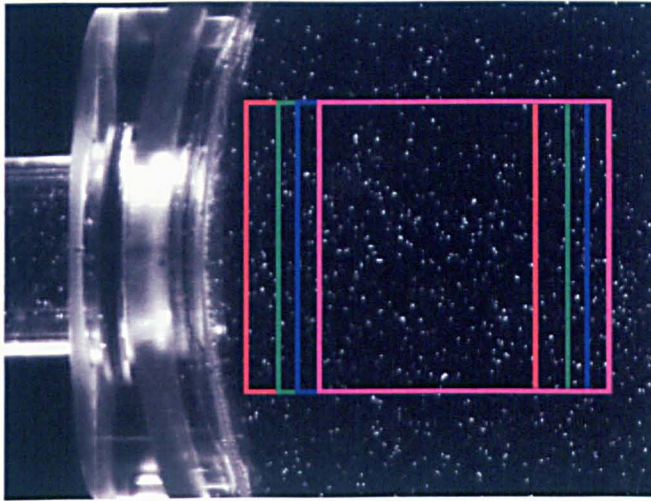


Figure 5.28 – A ‘zoom-in’ view of the particle displacement vectors in close proximity to the manhole inlet and outlet for the CHP under the post-threshold conditions (Flow from left to right)



Mask	Distance from the Inlet	
	(Pixel)	(mm)
Red	11.5	3.48
Green	29.5	8.94
Blue	38.5	11.67
Pink	47.5	14.39

Figure 5.29 – Positions of the rectangular mask for the investigation of the effects of the inlet boundary

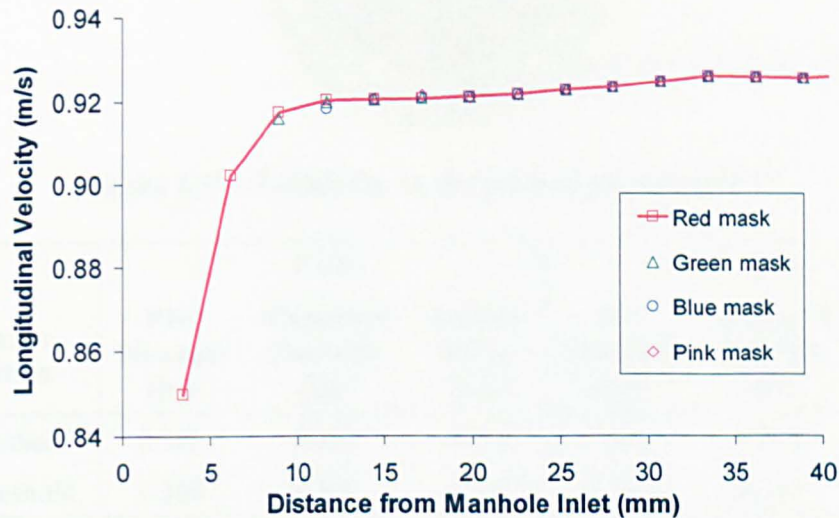


Figure 5.30 – Comparisons of the longitudinal velocity profile along the pipe centreline for the four masks on the CHP under the post-threshold conditions

5.5.4.4.3 Validation using Pipe Flow Measurements

Without flow data within the manhole obtained from other velocity measurement devices, the velocity evaluated from the PIV analysis was verified by comparing the discharge values estimated from the PIV measurements and measured by the Venturi meter. To estimate the discharge through the system from the PIV measurements, velocity data from the fully developed flow within the upstream pipe, approximately 36 mm upstream of the manhole inlet, was used. This sampling point was found to be free from the boundary effects mentioned in Section 5.5.4.4.2.

The assessment was undertaken for the central planes (CVP and CHP) under the pre- and post-threshold conditions. The discharge was calculated by the method stated below:

1. Extract the velocity profile from the sampling position at the upstream pipe.
2. Divide the pipe cross-section into a number of concentric rings (the number depends on the amount of data point on the profile (Figure 5.31)).
3. Estimate the flowrate of the area of the ring corresponding to a velocity data point.
4. Sum all the flowrates to give the discharge through the cross section.

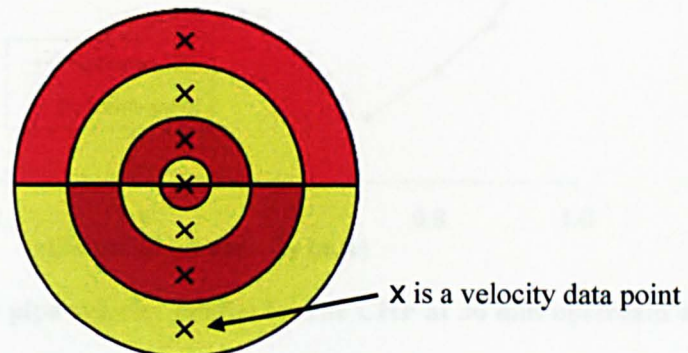


Figure 5.31 – Estimation of discharge from pipe velocity

Hydraulic Condition	CVP			CHP		
	PIV Flowrate (l/s)	Measured Flowrate (l/s)	Absolute Error (%)	PIV Flowrate (l/s)	Measured Flowrate (l/s)	Absolute Error (%)
Pre-threshold	0.352	0.352	0.014	0.351	0.346	1.479
Post-threshold	0.360	0.345	4.282	0.348	0.344	1.096

Table 5.4 – Comparisons of PIV estimated flowrate and measured flowrate

Table 5.4 shows the comparisons of the flowrates estimated from the PIV pipe data and measured by the Venturi meter. It is encouraging that the PIV data matches well with the measured flowrate, providing confidence in the PIV velocity measurements. The errors between the two sets of data (PIV and Venturi meter) appear to be less than 5 %, although the PIV estimated flowrates are consistently greater than those measured. This estimation error might result from insufficient number of data points, only 9 points, defining the velocity profile across the pipe. Examples of the velocity profiles are shown in Figure 5.32. The difference between the two profiles might be due to the error in sub-pixel estimation.

It may be noticed that the measured flowrate in the CVP pre-threshold study is marginally greater than the operating flowrate in the other studies by 2 %. This is due to the difficulty in adjusting the flowrate via the discharge valve.

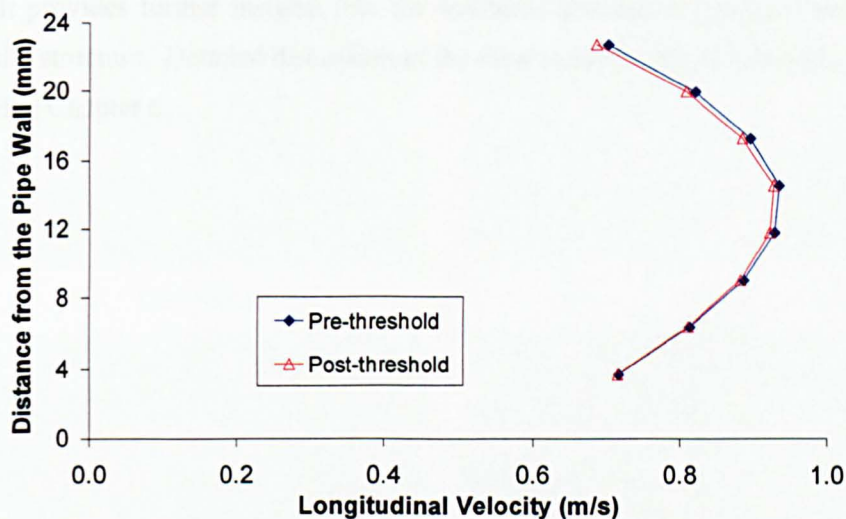


Figure 5.32 – Examples of the pipe velocity profile for the CHP at 36 mm upstream of the inlet

5.5.4.4.4 Cross-reference to the LIF data

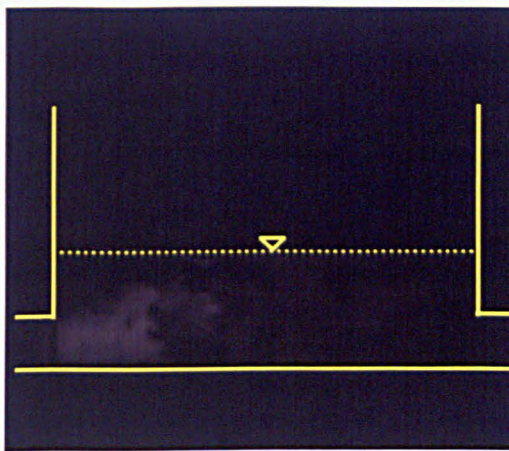
The complexity of the three-dimensional flow field within the manhole under the two contrasting hydraulic conditions formed a challenge in the PIV flow visualisation experiments. Measurement errors are likely to occur in the regions where the fluid flows ‘in and out of the illumination plane’ and travels at very high speed, such that particles do not remain in plane between successive frames leading to erroneous vector estimations. To examine the validity of the PIV measured flow fields, the data was compared to the LIF flow images. This comparison suggests whether the flow pattern obtained from PIV is plausible.

The LIF and PIV data of the flow field for the investigated planes under the pre- and post-threshold conditions is given in Figure 5.33 - Figure 5.42. For presentation purposes, four LIF images at different times after the first arrival of the dye in the manhole (0.5 s, 2 s, 4 s and 6 s) (a-d); the qualitative flow field identified from the 24 s LIF image recording (e); and the PIV results (f) are presented in these figures. The four LIF images suggest the primary flow pattern on the plane (blue arrows in the identified flow field), while secondary circulations (green arrows in the identified flow field) were determined from the 24 s recorded images. The 24 s LIF data for the ten test cases are attached in the form of a CD with the thesis.

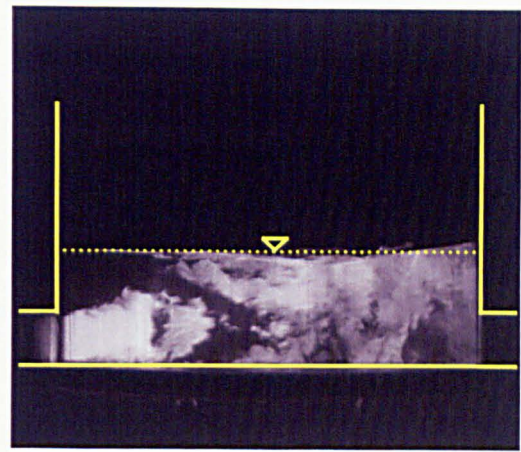
In general, the LIF and PIV results show great similarity over the flow patterns for the five planes under the two surcharge conditions. The shape of the jet, as well as the large and small

eddy motions, appear to be determined correctly by the PIV technique. This comparison provides more confidence in the PIV measurements for further applications.

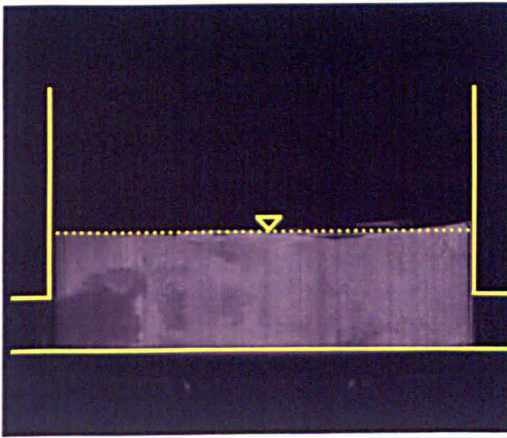
The comprehensive picture of flow visualisation in the manhole structure is novel in manhole research. It provides further insights into the hydraulic and solute transport processes within this hydraulic structure. Detailed discussion of the flow field and solute transport characteristics is presented in Chapter 6.



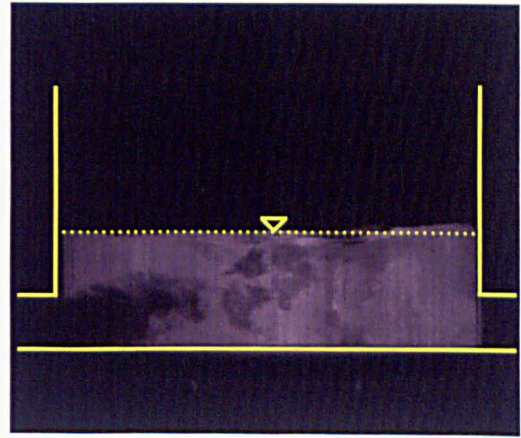
(a) – 0.5 s after first arrival



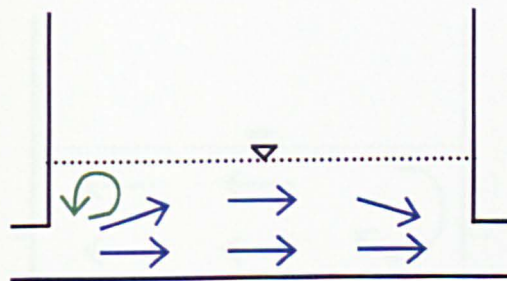
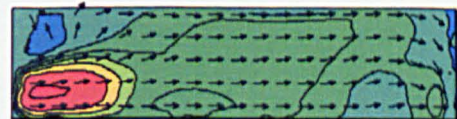
(b) – 2.0 s after first arrival



(c) – 4.0 s after first arrival



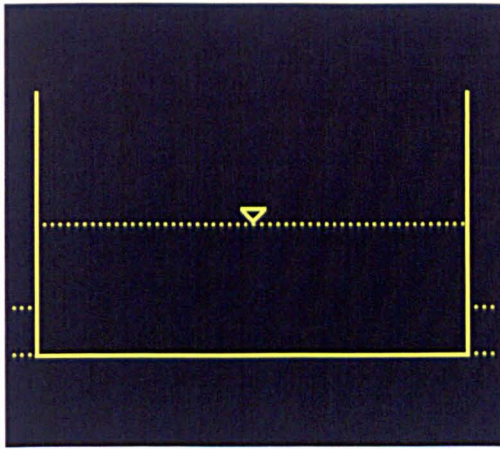
(d) – 6.0 s after first arrival

(e) – Flow pattern obtained from 24 s LIF data
(Blue – Pri. flow; Green - Sec. circulations)

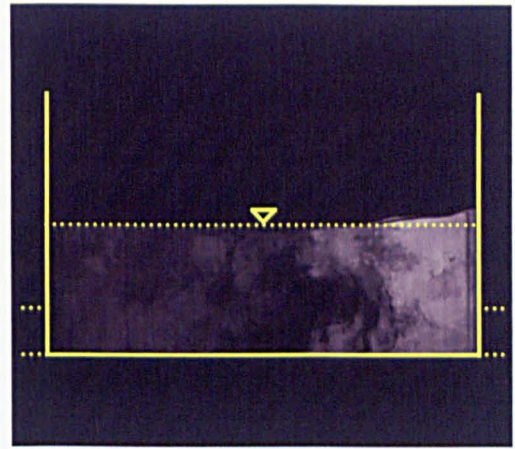
Color bar for longitudinal velocity (m/s):
 -0.30 -0.15 0.00 0.15 0.30 0.45 0.60 0.75 0.90

(f) – PIV results (Vector – Flow direction;
Contour - Longitudinal velocity)

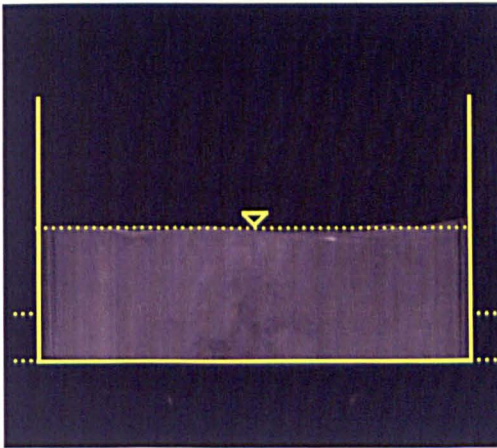
Figure 5.33 – Comparisons of the LIF and PIV flow field for the CVP at the pre-threshold condition (Flow from left to right)



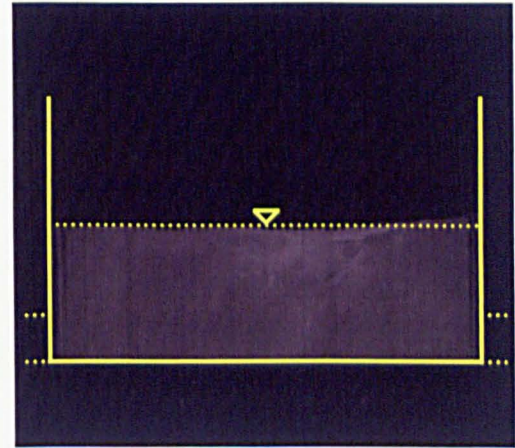
(a) – 0.5 s after first arrival



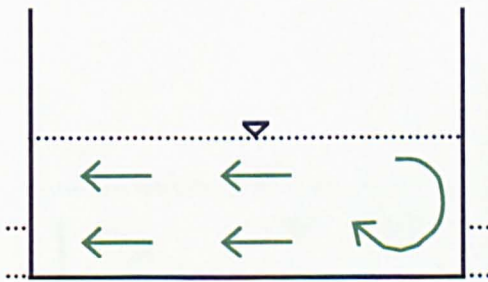
(b) – 2.0 s after first arrival



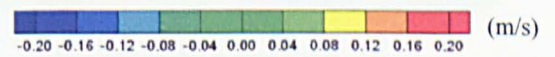
(c) – 4.0 s after first arrival



(d) – 6.0 s after first arrival

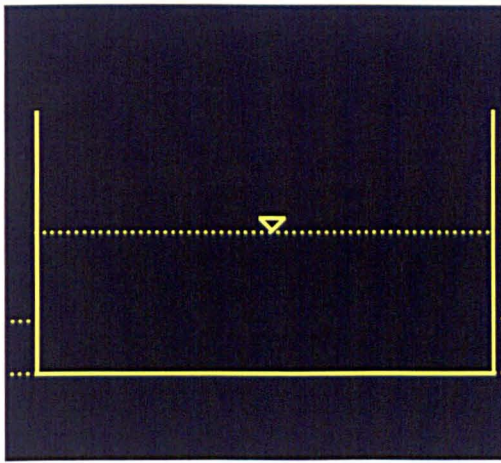


(e) – Flow pattern obtained from 24 s LIF data (Blue – Pri. flow; Green - Sec. circulations)

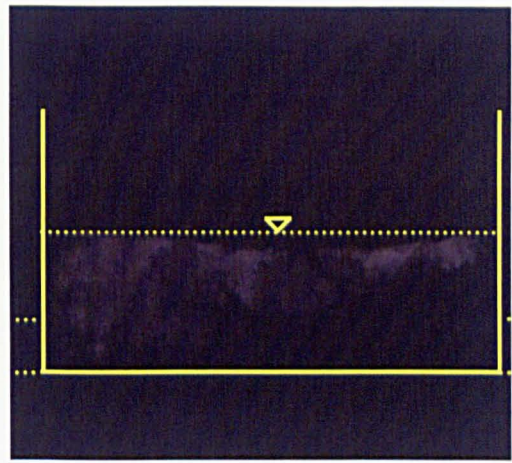


(f) – PIV results (Vector – Flow direction; Contour - Longitudinal velocity)

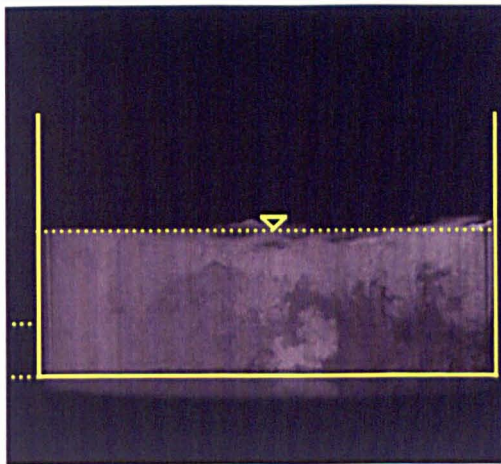
Figure 5.34 – Comparisons of the LIF and PIV flow field for the LVP at the pre-threshold conditions (Flow from left to right)



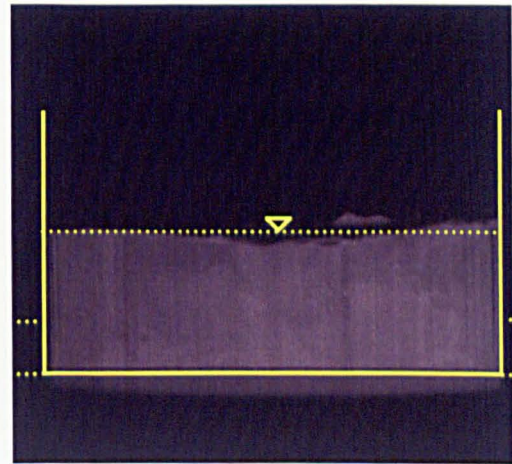
(a) – 0.5 s after first arrival



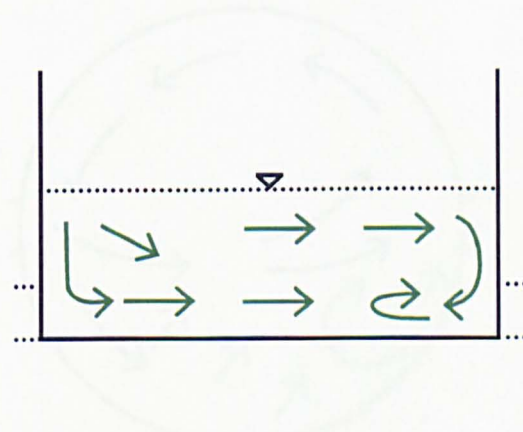
(b) – 2.0 s after first arrival



(c) – 4.0 s after first arrival



(d) – 6.0 s after first arrival

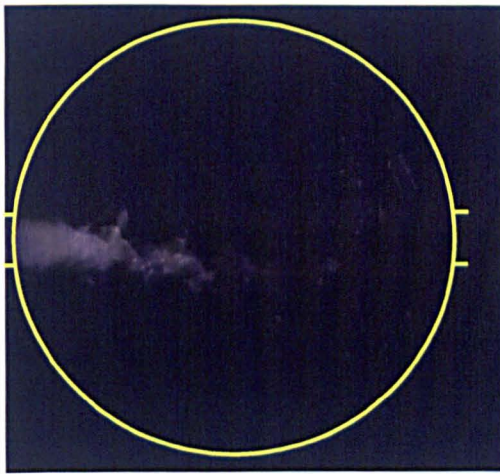


(e) – Flow pattern obtained from 24 s LIF data
(Blue – Pri. flow; Green - Sec. circulations)

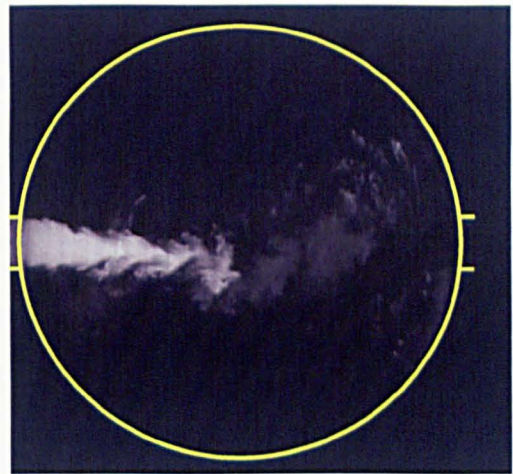


(f) – PIV results (Vector – Flow direction;
Contour - Longitudinal velocity) (m/s)

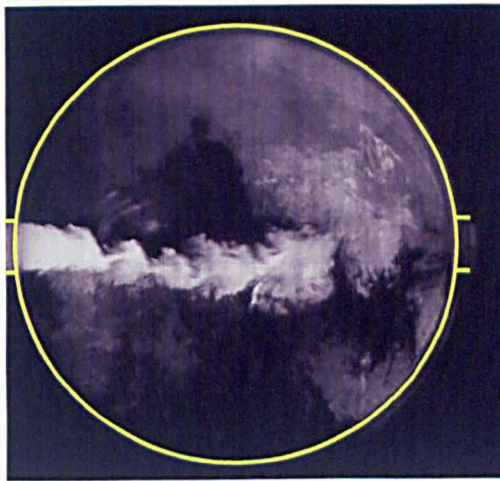
Figure 5.35 – Comparisons of the LIF and PIV flow field for the RVP at the pre-threshold conditions (Flow from left to right)



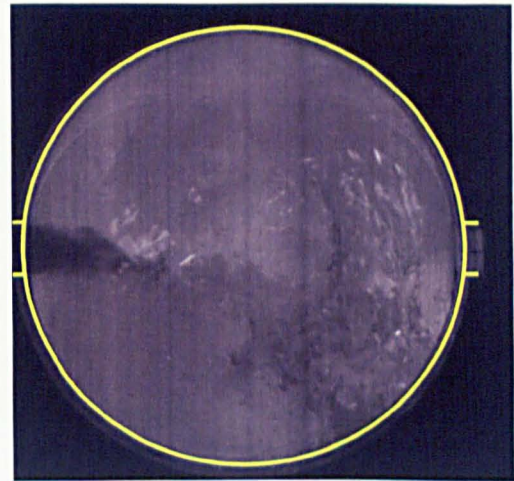
(a) – 0.5 s after first arrival



(b) – 2.0 s after first arrival



(c) – 4.0 s after first arrival



(d) – 6.0 s after first arrival

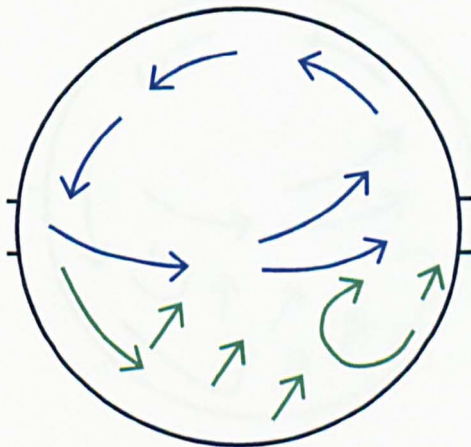
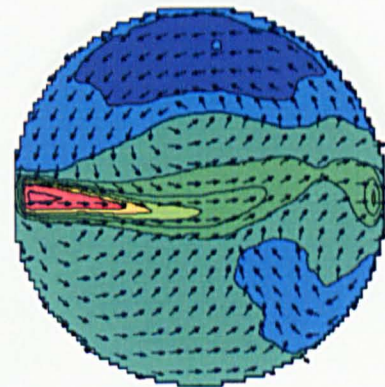
(e) – Flow pattern obtained from 24 s LIF data
(Blue – Pri. flow; Green - Sec. circulations)(f) – PIV results (Vector – Flow direction;
Contour - Longitudinal velocity)

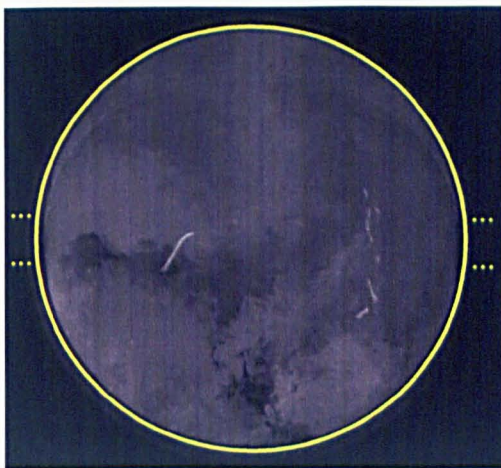
Figure 5.36 – Comparisons of the LIF and PIV flow field for the CHP at the pre-threshold conditions (Flow from left to right, top view)



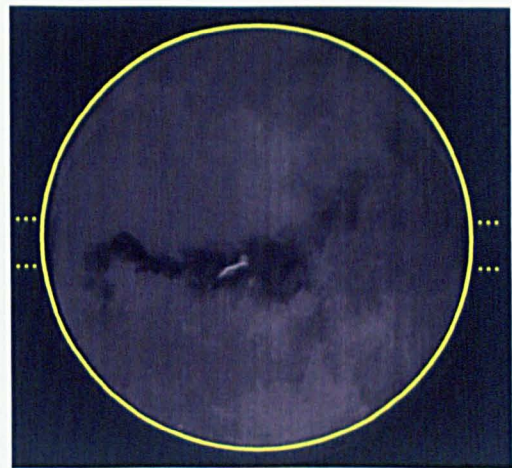
(a) – 0.5 s after first arrival



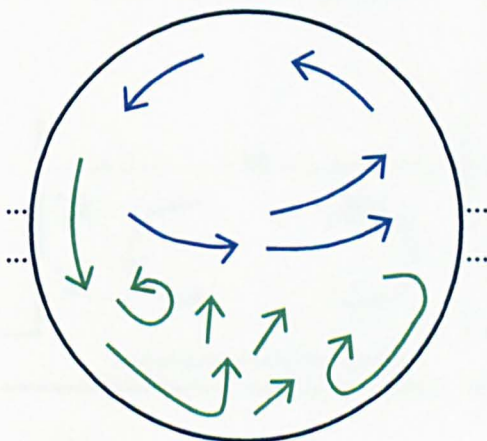
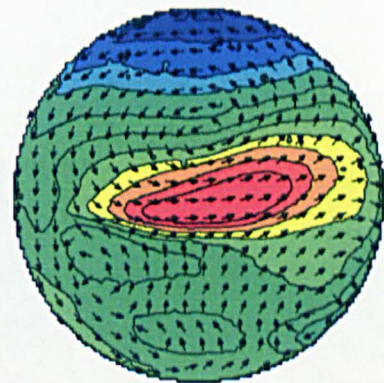
(b) – 2.0 s after first arrival



(c) – 4.0 s after first arrival



(d) – 6.0 s after first arrival

(e) – Flow pattern obtained from 24 s LIF data
(Blue – Pri. flow; Green - Sec. circulations)

(m/s)
 -0.20 -0.16 -0.12 -0.08 -0.04 0.00 0.04 0.08 0.12 0.16 0.20

(f) – PIV results (Vector – Flow direction;
Contour - Longitudinal velocity)

Figure 5.37 – Comparisons of the LIF and PIV flow field for the MSHP at the pre-threshold conditions (Flow from left to right, top view)

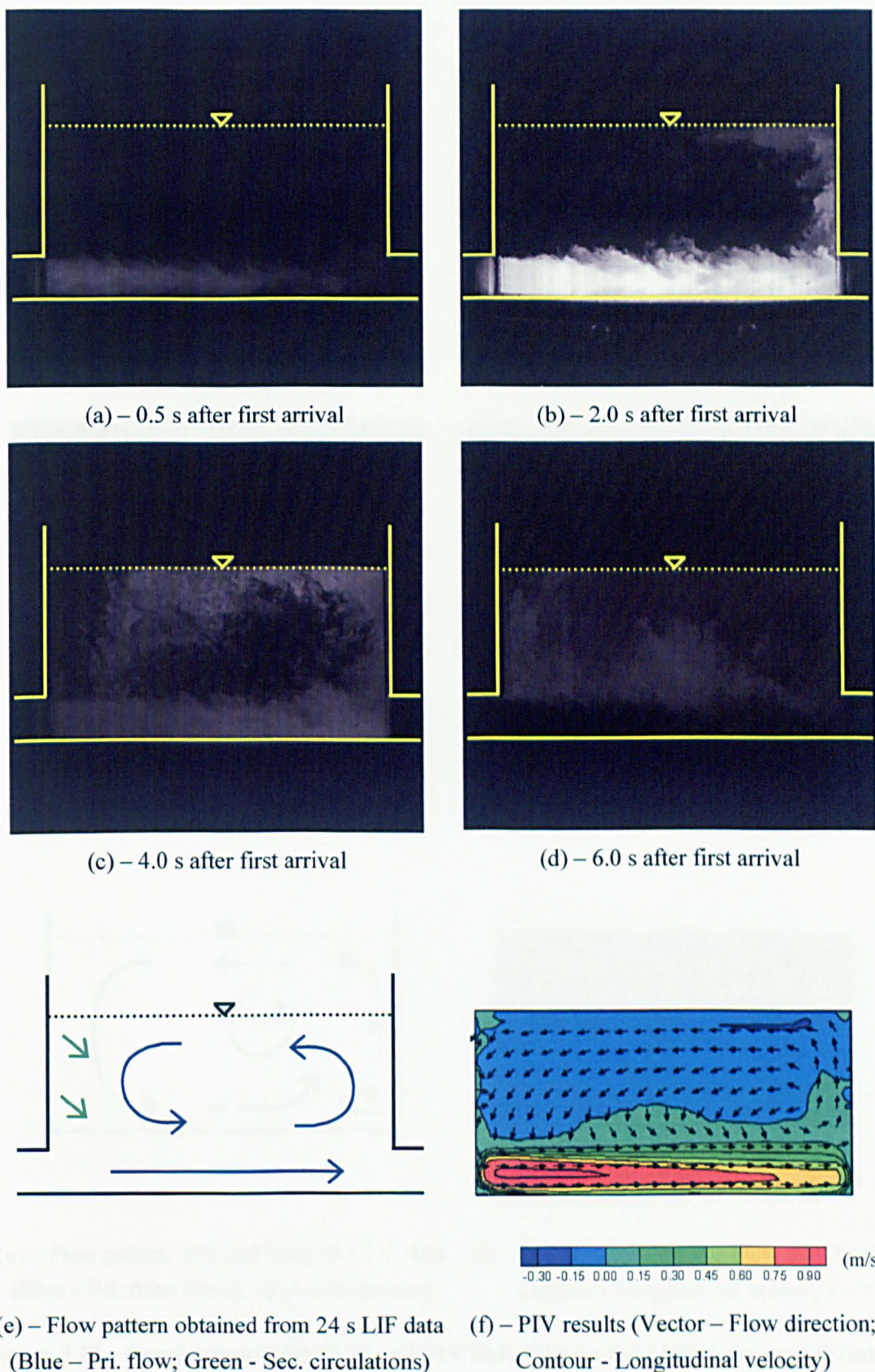


Figure 5.38 – Comparisons of the LIF and PIV flow field for the CVP at the post-threshold conditions (Flow from left to right)

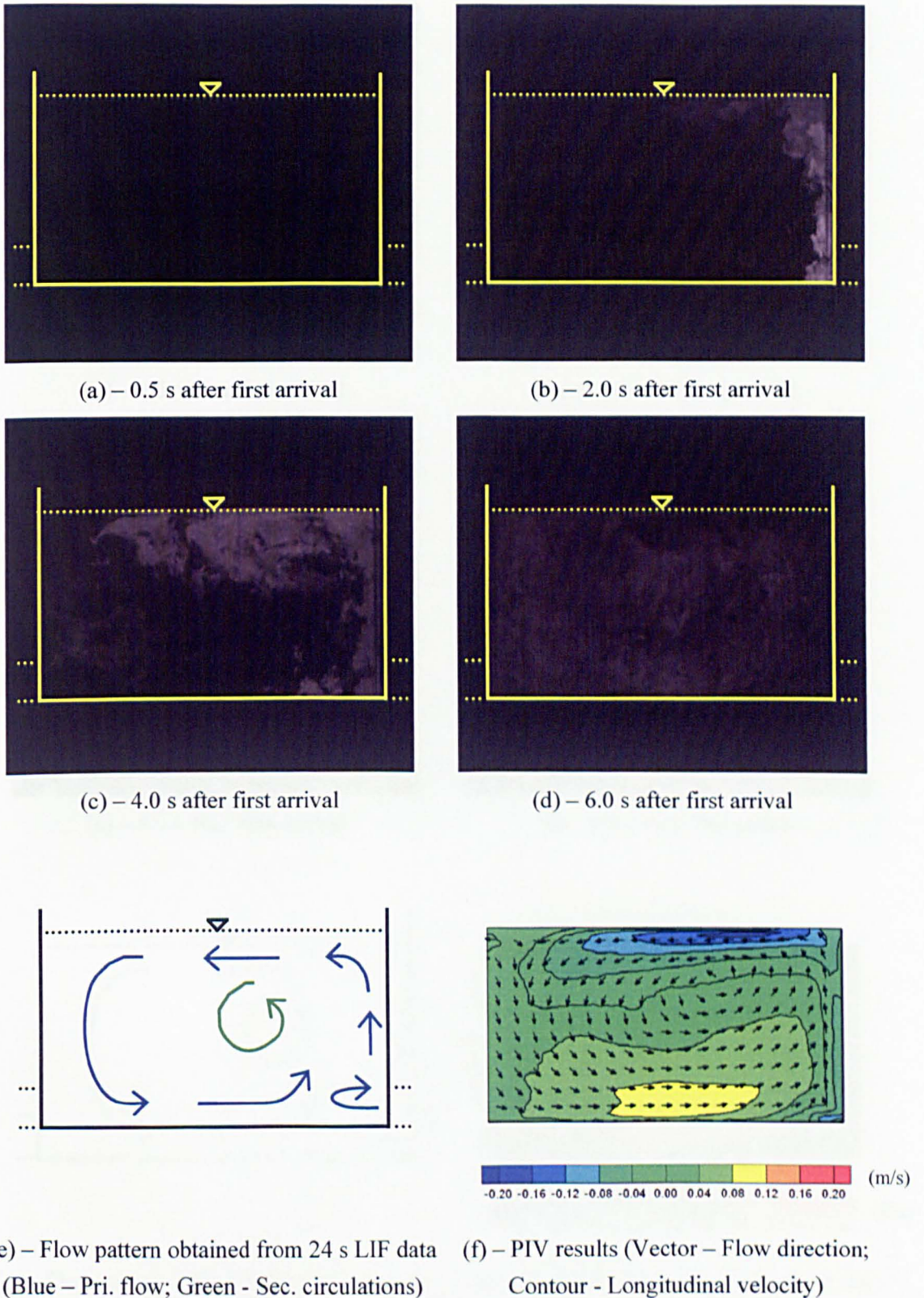
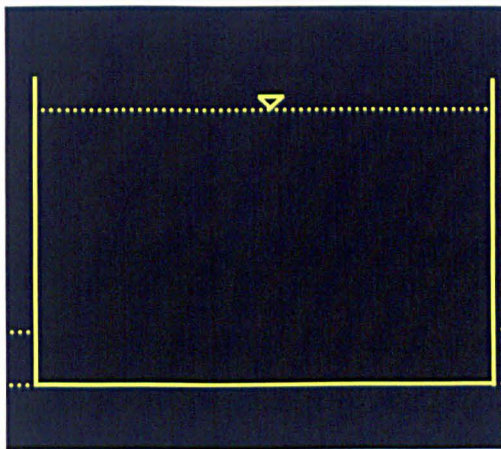
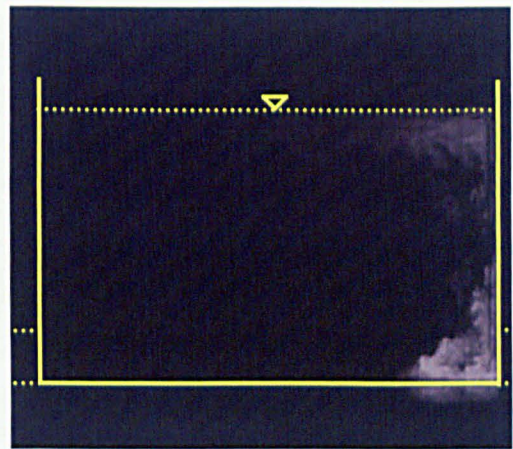


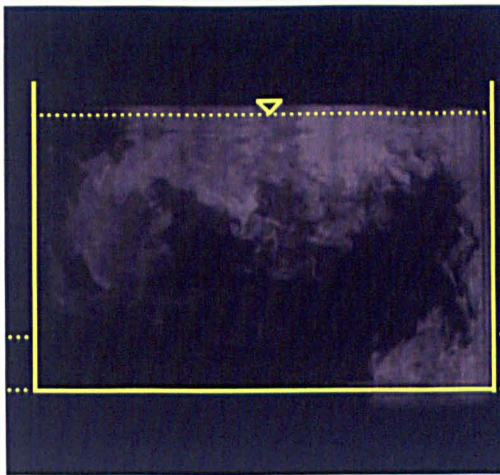
Figure 5.39 – Comparisons of the LIF and PIV flow field for the LVP at the post-threshold conditions (Flow from left to right)



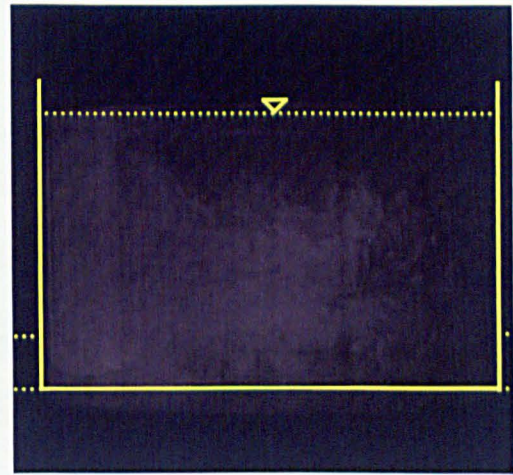
(a) – 0.5 s after first arrival



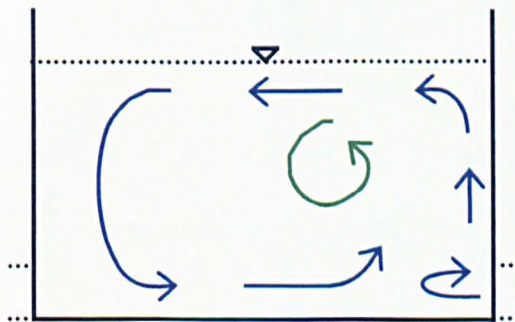
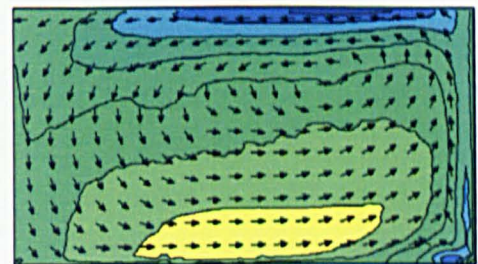
(b) – 2.0 s after first arrival




(c) – 4.0 s after first arrival



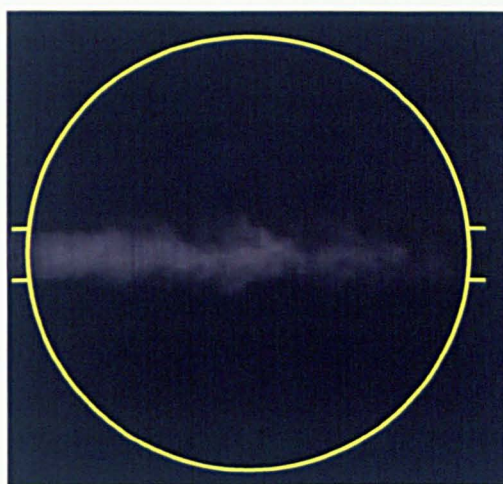
(d) – 6.0 s after first arrival

(e) – Flow pattern obtained from 24 s LIF data
(Blue – Pri. flow; Green - Sec. circulations)

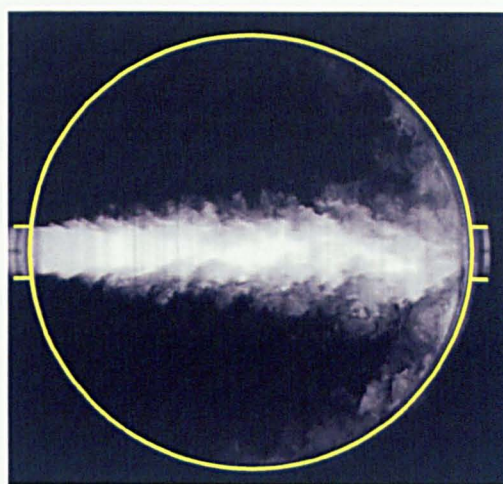
 (m/s)

(f) – PIV results (Vector – Flow direction;
Contour - Longitudinal velocity)

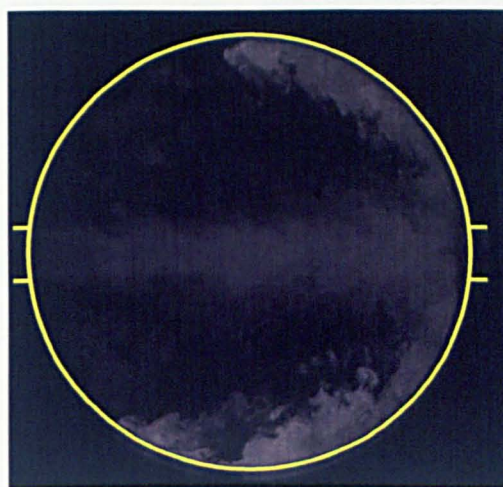
Figure 5.40 – Comparisons of the LIF and PIV flow field for the RVP at the post-threshold conditions (Flow from left to right)



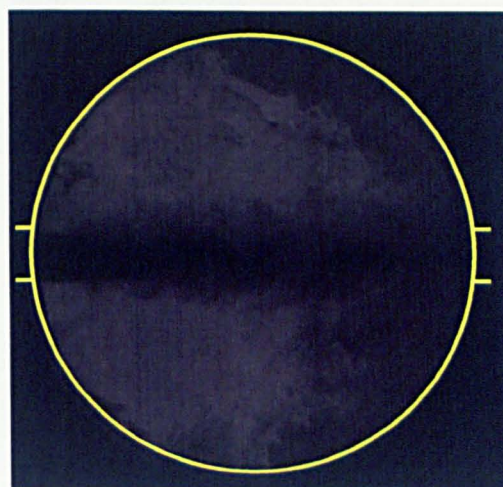
(a) – 0.5 s after first arrival



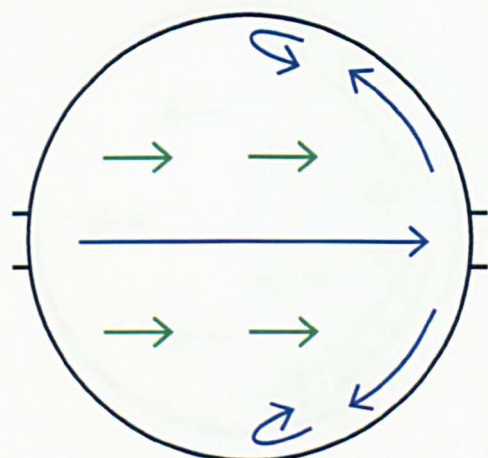
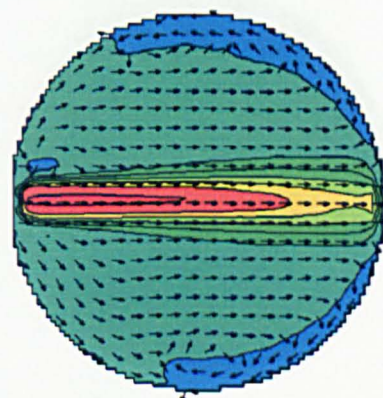
(b) – 2.0 s after first arrival



(c) – 4.0 s after first arrival



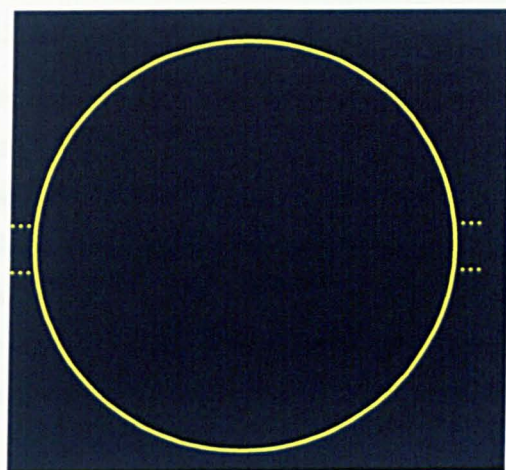
(d) – 6.0 s after first arrival

(e) – Flow pattern obtained from 24 s LIF data
(Blue – Pri. flow; Green - Sec. circulations)

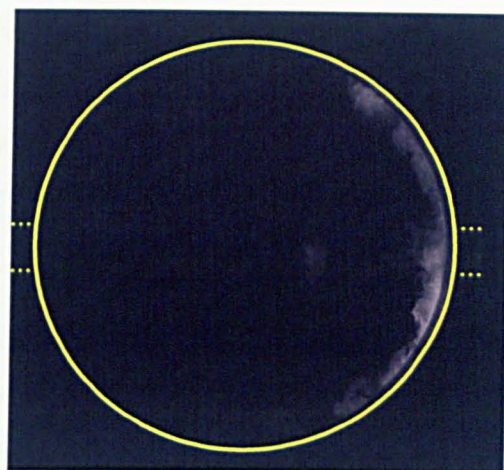
(m/s)
 -0.30 -0.15 0.00 0.15 0.30 0.45 0.60 0.75 0.90

(f) – PIV results (Vector – Flow direction;
Contour - Longitudinal velocity)

Figure 5.41 – Comparisons of the LIF and PIV flow field for the CHP at the post-threshold conditions (Flow from left to right, top view)



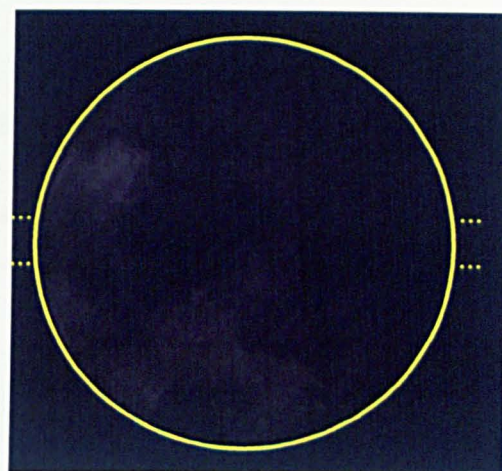
(a) – 0.5 s after first arrival



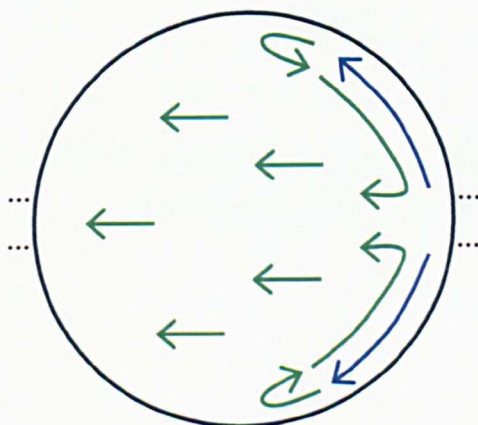
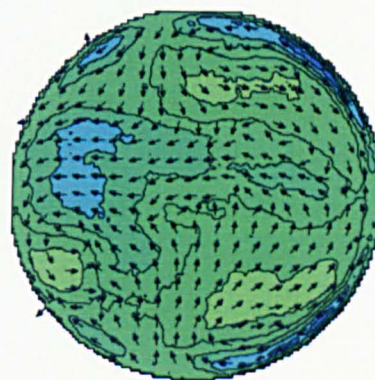
(b) – 2.0 s after first arrival



(c) – 4.0 s after first arrival



(d) – 6.0 s after first arrival

(e) – Flow pattern obtained from 24 s LIF data
(Blue – Pri. flow; Green - Sec. circulations)

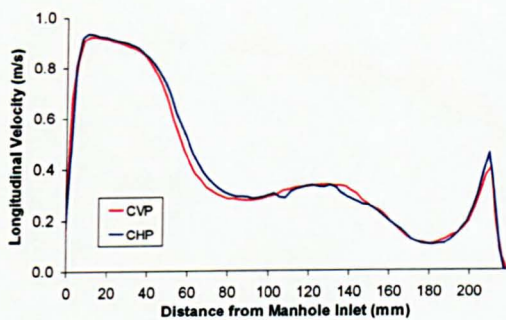
-0.10 -0.08 -0.06 -0.04 -0.02 0.00 0.02 0.04 0.06 0.08 0.10 (m/s)

(f) – PIV results (Vector – Flow direction;
Contour - Longitudinal velocity)

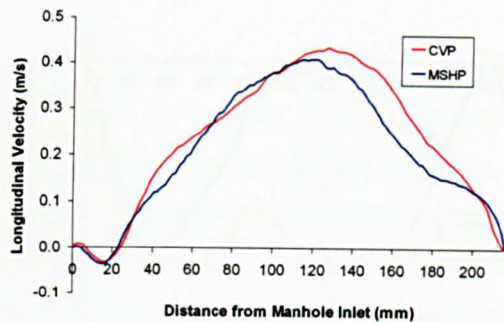
Figure 5.42 – Comparisons of the LIF and PIV flow field for the MSHP at the post-threshold conditions (Flow from left to right, top view)

5.5.4.4.5 Comparisons of the Velocity Profiles at the Lines of Intersection

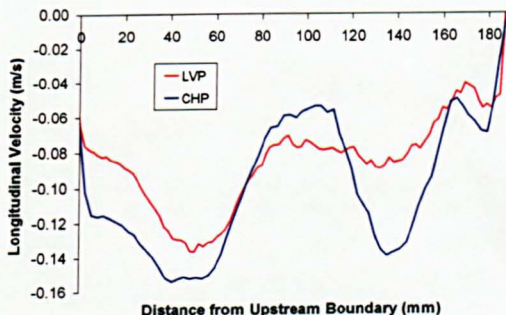
The consistency of the measured data obtained from the vertical and horizontal planes can be verified by comparing the longitudinal velocity at the line of intersection. There are six lines of intersection between the five investigation planes. For each of the intersection lines, the velocity profile obtained from different planes is compared. Figure 5.43 and Figure 5.44 compare the longitudinal velocity profile at the lines of intersection for the pre- and post-threshold conditions. In general, the results show reasonably good similarity between the vertical and horizontal plane profiles. The maximum difference in velocity between the profiles in the twelve cases appears to be 0.05 m/s. The variations of the velocity measurements between the vertical and horizontal planes may be explained by slight misalignment of the mirrors and the camera; small variations in the operating flowrate throughout the PIV experiments; and non-simultaneous measurement. Note that in Figure 5.44b, the velocity profile for the two planes appears to exhibit different forms. This is because the location of the profiles is close to the centre of the circulation in the dead zone where the velocity is very small. A slight misalignment could lead to a significant change in the profile shape. Nevertheless, careful examination of the profiles suggests that the difference in the velocity is still less than 0.05 m/s.



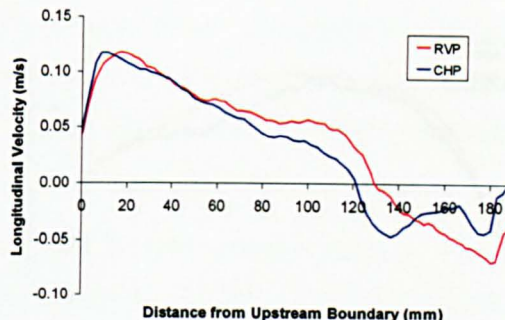
(a) – CVP vs CHP



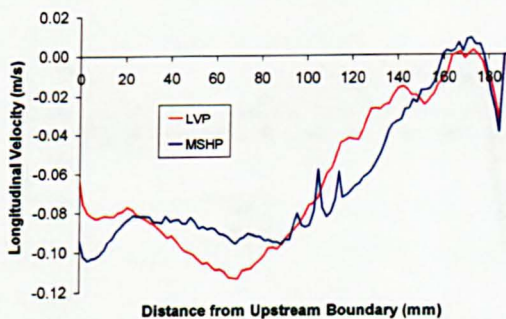
(b) – CVP vs MSHP



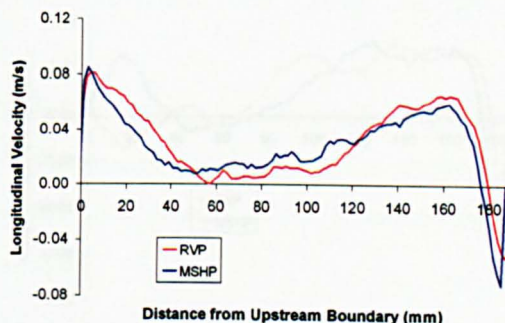
(c) – LVP vs CHP



(d) – RVP vs CHP

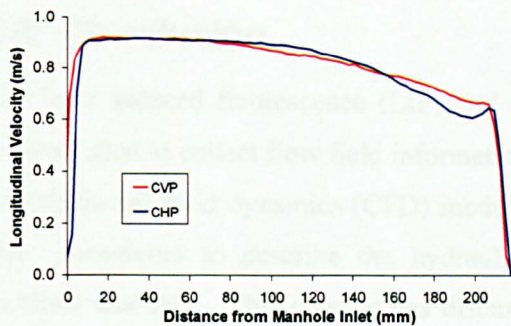


(e) – LVP vs MSHP

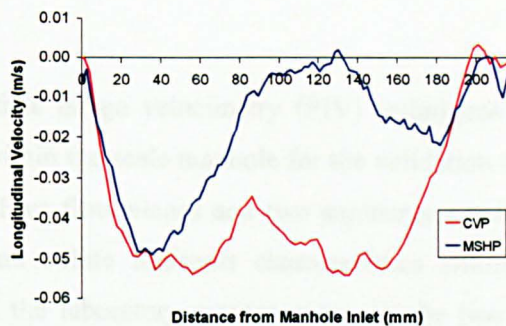


(f) – RVP vs MSHP

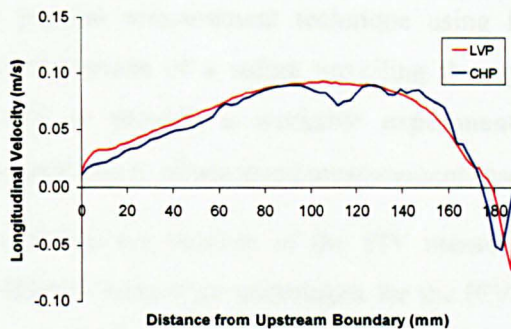
Figure 5.43 – Comparisons of the longitudinal velocity at the lines of intersection between the vertical and horizontal planes for the pre-threshold conditions



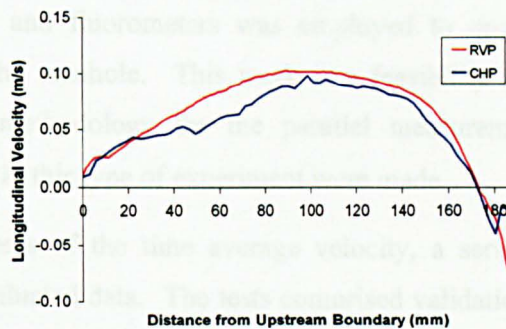
(a) – CVP vs CHP



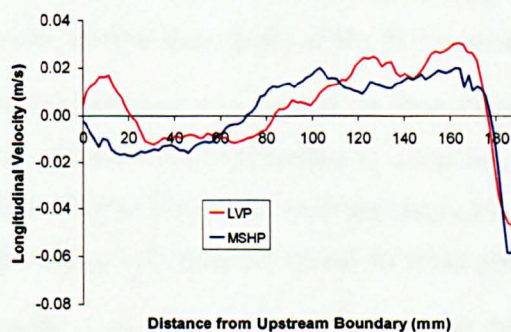
(b) – CVP vs MSHP



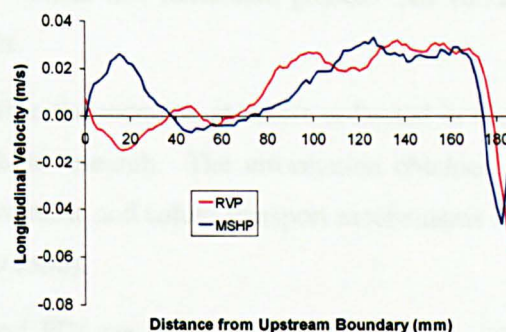
(c) – LVP vs CHP



(d) – RVP vs CHP



(e) – LVP vs MSHP



(f) – RVP vs MSHP

Figure 5.44 – Comparisons of the longitudinal velocity at the lines of intersection between the vertical and horizontal planes for the post-threshold conditions

5.6 Conclusion

The laser induced fluorescence (LIF) and particle image velocimetry (PIV) techniques have been adopted to collect flow field information within the scale manhole for the validation of the computational fluid dynamics (CFD) models. Five flow planes and two surcharge conditions were considered to describe the hydraulic and solute transport characteristics within the manhole chamber. This chapter has discussed the laboratory arrangements for the two flow visualisation experiments and the data analysis associated with the recorded data.

A parallel measurement technique using LIF and fluorometers was employed to quantify concentrations of a solute travelling through the manhole. This work is a feasibility study aimed to provide a workable experimental methodology for the parallel measurements. Suggestions to obtain good measurement results in this type of experiment were made.

To ensure the validity of the PIV measurements of the time average velocity, a series of validation tests were undertaken for the PIV evaluated data. The tests comprised validation of the pipe flow measurements; cross-reference to the LIF images; and verification of the consistency of the PIV data obtained from the vertical and horizontal planes. All validation results confirm the validity of the PIV evaluations.

The comprehensive picture of the flow field within the manhole structure collected in the two flow visualisation experiments is novel in manhole research. The information obtained from this work provides better understanding of the hydraulic and solute transport mechanisms in this type of manhole structure (manhole ID to pipe ID ratio).

Results of the flow fields collected from LIF and PIV are discussed, in conjunction with the CFD predicted data, in Chapter 6.

6 Computational Fluid Dynamics Simulations

6.1 Introduction

This chapter describes the methodology used in the generation of computational fluid dynamics (CFD) manhole models; the associated sensitivity studies for the model set-up parameters; and manhole model validation using the laboratory measurements, including the tracer and flow field data described in Chapter 3 and Chapter 5. The findings of this chapter are used for the generation of larger scale manhole models in Chapter 7.

Computational fluid dynamics (CFD) uses the fundamental laws of physics to describe the movement of fluid flow. A fluid flow solution will be exact if the temporal and spatial changes in the fluid properties, such as velocity and pressure, can be represented. Recent advances in computational powers have made CFD an increasingly accessible and useful tool for fluid mechanics research. Current supercomputers can resolve turbulent fluid flow problems exactly using direct numerical simulation (DNS). However, a DNS solution requires enormous computational resources and therefore is not a common approach adopted in the engineering industry. In contrast, the Reynolds averaged Navier Stokes (RANS) equations, which rely on approximations, are still the most popular approach to solving turbulent flows. This is mainly because they can provide quick solutions with adequate information regarding the turbulent processes (Versteeg and Malalasekera, 1995).

CFD-based software tools enable engineers to simulate flow patterns and associated transport mechanisms within both natural and engineered structures. This computational technique has a significant benefit over laboratory or field studies, in that once a numerical model is validated it may be used to examine the impact of changes to the geometry, scale or flowrate with comparative ease. The model calculates the fluid properties at all points defined within the domain. It may be used to investigate the fluid properties within structures for which access or safety issues may make instrumentation impossible (Guymer *et al.*, 2007). This demonstrates that CFD provides benefits in terms of information, time and cost. Owing to these benefits, CFD modelling has been employed to examine the scale effects of surcharged manholes on the hydraulic and solute transport characteristics. There are various software packages available for CFD modelling. The decision was made to use Fluent 6.2 (Fluent, 2005) throughout the study. This was because of the software availability and the experience held in the Department of Civil and Structural Engineering Department at the University of Sheffield.

One main problem with CFD application in the simulation of hydraulic structures is the lack of standard modelling protocols (Stovin *et al.*, 2002). The choice of set-up parameters, for example the arrangement of computational mesh, spatial and temporal discretisation schemes and turbulence model, governs the accuracy of CFD-based analysis. Inappropriate choices of the set-up parameters may lead to unacceptably poor model results. Therefore, sensitivity studies of set-up parameters were considered in the CFD manhole study and consideration was given to the most important parameters which might impose a significant impact on the numerical accuracy and computational stability. They are: grid arrangement, spatial discretisation scheme, turbulence model and solute transport model. To evaluate the simulation accuracy of the flow field and solute transport predictions generated from the different set-up parameters, the numerical results were compared with the flow field measurements and recorded tracer data (Chapter 3 and Chapter 5). The aim of the detailed investigation is to develop a modelling protocol for manhole simulations.

Prior to the detailed CFD study of the scale manhole simulation, a feasibility study was undertaken to investigate whether CFD could replicate the hydraulic and solute transport characteristics within a manhole structure. A particular focus in this study was to determine whether the model could replicate the hydraulic transition threshold observed in laboratory data. The study was carried out based on the prototype manhole model (800 mm ID manhole, Guymer *et al.*, 2005). The reason for this choice is because the study was performed prior to the construction of the scale manhole model in the laboratory. The feasibility study for the CFD manhole simulations is highlighted in Section 6.2. Section 6.3 presents the sensitivity studies of the set-up parameters for modelling manholes and validation of the flow field and tracer predictions based on the scaled laboratory manhole (218 mm ID); and this chapter is concluded in Section 6.4.

6.2 Feasibility Study of Manhole Simulations

In Guymer *et al.* (2005), the laboratory-recorded temporal concentration profiles (TCPs) of a neutrally buoyant solute passing through the 800 mm ID manhole models showed interesting solute transport characteristics. A threshold surcharge level has been identified and the temporal concentration profiles before and after the threshold level show distinctive shapes (see Chapter 4 for more details). The change in the shape of the TCPs suggests that a transition of the mixing mechanism within the same system has occurred; and the transition of the mixing mechanism is directly correlated to the change of the internal flow structure. The hydraulic transition within the same system clearly represents an interesting test for the CFD manhole simulations. The existence or not of a hydraulic transition in the numerical models is thought to

be critical in determining CFD could be used for studying the effects of physical scale of surcharged manholes.

This section describes the feasibility study of the CFD manhole simulations. As the study was performed before the physical experiments of the laboratory scale manhole model (218 mm ID manhole), the work investigated the 800 mm ID manhole (prototype) and used the tracer data collected by Guymer *et al.* (2005) for model validation. The meshing strategy and modelling methodology for manhole simulations are discussed in this section.

6.2.1 CFD Model of the Prototype

The CFD manhole model was constructed in three-dimensions as per the prototype model presented in Guymer *et al.* (2005) (Figure 6.1). It was an 800 mm ID manhole with 88 mm ID delivery pipes and no benching. The centreline of the delivery pipes passed through the vertical axis of the manhole; and the pipe and manhole inverts were level. The model inlet and outlet were defined at the upstream and downstream pipes 1.35 m away from the manhole centreline, where tracer was sampled in the laboratory experiments. The flow conditions considered in the feasibility study were a discharge of 2 l/s with six surcharge ratios which are 0.69, 1.02, 1.70, 2.05, 2.41 and 3.41. The first four ratios (0.69, 1.02, 1.70 and 2.05) correspond to the pre-threshold hydraulic regime in the laboratory data and the rest (2.41 and 3.41) correspond to the post-threshold. Since the laboratory experiment for the prototype was conducted under steady state conditions, a steady state simulation was assumed in the study.

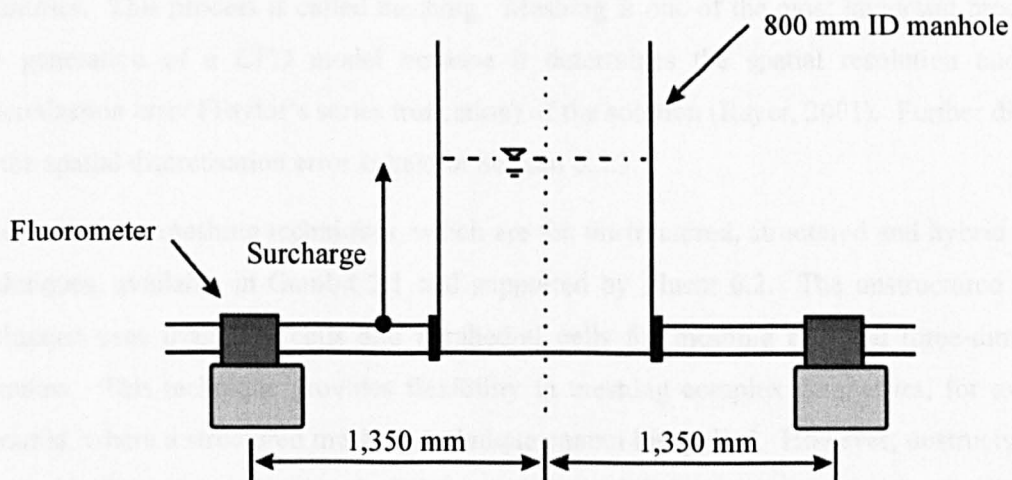


Figure 6.1 – Laboratory configuration used in the prototype experiments (after Guymer *et al.*, 2005)

Generation of a CFD model comprises three sequential stages:

1. Pre-processing - Define the domain and the properties inside the domain
2. Solver process - Solve the partial differential equations
3. Post-processing - Display results

The CFD software package used in this research was produced by Fluent, Inc. Gambit 2.1 (Fluent, 2003) was used for the domain and mesh generation in the pre-processing. Simulations of the fluid flow and solute transport were undertaken using Fluent 6.2 (Fluent, 2005), which is a finite volume based CFD software package. Fluent 6.2 and TecPlot 8.0 (Amtec Engineering Inc.) were adopted to display the computational results; and the analysis of the tracer predictions was performed using Matlab (www.mathworks.com) and MS Excel.

6.2.1.1 Pre-processing

The objectives of the pre-processing were to define a mesh model (domain) representative of the physical prototype model and to specify the fluid and boundary conditions within the domain.

6.2.1.1.1 Meshing

The geometrical information of the prototype model determined how the outline of the domain was created. The domain was then discretised into a number of control volumes, or cells, to be used for the calculation of the fluid flow properties, such as velocity, pressure and turbulence quantities. This process is called meshing. Meshing is one of the most important processes in the generation of a CFD model because it determines the spatial resolution and spatial discretisation error (Taylor's series truncation) of the solution (Rayer, 2001). Further discussion of the spatial discretisation error is held in Section 6.3.3.

There are three meshing techniques, which are the unstructured, structured and hybrid meshing techniques, available in Gambit 2.1 and supported by Fluent 6.2. The unstructured meshing technique uses triangular cells and tetrahedral cells for meshing two and three-dimensional domains. This technique provides flexibility in meshing complex geometries, for example a pyramid, where a structured meshing technique cannot be applied. However, unstructured cells are more likely to generate undesirable numerical diffusion than structured cells, leading to inaccurate simulated results (Rayer, 2001). Therefore, as a general rule of thumb, structured cells should be introduced wherever possible. The structured meshing technique uses quadrilateral and hexahedral cells for meshing two-dimensional and three-dimensional structures. The hybrid technique mixes triangular and quadrilateral cells or tetrahedral and hexahedral cells in two or three-dimensional domains.

The complex geometry of the circular manhole posed difficulties in meshing with solely structured cells. A circular cylinder, for example a straight pipe, can be meshed with structured cells with ease using the Quad-pave scheme coupled with the Cooper scheme. The Quad-pave scheme creates semi-structured cells on the non-quadrilateral face; and the Cooper scheme projects a mesh pattern from one end through the volume (Fluent, 2003). However, due to the geometry of the prototype model, using the above technique to mesh the pipe and the manhole independently did not create an identical mesh pattern at the interface between the pipe and the manhole cylindrical surface. Therefore, unstructured cell elements were required in either the pipe or the manhole. Saiyudthong (2004) suggested that the number of unstructured cells to be used in the manhole model could be minimised by the introduction of a 'mesh transition' box/section in proximity to the interface bridging the meshes of the pipe and the manhole. Two meshing strategies of the CFD model, each with different arrangements of the 'mesh transition' box, were developed and are described as follows:

6.2.1.1.1.1 Version 1

This meshing strategy followed the approach used in Saiyudthong (2004). The entire manhole model was divided into three sections, which are the upstream pipe, the downstream pipe and the circular manhole chamber. The circular pipes were graded with semi-structured cells using the Quad-pave scheme associated with the Cooper scheme. A 'mesh transition' box, which was made up of unstructured cell elements, was provided at the interface inside the manhole linking the meshes of the pipes and the manhole. The Quad-pave scheme in conjunction with the Cooper scheme was adopted for creating structured cells in the remaining manhole structure. A schematic diagram of the manhole model generated by this meshing strategy is provided in Figure 6.2.

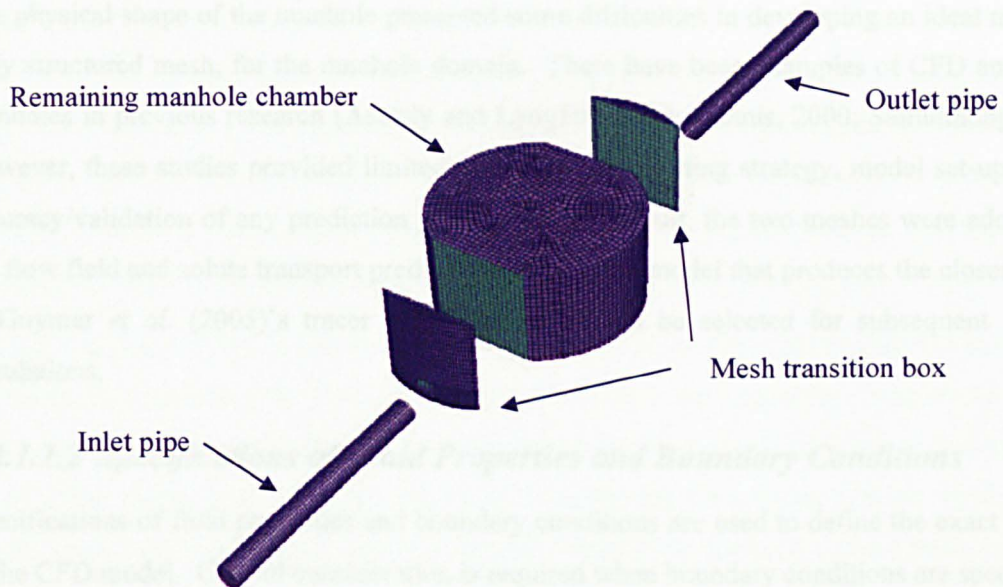


Figure 6.2 – 3D view of the version 1 mesh model

6.2.1.1.1.2 Version 2

The second version of the meshing strategy split the entire domain into two volumes. The two volumes are a continuous pipe comprising the inlet pipe, the outlet pipe and the section that runs through the manhole, and the remainder of the manhole. The ‘mesh transition box’ fitted was a rectangular box surrounding the pipe section that runs through the manhole. Using this strategy, most of the manhole was mapped with structured elements. There were a small number of unstructured cells near the bottom of the mesh transition box due to sharp corners. These unstructured cells occupied less than 1 % of the entire manhole model volume. Figure 6.3 shows the model adopted with the version 2 meshing strategy.

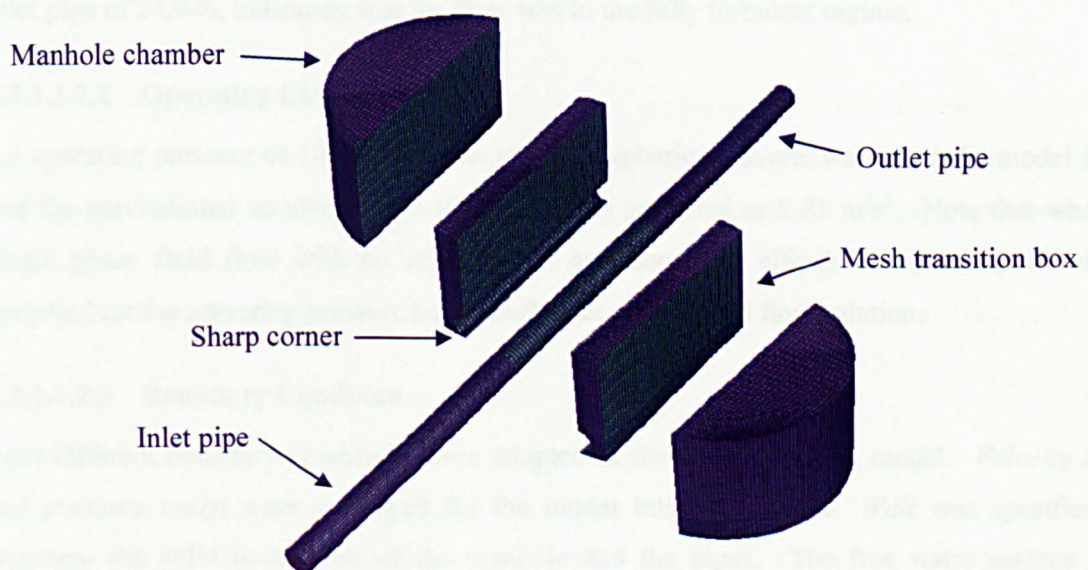


Figure 6.3 – 3D view of the version 2 mesh model

The physical shape of the manhole presented some difficulties in developing an ideal mesh, i.e. fully structured mesh, for the manhole domain. There have been examples of CFD analysis of manholes in previous research (Asztely and Lyngfelt, 1996; Dennis, 2000; Saitudthong, 2004). However, these studies provided limited discussion on meshing strategy, model set-up and the accuracy/validation of any prediction produced. As a result, the two meshes were adopted for the flow field and solute transport predictions. The mesh model that produces the closest results to Guymer *et al.* (2005)'s tracer measurements would be selected for subsequent manhole simulations.

6.2.1.1.2 Specifications of Fluid Properties and Boundary Conditions

Specifications of fluid properties and boundary conditions are used to define the exact problem in the CFD model. Careful consideration is required when boundary conditions are specified.

6.2.1.1.2.1 Fluid Properties

The fluid defined in the model was water with a temperature of 25 °C, a density of 998.2 kg/m³ and a dynamic viscosity of 0.001003 kg/ms. It was assumed that the fluid is incompressible and the fluid properties are constant throughout the simulation. The assumption of the incompressible fluid should be valid because the Mach number for this fluid flow problem is less than 0.01 ($=$ speed of the flow (\sim 1 m/s) / speed of sound in water at 25 °C (1,497 m/s)), such that the change in the fluid density in response to the change in pressure or velocity is negligible (Douglas *et al.*, 1985).

The flow conditions examined in the feasibility study were a flowrate of 2 l/s and a range of surcharge ratios from 0.69 to 3.41. This generated a corresponding Reynolds number at the inlet pipe of 24,946, indicating that the flow was in the fully turbulent regime.

6.2.1.1.2.2 Operating Conditions

An operating pressure of 101,325 Pa, i.e. one atmospheric pressure, was set at the model inlet and the gravitational acceleration in the model was specified as 9.81 m/s². Note that when a single phase fluid flow with no stratification and buoyancy effects is modelled, the value specified for the operating pressure has no influence on the fluid flow solution.

6.2.1.1.2.3 Boundary Condition

Four different boundary conditions were adopted in the CFD prototype model. *Velocity inlet* and *pressure outlet* were employed for the model inlet and outlet. *Wall* was specified to represent the solid boundaries of the manhole and the pipes. The free water surface was approximated by a rigid lid approach using the *symmetry* boundary condition.

Velocity inlet

A *velocity inlet* is used when the velocities of the fluid at the inlet boundary are known. The mass flow rate and the momentum flux through this boundary are calculated from the specified velocities and the area of the face cells (Fluent, 2005). For turbulent flow problems, the boundary condition also requires inputs for turbulence levels, in terms of turbulent kinetic energy and turbulent dissipation rate.

Since it was not possible to know the exact flow profile at the upstream monitoring station from the tracer data measured by Guymer *et al.* (2005), a fully developed flow was assumed at the CFD model inlet. This assumption should be acceptable as there was more than 2 m of straight pipe section between the last pipe bend and the upstream fluorometer (i.e. 20 diameters), by which point a fully developed condition would generally be assumed to have been established (Howarth, 1985). The inlet boundary was given a fully developed profile, including velocity and turbulence information, generated from a separate straight pipe. The additional straight pipe model was simulated using a *periodic* boundary condition and the description of the model can be found in Section 6.2.1.4.

Pressure outlet

When a *pressure outlet* is adopted, the flow quantities, with the exception of the static pressure, at the boundary are extrapolated from the cells upstream. Inputs are required for the static pressure and the turbulence properties of (potential) backflow.

Static pressure represents the pressure relative to the operating pressure of the model. The static pressure defined at the outlet boundary provides a reference location for the reporting of pressure change within domain (Grimm, 2004). In the prototype model, the value specified for the static pressure was 0 Pa.

The properties of backflow would be used by the model only when a backward flow was predicted. However, for computational stability reasons, values for the turbulence properties same as those at the inlet were specified. This was because at the beginning of the numerical calculations, i.e. when the solution deviates significantly from the final answer, the manhole model may estimate a reverse flow at the outlet even though the reverse flow did not exist in the converged solution.

Wall

A *Wall* boundary condition was applied to represent the solid boundaries of the prototype. In the CFD models, wall functions were used to model the viscous affected flow in the vicinity of the wall and the reason for this is to save computational resources and time (Section 2.6.4.3).

Although the wall functions may not completely describe the viscous sub-layer flow regime, a good approximated flow in the wall adjacent cell can be obtained if the wall functions are valid. The function is proved valid when the wall adjacent cell's centroid is located within the log-law region, $30 < y^+ < 300$ (Fluent, 2005).

However, in the numerical models, it was not possible to control y^+ values for every wall-adjacent cell to within the valid range. This is because the velocity, and hence the y^+ value, in the dead zone regions of the chamber is extremely low. An unreasonably large cell would be needed in order to validate the wall functions and this would mean a reduction in the spatial resolution of the flow field. Nevertheless, it is thought that the prediction inaccuracy of the near wall flow in the manhole should not influence the simulation results of the general flow pattern inside the structure. This is supported by the fact that the flow field within the manhole is primarily characterised by the turbulent jet (not wall turbulence) and the prediction of the turbulent jet flow is heavily reliant upon the turbulence model. For the straight pipe flows (inlet and outlet pipes), since the flow characteristics is dependent upon the turbulence generated at the pipe wall surface, the validity of the wall functions is important. The size of the wall adjacent cells at the pipe was adjusted so as to ensure the wall functions were valid.

Two wall functions, which are the standard and non-equilibrium wall functions, are available in Fluent 6.2. Consideration was given to the non-equilibrium wall functions, as this is suggested by the Fluent manual (Fluent, 2005) for use in complex flows involving separation, reattachment and impingement.

When wall functions are used, the roughness effects on the wall-bounded flows can be accounted for in Fluent 6.2 by specifying two roughness parameters, which are the roughness height and the roughness constant. The roughness height in the software is defined as the height of a sand grain. Therefore, for other types of surface, an equivalent sand grain roughness height has to be estimated. The value of the roughness constant is dependent upon the type of the given roughness (Fluent, 2005). However, there is no clear guideline in the Fluent manual for choosing the appropriate value for a specific roughness surface. Grimm (2004) estimated the parameter values for an 88 mm ID Perspex pipe using theoretical head loss data, estimated by the Darcy-Weisbach and Colebrook-White equations (Chadwick and Morfett, 1998). His study suggested that an equivalent roughness height of 8×10^{-5} m with the constant value of 0.5 would create similar friction losses to the theoretically predicted; and should be used for the 88 mm ID Perspex pipe. As the prototype model was made of PVC for the manhole body and Perspex for the delivery pipes, Grimm (2004)'s suggested values were inputted for the smooth surfaces.

Symmetry

In the absence of wind-induced effects and heat exchange between air and water, a free surface can be approximated using a *symmetry* plane (Rodi, 1993). This approach, called the rigid lid approximation, was adopted in the CFD manhole models. A *symmetry* plane assumes a slip surface and a zero flux of all quantities across the boundary. Therefore, the normal velocity component and the normal gradients of all flow variables at the *symmetry* plane are zero. These boundary conditions should be appropriate when the free surface is flat and not influenced by the wind-induced shear forces.

The rigid lid approximation approach ignores free surface fluctuations and the effects of which on the flow field. For vigorous free surface fluctuations, this approach might not be suitable for use. Dennis (2000) reported a variety of surface flow conditions in a surcharged manhole. At low surcharges and high flowrates, the surface flow appeared to be chaotic and fluctuating with time. The use of the rigid lid approximation for modelling low surcharge manhole models therefore forms another interesting test in the feasibility study.

It is possible to model the free water surface in manholes using CFD. This can be achieved by using the VOF approach, which can account for more than two immiscible fluids by solving a single set of momentum equations (Fluent, 2005). Successful application of this approach to modelling free surface can be found in Stovin *et al.* (2002); Tritthart and Gutknechy (2007). However, consideration was not given to the multiphase modelling approach mainly because of its substantial demand for computational resources.

6.2.1.2 Solver Process

The objectives in the solver process were to predict the flow field in the manhole chamber using the data defined in the pre-processing and the turbulence model; and to replicate the tracer test undertaken by Guymer *et al.* (2005) using a solute transport model. The solute transport prediction was made on the basis of a flow field solution, and therefore was performed after the flow field simulation had been completed.

6.2.1.2.1 Flow Field Model

The Reynolds averaged Navier Stokes (RANS) equations coupled with the k - ϵ eddy viscosity model was considered as the flow field solver in the feasibility study. This was chosen because it was expected to provide quick solutions with adequate information regarding the turbulent processes (Versteeg and Malalasekera, 1995). Three variants of the k - ϵ eddy viscosity model, which are the standard, the renormalisation group (RNG) and the realisable k - ϵ turbulence models, are available in Fluent 6.2 and consideration was given to the RNG k - ϵ turbulence

model. The selection of the model was based on its enhanced ability to deal with swirling flow (Fluent, 2005), which has been observed in a surcharge manhole (Guymer *et al.*, 1998); and the research group's previous modelling experience. Details of the RNG $k-\varepsilon$ turbulence model can be found in Yakhot and Orszag (1986) and Yakhot *et al.* (1992). Note that the RSM, which is claimed to be a better RANS model to describe turbulence, will be examined in conjunction with the RNG $k-\varepsilon$ turbulence model in the parametric study of turbulence model (Section 6.3.5.2).

The numerical equations of the RNG $k-\varepsilon$ turbulence model contain constants that could be modified for different turbulent flow applications. However, the default values of the coefficients provided in Fluent 6.2 were employed in the simulation (Table 2.4), as they were claimed to be appropriate for a wide range of turbulent flows (Fluent, 2005). Steady state calculations were used to predict the flow field within the surcharged manhole.

Fluent 6.2 employs a control volume based technique to convert the governing equations, which comprise partial differential equations, to algebraic equations that can be solved numerically. This control volume technique integrates the governing equations about each control volume, i.e. cell, yielding discrete equations for dependent variables, such as velocity, pressure, turbulent kinetic energy and dissipation rate. The discrete equations are solved using spatial discretisation scheme, and temporal discretisation scheme when unsteady state calculations are required. Fluent 6.2 provides a number of spatial and temporal discretisation schemes (see Section 2.6.6). In general, second order discretisation schemes should be used whenever possible, as they result in smaller Taylor series truncation error compared with first order accurate approaches (Versteeg and Malalasekera, 1995).

However, the second order approaches may sometimes be unstable; and in the CFD prototype models, the numerical solution diverged when a second order scheme was used to solve the momentum term. This might be due to poor quality of mesh in the models. Therefore, the calculation of the momentum term in the numerical models was based on a first order scheme. The use of first order scheme for the momentum term is acceptable in this preliminary study as it is not intended to generate the most accurate flow field and solute transport predictions from these CFD models, but to demonstrate the existence or not of a hydraulic transition. Table 6.1 summarises the spatial discretisation schemes employed for the CFD prototype models. Further information of the spatial discretisation schemes can be found in Fluent (2005); Turnbull (2003); Versteeg and Malalasekera (1995). Note that in the detailed manhole simulations (Section 6.3), better quality of meshes was created for the domain and the numerical models were solved using second order finite difference approaches without numerical instability.

Terms/Equations	Discretisation Scheme
Pressure	<i>Linear</i>
Pressure-velocity coupling	<i>SIMPLEC</i>
Momentum	<i>First order upwind</i>
Turbulent kinetic energy	<i>Second order upwind</i>
Turbulent dissipation rate	<i>Second order upwind</i>

Table 6.1 – Spatial discretisation schemes used for the steady state flow field solver in the feasibility study

In the feasibility study, the single precision solver (32 bits) of Fluent 6.2 was used for the flow field calculations. The calculations were determined as ‘complete’ when the scaled residual of each governing equation had become constant. The scaled residual is the sum of the error, or imbalance, of the governing equation for a variable over all computational cells divided by a scaling factor. Further details of residuals and scaled residuals can be found in Awbi (2003).

6.2.1.2 Solute Transport Model

Solute transport in a fluid flow may be simulated using Eulerian models or Lagrangian models. Eulerian models treat solutes as a secondary continuum phase and the transport equations for the second phase are solved based on a stationary reference frame (domain), similar to the way the carrier phase is resolved. The Lagrangian approach assumes that solutes may be represented by a large number of individual particles and predicts the trajectories of each particle injected in the model on the basis of a moving reference frame. Fluent 6.2 supports the two architectures for solute transport prediction. The Eulerian and Lagrangian models provided in the CFD software package are called the species model and the particle tracking model. Details of the two approaches have been presented in the literature review (Section 2.6.5).

Feasibility studies of using the two solute transport models (the species model and particle tracking model) for the prediction of a neutrally buoyant solute travelling through urban drainage structures have been undertaken by Grimm (2004), in a straight pipe, and Stovin *et al.* (in press), in storage tanks. Their studies concluded that the two models were both able to show solute dispersion and the results generated from the two models were highly comparable to the laboratory data. However, the computational time required for the two approaches was vastly different. It took more than ten times longer for the species model simulation to run in comparison to its counterpart. For this reason, the particle tracking technique was adopted for modelling a neutrally buoyant solute travelling through the CFD manhole models.

Prediction of particle trajectory in the particle tracking model is based on the ‘force balance’ equation on the tracking particle (Equation 2.58). As the flow conditions examined in the feasibility study were in the fully turbulent regime, the major force that leads to particle acceleration or deceleration was the change in instantaneous velocity of the carrier fluid. Gravitational force and Brownian force were not important in the transport process because neutrally buoyant particles were used in the simulation and the fluid flowed under fully turbulent conditions (non-stationary).

Since the RNG k - ε turbulence model generated a time average flow field solution, the change in instantaneous velocity of the carrier fluid was accounted for using the stochastic tracking process. The stochastic process generates random fluctuating velocities, representative of the turbulent eddy fluctuations, for the carrier fluid based on the local turbulent kinetic energy and a normally distributed random number; and a new fluctuating velocity is generated over the smaller of the eddy lifetime (Equation 2.66) or the maximum allowable time step defined. Further information of the stochastic tracking process can be found in the literature review (Section 2.6.5.2.1).

The properties of the particles injected in the particle tracking simulations were specified according to the properties of the tracer used in the laboratory experiments (Guymer *et al.*, 2005) and the recommendations given by Grimm (2004). The particle had a density of 998.2 kg/m^3 , the same density as water, and a diameter of $1 \times 10^{-6} \text{ m}$. Grimm (2004) suggested that the effects of particle size on the particle tracking results become negligible when the particle specified in the particle tracking model was smaller than $1 \times 10^{-6} \text{ m}$. In each of the particle tracking simulations, the particle injection was made uniformly over the inlet plane with an initial particle velocity of 0 m/s at a single instant in time, i.e. an instantaneous upstream injection; and the tracking finished when the particle had left the system or the maximum allowable calculation steps (for those particles permanently trapped in a dead zone) had reached. The uniform injection corresponded to an assumption that the dye had been cross-sectionally well mixed at the upstream fluorometer, after the longitudinal mixing of a 10 m long pipe section (88 mm ID), greater than 100 pipe diameters (IDs) (Guymer and O’Brien, 2000; Guymer *et al.*, 2005). The value specified for the initial particle velocity should not influence the overall particle tracking results, as the particles with the given density and diameter interact almost immediately with the carrier phase after released (Grimm, 2004). To eliminate the random effects created by the stochastic tracking process, approximately $60,000$ particle injections were made in each run to generate statistically meaningful results. Selection of the number of injection followed Grimm (2004)’s recommendations. A sensitivity test for the

number of particle injection showed that almost identical particle tracking results were attained when the number of injections was reduced by half.

The particles carried by the flow may affect the flow structure of the carrier phase. This interactive effect between the two phases can be modelled in particle tracking, by including an extra source term in the flow equations of the carrier phase estimated from the particle momentum. The flow field is re-calculated after a batch of particles is injected and then a new particle tracking result is made based on the revised flow field solution. Repetition of the process until the flow field and particle tracking results no longer change with additional iterations yields the final solution.

However, for the concentration and the density of the tracer employed in the laboratory experiments, it may be assumed that the tracer completely follows the flow path of water and does not influence the inherent flow structure within the manhole. For this reason, the interactive effect between the injected particles and the carrier phase was not considered in this study.

To enable comparisons between the particle tracking results and the tracer measurements to be made, two monitoring planes were set at the CFD model inlet and outlet, where the fluorometers were located in the laboratory configurations. The basic settings of the particle tracking model used in the feasibility study are summarised in Table 6.2.

Model Configurations	Setting/Value
Number of particle injection	Approximately 60,000
Particle density	998.2 kg/m ³ (same as water)
Particle size	1 x 10 ⁻⁶ m (uniform size)
Injection method	Uniform instantaneous injection over the inlet plane
Maximum allowable calculation step	500,000
Brownian force	No
Gravitational force	Yes
Stochastic modelling	Yes
Interaction with carrier phase	No

Table 6.2 – Basic settings for the particle tracking model

6.2.1.3 Post-processing

Results of the flow field and solute transport predictions were prepared and analysed using several software packages. Contour plots were generated using Fluent 6.2. Analysis of the

solute transport predictions was performed using MATLAB (www.mathworks.com) and MS Excel.

6.2.1.4 Generation of a Fully Developed Profile for Pipes

The fully developed flow profile specified at the CFD prototype model inlet was created from a separate straight pipe model, with a diameter identical to the manhole inlet pipe, 88 mm ID, and a length of 10 pipe diameters (IDs). The pipe model was generated in three-dimensions with a *periodic* boundary condition defined at the model inlet and outlet. The *periodic* boundary condition assumes that the model inlet and outlet obtain identical velocity distribution but with different pressure values to account for the energy loss over the pipe. This assumption matches the hydraulic conditions that would appear in a straight pipe with a fully developed flow. A *wall* boundary condition was used to represent the solid pipe boundary and the roughness parameters were inputted in accordance with Section 6.2.1.1.2.3. Note that the results of the *periodic* pipe were insensitive to pipe length. For instance the same results were obtained when a length of 5 and 20 pipe diameters was used.

The fluid properties were specified as reported in Section 6.2.1.1.2.1. The RNG $k-\varepsilon$ turbulent model associated with the standard wall functions was used to solve the flow field in the pipe. The governing equations for momentum, turbulent kinetic energy and turbulent dissipation rate were calculated using the *second order upwind* scheme; for the pressure term was the *second order* scheme; the *SIMPLE* scheme was selected for the pressure-velocity coupling. All these model settings followed the recommendations for modelling pipe flows given by Grimm (2004). Mathematical expression and detailed description of these spatial discretisation schemes may be found in Barth and Jespersen (1989); Patankar and Spalding (1972).

Figure 6.4 shows the fully developed flow profiles generated from the straight pipe. These profiles were inputted to the inlet of the prototype model.

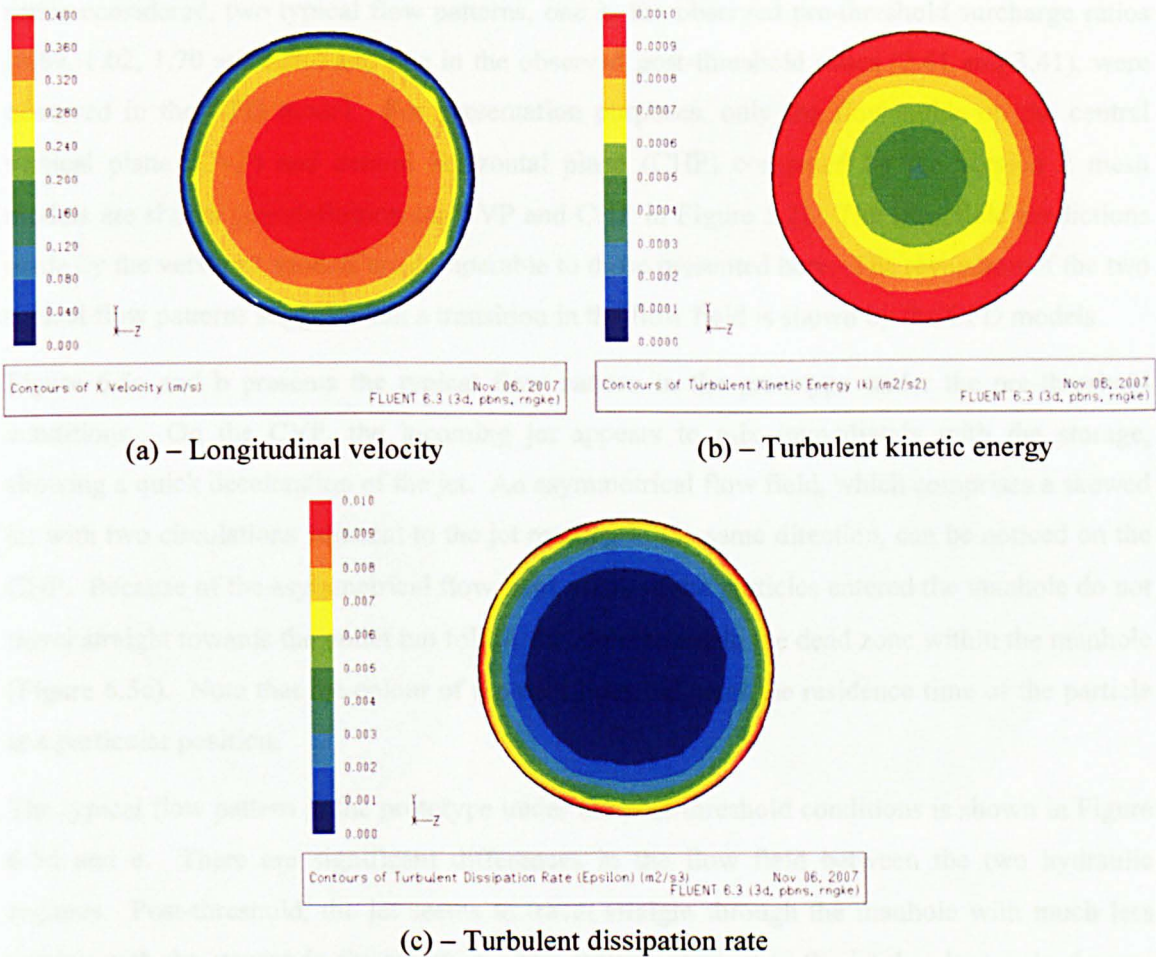


Figure 6.4 – Fully developed flow profiles used in the prototype model

6.2.2 Results of the Feasibility Study

This sub-section presents the flow field and particle tracking results of the CFD prototype model. One of the aims of this work is to see the existence or not of a transition in the hydraulic and solute transport characteristics in the surcharged manhole. The verification of the CFD predictions was based on the comparisons with the laboratory tracer data obtained by Guymer *et al.* (2005). Note that the results generated from the two mesh models (version 1 and version 2) are presented, and the mesh model that creates closer results to the observations is used for the subsequent manhole simulations.

6.2.2.1 Flow Field Results

One of the advantages of CFD is that it calculates the fluid properties at all points defined within the domain, enabling detailed examination of the flow field on any plane of interest within the domain. The flow information provides insights into the mixing process in the manhole, as solute transport is the consequence of fluid motion. For the range of surcharge

ratios considered, two typical flow patterns, one in the observed pre-threshold surcharge ratios (0.69, 1.02, 1.70 and 2.05) and one in the observed post-threshold ratios (2.41 and 3.41), were observed in the CFD model. For presentation purposes, only the flow fields on the central vertical plane (CVP) and central horizontal plane (CHP) computed by the version 2 mesh models are shown (see definition for CVP and CHP in Figure 5.2). The flow field predictions made by the version 1 models are comparable to those presented here. The revelation of the two typical flow patterns suggests that a transition in the flow field is shown by the CFD models.

Figure 6.5a and b presents the typical flow pattern in the prototype under the pre-threshold conditions. On the CVP, the incoming jet appears to mix immediately with the storage, showing a quick deceleration of the jet. An asymmetrical flow field, which comprises a skewed jet with two circulations adjacent to the jet rotating in the same direction, can be noticed on the CHP. Because of the asymmetrical flow field, some of the particles entered the manhole do not travel straight towards the outlet but follow the circulations in the dead zone within the manhole (Figure 6.5c). Note that the colour of the path lines indicates the residence time of the particle at a particular position.

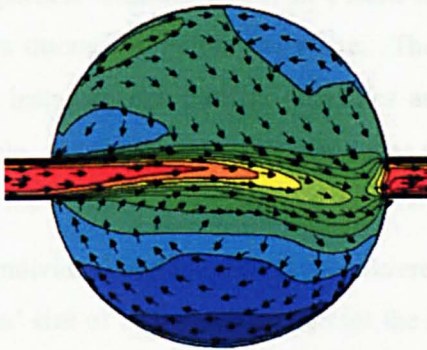
The typical flow pattern in the prototype under the post-threshold conditions is shown in Figure 6.5d and e. There are significant differences in the flow field between the two hydraulic regimes. Post-threshold, the jet seems to travel straight through the manhole with much less mixing with the storage in the structure. The regime adjacent to the jet develops a dead zone. Figure 6.5f shows the particle path lines in the manhole at post-threshold hydraulic conditions. As may be expected, most of the particles propagate straight through, or short circuit, the chamber and those particles entrained in the dead zone remain for a long period of time (e.g. greater than 60 s) before it is re-entrained to the main flow. Note that the particle tracking was set to terminate at the particle residence time greater than approximately 70 s. The lines are cut-off at red for this reason.

6.2.2.2 Particle Tracking Results

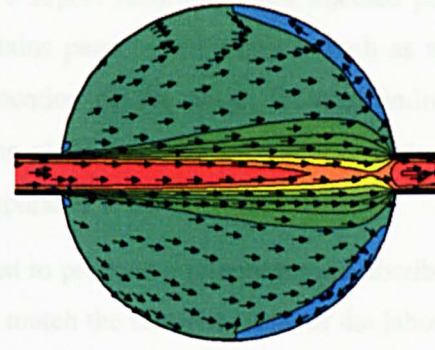


(a) – CVP, Pre-threshold

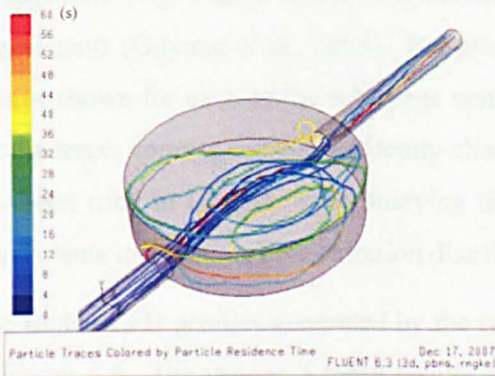
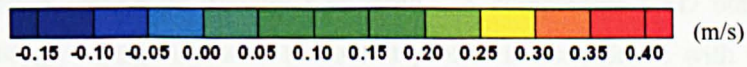
(d) – CVP, Post-threshold



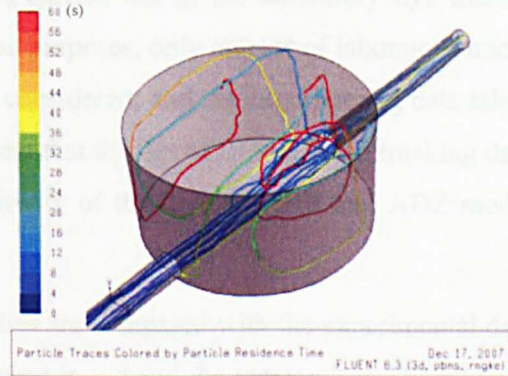
(b) – CHP, Pre-threshold



(e) – CHP, Post-threshold



(c) – Particle path lines, Pre-threshold



(f) – Particle path lines, Post-threshold

Figure 6.5 – Typical flow patterns (coloured by longitudinal velocity) and particle flow path (coloured by particle residence time) in pre-threshold ($S = 1.02$) and post-threshold ($S = 3.41$)

6.2.2.2 Particle Tracking Results

There was no flow field data of the physical prototype model available for the validation of the CFD models. The laboratory tracer data published by Guymer *et al.* (2005) was therefore used to evaluate the accuracy of the CFD models' solute transport predictions. This is a direct validation method for solute transport predictions. However, it is important to note that the validation results do not necessarily represent the accuracy of the flow field predictions, as the particle tracking model comprises additional numerical modelling assumptions and possibly more numerical errors have been introduced by particle tracking.

The particle tracking model in Fluent 6.2 produces a report recording each injected particle passes through a monitoring plane. The report contains particle information, such as arrival time, instantaneous particle velocities and particle location on the plane, for each individual particle. As the model outlet was set as the monitoring plane and the injection was made at the inlet, the reported arrival times should be directly comparable to the measured.

The individual particle arrival times were amalgamated to produce a retention time distribution. A 'bin' size of 0.09 s was chosen for the histogram to match the sampling time of the laboratory tracer data. Since the CFD profile is the response to an instantaneous injection (i.e. a retention time distribution, RTD) and the recorded data corresponds to a Gaussian upstream distribution, the two sets of profiles cannot be directly compared. A comparable CFD outlet trace was therefore routed through superposition of the outlet profile in accordance with the measured inlet profile (e.g. Figure 2.15). Repeat tests were carried out in the laboratory dye tracing experiments (Guymer *et al.*, 2005). For presentation purposes, only one set of laboratory tracer data is shown for each of the surcharge conditions considered; and the experimental data taken for the tracer comparison was randomly chosen. Note that this set of CFD particle tracking data has been used in Chapter 4 for studying the sensitivity of the derived ADE and ADZ model coefficients to upstream concentration distribution.

The routed CFD profiles generated by the two meshes are compared with the experimental data in Figure 6.6. The version 1 mesh results are coloured in red and the version 2 mesh results in blue. A measure of the goodness of fit, R_r^2 , (Young *et al.*, 1980; Section 4.2.1) between the predicted and measured profiles was used to determine which model prediction is in closer agreement with the measurements. Comparison of the R_r^2 value suggests the version 2 mesh results in a closer fit to the laboratory observations, with the exception of the surcharge ratios of 1.70 and 2.05. The comparison is discussed further as follows:

Figure 6.6a and b show the results of the predictions for the surcharge ratios of 0.69 and 1.02. These surcharge levels correspond to two low pre-threshold surcharge ratios in the Guymer *et al.*

(2005)'s laboratory data. It can be observed that the version 2 mesh results (blue lines) are generally in better agreement with the measured profiles (higher R_r^2 values) than the version 1 mesh results (red lines). The former model results reveal an excellent prediction of the peaks, while the latter sets of data show a significant deviation from the measured: in Figure 6.6a, the peak predicted by the version 1 model is over-estimated by approximately 50 %; and in Figure 6.6b, the version 1 mesh model results in an under-estimated and delayed peak. After the peak, all CFD predictions deviate from the measured profiles by showing a secondary peak in the downstream profiles at times between 40 s and 50 s. The secondary peak corresponds to the results from particles that circulated around the manhole rather than short-circuited the structure (Figure 6.5c). The occurrence of the secondary peak in the predicted profiles rather than a near-exponential decaying tail as observed in the laboratory traces is investigated in Section 6.2.2.3 and Section 6.3.6. Beyond this (time > 60 s), both mesh models appear to describe the last section of the recession tail very well.

At surcharge ratios of 1.70 and 2.05, i.e. two high pre-threshold surcharge ratios, all CFD model results provide a poor description of the downstream concentration distributions (Figure 6.6c and d). There is a noticeable difference in the peak concentration and the shape of the recessing tail between the CFD and experimental data. The version 2 mesh models consistently over-estimate the peak concentration value; whilst the version 1 models predict a lower peak than the measured in Figure 6.6c and a higher peak than the recorded in Figure 6.6d. In Figure 6.6c, the predicted peak (version 2 mesh only) arrives sooner than the measurements suggest. As in Figure 6.6a and b, the synthetic profiles reveal an obvious secondary peak at times between 40 s and 60 s. Again, this is not evident in the measured distributions. Comparing the R_r^2 values for the predictions made by the two mesh models, the version 1 model results appear to produce a better fit to the observed tracers. However, the predictions are generally quite poor.

Figure 6.6e and f show the comparisons of the downstream concentration distributions after the hydraulic transition, i.e. in post-threshold. It is encouraging that both CFD mesh models are able to account for the hydraulic transition and reflect this in the solute transport predictions. The routed profiles are now characterised by a Gaussian distribution at times between 10 s and 25 s, and followed by a long tail with very low concentrations. The shape of the downstream distributions appears to be independent of surcharge ratio. All these qualitatively agree with the laboratory observations. However, an assessment of the simulation accuracy suggests that the numerical predictions tend to over-estimate and delay the peak concentration of the downstream profiles. Comparing the two model results, the version 2 model results show a closer peak as well as a better goodness of fit, R_r^2 , to the observed. Similar to the other surcharge cases considered in this study, the routed profiles indicate a secondary peak in the downstream tracer

distribution. A similar feature is evident in the measured profile, however, occurring sooner than the CFD results suggest.

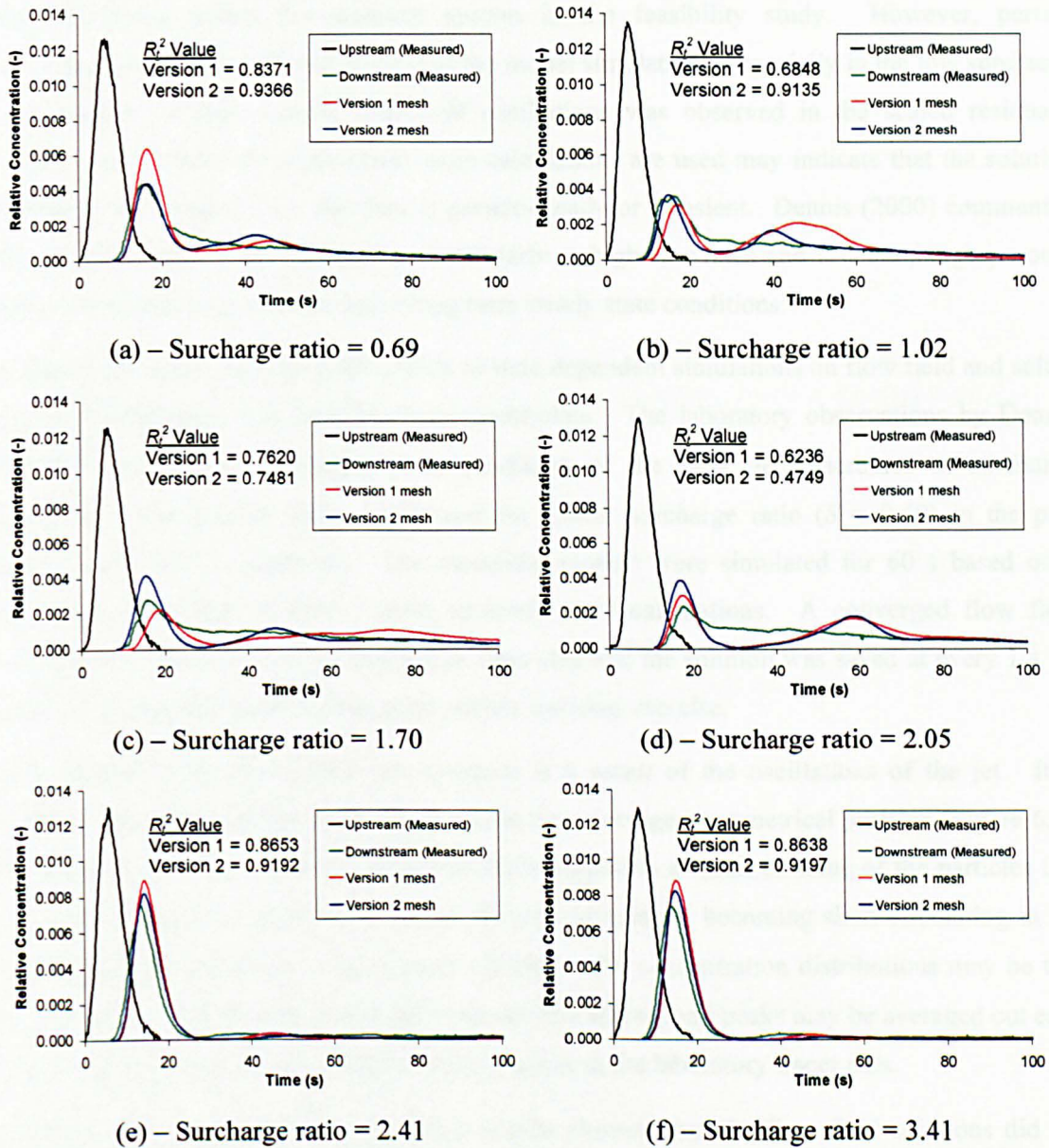


Figure 6.6 – Comparisons of laboratory observations and routed CFD profiles

Determination of which meshing strategy should be used for the subsequent manhole simulations was based on the simulation accuracy of the solute transport predictions. This subsection has shown the comparisons of the tracers at six different surcharge conditions. The version 2 mesh model results generally produce a better fit to the actual data. Therefore, this meshing strategy was adopted in the later manhole simulations.

6.2.2.3 Effects of Time Dependent Simulations

A time average turbulence model with steady state calculations has been used to simulate the fluid dynamics within the manhole system in the feasibility study. However, perfect convergence was not achieved in most of the model simulations, especially in the low surcharge ratio models, in that a small degree of oscillations was observed in the scaled residuals. Oscillations in residuals when steady state calculations are used may indicate that the solution changes with iterations, i.e. the flow is pseudo-steady or transient. Dennis (2000) commented that the flow field within manholes, particularly at high flowrates and low surcharges, would behave in an unsteady manner under long term steady state conditions.

A sensitivity study examining the effects of time dependent simulations on flow field and solute transport predictions has therefore been undertaken. The laboratory observations by Dennis (2000) reported that the degree of unsteadiness of the flow field increases as surcharge decreases. The present study considered the lowest surcharge ratio ($S = 0.69$) in the pre-threshold hydraulic conditions. The numerical models were simulated for 60 s based on a simulation time step of 0.01 s using unsteady state calculations. A converged flow field solution was obtained in every simulation time step and the solution was saved at every 1 s for flow field examination and subsequent particle tracking exercise.

The transient flow field within the manhole is a result of the oscillations of the jet. It is hypothesised that if the jet oscillates about the time average asymmetrical position (Figure 6.7), the magnitude of the secondary peak may be mitigated as a result of some of the particles that circulated around the manhole in the steady state simulation becoming short-circulating in the time dependent simulation. The overall effects on the concentration distributions may be that the secondary peak and the trough between the first and second peaks may be averaged out each other, resulting in a near-exponential trailing tail as in the laboratory tracer data.

However, the time dependent simulation results showed that the flow field solutions did not change with simulation time. The same conclusion is given in the particle tracking results that the retention time distribution (RTD) collected in various times appears to be identical. There are some minor discrepancies between the RTDs, but these are believed to be the random effects of the stochastic tracking process.

The present study has shown that the use of unsteady state calculations do not influence the flow field and particle tracking solutions.

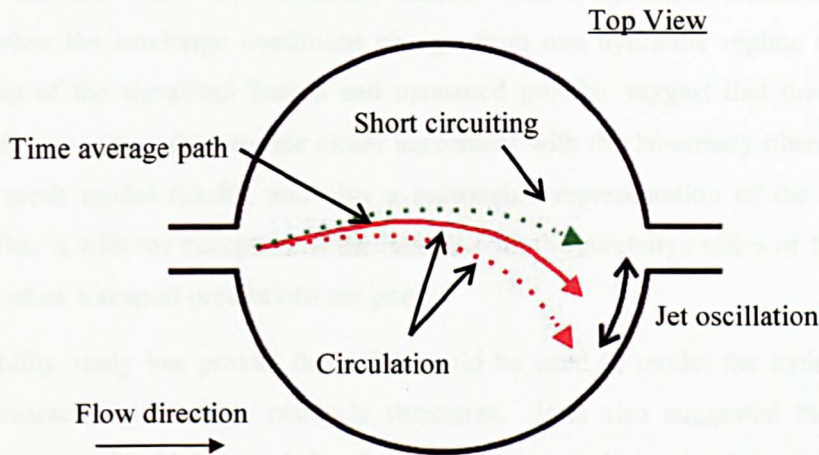


Figure 6.7 – Hypothetical relationship between jet oscillation and particle path line

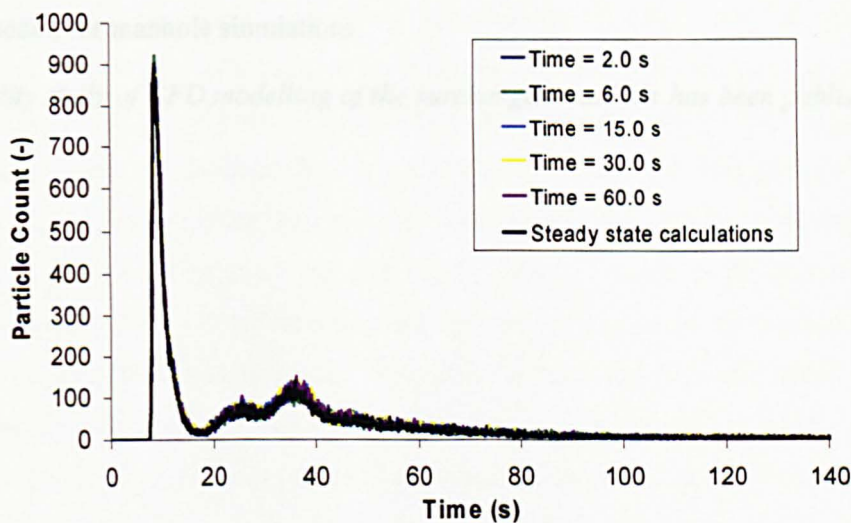


Figure 6.8 – Retention time distribution at different times

6.2.2.4 Conclusions of the Feasibility Study

A feasibility study of CFD manhole simulations was undertaken to investigate whether CFD could simulate the hydraulic and solute transport characteristics within the prototype manhole model. Numerical models of the structure have been created and six surcharge conditions, covering the pre-threshold and post-threshold surcharge range, under one discharge condition have been studied. Due to the complex geometry of the manhole system, it was not possible to develop an ideal mesh (with only structured cell elements) for the model domain. Two meshing strategies for the model have been proposed and evaluated in the study.

The RNG $k-\epsilon$ turbulence model associated with the non-equilibrium wall functions was adopted to predict the flow field; and then the particle tracking model was employed to simulate the tracer experiments undertaken in Guymer *et al.* (2005). The flow field and particle tracking

results for the two mesh models clearly indicate that a hydraulic transition occurs in the structure when the surcharge conditions change from one hydraulic regime to another. The comparisons of the simulated tracers and measured profiles suggest that the version 2 mesh model predictions generally provide closer agreement with the laboratory observations than the version 1 mesh model results; and also a reasonable representation of the measured tracer profiles. This is with the exception of the models with the surcharge ratios of 1.70 and 2.05, for which the solute transport predictions are poor.

This feasibility study has proved that CFD could be used to model the hydraulic and solute transport characteristics within manhole structures. It is also suggested that the version 2 meshing strategy should be used for the subsequent manhole simulations. The following section discusses the scale manhole simulations and the parametric studies of model set-up parameters, such as mesh arrangement, spatial discretisation, turbulence model and solute transport model, for manhole simulations.

The feasibility study of CFD modelling of the surcharged manhole has been published in Lau et al. (2007).

6.3 Scale Manhole Simulations

The feasibility study reported in the previous section has demonstrated that the hydraulic and solute transport characteristics of a surcharged manhole could be replicated using a CFD-based approach. Two meshing strategies for circular manholes were developed and the study highlighted the effects of the meshing strategies on the solute transport predictions. Since the previous study was a preliminary investigation, consideration was not given to the choice of modelling options, for example grid density, spatial discretisation and turbulence model, that the flow field results might be sensitive to. In addition, direct comparisons of the flow field were not made. There is inevitably some uncertainty about the accuracy of the flow field solutions, although the tracer predictions indicated that the CFD results adequately replicate the laboratory measurements and a hydraulic transition within the manhole can also be identified.

Following the feasibility study, a detailed investigation of CFD modelling for surcharged manholes was carried out. The aims of the study are to assess the effects of the choice of the modelling options (Table 6.3) on the flow field and solute transport predictions; and to use the findings from these parametric studies to develop a standard modelling protocol for manhole simulations. The standard modelling protocol developed in this chapter is adopted to generate larger scale manholes in Chapter 7 for studying the effects of scale on the hydraulic and solute transport characteristics. To achieve the aims of the present study the scale manhole model (218 mm ID manhole) was investigated. This was because flow field and tracer measurements of this manhole were available for model validation. Two hydraulic conditions, one in pre-threshold and one in post-threshold, were examined in the detailed CFD manhole simulation study.

Four sensitivity studies were considered in the current investigation and they are summarised in Table 6.3. These studies are thought to be the most important to the accuracy of the flow field and solute transport predictions. In general, numerical errors of CFD results can be caused by a number of factors. In the case of the manhole models, they are: simplification of model geometry; error caused by computational grid (i.e. grid resolution); Taylor series truncation error introduced by finite difference scheme (or spatial discretisation scheme); and error from the numerical model. The grid refinement study and the parametric study for spatial discretisation were intended to provide appropriate modelling approaches to minimising the numerical error caused by grid resolution and truncation error. The sensitivity studies of turbulence and solute transport models were intended to suggest appropriate models for modelling flow field and solute transport that would lead to the least numerical error.

Model simplification was made to the free surface in the manhole and this undoubtedly introduced some error to the flow field and solute transport predictions. However, due to the limitations of computational resources, it was not possible to consider a two phase (water and air) model which can account for the effects of the free surface. Nevertheless, the single phase model should be acceptable because confidence in this simplification has been provided by the acceptable results generated in the feasibility study.

Parametric Studies	Objectives
Grid refinement	Identification of the mesh density required to obtain a grid independent flow field solution so that the errors associated with grid resolution, arise from interpolation between neighbouring grid points, are minimised
Spatial discretisation scheme	Identification of appropriate schemes to minimise truncation error and obtain stable solutions
Turbulence model	Identification of appropriate turbulence models to reduce the numerical errors caused by RANS turbulence model
Solute transport model	Identification of appropriate solute transport models

Table 6.3 – Parametric studies considered and the aims of each study

6.3.1 Consideration of the Hydraulic Conditions

Selection of the hydraulic conditions in the present CFD manhole study was based on the flow visualisation experiments described in Chapter 5. Consideration was given to one pre-threshold and one post-threshold hydraulic condition, assuming that the two detailed investigations would be sufficient to demonstrate the validity of the CFD simulations of the manhole over the full range of surcharge ratios. The two conditions chosen for the study are a mid-point from the pre-threshold depth range ($S = 1.17$) and a mid-point from the post-threshold dataset ($S = 3.27$) at a discharge of 0.35 l/s, which was a mid-point from the discharge range (Table 5.1).

6.3.2 Basic Setup of the CFD Scale Manhole Models

The geometry of the CFD scale manhole models was created according to the experimental configurations as shown in Figure 3.1. The model comprised an inlet pipe of 24 mm internal diameter (ID) from the upstream fluorometer to the manhole inlet; the circular manhole chamber of 218 mm ID; and a 24 mm ID outlet pipe to the downstream fluorometer. Specifications of fluid properties and boundary conditions followed the settings defined in the feasibility study (Table 6.4).

In order to reduce the number of tests in the parametric studies, only the higher order accurate modelling options were considered. For spatial discretisation scheme, consideration was only

given to second order accurate approaches. For turbulence model, the RSM turbulence model and the RNG $k-\varepsilon$ turbulence model coupled with the non-equilibrium wall functions were examined. The modelling options used throughout each parametric test are described in the sensitivity studies.

Model Configurations	Setting/Value
Fluid properties	
<i>Density</i>	998.2 kg/m ³
<i>Dynamic viscosity</i>	1.003 kg/ms
Boundary conditions	
<i>Inlet</i>	<i>Velocity inlet</i> (Inputted with a fully developed flow profile, see example in Section 6.2.1.4)
<i>Outlet</i>	<i>Pressure outlet</i>
<i>Wall</i>	<i>Wall</i> (Roughness height = 8×10^{-5} m; roughness constant = 0.5)
<i>Free surface</i>	<i>Symmetry</i> (Rigid lid approximation)

Table 6.4 – Fluid properties and boundary conditions for the CFD scale manhole models

6.3.3 Grid Refinement Study

In finite volume based CFD, the domain is divided into a grid or mesh of small volumes, called cells. The resolution of the grid governs the accuracy of the numerical predictions as the computation relies on interpolation between neighbouring grid points. In principle, the errors associated with grid resolution can be minimised by increasing the number of grid points. An ideal CFD solution should be independent of the computational grid, i.e. the results do not change with further refinement of the mesh. However, such an ideal solution is strictly unattainable (Awbi, 2003) and a nearly grid independent solution is more practical to achieve. A grid refinement study was undertaken to determine the cell size/mesh density required to obtain a nearly grid independent solution.

As the flow dynamics differ noticeably in the two contrasting hydraulic regimes, the study was conducted for both the pre- and post-threshold surcharged manhole models ($S = 1.17$ and $S = 3.27$). For each model, three different mesh densities were tested with the number of cells in the domain being approximately doubled in each refinement step. Details of the meshes considered during the grid refinement study are given in Table 6.5.

A minor modification was made to the meshing strategy for the manholes. A boundary layer (one cell thick, cell size = 2 mm) was applied to the pipe sections. This was to obtain better y^+ values in the range of 30 and 300, validating the wall functions adopted in the pipes.

Surcharge Ratio (-)	Model	Total Number of Cells	Average Cell Volume (mm ³)	Average Cell Size (mm)
$S = 1.17$ (Total volume = 2,178,544 mm ³)	Mesh 1	133,308	16.34	2.54
	Mesh 2	293,352	7.43	1.95
	Mesh 3	444,648	4.90	1.70
$S = 3.27$ (Total volume = 4,059,643 mm ³)	Mesh 1	224,280	18.10	2.63
	Mesh 2	464,280	8.74	2.06
	Mesh 3	783,954	5.18	1.73

Table 6.5 – Details of the meshes considered during the grid refinement study

The RSM turbulence model with the non-equilibrium wall functions and second order accurate spatial discretisation schemes were chosen for the flow field predictions. There are a number of modelling options available for the RSM turbulence model but the default set in Fluent 6.2 was adopted. The governing equations for momentum, turbulent kinetic energy, turbulent dissipation rate and Reynolds stresses were calculated using the *second order upwind* scheme; for the pressure term, the *second order* scheme was used; the *SIMPLE* scheme was selected for the pressure-velocity coupling. Detailed description of these spatial discretisation schemes may be found in Barth and Jespersen (1989); Patankar and Spalding (1972). Note that the RSM was selected as the flow field solver in this study, instead of the RNG $k-\varepsilon$ turbulence model, because the cell density required for a grid independent solution in the RSM is expected to be higher than, or similar to, the RNG model. This is because the RSM resolves all the terms (e.g. pressure, velocities and ε) that the RNG $k-\varepsilon$ turbulence model would calculate but also considers additional terms (Reynolds stresses) in the flow. The additional terms may require a more stringent cell arrangement for a grid independent solution. As a result, if a given mesh model generates a grid independent solution in the RSM, the same mesh will be likely to produce a grid independent solution in the RNG $k-\varepsilon$ turbulence model (simpler model).

The dependence of the flow field solution upon mesh density was examined by comparing the longitudinal velocity predictions of mesh 1 and mesh 2 models to the results of mesh 3 model. The mesh 3 model results are considered to be the closest to grid independent solutions because these models have the highest density mesh in the present study. The longitudinal velocity was chosen for the comparison because it is the major component of the three velocity vectors and is able to show the flow structure within the manhole.

CFD can produce results for any two-dimensional plane within the domain for subsequent analysis. The planes of investigation selected in this analysis are the vertical and horizontal planes at the centreline of the pipe, (CVP and CHP). Selection of these planes is because the

planes sliced through the centre of the turbulent jet and the circulations besides the jet, where the largest gradient of the dependent variables can be observed. The effects of the cell size on large variable gradients are expected to be more obvious.

Figure 6.9 and Figure 6.10 compare the longitudinal velocity results obtained from the three mesh models under pre- and post-threshold conditions respectively. In each figure, three contour plots are provided:

1. The first plot comprises the superposition of contours of the longitudinal velocity predicted in the three models; the flooded contour associated with the solid black line represents mesh 3 data; the dashed line and the 'dash-dot-dot' line correspond to the mesh 2 and 1 results respectively;
2. The second figure shows the difference of the flow variable between the mesh 3 and mesh 2 solutions (Equation 6.1).
3. The final figure shows the difference of the flow variable between the mesh 3 and mesh 1 predictions (Equation 6.1).

$$\text{Difference} = \text{Prediction of Mesh 3} - \text{Prediction of Mesh 2 or 1} \quad 6.1$$

A method for quantifying the difference of the flow variable between two sets of data over the entire plane has been adopted in this thesis. This is by using a cumulative distribution of percentage difference estimated by Equation 6.2; the median value of the distribution was assumed to be the average percentage difference over the plane; and was used to aid the determination of a nearly grid independent flow field solution from a given mesh density model. Note that Equation 6.2 is the general form for the estimation of percentage difference. u_1 in this study was defined as the longitudinal velocity of the mesh 3 mode.

$$\% \text{ Diff} = \frac{\text{abs}(u_1 - u_2)}{\text{abs}(u_1)} \times 100\% \quad 6.2$$

Comparison of the pre-threshold model predictions (Figure 6.9) suggests that the results produced from the mesh 2 model approach the grid independent solution, while noticeable difference between the coarsest and finest mesh models can be observed. The deviation of the solutions (Figure 6.9e and f) predominantly appears at the asymmetric jet, where larger cell size (mesh 1) tends to over-estimate the jet velocity within the manhole. The skewness of the jet appears to be independent of cell spacing. In Figure 6.9c-f, there are some noticeable discrepancies at the model boundary. However, these are expected to be the combined effects of the cell size of the wall adjacent cell and the wall functions applied. Using the cumulative distribution to estimate the median percentage difference between the mesh 2 and 3 models

yields 1.0 % and 0.9 % for the CVP and CHP respectively; for the mesh 1 model, the median percentage difference is 1.9 % and 2.4 % for the CVP and CHP. Note that discussion of the pre- and post-threshold flow fields is presented in Section 6.3.5.

Figure 6.10 shows the effects of cell size on the post-threshold flow field predictions. In general, the three mesh model results show great similarity, and the solution obtained from the mesh 1 model seems to approach the grid independent solution. There are some minor variations between the mesh 3 model and mesh 2/mesh 1 models at the outlet pipe (Figure 6.10c-f). However, the error relative to the local value of the variable is less than 4 %. As in the pre-threshold flow field comparisons, there are some discrepancies at the model boundary. The median percentage difference between the mesh 2 and 3 models is 2.3 % and 1.3 % for the CVP and CHP; and 1.9 % and 2.1 % for the CVP and CHP between the mesh 1 and 3 models.

The cumulative distributions of the percentage difference for the two planes under the two hydraulic conditions are presented in Figure 6.11. These figures confirm that comparing the same cumulative percentage, the percentage difference between the mesh 2 and mesh 3 models is smaller than the mesh 1 and mesh 3 models in all cases, with the exception of Figure 6.11c where the two distributions are almost identical.

The present study shows that further refinement of the grid smaller than approximately 2 mm (average cell size in Table 6.5) does not have a significant effect on the flow field prediction (less than 2 % difference). For this reason, the mesh 2 models have been used for the subsequent parametric tests and manhole simulations.

In fact, the same conclusion was reached when other variables, for example turbulent kinetic energy, Reynolds stresses, were used for the comparison (figures not shown).

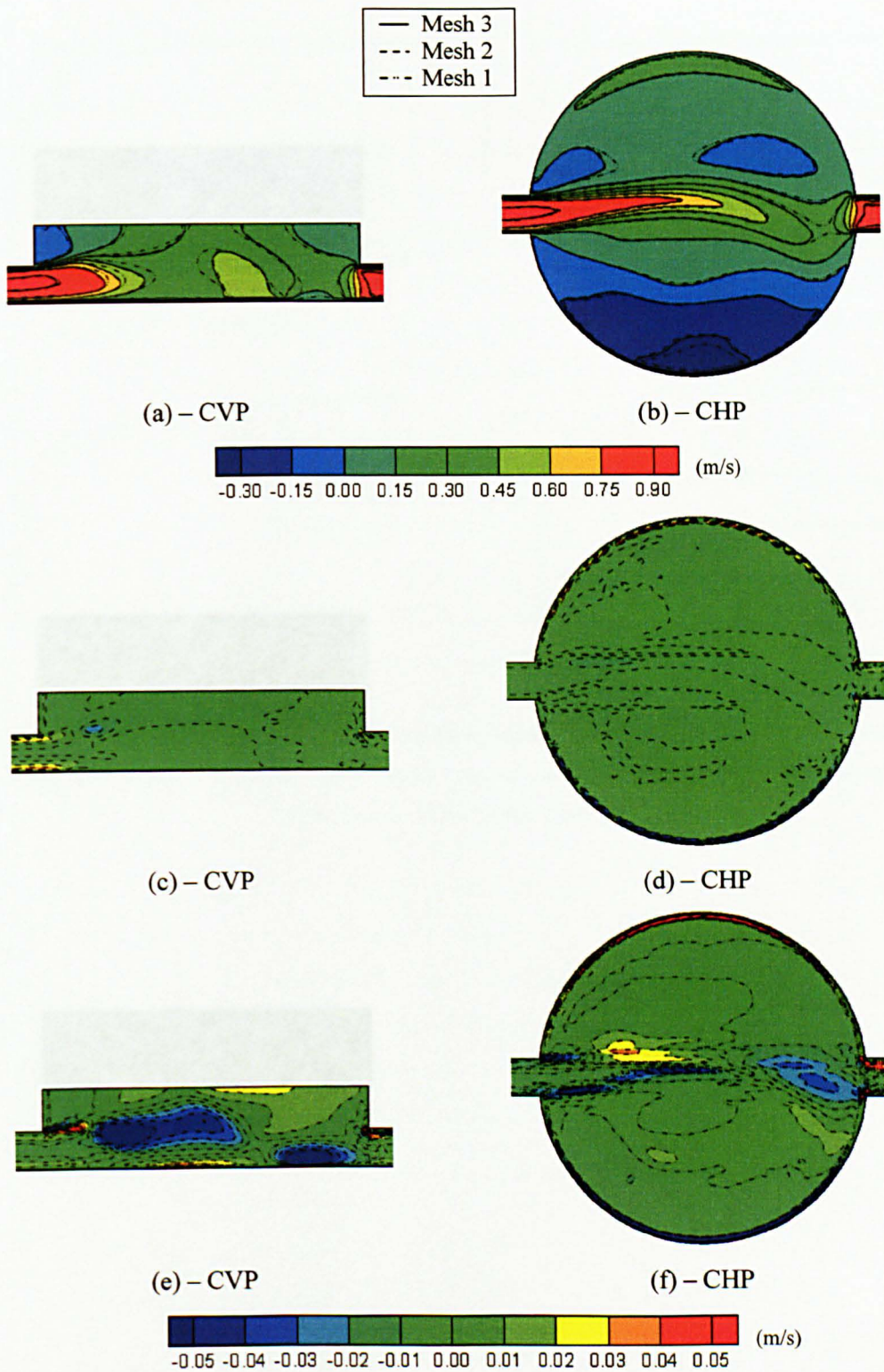


Figure 6.9 – Comparisons of the longitudinal velocity of the pre-threshold models (Flow from left to right): (a, b) – Superposition of the three contours; (c, d) – Difference between mesh 3 and mesh 2 results; (e, f) – Difference between mesh 3 and mesh 1 results

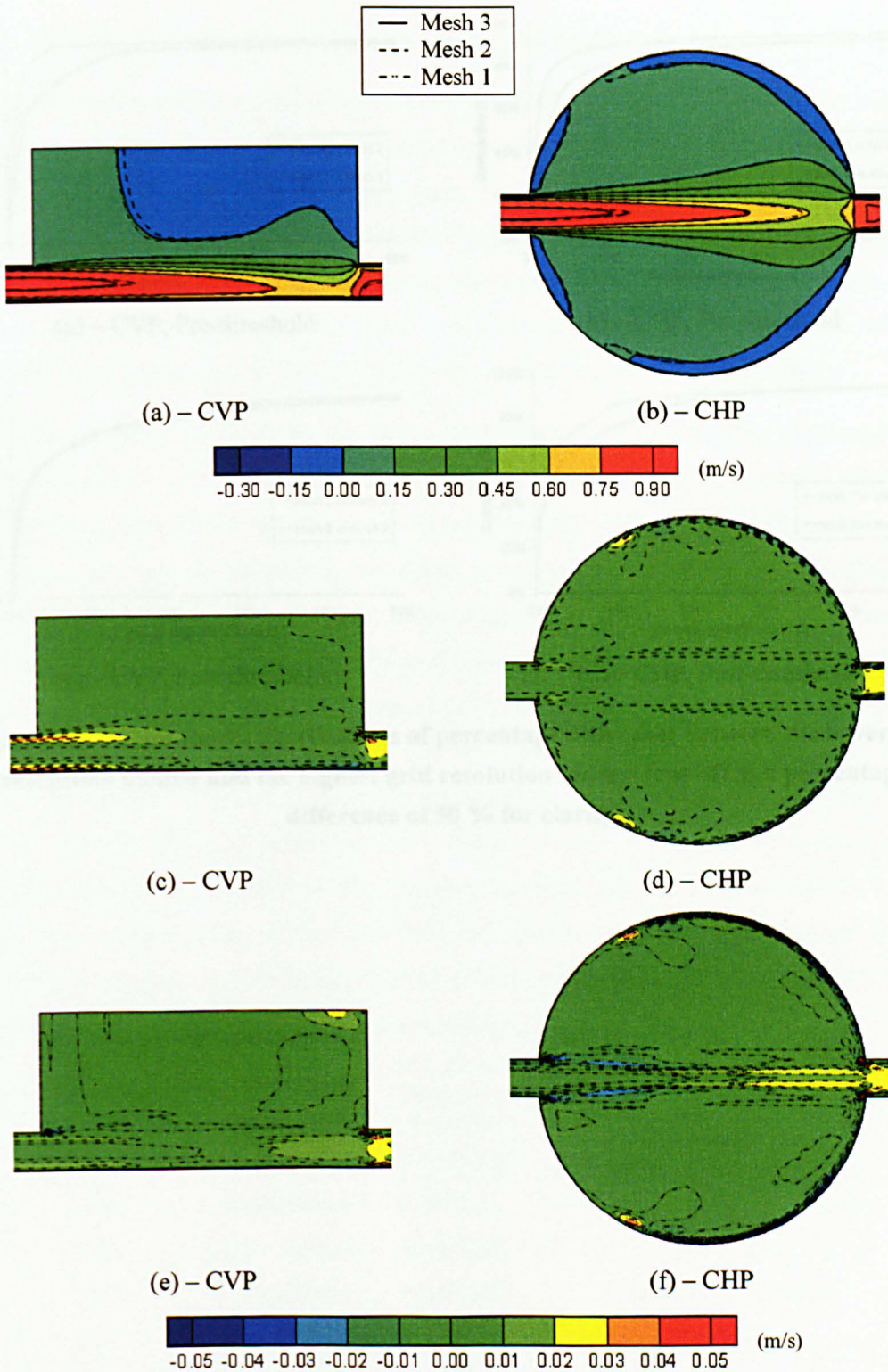
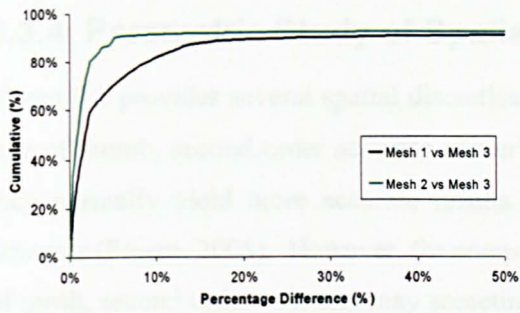
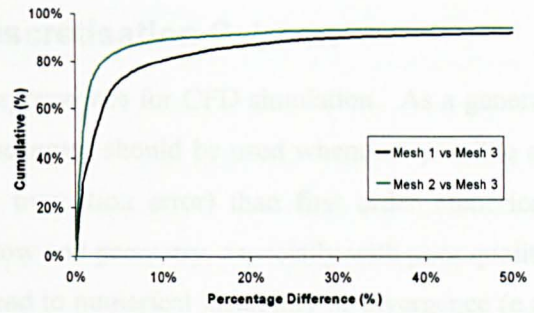


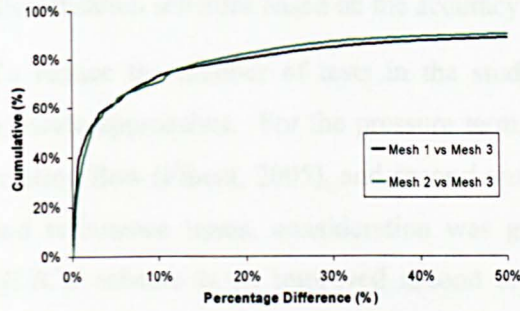
Figure 6.10 - Comparisons of the longitudinal velocity of the post-threshold models (Flow from left to right): (a, b) – Superposition of the three contours; (c, d) – Difference between mesh 3 and mesh 2 results; (e, f) – Difference between mesh 3 and mesh 1 results



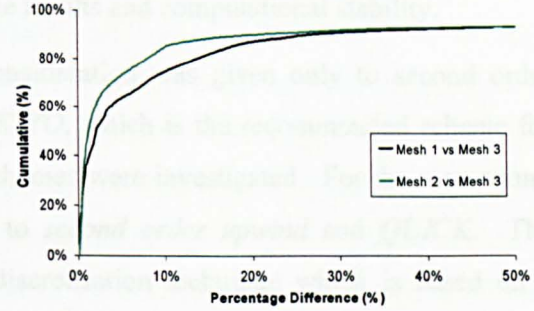
(a) – CVP, Pre-threshold



(b) – CHP, Pre-threshold



(c) – CVP, Post-threshold



(d) – CHP, Post-threshold

Figure 6.11 – Cumulative distributions of percentage difference between the lower grid resolution models and the highest grid resolution models (cut-off at a percentage difference of 50 % for clarify)

6.3.4 Parametric Study of Spatial Discretisation Scheme

Fluent 6.2 provides several spatial discretisation approaches for CFD simulation. As a general rule of thumb, second order accurate numerical schemes should be used whenever possible as they normally yield more accurate results (less truncation error) than first order numerical schemes (Fluent, 2005). However, for complex flow and geometry, especially with poor quality of mesh, second order schemes may sometimes lead to numerical instability or divergence (e.g. Section 6.2.1.2.1). A parametric study was performed to determine the best combination of discretisation schemes based on the accuracy of the results and computational stability.

To reduce the number of tests in the study, consideration was given only to second order accurate approaches. For the pressure term, *PRESTO*, which is the recommended scheme for rotating flow (Fluent, 2005), and *second order* schemes were investigated. For the momentum and turbulence terms, consideration was given to *second order upwind* and *QUICK*. The *QUICK* scheme is an improved second order discretisation technique which is based on a weighted average of *second order upwind* and central interpolations of the variable (Leonard, 1979). It would typically be more accurate on structured grids aligned with the flow direction; in other cases, *QUICK* would interpolate the face value of the variable in the same way as *second order upwind*. The sets of discretisation schemes tested in the study are summarised in Table 6.6. Details of the spatial discretisation techniques can be found in Barth and Jespersen (1989); Leonard (1979); Patankar (1980); Patankar and Spalding (1972). Note that the selection of pressure-velocity coupling scheme was not considered in this study. This stemmed from the fact that these schemes only influence the rate of convergence (Fluent, 2005). *SIMPLEC* was used in the manhole simulations to improve convergence speed.

Discretisation Scheme Combination	Pressure	Pressure-Velocity Coupling	Momentum, Turbulence Terms
DS 1	<i>Second order</i>	<i>SIMPLEC</i>	<i>Second order upwind</i>
DS 2	<i>Second order</i>	<i>SIMPLEC</i>	<i>QUICK</i>
DS 3	<i>PRESTO</i>	<i>SIMPLEC</i>	<i>Second order upwind</i>
DS 4	<i>PRESTO</i>	<i>SIMPLEC</i>	<i>QUICK</i>

Table 6.6 – Combinations of spatial discretisation schemes considered in the parametric study

Similar to the grid refinement study, the default modelling options for the RSM turbulence model coupled with the non-equilibrium wall functions was employed for the flow field predictions. Computation of the flow was based on the mesh 2 (grid independent mesh) models.

Evaluation of the four sets of discretisation schemes was based on flow field variation and computational stability. Flow field variation is once more shown by assessing the difference in the longitudinal velocity prediction on the CVP and CHP between different configurations; and the median percentage difference. Computational stability was judged by the convergence of each term's scaled residuals during calculation. A stable solution is indicated by scaled residual curves with low and constant values (Fluent, 2005). This represents small errors in the calculation of the governing equations and a unique solution.

Assessment of the flow field variations suggested that the flow field predictions in both the pre- and post-threshold hydraulic regimes were barely affected by the choice of pressure interpolation scheme (DS 1 vs DS 3 and DS 2 vs DS 4, figures not shown). The shape of the jet and the magnitude of the flow velocity between the models were highly comparable; for example, comparing DS 2 and DS 4, the median percentage difference (Equation 6.2, with $u_i =$ DS 4) in the longitudinal velocity between the pre-threshold models on the CVP and CHP is less than 1 % (Table 6.7); similar values are obtained for the post-threshold models and in the comparisons of the DS 1 and DS 3 results (with $u_i =$ DS 3). Figure 6.12 shows that the cumulative distributions of percentage difference between 'DS 1 and DS 3' and 'DS 2 and DS 4' are highly comparable.

When the PRESTO scheme was used, the calculations generally yielded lower residuals and a lesser degree of oscillation in the scaled residual curves. Therefore, this numerical scheme was judged to be more stable and was employed in the subsequent sensitivity tests.

Comparisons of the flow field predictions associated with *second order upwind* and *QUICK* schemes (DS 3 vs DS 4) suggested that the flow field results are not significantly affected by the choice of (second order accurate) discretisation schemes for the momentum and turbulence terms, although minor variations in the pre-threshold flow field were observed (Figure 6.13). In comparison with the *QUICK* results (DS 4), the *second order upwind* scheme (DS 3) produced a more skewed jet with marginally quicker velocity decay in the jet core. Nevertheless, the median percentage difference in the longitudinal velocity (with $u_i =$ DS 4) for the two planes under this hydraulic condition was negligible, with 1.5 % and 1.8 % for the CVP and CHP respectively (Table 6.7). The post-threshold flow fields simulated by DS 3 and DS 4 were nearly identical (Figures not shown).

The effects of the choice of the second order accurate discretisation schemes (*second order upwind* vs *QUICK*) on the resultant flow field do not appear to be significant. For example, in pre-threshold, 80 % of the data points have a percentage difference of less than 10 %; and 70 % of the data points for the post-threshold case. The small differences between DS 3 and DS 4

results may be explained by the fact that the two schemes are both second order accurate, i.e. same order of magnitude for truncation error; and in fact, they employ the same technique to solve the flow field solution when the flow direction is not aligned with structured grids. However, careful examination of the cumulative curves in Figure 6.12 suggests that the effect of the discretisation scheme is relatively more significant in the post-threshold case than in the pre-threshold case. An explanation can be offered is that the straight through jet is aligned with the structured grids (Figure 6.3), in which the *QUICK* scheme is third order accurate in the truncation errors (Leonard, 1979; Versteeg and Malalasekera, 1995). In terms of numerical stability, the DS 3 and DS 4 models attained similar characteristics of the scaled residual curves in both the pre-threshold and post-threshold cases. *QUICK* is selected because the numerical scheme is inherently an improved version of *second order upwind* (Leonard, 1979).

Based on the results presented above, the parametric study suggests that *PRESTO* and *QUICK* should be used for CFD simulation of surcharged manholes. In the following parametric test which investigates the effects of the turbulence modelling options (Section 6.3.5.2), the flow field solution is found to be more dependent upon the choice of turbulence model than the choice of second order accurate discretisation scheme.

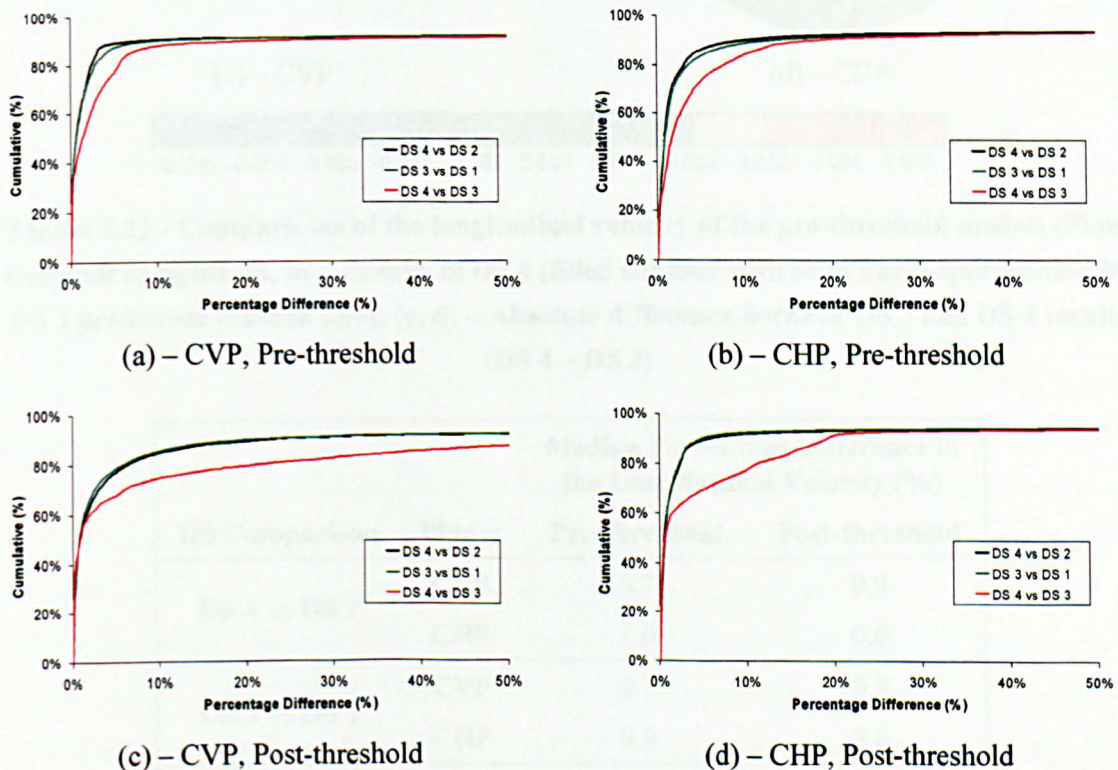


Figure 6.12 – Cumulative distributions of percentage difference between discretisation scheme configurations (cut-off at a percentage difference of 50 % for clarify)

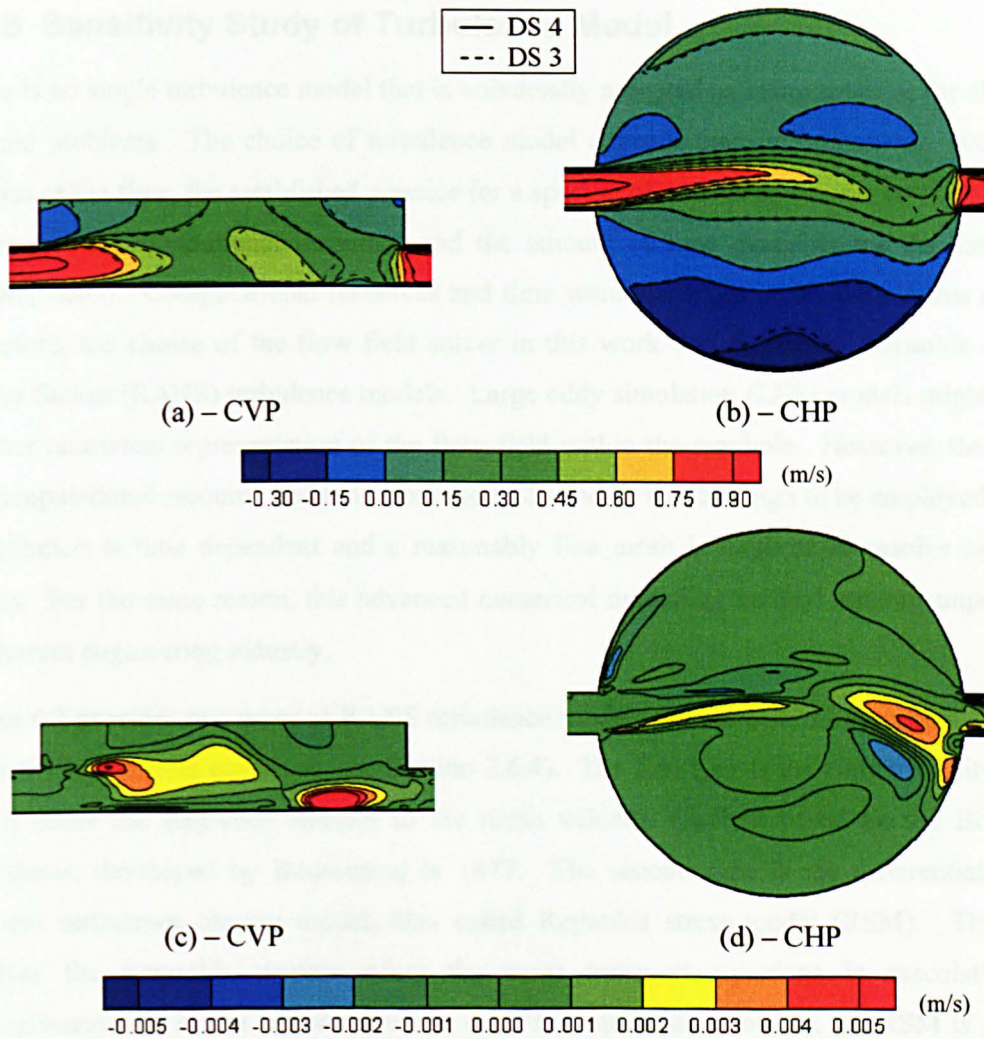


Figure 6.13 - Comparisons of the longitudinal velocity of the pre-threshold models (Flow from left to right): (a, b) – Results of DS 4 (filled contour with solid line) superposition by DS 3 prediction (dashed line); (c, d) – Absolute difference between DS 3 and DS 4 results (DS 4 – DS 3)

DS Comparison	Planes	Median Percentage Difference in the Longitudinal Velocity (%)	
		Pre-threshold	Post-threshold
DS 4 vs DS 2	CVP	0.7	0.9
	CHP	1.0	0.6
DS 3 vs DS 1	CVP	0.7	0.8
	CHP	0.9	0.6
DS 4 vs DS 3	CVP	1.5	0.9
	CHP	1.8	0.6

Table 6.7 – Median percentage difference in the longitudinal velocity between discretisation scheme configurations

6.3.5 Sensitivity Study of Turbulence Model

There is no single turbulence model that is universally accepted as being superior for all classes of fluid problems. The choice of turbulence model depends upon considerations such as the physics of the flow, the established practice for a specific class of problem, the level of accuracy required, the computational resources and the amount of time available for the simulations (Fluent, 2005). Computational resources and time were the major constraints in this research. Therefore, the choice of the flow field solver in this work was limited to Reynolds averaged Navier Stokes (RANS) turbulence models. Large eddy simulation (LES) models might provide a better numerical representation of the flow field within the manhole. However, the demand for computational resource and time from the LES models was too high to be employed because the solution is time dependent and a reasonably fine mesh is required to resolve turbulence eddies. For the same reason, this advanced numerical modelling method remains unpopular in the current engineering industry.

Fluent 6.2 provides two types of RANS turbulence models to deal with the Reynolds stresses in the RANS governing equations (see Section 2.6.4). The first type is the eddy viscosity models which relate the Reynolds stresses to the mean velocity gradient based on the Boussinesq hypothesis, developed by Boussinesq in 1877. The second type is the differential second-moment turbulence closure model, also called Reynolds stress model (RSM). This model resolves the Reynolds stresses using the exact transport equations in association with approximations to model various terms to close the equations. To date, the RSM is generally viewed to be the most accurate approach to describing turbulent structures in a flow among all RANS turbulence models.

The aim of the parametric study is to identify the most appropriate turbulence model, based on numerical accuracy and computational stability. The Fluent software provides numerous variants of the k - ϵ eddy viscosity model and RSM. Due to limited time, it was not possible to investigate all of the modelling options available in Fluent 6.2. Consideration was given to the RNG k - ϵ turbulence model and the RSM in association with the quadratic pressure strain (QPS) model in this study. The RNG k - ϵ turbulence model is an improved form of the standard k - ϵ turbulence model, which provides a more accurate solution when dealing with swirling flows (Fluent, 2005). This is also the current industrial standard turbulence model (personal communication with Fluent engineer). The RSM in conjunction with the QPS modelling option should be the most sophisticated and accurate RANS model describing anisotropic turbulence in Fluent 6.2 (Speziale *et al.*, 1991).

An overview of the turbulence models available in Fluent 6.2 and the final choice of the models considered in this study are presented in Figure 6.14 and Table 6.8. There are modelling options for the RNG and RSM models. A brief summary of these modelling options is provided in the following sub-section. Further details of the turbulence models can be found in Fluent (2005); Speziale *et al.* (1991); Versteeg and Malalasekera (1995); Yakhot *et al.*, (1992).

In the sensitivity study, the simulations used the mesh 2 models and the DS 4 configuration (Table 6.6). The non-equilibrium wall functions were employed to model the near wall viscous affected flow.

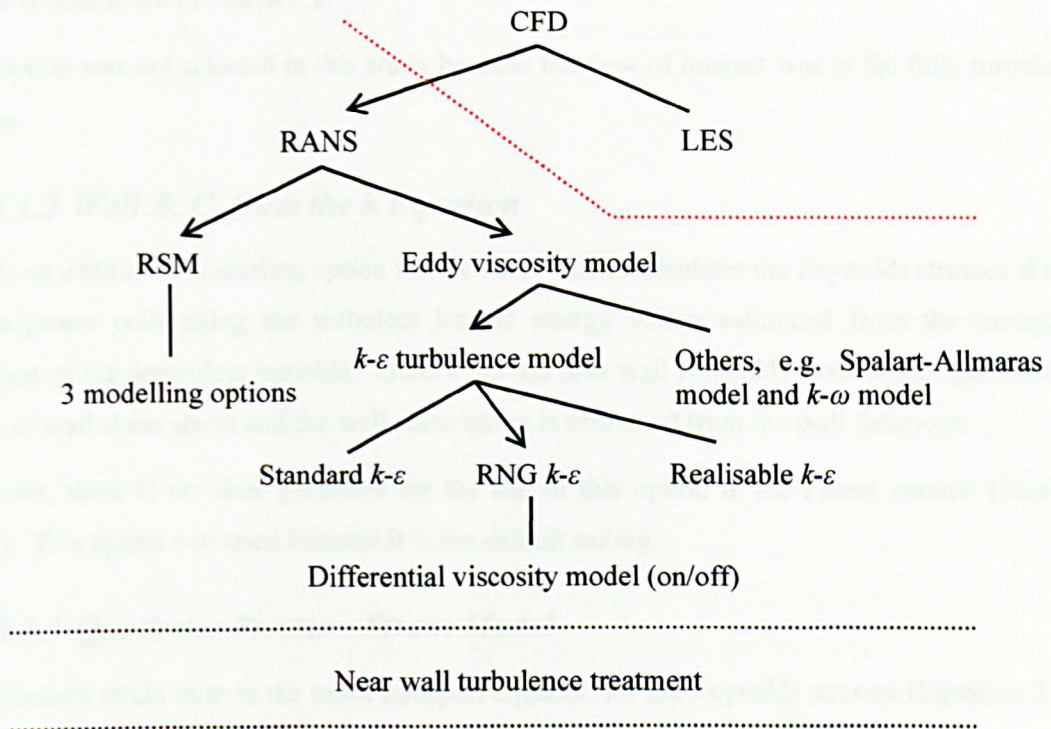


Figure 6.14 – Overview of the turbulence models available in Fluent 6.2

Turbulence Model	Modelling Options			
	Differential Viscosity Model	Wall B.C. from k Equation	Quadratic Pressure Strain Model	Wall Reflection Effects
RNG $k-\epsilon$	Off			
RSM with QPS		On	On	

Table 6.8 – Turbulence model configurations considered in the parametric tests

6.3.5.1 Modelling Options for the RNG and RSM Models

The modelling options for the two turbulence models considered in this parametric study are briefly described as follows:

6.3.5.1.1 Differential Viscosity Model

The differential viscosity model is an additional modelling option available in the RNG k - ϵ turbulence model. The model provides a different approach to dealing with the turbulent viscosity for a better representation of low Reynolds number flows. By default, this modelling option is deselected in Fluent 6.2.

This option was not selected in this study because the flow of interest was in the fully turbulent regime.

6.3.5.1.2 Wall B. C. from the k Equation

This is an additional modelling option for the RSM which calculates the Reynolds stresses at the wall-adjacent cells using the turbulent kinetic energy values estimated from the transport equation of the dependent variable. Otherwise, the near wall Reynolds stresses are specified in terms of wall shear stress and the wall shear stress is estimated from the wall functions.

However, there is no clear guideline for the use of this option in the Fluent manual (Fluent, 2005). This option was used because it is the default setting.

6.3.5.1.3 Quadratic Pressure Strain Model

The pressure strain term in the exact transport equation for the Reynolds stresses (Equation 2.54) can be modelled using the linear pressure strain (LPS) model, developed by Launder *et al.* (1975), or the quadratic pressure strain (QPS) model, proposed by Speziale *et al.* (1991). The QPS model is a more sophisticated model than the LPS model, which describes the Reynolds stresses in a quadratic form (Younis *et al.*, 1996). It has been shown to give superior flow predictions in a variety of simple shear flows (Fluent, 2005). The QPS model was used in this study for these reasons.

The LPS model is the default option for the RSM.

6.3.5.1.4 Wall Reflection Effects

Wall reflection effects, or the wall reflection term, may be included in the pressure strain equation only when the linear pressure strain (LPS) model is used. The wall reflection term is responsible for the redistribution of normal stresses near the wall, which dampens the normal

stress perpendicular to the wall while enhancing the stresses parallel to the wall. By default, this is selected.

6.3.5.2 Assessment of Flow Field Simulation Accuracy

To assess the simulation accuracy, and use this to decide which model is superior, the computational results are compared to the PIV measurements. Two types of assessment were performed in the validation study: a qualitative assessment was carried out to examine the difference in the flow patterns by comparing the vector directions between the two sets of data; a quantitative assessment was then followed to quantify the discrepancy between the predicted and measured longitudinal velocity. The quantitative assessment was based on the direct comparison of the contours using Equation 6.3 and the cumulative distribution of percentage difference (Equation 6.2, with $u_l = \textit{Long. Velocity}_{PIV}$). The median value is defined as the average percentage difference over the entire plane.

$$\textit{Velocity Difference} = \textit{Long. Velocity}_{CFD} - \textit{Long. Velocity}_{PIV} \quad 6.3$$

Turbulence kinetic energy and turbulent intensity were also evaluated from the PIV data. However, these datasets were judged to be unreliable because the time average turbulence results varied noticeably between repeat tests (see Section 5.5.4.4.1). The turbulence data was not considered for the flow field validation in this study.

The decision as to which turbulence model to adopt was made based on the flow field validation for the CVP and CHP under the two contrasting hydraulic conditions. Section 6.3.5.3 presents the validation of the flow field for the non-central planes predicted by the selected turbulence model.

In the flow field validation study, the following (*italic*) terms are used to describe the position of the manhole in this thesis:

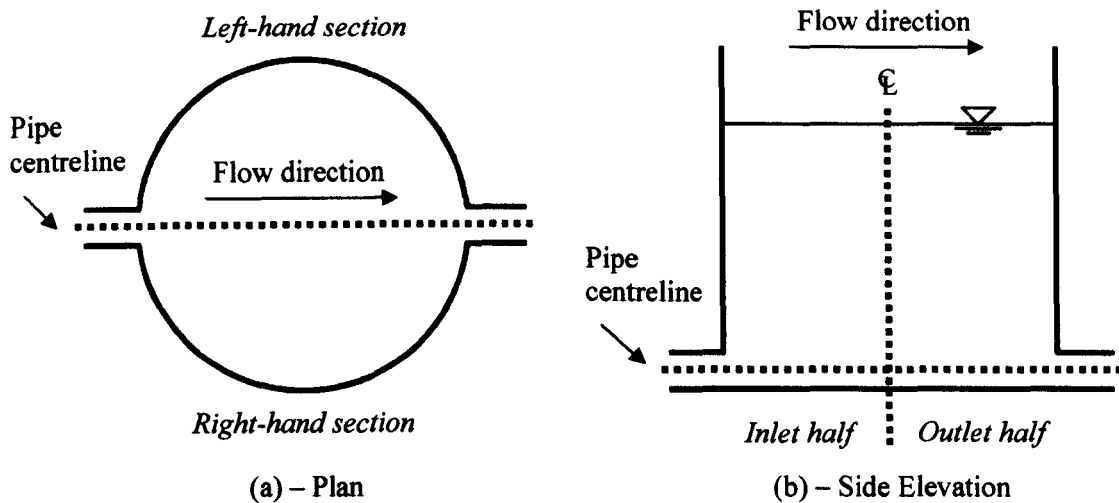


Figure 6.15 – Terms defined in the flow field validation study

6.3.5.2.1 RNG k - ϵ Turbulence Model

This sub-section presents comparisons between the flow field predictions made by the RNG k - ϵ turbulence model and the PIV measurements. The discussion begins with the pre-threshold hydraulic conditions and then the post-threshold regime. As mentioned in the previous sub-section, the comparisons focus on the flow fields on the CVP and CHP. It is important to note that the manhole PIV measurements closer than 15 mm to the inlet and outlet boundaries should not be used for validation due to the physical boundary effects of the manhole (Section 5.5.4.4.2). The data presented was post-processed using TecPlot 8.0.

6.3.5.2.1.1 Pre-threshold

Figure 6.16 and Figure 6.17 show the computed and measured flow fields for the CVP and CHP under the pre-threshold conditions. In general, the computed flow patterns are, qualitatively, in good agreement with the measured data. On the CVP (Figure 6.16c), the two sets of data show similar vector plots, suggesting an approximately uni-directional flow towards the outlet. On the CHP (Figure 6.17c), a skewed jet deviating towards the left of the inflow is evident in both datasets. The skewed jet introduces an anti-clockwise circulation in the left-hand section of the manhole and a circulation in the same direction in the right-hand section. In the right-hand section, minor discrepancies of the vector plots in close proximity to the manhole inlet and outlet are observed. Close to the inlet, the CFD results suggest an additional small anti-clockwise circulation, which is not observed in the PIV measurements; near the outlet, the PIV results reveal a small clockwise circulation but this secondary flow feature has not been predicted in the CFD data. Note that in the PIV experiments and CFD simulations, the skewed

jet did not always deviate towards the same side. The direction of the jet deviation was entirely random.

Careful examination of the longitudinal velocity on the two planes suggests that the simulated data deviates moderately from the 6 s time average PIV results (Figure 6.16d and Figure 6.17d). The major difference between the two data is at the asymmetric jet, in that there is a large area with a variation of more than 0.2 m/s. The numerical model predicts a stronger jet with a lower degree of asymmetry and jet spreading in the manhole chamber; while the PIV data indicates a weaker and more skewed jet in the structure. The PIV data also shows a larger amount of momentum loss in the jet within half the manhole diameter distance. In the right-hand section (on the CHP), there is another noticeable variation in the longitudinal velocity close to the manhole outlet. This is caused by the CFD model's failure to predict the small clockwise circulation in the region.

The discrepancies in the longitudinal velocity between the numerical model results and PIV measurements do not necessarily mean that the CFD results for the pre-threshold case are erroneous. Under the pre-threshold hydraulic conditions, the PIV flow measurements reveal temporal variations, and there appear to be two possible shapes of the jet (Figure 6.18). One possible form is the skewed jet shown in Figure 6.18a. This form appears to be dominant in the pre-threshold flow field and therefore is revealed in the measured time average results. Another possible form, which occurs in the flow occasionally, is an approximated straight through jet flow (Figure 6.18b). Comparing the two possible forms of the jet to the CFD prediction, the numerical prediction made by the RNG $k-\varepsilon$ turbulence model matches the latter jet shape quite closely.

The median percentage difference (Equation 6.2, with $u_l = \text{Long. Velocity}_{PIV}$) for the CVP and CHP under the pre-threshold hydraulic regime evaluated from the cumulative distributions, shown in Figure 6.19a-b, is 37 % and 52 % respectively. Concern may be expressed that the prediction error is significant for the two planes. However, it is important to recall that the values also account for the boundary effects in the PIV dataset, such as the erroneous velocity in close proximity to the inlet and outlet. These effects could possibly increase the median value because there are more data points with a high percentage difference value. The actual values should be much smaller than the calculations suggest. Nevertheless, it is clear that the flow field prediction for the CHP under the pre-threshold hydraulic conditions deviates moderately from the PIV time average data. Note that it is possible to exclude the boundary affected areas, such as the inlet, outlet and possibly the manhole wall, of the PIV data in the parameter calculation. However, this was not considered because the actual extent of these areas in the PIV data (apart from the inlet and outlet) was not clearly understood.

6.3.5.2.1.2 Post-threshold

The flow field on the CVP and CHP under the post-threshold hydraulic conditions predicted by the RNG k - ϵ turbulence model is compared to the PIV measurements in Figure 6.20 and Figure 6.21. Qualitative comparisons of the flow pattern suggest that the CFD simulation shows close agreement with the observed data (Figure 6.20c and Figure 6.21c). On the CVP, a straight through flow towards the outlet in conjunction with an anti-clockwise circulation above the jet is revealed in the two sets of data. On the CHP, there is a near-symmetrical flow pattern about the pipe centreline; a straight through flow co-exists with two approximately symmetrical circulations, returning towards the manhole centreline, at either side of the jet. A small degree of discrepancy between the vector plots can be observed in the secondary circulations. For example, in the region immediately above to the shear layer of the jet on the CVP; and near the end of the return currents along the manhole wall on the CHP. The return currents appear to be larger in the PIV data.

Quantitative comparisons of the longitudinal velocity on the CVP and CHP suggest a high degree of similarity between the CFD and PIV results (Figure 6.20d and Figure 6.21d). The maximum deviation on the two planes appear to be approximately 0.1 m/s (ignoring the boundary affected areas) and the relatively higher disagreement (the yellow contours) occurs in the jet shear layer and near the end of the return currents on the CHP.

The average percentage difference for the CVP and CHP under this hydraulic regime is 31 % and 24 %. As in the pre-threshold case, these values include the boundary effects in the PIV dataset. Therefore, the actual values should be smaller than the calculations suggest.

6.3.5.2.2 RSM Turbulence Model

This sub-section presents the validation of the flow field predicted by the RSM. As in the previous sub-section, it begins with the verification of the pre-threshold flow field prediction and then the post-threshold flow field simulation.

6.3.5.2.2.1 Pre-threshold

Anisotropic turbulence in a flow can be resolved using the RSM turbulence model. In theory, the RSM should provide a more realistic and accurate solution for turbulent flows than the RNG k - ϵ turbulence model. However, when comparing the flow fields computed by the RSM and RNG model (Figure 6.22b vs Figure 6.16b; Figure 6.23b vs Figure 6.17b), there appears to be little difference between the two sets of computational data. The higher order turbulence model obtains a marginally stronger jet flow on both planes, associated with a slightly different vortex position of the circulation in the left-hand section on the CHP. In general, the comparisons of

the vector plots between the RSM and PIV data result in the same conclusion as in Section 6.3.5.2.1.1 (Figure 6.22c and Figure 6.23c): the vector plots predicted by the numerical model are generally in good agreement with the measured plots, however, with some discrepancies in right-hand section on the CHP.

The quantitative assessment suggests that the shape of the skewed jet from the model does not match that of the 6 s time average data, leading to a large area with a variation in the velocity of above 0.2 m/s (Figure 6.22d and Figure 6.23d). However, it is not certain that the discrepancy is attributed to simulation errors. This is because there were two possible forms of the jet under the pre-threshold hydraulic conditions (Figure 6.18) and the prediction falls into one of the two. Apart from the disparity in the shape of the jet, there are two areas on the CHP showing poor agreement between the two sets of data. The one in the right-hand section (CHP) is due to the numerical model's inability to predict a circulation in the region; the other in the opposite side is due to the fact that the model obtains a different vortex position.

The average percentage difference for this prediction is 39 % and 50 % for the CVP and CHP respectively. These two values are comparable to the values for the RNG model and similarly the cumulative distributions of percentage difference in Figure 6.19. Further discussion of the comparisons is presented in Section 6.3.5.2.3.

6.3.5.2.2 Post-threshold

When the RSM post-threshold prediction is compared to the RNG model results, a small degree of dissimilarity of the flow pattern is observed (Figure 6.24 vs Figure 6.20; Figure 6.25 vs Figure 6.21). The dissimilarity emerges in the recirculation zone on the CVP. Instead of a single anti-clockwise circulation in the storage as predicted by the RNG model (Figure 6.20b), the dead zone appears to be segregated into two zones: an anti-clockwise circulation in the outlet half section (induced by the turbulent jet); and a forward flow (flow entrained from out of the plane) in the inlet half section (Figure 6.24b). Further variations can be observed at the strength of the short-circulating jet and the size of the return currents along the edge of the manhole wall on the CHP. The RSM model tends to predict a stronger jet flow and a longer/larger return current along the manhole boundary.

The qualitative comparisons of the RSM prediction and PIV measurements suggest that the vector plots are comparable. This is with the exception of the recirculation zone in the storage on the CVP; and the return currents (entrained from outside the CHP) in proximity to the manhole wall in the inlet half section on the CHP (Figure 6.24c and Figure 6.25c).

Figure 6.24d and Figure 6.25d show the quantitative assessment of the simulation accuracy for the post-threshold flow field. On the CVP, there are some discrepancies at the shear layer of the

jet and in the inlet half section in the dead zone. The maximum deviation of the variable on this plane approximates to 0.16 m/s. On the CHP, the numerical prediction of the longitudinal velocity is in excellent agreement with the PIV data, although a maximum variation approaching 0.12 m/s may be noticed in close proximity to the manhole outlet. Note that this is not caused by the boundary effect in the PIV data.

The average percentage difference for the CVP and the CHP in the RSM prediction is 50 % and 28 % respectively. Those values are higher than those of the RNG simulation (31 % for CVP; 24 % for CHP). The cumulative curves in Figure 6.19 also show that the RNG model results are marginally closer to the measured data (lower values for percentage difference) than the RSM model. Further discussion of the comparisons is presented in the following sub-section.

6.3.5.2.3 Selection of the Turbulence Model

In general, the predictions made by the two turbulence models are comparable and both simulation results show reasonable agreement with the experimental data. For the low surcharge models, there are some discrepancies between the predictions and the 6 s time average longitudinal velocity measurements associated with the shape of the jet and the circulation in the right-hand section on the CHP. However, it is wrong to suggest that the pre-threshold flow field predictions are erroneous. This is because the flow field visualisation data reveals two distinctive forms of the incoming jet in pre-threshold and the numerical predictions replicate one of the two. More importantly, in Section 6.3.6, despite the discrepancies in flow field the particle tracking results obtained reasonable agreement with the measured tracer profiles. This indirectly indicates that the pre-threshold flow field simulation results are acceptable. For the high surcharge models, the flow field predictions made by the two models are in good agreement with the PIV data. However, the RSM estimates a flow pattern in the storage on the CVP different from the measured.

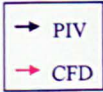
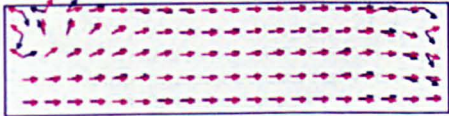
Determination of the turbulence model for further manhole simulations was based on numerical accuracy and computational stability. Careful examination of the two model results suggests that the flow field predicted by the RNG model appears to match the PIV data marginally better than the RSM, implying that the extra computational expense required by the RSM to solve turbulence anisotropy does not necessarily lead to improved predictions. Grimm (2004) also reached a similar conclusion for his straight pipe model. The flow field predictions for the straight pipe made by the $k-\varepsilon$ turbulence model and the RSM were highly comparable; and no significant improvement was observed when the RSM was used.

Regarding computational stability, the RSM is less computationally stable in comparison to the RNG k - ϵ turbulence model, because of the additional Reynolds stress terms in the RSM. As a result, the RNG model was chosen for the subsequent manhole simulations.



(a) – PIV

(b) – CFD



(c) – Difference in vector direction



(d) – Difference in longitudinal velocity

Figure 6.16 – Comparisons of the flow field on the CVP predicted by the RNG $k-\epsilon$ turbulence model and measured from PIV for the pre-threshold conditions (Flow from left to right)

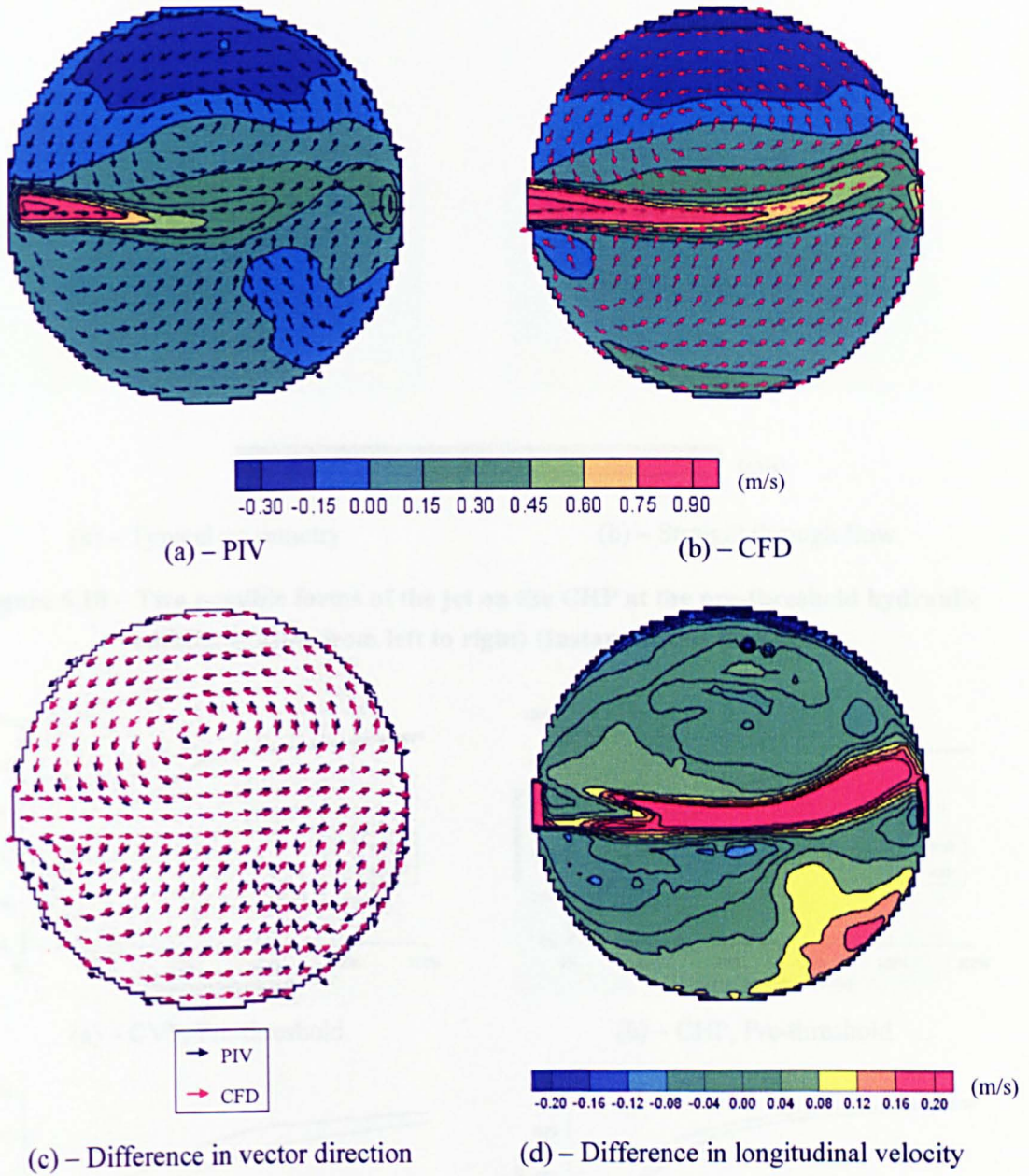


Figure 6.17 – Comparisons of the flow field on the CHP predicted by the RNG $k-\epsilon$ turbulence model and measured from PIV for the pre-threshold conditions (Flow from left to right)

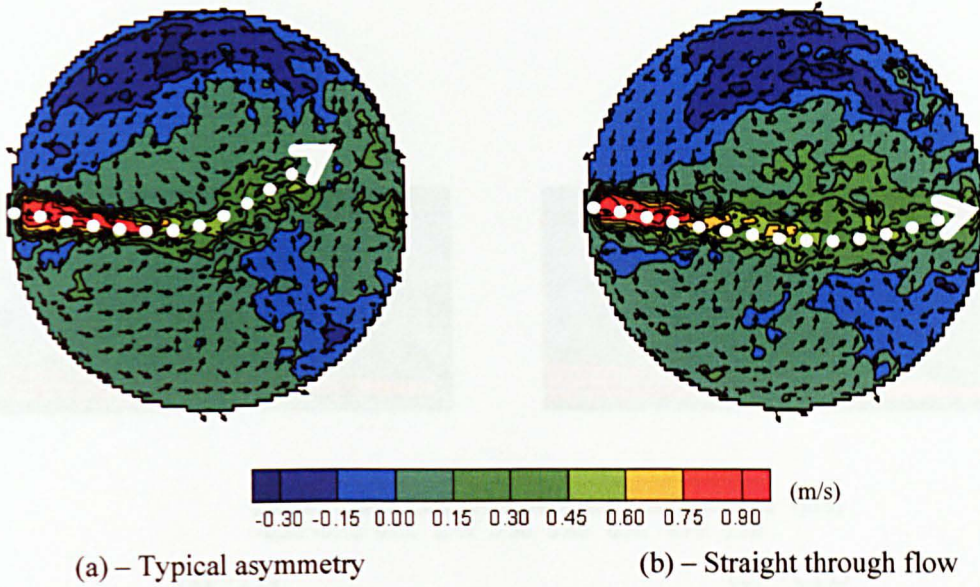


Figure 6.18 – Two possible forms of the jet on the CHP at the pre-threshold hydraulic conditions (Flow from left to right) (Instantaneous flow field)

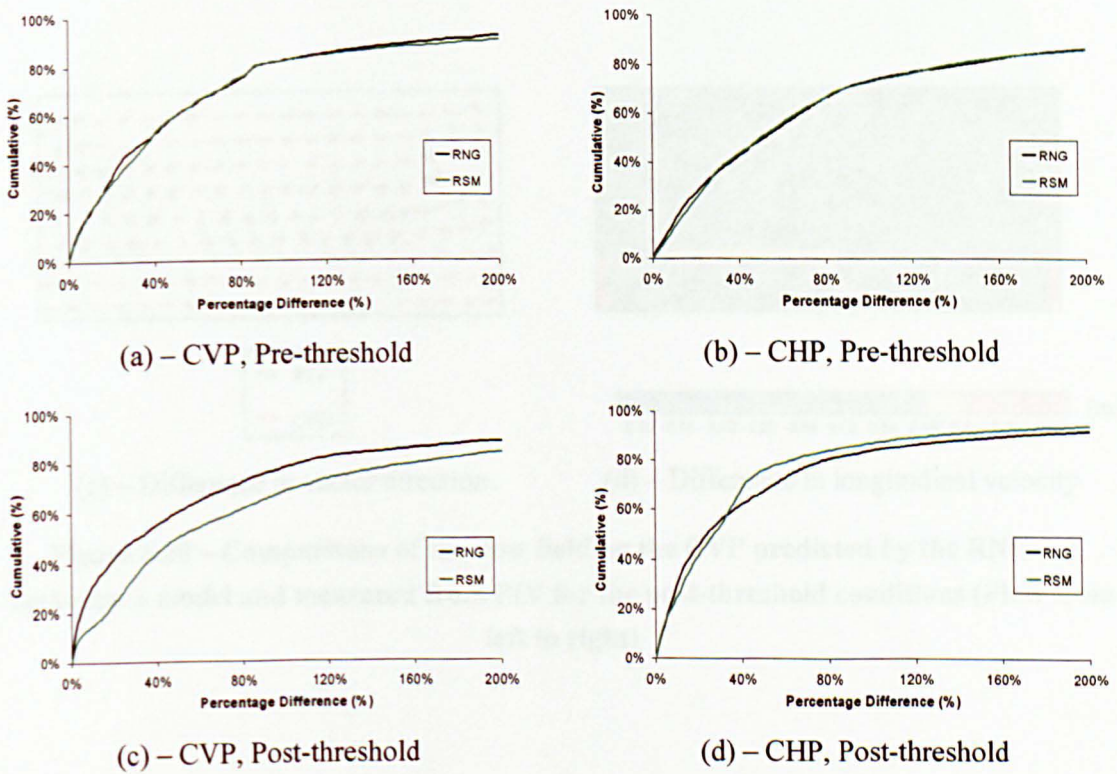


Figure 6.19 – Cumulative distributions of percentage difference between simulated and measured longitudinal velocity

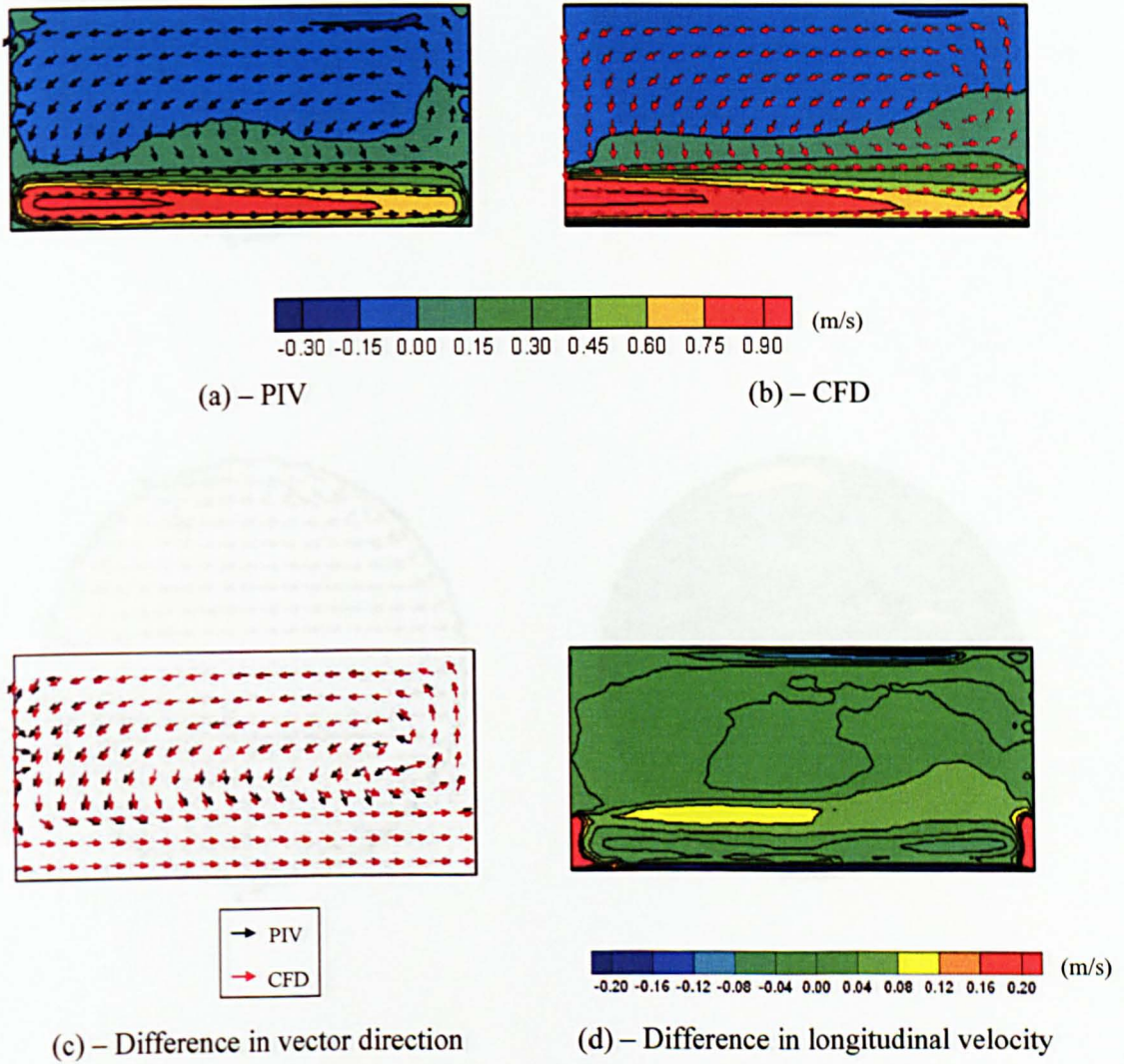


Figure 6.20 – Comparisons of the flow field on the CVP predicted by the RNG $k-\epsilon$ turbulence model and measured from PIV for the post-threshold conditions (Flow from left to right)

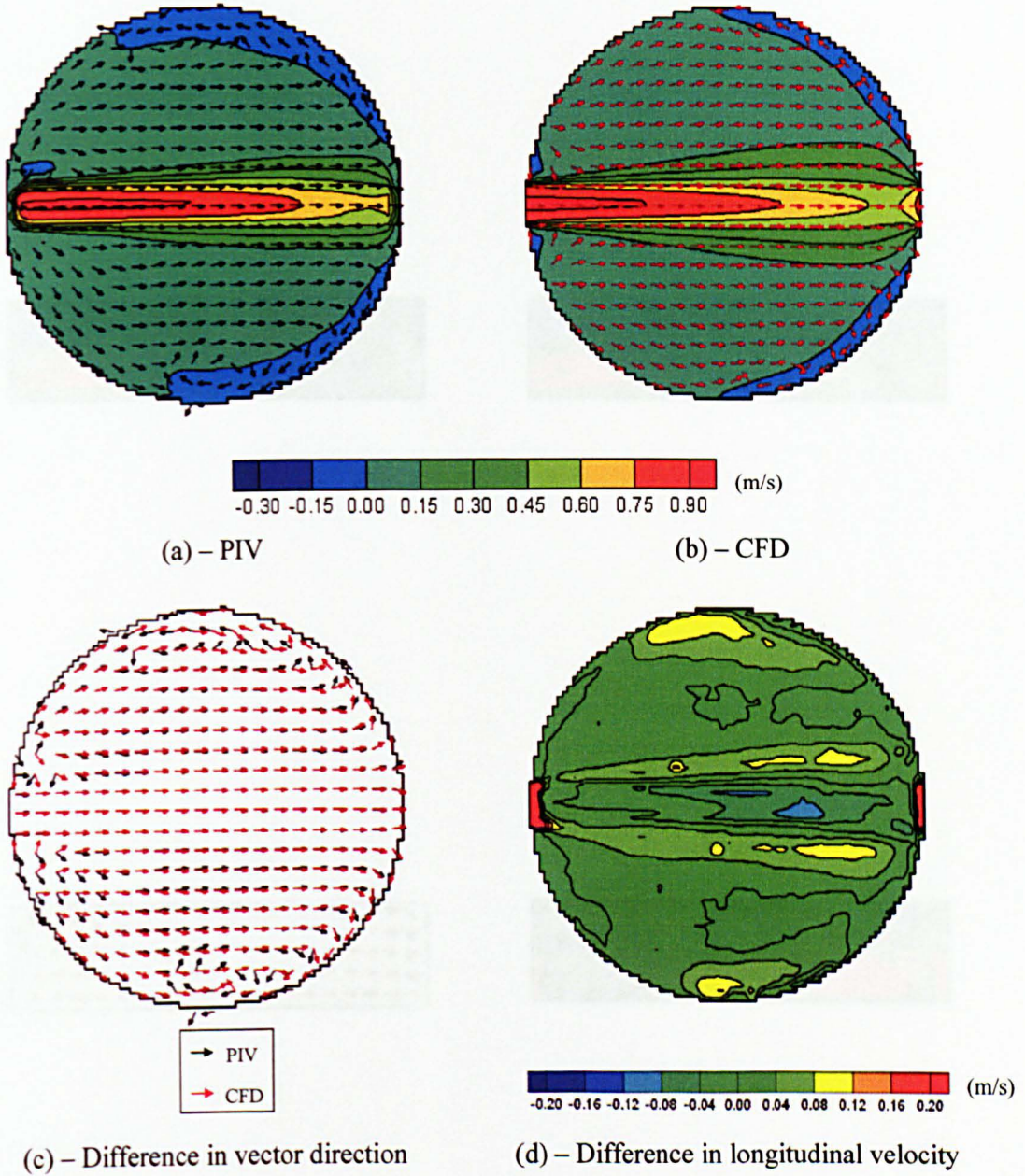


Figure 6.21 – Comparisons of the flow field on the CHP predicted by the RNG $k\text{-}\epsilon$ turbulence model and measured from PIV for the post-threshold conditions (Flow from left to right)

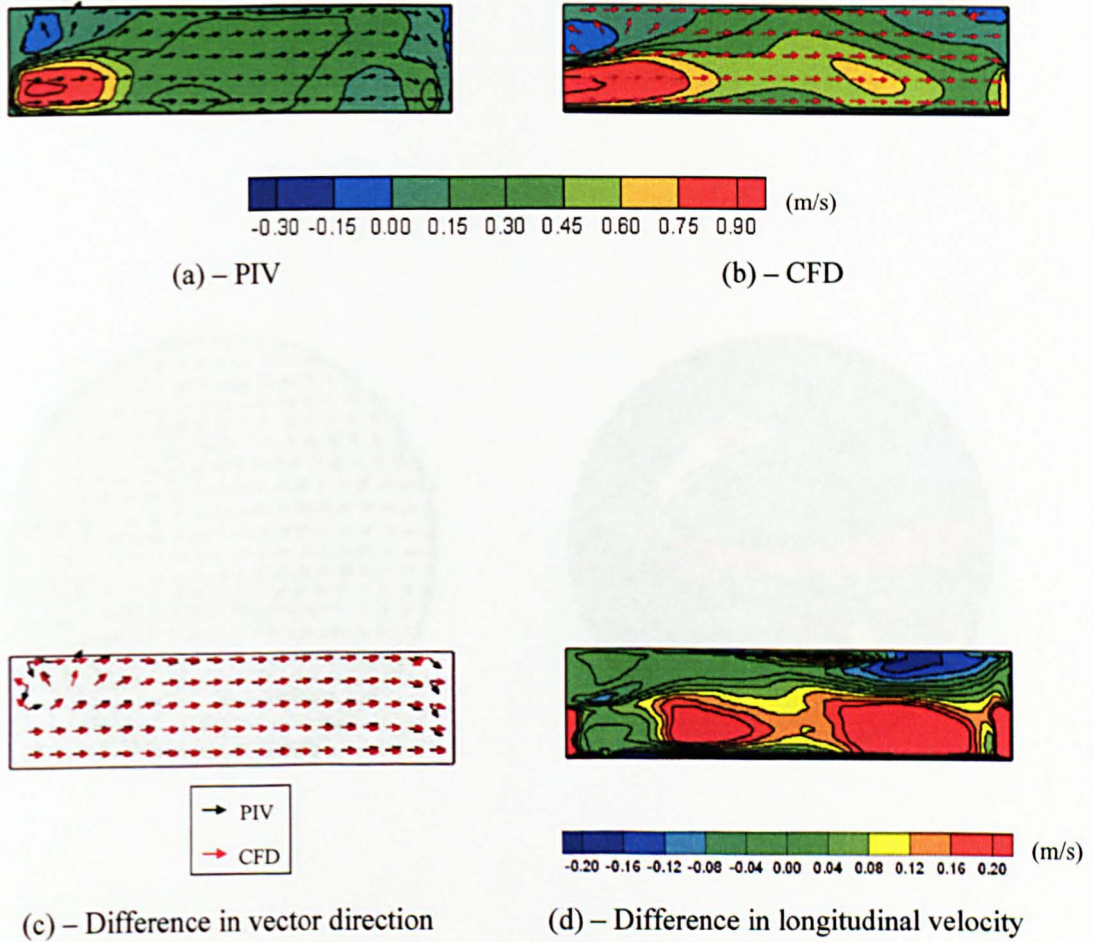


Figure 6.22 – Comparisons of the flow field on the CVP predicted by the RSM turbulence model and measured from PIV for the pre-threshold conditions (Flow from left to right)

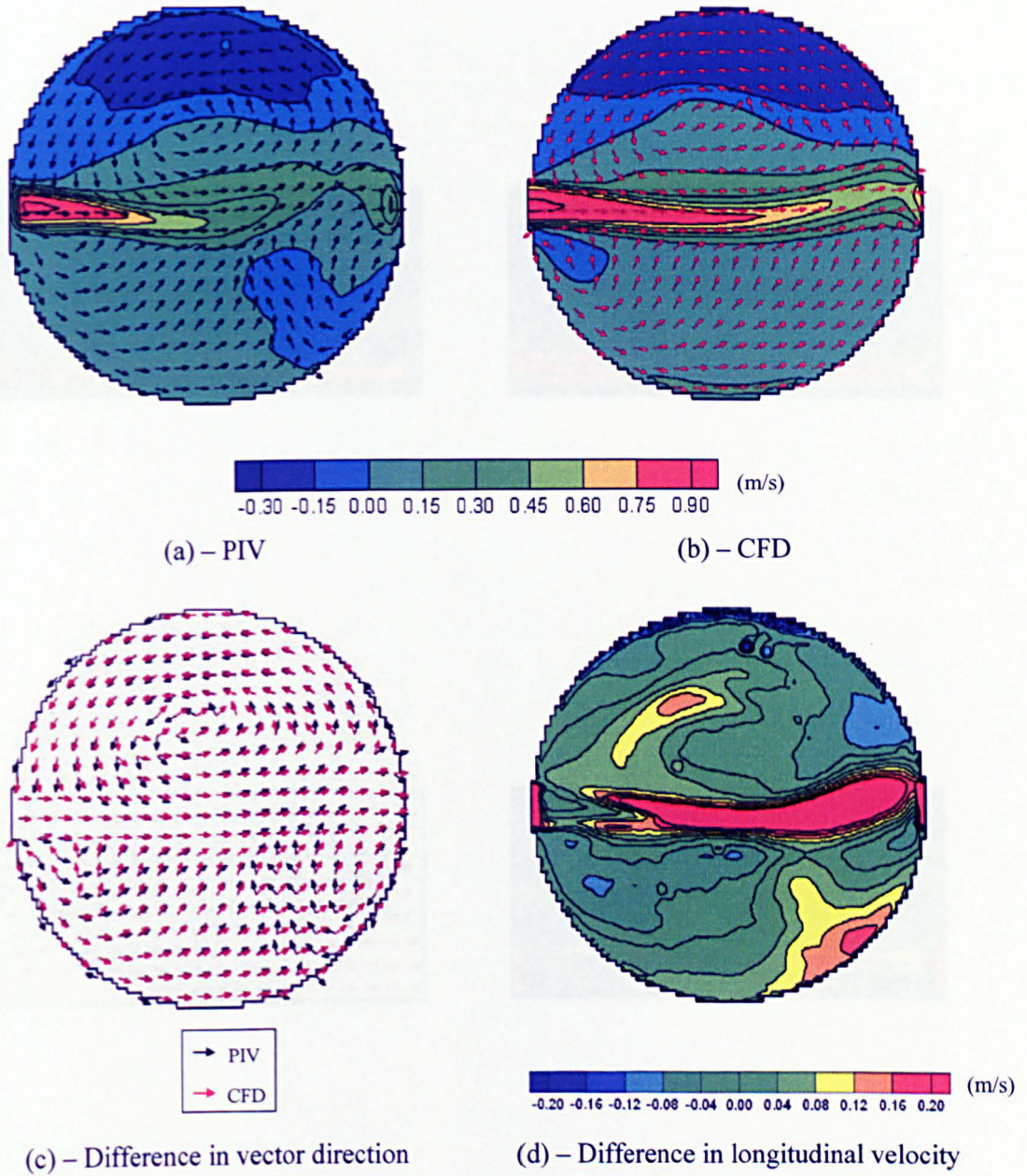


Figure 6.23 – Comparisons of the flow field on the CHP predicted by the RSM turbulence model and measured from PIV for the pre-threshold conditions (Flow from left to right)

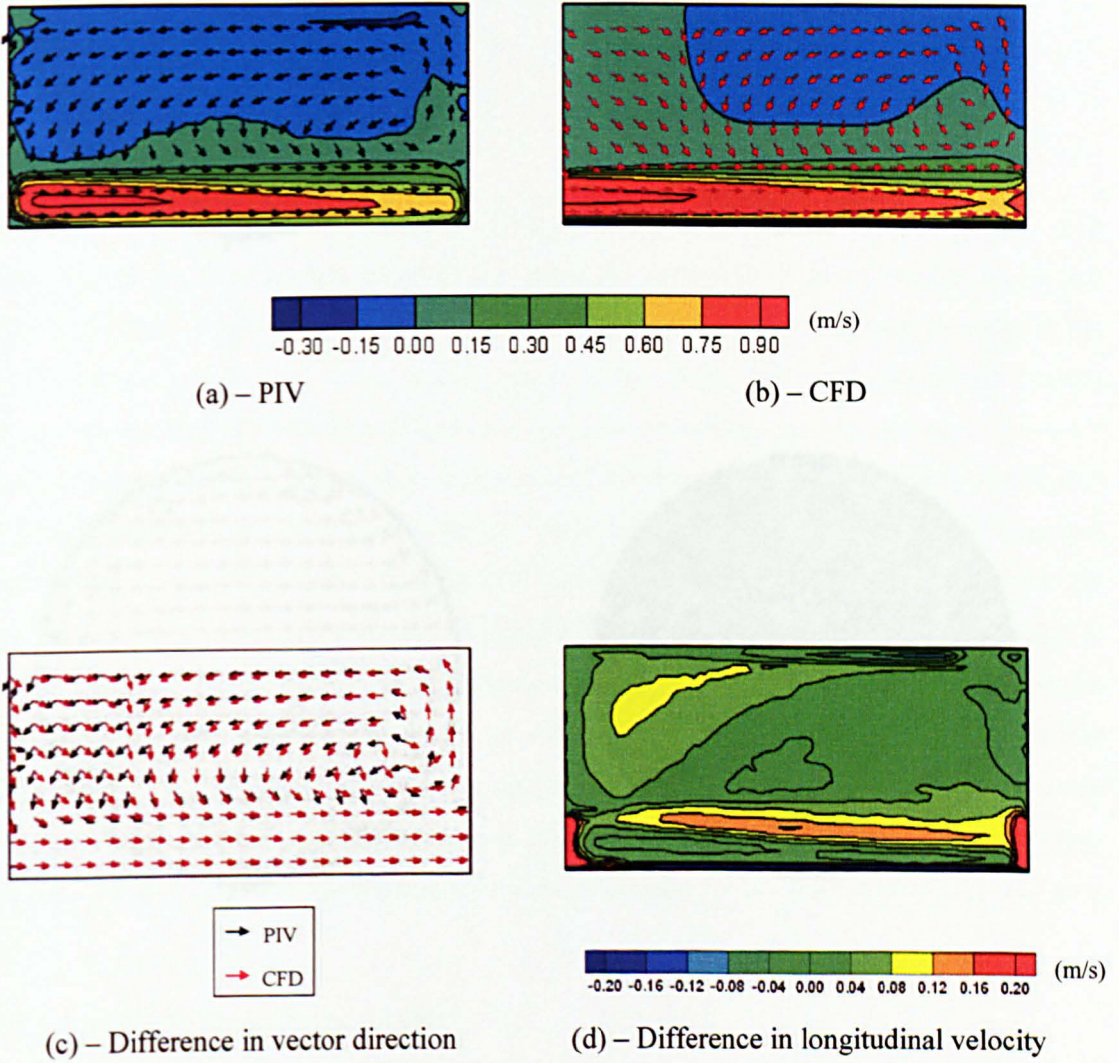


Figure 6.24 – Comparisons of the flow field on the CVP predicted by the RSM turbulence model and measured from PIV for the post-threshold conditions (Flow from left to right)

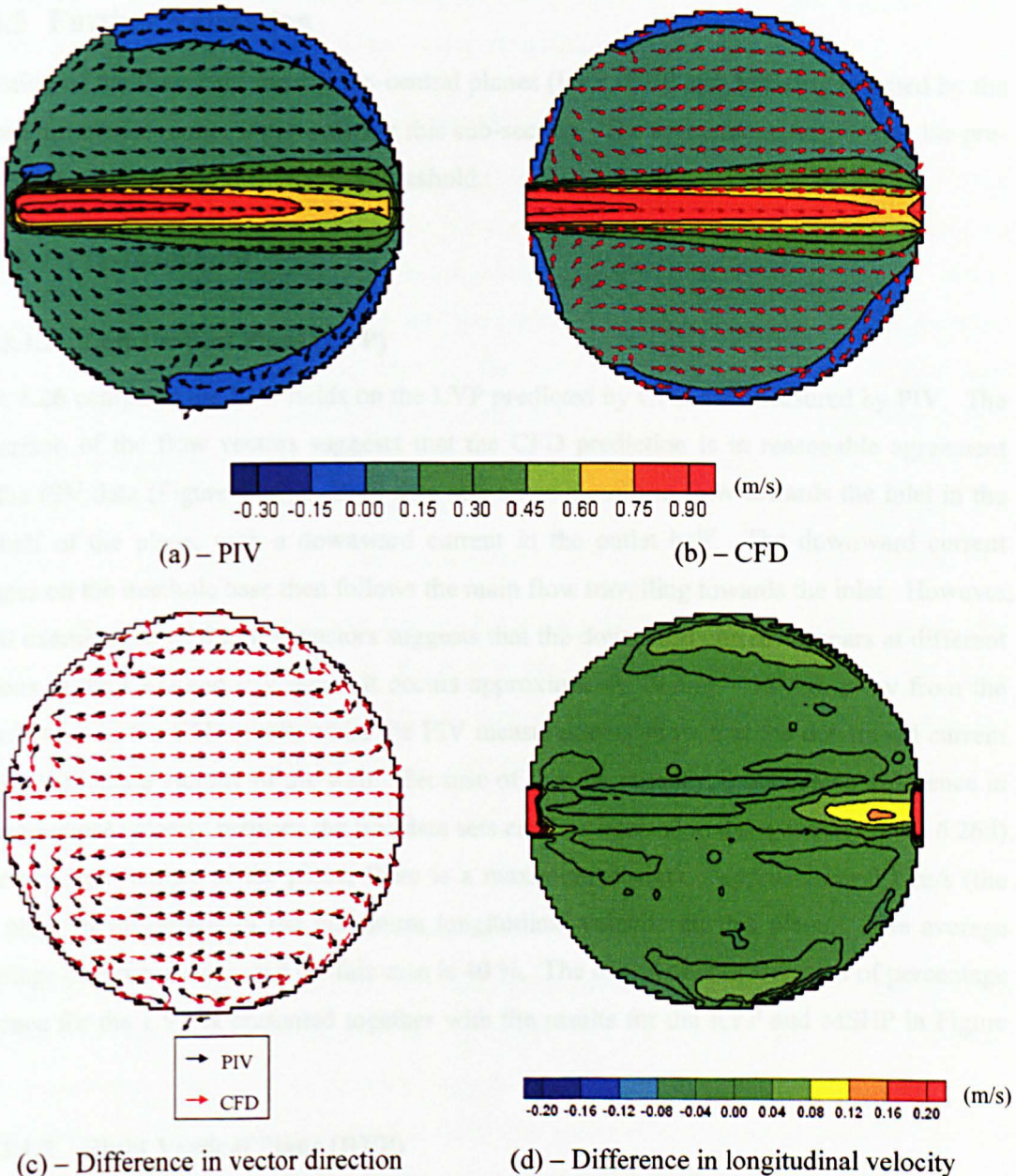


Figure 6.25 – Comparisons of the flow field on the CHP predicted by the RSM turbulence model and measured from PIV for the post-threshold conditions (Flow from left to right)

6.3.5.3 Further Validation

Validation of the flow field for the non-central planes (LVP, RVP and MSHP) predicted by the selected turbulence model is presented in this sub-section. The assessments begin with the pre-threshold predictions and then the post-threshold.

6.3.5.3.1 *Pre-threshold*

6.3.5.3.1.1 Left Vertical Plane (LVP)

Figure 6.26 compares the flow fields on the LVP predicted by CFD and measured by PIV. The comparison of the flow vectors suggests that the CFD prediction is in reasonable agreement with the PIV data (Figure 6.26c). Both data sets show a uniform flow towards the inlet in the inlet half of the plane, with a downward current in the outlet half. The downward current impinges on the manhole base then follows the main flow travelling towards the inlet. However, careful examination of the flow vectors suggests that the downward current appears at different positions in the CFD and PIV data. It occurs approximately 10 mm – 15 mm away from the manhole wall in the CFD result, while the PIV measurements show that the downward current is in the immediate vicinity of the wall. Because of this discrepancy, a noticeable difference in the longitudinal velocity between the two data sets can be observed in these areas (Figure 6.26d). At the top right corner of the plane, there is a maximum deviation approaching 0.2 m/s (the same order of magnitude of the maximum longitudinal velocity on this plane). The average percentage difference estimated for this case is 40 %. The cumulative distribution of percentage difference for the LVP is presented together with the results for the RVP and MSHP in Figure 6.32.

6.3.5.3.1.2 Right Vertical Plane (RVP)

The predicted flow field on the RVP under the pre-threshold conditions is compared with the PIV data in Figure 6.27. In the qualitative assessment of the simulation accuracy, poor agreement in the flow vectors between the CFD and PIV data is evident in Figure 6.27c. The measured data suggests that the flow field is generally dominated by a primary current flowing towards the outlet, in association with a clockwise circulation at the right bottom corner of the plane. However, the CFD prediction reveals a circulation rotating in the opposite direction governing the flow field on the RVP.

The discrepancies in the flow vectors lead to noticeable variations in the longitudinal velocity between the CFD and PIV data (Figure 6.27d). The figure suggests that the maximum variation approximates to 0.2 m/s and the areas associated with the larger variation exist in the outlet half

of the plane. The median percentage difference for the RVP is 155 %. This suggests a poor description of the flow field on this plane by the numerical model.

6.3.5.3.1.3 Mid Surge Horizontal Plane (MSHP)

The longitudinal velocity results of the CFD prediction and PIV experiment for the MSHP under the pre-threshold hydraulic conditions are compared in Figure 6.28. The flow field in the left-hand section is highly comparable between the two datasets (Figure 6.28c). The two sets of data show an anti-clockwise circulation and the circulation vortex locates at similar position. However, there is weaker consistency between the CFD and PIV flow fields in the right-hand section. The PIV data suggests that the flow pattern in the right-hand section comprises an anti-clockwise circulation in the inlet half and a circulation with the opposite direction in the outlet half. In the CFD flow field, there appears to be an anti-clockwise circulation dominating the flow field in the right-hand section, with a clockwise circulation near the end of the skewed jet.

The quantitative assessment suggests that as in the qualitative validation, a good agreement between the CFD and PIV flow data is obtained in the left-hand section; however, in the right-hand section, there are some noticeable discrepancies associated with the longitudinal velocity in close proximity to the skewed jet. The average percentage difference for the MSHP is 54 %.

6.3.5.3.2 Post-threshold

6.3.5.3.2.1 Left Vertical Plane (LVP) and Right Vertical Plane (RVP)

Comparisons of the flow fields on the LVP under the post-threshold hydraulic conditions are presented in Figure 6.29. The qualitative assessment in Figure 6.29c shows good similarity between the two results. The two datasets suggest that a single anti-clockwise circulation, with the circulation centre located at approximately the centre of the plane, dominates the flow pattern. Small discrepancies in the flow vectors may be observed in close proximity to the circulation centre and the manhole wall in the outlet half section. In the quantitative assessment, Figure 6.29d confirms that the difference between CFD and PIV flow fields is small.

Since the flow field under the post-threshold conditions is nearly symmetrical above the vertical plane at the pipe centreline (CVP), the assessment of the simulation accuracy for the RVP provides the same conclusion as above (Figure 6.30). The flow field on the two non-central vertical planes generally shows good agreement with the PIV measurements. The median percentage difference for the LVP and RVP is 30 % and 35 % respectively. The cumulative distributions of percentage difference for all the non-central planes in post-threshold are presented in Figure 6.32.

6.3.5.3.2 Mid Surge Horizontal Plane (MSHP)

Figure 6.31 compares the flow fields on the MSHP under the post-threshold conditions. The PIV data shows a nearly symmetrical flow pattern about the pipe central axis (Figure 6.31a). Some deviation away from the symmetry may be observed in the inlet half of the plane, particularly in close proximity to the manhole wall. In the outlet half of the plane, the fluid from the left- and right-hand quarters appears to flow towards the pipe central axis; then merges and travels towards the inlet half. In the inlet half of the plane, there appears to be an approximately uni-directional flow towards the manhole inlet. The CFD data suggests similar flow patterns (Figure 6.31b). However, direct comparison of the flow vectors suggests a poor fit between the two sets of data (Figure 6.31c). Quantitative analysis of the simulation accuracy reveals that the two flow field results deviate from each other within ± 0.08 m/s. The average percentage difference between the CFD and PIV data for this case is estimated to be 74 %, indicating that the flow field prediction is poor.

6.3.5.3.3 Discussion

The complexity of the flow structure within the scale manhole forms a challenge to modelling in CFD. The flow dynamics changes with regard to different hydraulic regimes and in each regime there are several types of turbulent flow prevailing in the flow structure, such as a parallel wall jet within the manhole; a vena-contracta at the outlet pipe in close proximity to the manhole chamber; flow impingement at the manhole wall; and secondary recirculations in the dead zone within the chamber. To obtain an optimised solution for each of these turbulent flows using the RANS turbulence models may require individual calibration of the parameter values in the numerical equation. Each calibration is case-specific and may not be applicable to other types of flow (Rodi, 1993). The turbulence model considered in the present study (RNG $k-\varepsilon$ turbulence model) used the default parameter values given by Fluent 6.2. Despite the fact that the default parameters have been validated with a wide range of flows (Fluent, 2005), prediction errors are expected and the present study has identified the potential source of errors in the flow field predictions made by the numerical model.

In the pre-threshold model, the flow field predictions seem to deviate moderately from the 6 s time average PIV measurements. Discrepancies in the flow field can be observed in the shape of the asymmetric jet and the secondary flow features in the right-hand section of the manhole. The actual flow field under the pre-threshold conditions appears to be time dependent under a long term steady state environment. For example, Figure 6.18 shows two possible forms of the jet within the system under the steady state conditions. The numerical model did not show any temporal variations of the flow field even when unsteady state calculations were used (Section

6.2.2.3). This might be attributed to the fixed lid approximation adopted for the free surface modelling, in that this restricted the variations of the free surface and hence the flow field. Improvement of the simulation accuracy might be achieved if the free surface was modelled properly using a VOF technique (Fluent, 2005). However, this modelling approach requires extensive computational resources and time and is not straightforward to apply. Further research is required to validate this technology and prove the robustness of the solution. Nevertheless, the fixed lid approximation modelling technique did provide tracer results comparable with the measured data (in the feasibility study and in the following sub-section). This indirectly supports the validity of the modelling approach, given that there might be some discrepancies between the actual and simulated flow fields.

For the post-threshold model, the validation of the flow field on the five planes provides a high level of confidence in the flow field simulations. The jet and the general flow structure are well described by the numerical model, although the flow patterns on the non-central planes computed by the model slightly deviate from the PIV data. The flow field deviation on the non-central planes would not significantly affect the resultant particle tracking results, because the straight through jet dominates the mixing in this hydraulic regime.

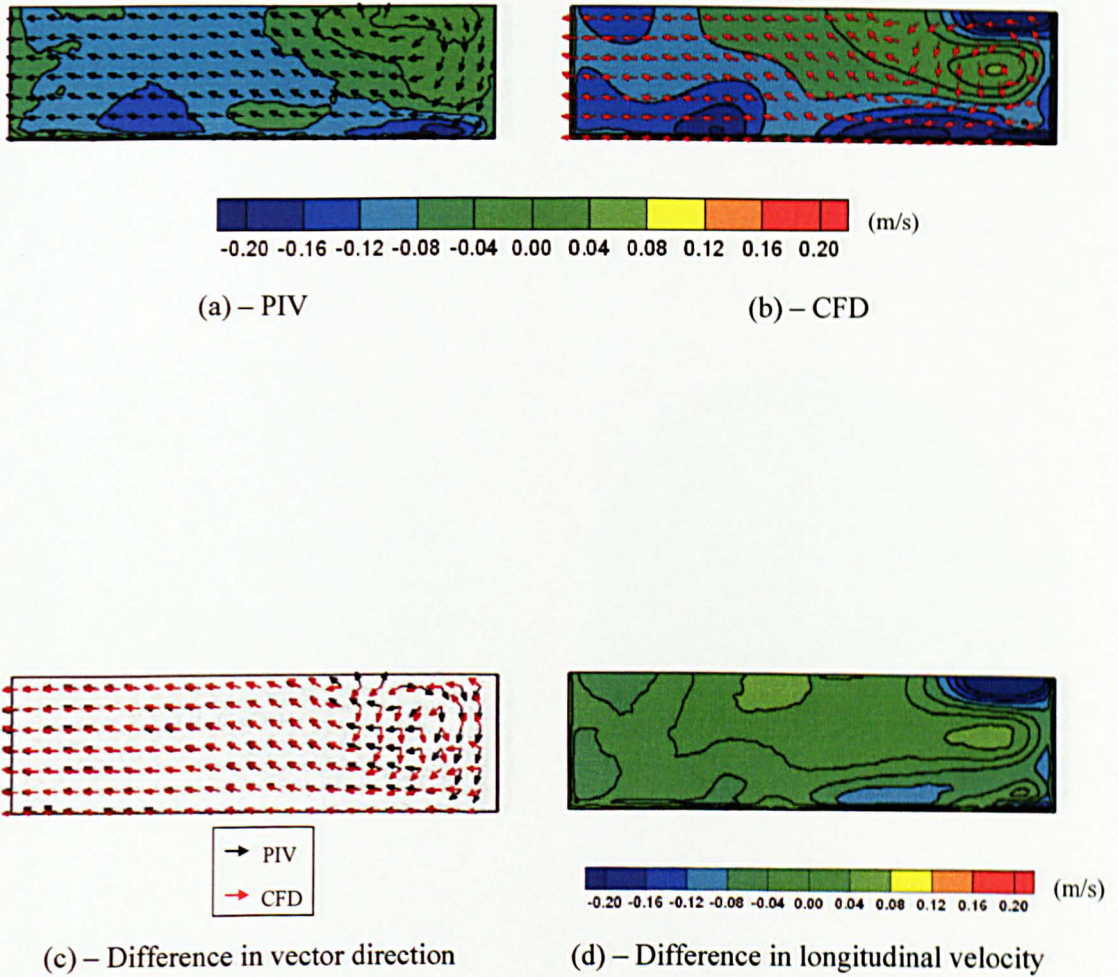


Figure 6.26 – Comparisons of the flow field on the LVP predicted by the RNG $k-\epsilon$ turbulence model and measured from PIV for the pre-threshold conditions (Flow from left to right)

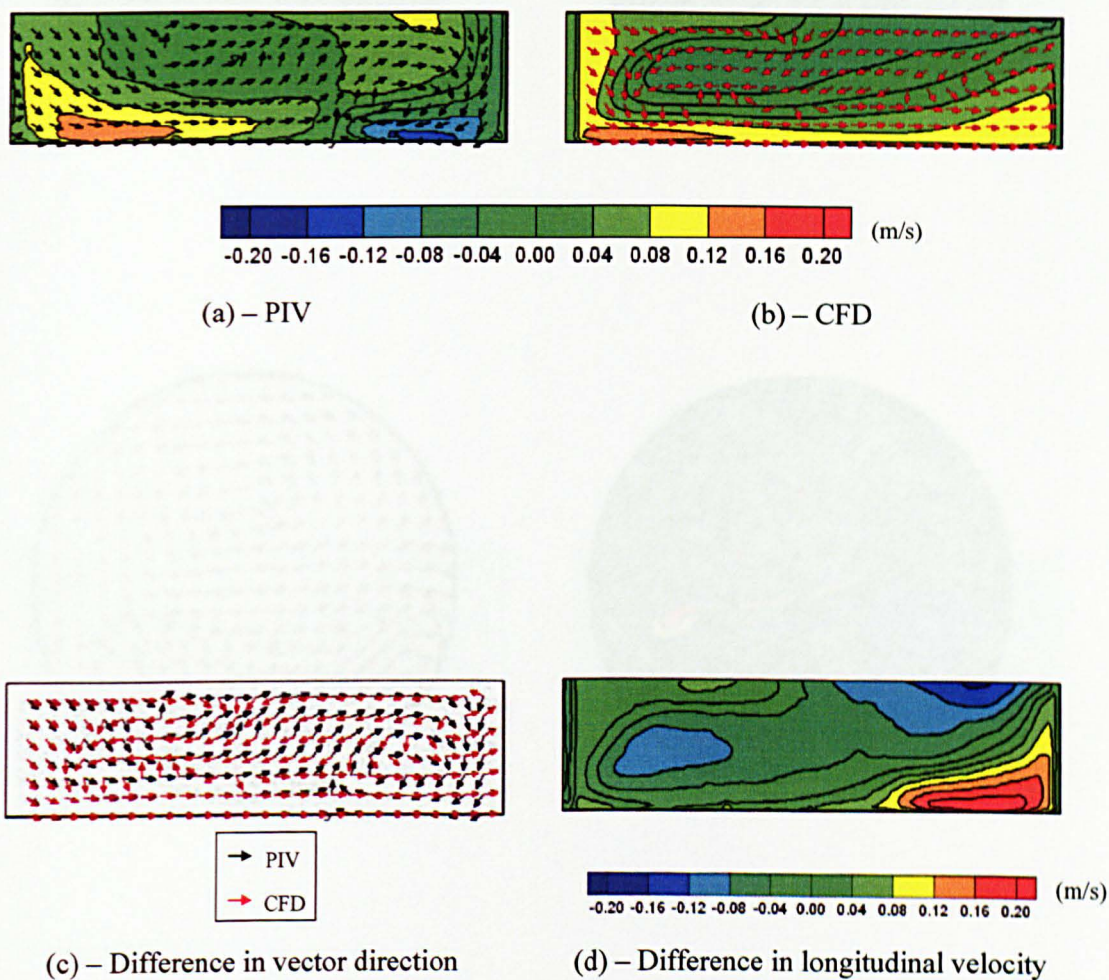


Figure 6.27 – Comparisons of the flow field on the RVP predicted by the RNG $k-\epsilon$ turbulence model and measured from PIV for the pre-threshold conditions (Flow from left to right)

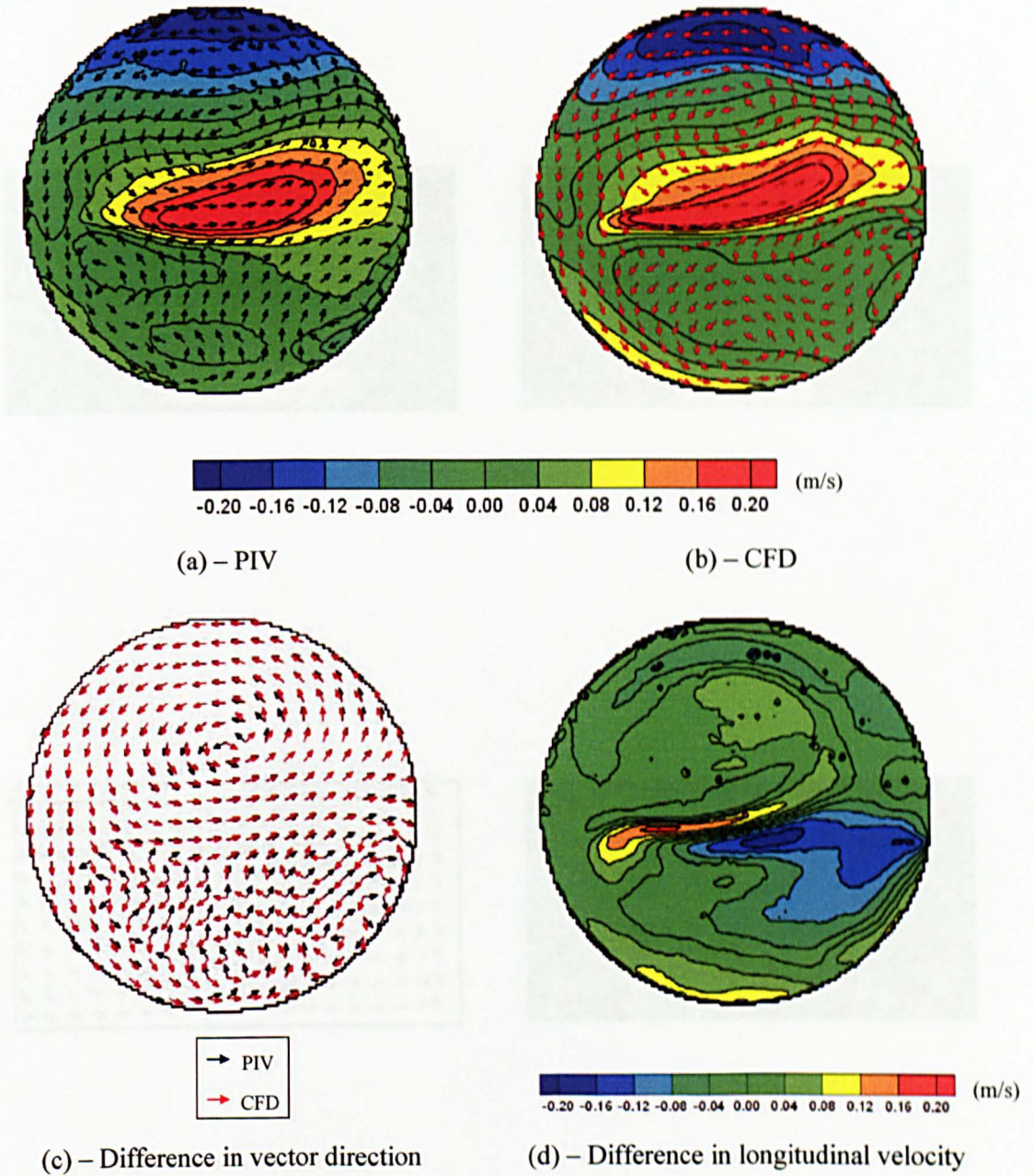


Figure 6.28 – Comparisons of the flow field on the MSHP predicted by the RNG $k-\epsilon$ turbulence model and measured from PIV for the pre-threshold conditions (Flow from left to right)

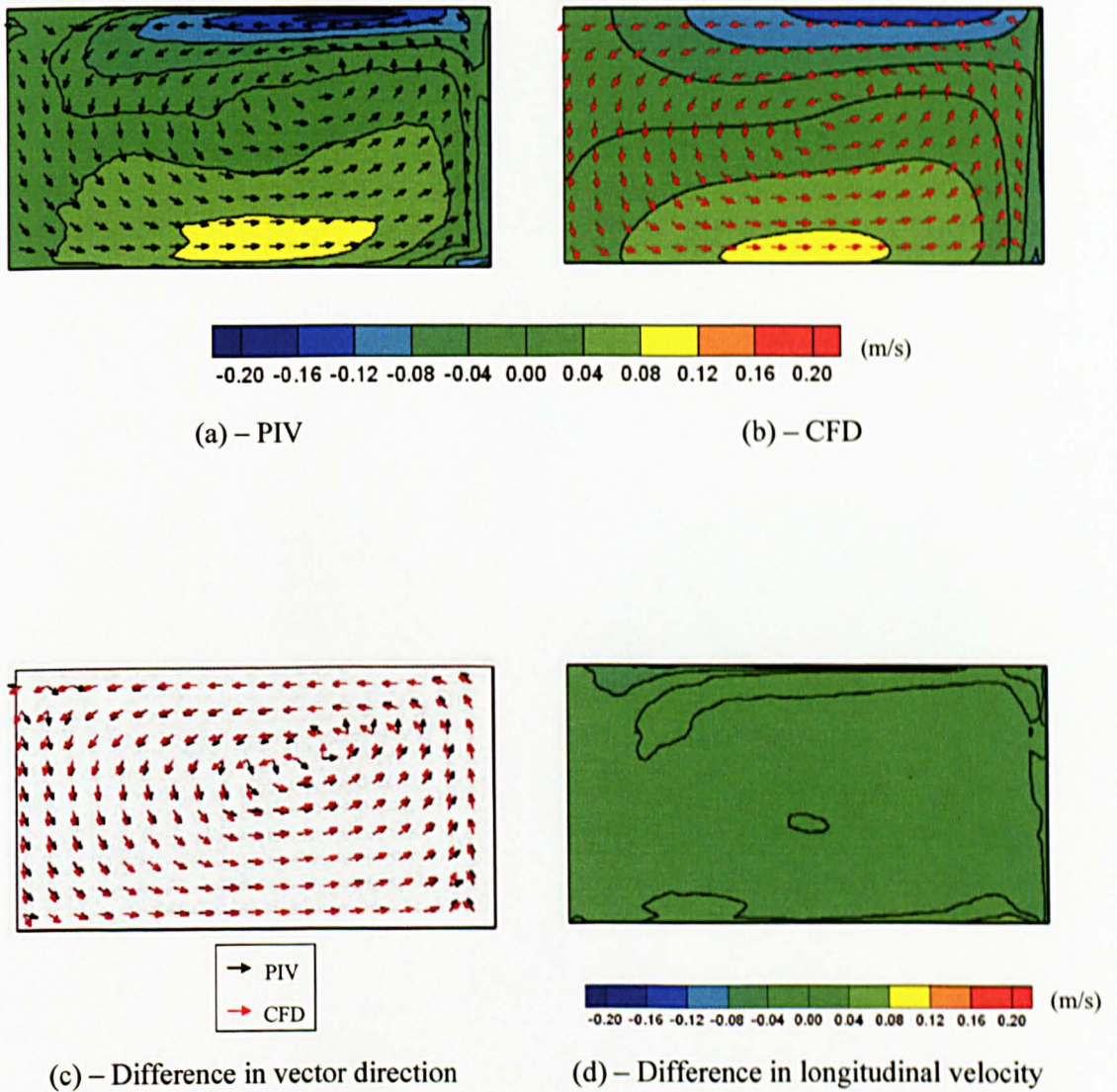


Figure 6.29 – Comparisons of the flow field on the LVP predicted by the RNG $k-\epsilon$ turbulence model and measured from PIV for the post-threshold conditions (Flow from left to right)

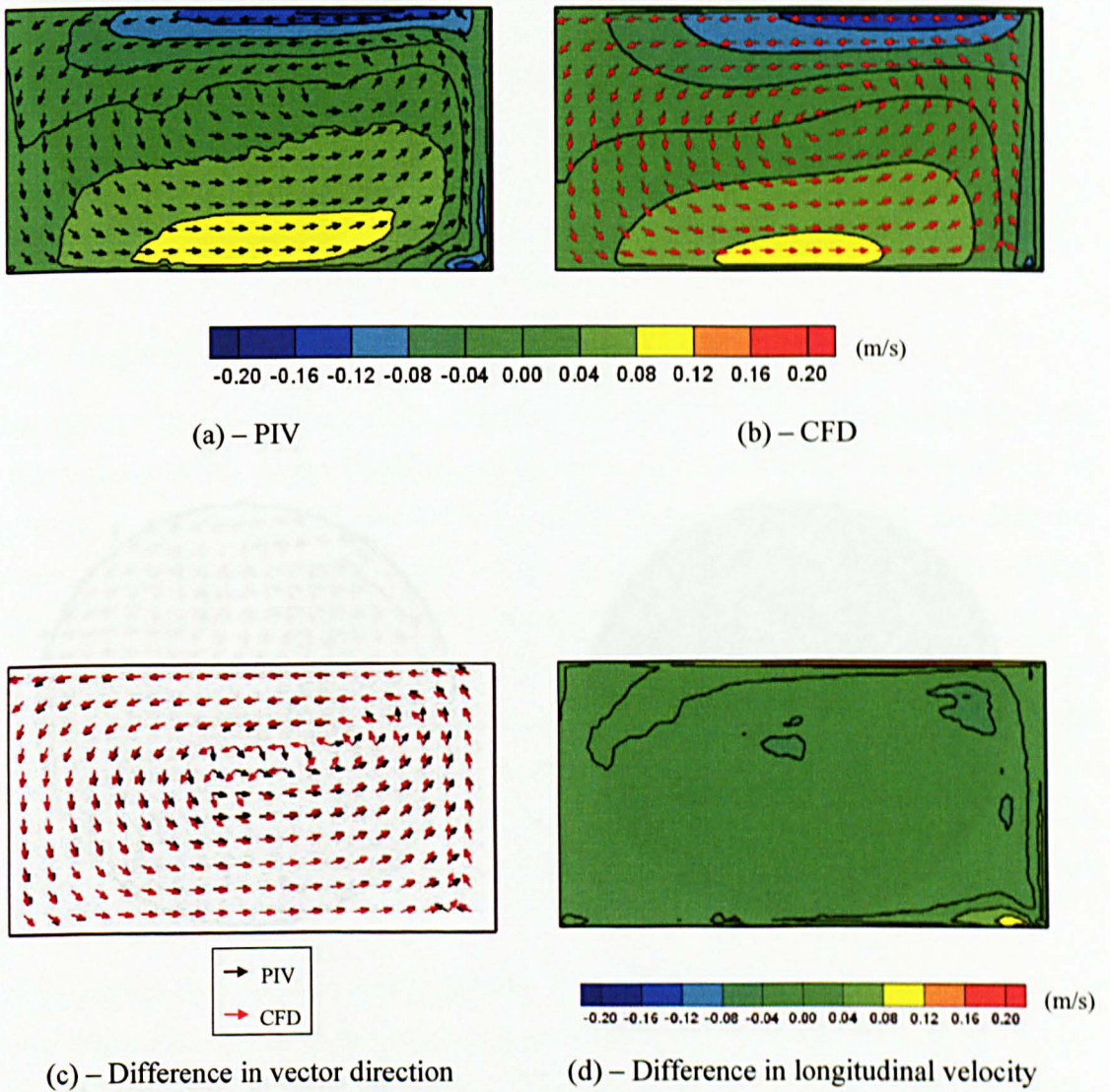


Figure 6.30 – Comparisons of the flow field on the RVP predicted by the RNG k - ϵ turbulence model and measured from PIV for the post-threshold conditions (Flow from left to right)

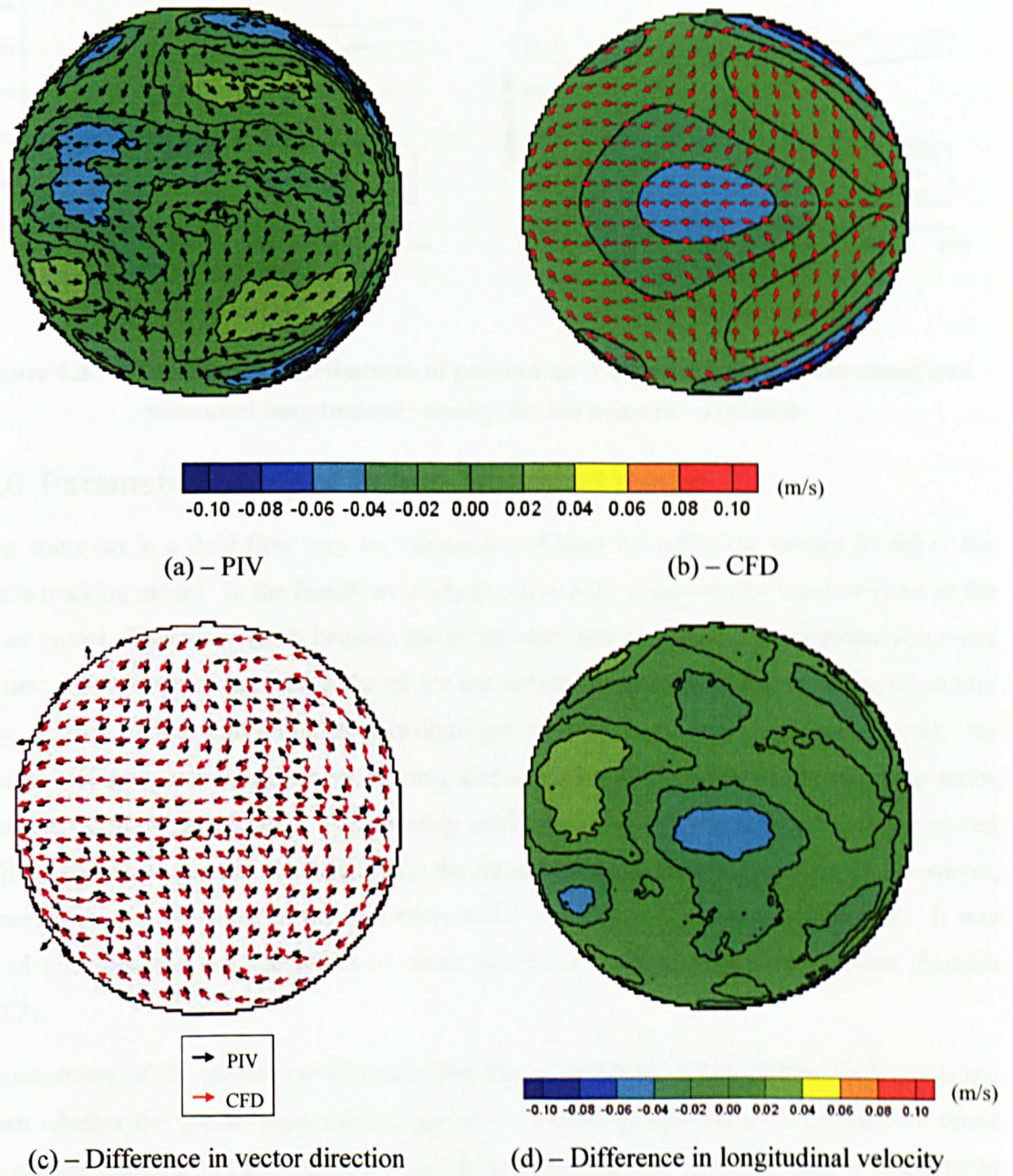


Figure 6.31 – Comparisons of the flow field on the MSHP predicted by the RNG $k-\varepsilon$ turbulence model and measured from PIV for the post-threshold conditions (Flow from left to right)

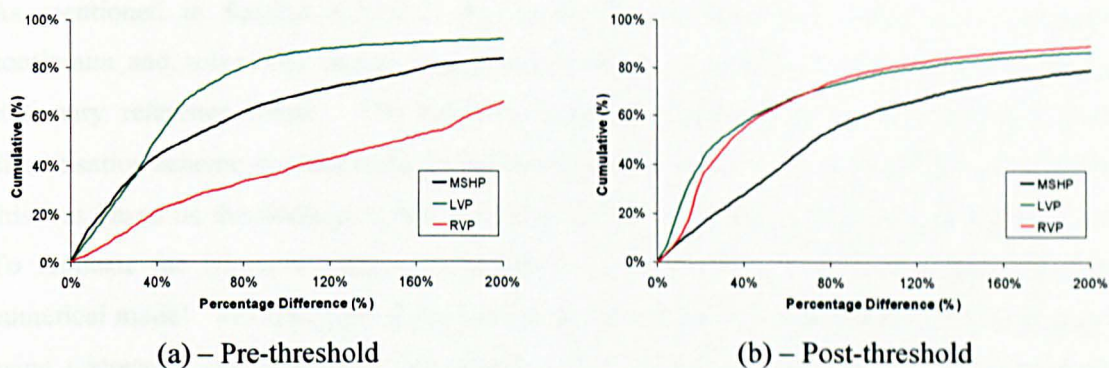


Figure 6.32 – Cumulative distributions of percentage difference between simulated and measured longitudinal velocity for the non-central planes

6.3.6 Parametric Study of Solute Transport Model

Solute transport in a fluid flow may be simulated in Fluent 6.2 using the species model or the particle tracking model. In the feasibility study (Section 6.2), consideration was not given to the species model. This was mainly because the model demands extensive computational resources and time. Particle tracking was adopted for the solute transport predictions in the feasibility study. The routed concentration distributions showed reasonable agreement with the experimental data, although there were some discrepancies in the shape of the recessing limbs of the pre-threshold predictions. A secondary peak was shown on the falling tail in the routed profiles, whilst this was not consistent with the measured tracer data (Figure 6.6a-d). However, the reason for the existence of the secondary peak, in CFD, is not clearly understood. It was proved that this was not the effect of either steady or unsteady state calculations (Section 6.2.2.3).

An assessment of the species model prediction was not made in the feasibility study. It is not known whether the species model would generate a better representation of the manhole tracer than particle tracking, in particular the shape of the recessing limb. For this reason, a sensitivity study of the two solute transport models was performed. The study considered the pre- and post-threshold hydraulic conditions ($S = 1.17$; $S = 3.27$).

6.3.6.1 Model Setup for the Sensitivity Study

The flow field solutions computed by the RNG $k-\epsilon$ turbulence model were employed in the study. For the solute transport models, the settings of the particle tracking model were specified according to Table 6.2; and the configurations of the species model were defined based on Grimm (2004) with a few modifications. A brief description of the set-up parameters for the species model is provided in the following paragraph.

As mentioned in Section 6.2.1.2.2, the species model simulates solutes as a secondary continuum and solves the transport equation in the same fashion as the primary phase in a stationary reference frame. The transport equation of the species model requires spatial discretisation scheme in order to be solved numerically. *QUICK* was selected in this study and this was based on the findings in the sensitivity study of discretisation scheme (Section 6.3.4). To replicate the laboratory tracer experiments, a short pulse of solute was injected in the numerical model. The transport of the passive solute within the model with time was predicted using uncoupled unsteady state calculations. The uncoupled calculations mean that during calculations only the species transport model was solved, assuming that the presence of the solute does not influence the inherent flow field structure. This processing technique improved computational speed as well as setting a comparable modelling procedure to the particle tracking model (Section 6.2.1.2.2). For the unsteady state calculations, a time step of 0.001 s and *second order implicit* scheme for temporal discretisation were adopted. This combination led to a time step independent solution. Details of temporal discretisation can be found in Fluent (2005). In the species model, turbulent diffusion of solutes in a flow is controlled by turbulent Schmidt number. For the purposes of the parametric study, the default value (0.7) in Fluent 6.2 was adopted homogeneously over the domain, although in reality the homogeneous number may vary from 0.5 to 1.0 depending upon flow types and conditions (Rodi, 1993; Shiono and Feng, 2003). Grimm (2004) also commented that the parameter may vary spatially within a flow and therefore the actual turbulent diffusion may not be described by using a single value.

Similar to the particle tracking model, sampling monitors were specified at the model inlet and outlet measuring the average solute concentration over the plane. The solute was injected in the form of a Gaussian distribution, with a mean of 2.35 s and a standard deviation of 0.85 s (Figure 6.33). The synthetic input should be representative of the average laboratory upstream profiles measured in the scale manhole tracer experiments. A summary of the model settings for the species model is provided in Table 6.9.

Model Configurations	Setting/Value
Solute conditions	
<i>Solute density</i>	998.2 kg/m ³ (same as water)
<i>Molecular diffusion coefficient</i>	1 x 10 ⁻¹⁰ m ² /s
<i>Injection method</i>	Uniform injection over the inlet plane based on a Gaussian profile
Species model configurations	
<i>Spatial discretisation scheme</i>	<i>QUICK</i>
<i>Temporal discretisation scheme</i>	<i>Second order implicit</i>
<i>Time step</i>	0.001 s
<i>Convergence criteria</i>	1 x 10 ⁻⁴ with a maximum of 20 iterations per time step
<i>Turbulent Schmidt number</i>	0.7
<i>Gravitational force</i>	Yes

Table 6.9 – Summary of the model configurations of the species model

6.3.6.2 Results

Pre- and post-threshold tracer results generated by the particle tracking model and the species model are presented in Figure 6.33 and Figure 6.34. Note that the particle tracking results were synthesised using superposition in accordance with the upstream distributions. In both test cases, the two simulated tracers show high similarity in terms of the shape of the downstream profile. Pre-threshold, the two CFD profiles show a significant reduction in the peak concentration (approximately 70 %) followed by a secondary peak at a time of approximately 7 s and a near-exponential decaying tail. Post-threshold, the computed profiles are characterised by a Gaussian distribution at times between 1 to 6 s, followed by a tail with very low concentrations.

However, careful examination of the tracers suggests that using the default parameter values for the transport models, particle tracking (PT Model) appears to be less diffusive in comparison to its counterpart. For example, in the pre-threshold predictions, the secondary peak predicted by particle tracking is higher than the species model results (Figure 6.33); in the post-threshold predictions, there is more short-circuiting in the particle tracking routed profile than in the species model distribution (Figure 6.34). Discussion of the results is presented in the following sub-section.

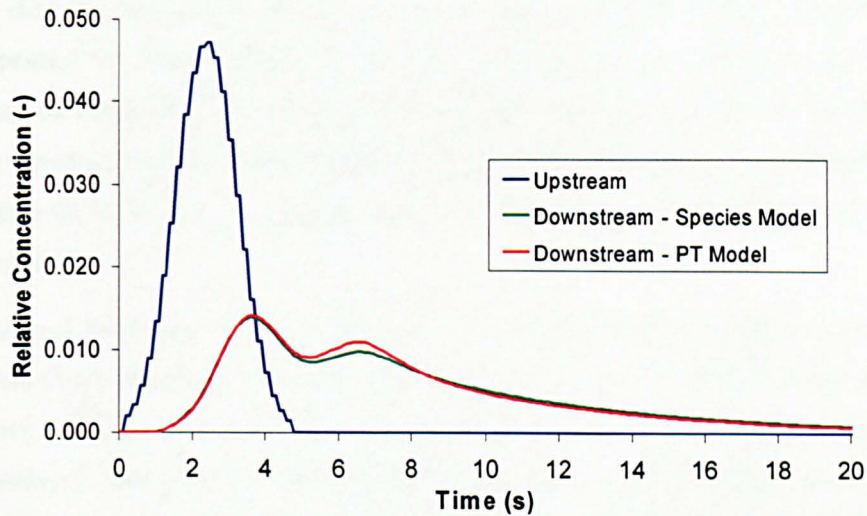


Figure 6.33 – Comparison of the species model and particle tracking predictions in the pre-threshold model ($S = 1.17$)

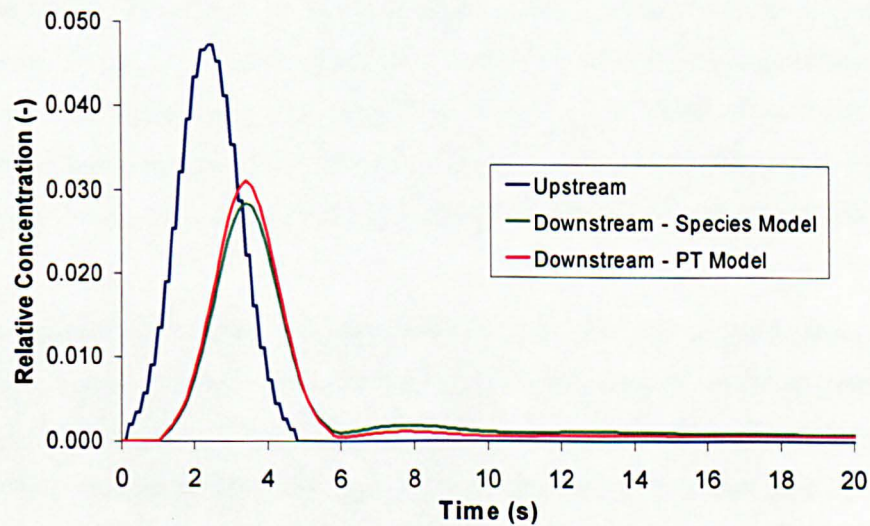


Figure 6.34 – Comparison of the species model and particle tracking predictions in the post-threshold model ($S = 3.27$)

6.3.6.2.1 Discussion

The aim of the study is to investigate whether the species model would generate a better representation of the manhole tracer than the particle tracking model, particularly the shape of the recessing limb. The results presented above have shown that using identical flow field solutions comparable downstream concentration predictions were generated by the two approaches. A secondary peak at the recessing tail exists in both pre-threshold particle tracking and species model distributions. This confirms that the occurrence of the secondary peak is not a function of the choice of the solute transport model.

When the default parameter values were used for the transport models, the particle tracking results appeared to be less diffusive. In fact, the difference in the diffusivity between the models may be reduced via model calibration, for example by varying the turbulent Schmidt number in the species model and/or adjusting the time scale constant, C_L , in the particle tracking approach (see the following sub-section) to obtain similar degree of turbulent diffusion from the numerical models.

The selection of the solute transport approach to simulating manhole mixing in the subsequent analysis was therefore based on computational time. It may be noticed that the species model traces shown in Figure 6.33 and Figure 6.34 are cut-off at 20 s. This is because the simulation was terminated at that point and did not run further due to the long computational time for the species model simulations. The time taken to simulate 20 s of solute transport in the manhole model was approximately 5 days (on a Sun Microsystems with 2.4 GHz AMD Opteron and 4 GB RAM). In contrast, for 60,000 injections in particle tracking to obtain statistically meaningful results, the simulation finished within 8 hours, which is less than 10 % of the time required to run the species model. In addition, the particle tracking results obtained 100 % mass recovery, i.e. conservation of mass; whilst the species model might have to run for 200 s to achieve 90 % mass recovery. The particle tracking model was chosen as the tool to investigate solute mixing in the subsequent manhole simulations because the simulation is highly time-efficient.

Similar conclusion to this study was reached by Grimm (2004), in a straight pipe, and Stovin *et al.* (in press), in storage tanks. Their studies found that the species model and particle tracking model generated similar solute transport predictions; however, the computational time required for the particle tracking model to run was much shorter than for its counterpart.

The following sub-section describes the validation of the particle tracking results.

6.3.6.3 Validation of the Particle Tracking Model

To evaluate the numerical errors introduced by particle tracking, the particle tracking results for the scale manhole models were validated against the laboratory measured data. Although a similar validation exercise was carried out in the feasibility study and the validation study has shown that the particle tracking results present reasonable agreement with published experimental data, there is some uncertainty in the validation because the numerical errors from grid resolution, spatial discretisation scheme and turbulence model were not minimised and/or quantified via sensitivity studies.

The particle tracking models were set up according to Section 6.2.1.2.2 and the simulations were undertaken using the flow fields computed by the RNG k - ε turbulence model and the RSM (Section 6.3.5). In the particle tracking model, the diffusivity of tracer particles is represented by the characteristic lifetime of eddy, which may be defined either as a constant or a random function of the fluid Lagrangian integral time (Equation 2.65 and Equation 2.67). The diffusivity of tracer particles in a flow can be adjusted by the time scale constant, C_L , in the equation of fluid Lagrangian integral time (Equation 2.66). The Fluent manual (Fluent, 2005) suggests that a value of 0.15 should be adopted when the k - ε model is used; a value of 0.3 should be applied when the RSM is used (Daly and Harlow, 1970). Different values are suggested for the two types of the RANS turbulence model because the turbulence models adopt different approaches to estimating turbulent kinetic energy in a fluid flow. In fact, Milojevic (1990) commented that the value of C_L reported in the literature could range from 0.135 to 0.41 and the predictions are sensitive to the coefficient.

Sensitivity of the coefficient to the predictions is observed when different values of the parameter were used to characterise the characteristic lifetime of eddy in the scale manhole models (Figure 6.35 and Figure 6.36). The time scale constant is conceptually used to manipulate the retention time of a particle in a given eddy. A larger value of the constant generally results in more spreading of the particles (Shirokar *et al.*, 1996). In Figure 6.36, it is evident that the peak concentration reduces with increasing time scale constant, suggesting more spreading of the particles carried by the main short-circuiting flow. This effect is also observed in the pre-threshold case although it is almost negligible. The explanation for the negligible effect in pre-threshold is that the spreading/mixing of the particles in this hydraulic regime is primarily dependent upon the asymmetrical jet (the inherent flow structure) that separates the particles which travel straight through the manhole and the particles which are entrained in the dead zone circulation; while post-threshold, the mixing of the particles is reliant upon the turbulent eddies at the short-circuiting jet, and therefore the resultant particle tracking result is sensitive to the change of the time scale constant.

However, without strong literature support for the selection of the parameter value the Fluent's default values and a constant function of the fluid Lagrangian integral time were used in this validation study.

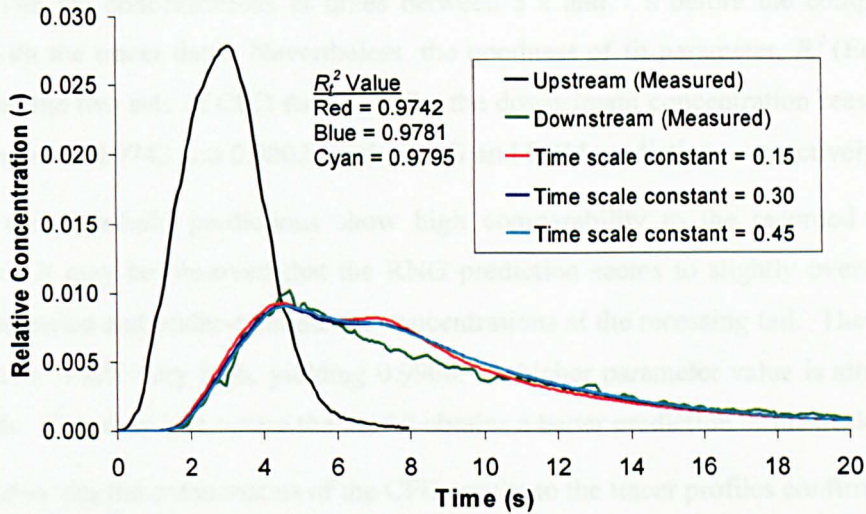


Figure 6.35 – Effects of the time scale constant value on particle tracking based on the RNG pre-threshold flow field solutions

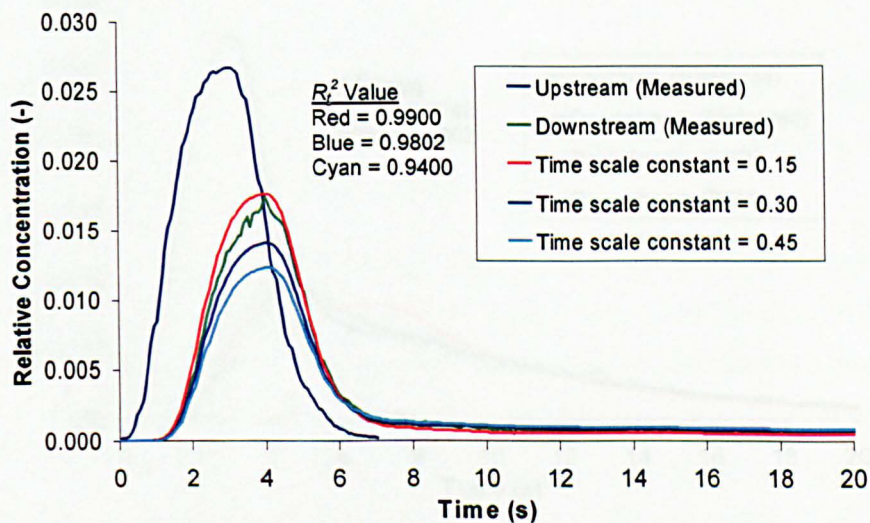


Figure 6.36 – Effects of the time scale constant value on particle tracking based on the RNG post-threshold flow field solutions

The effects of the turbulence model on the particle tracking results and the validation of the CFD profiles are shown in Figure 6.37 and Figure 6.38. Pre-threshold, both sets of result present high degree of similarity to the recorded data although some minor discrepancies may be observed (Figure 6.37). The RNG pre-threshold profile appears to have an earlier rising limb followed by a slightly suppressed peak; the CFD profile also shows a pronounced secondary peak in the recessing limb while this is not obvious in the experimental data. The discrepancies between the RSM model prediction and the observed tracer data differ from that between the RNG and the recorded profile. The RSM pre-threshold profile obtains a marginally earlier and higher peak than the measurements suggest; after the peak, the predicted profile appears to

under-estimate the concentrations at times between 5 s and 7 s before the computed profile collapses with the tracer data. Nevertheless, the goodness of fit parameter, R_r^2 (Equation 4.1), suggests that the two sets of CFD data describe the downstream concentration reasonably well, with a R_r^2 value of 0.9742 and 0.9802 for the RNG and RSM predictions respectively.

The CFD post-threshold predictions show high comparability to the recorded downstream distribution. It may be observed that the RNG prediction seems to slightly over-estimate the peak concentration and under-estimate the concentrations at the recessing tail. The R_r^2 value for this prediction is still very high, yielding 0.9900. A higher parameter value is attained for the RSM profile. This may be because the model obtains a better prediction of the peak.

It is concluded that the comparisons of the CFD results to the tracer profiles confirm the validity of the numerical predictions. Sensitivity of the choice of the turbulence model to the tracer prediction is observed, however, the effect is not significant.

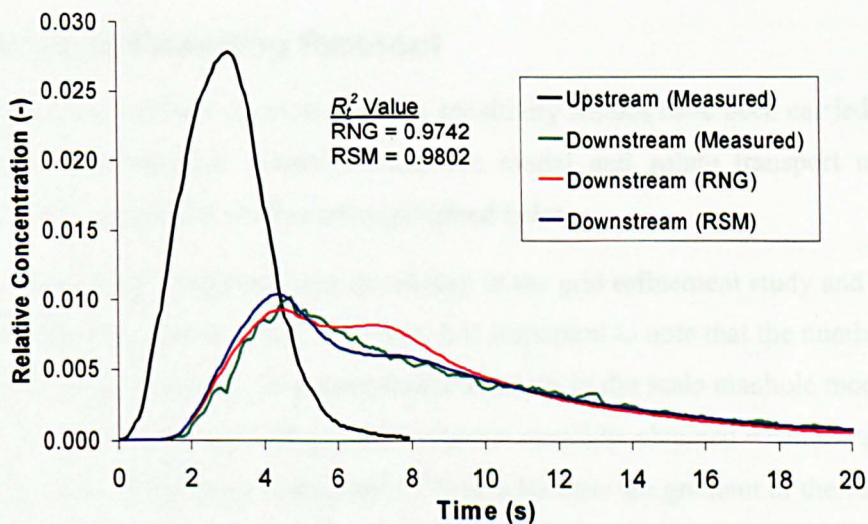


Figure 6.37 – Effects of the turbulence models (RNG and RSM) on particle tracking in the pre-threshold hydraulic conditions

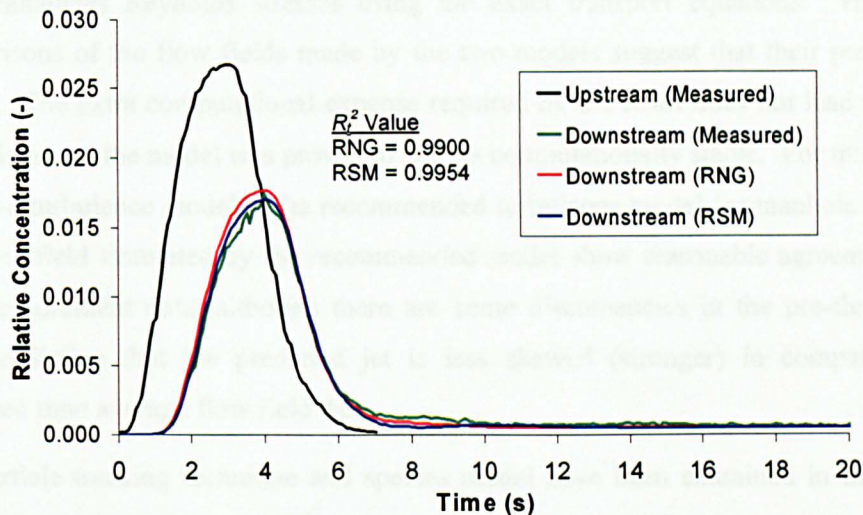


Figure 6.38 – Effects of the turbulence models (RNG and RSM) on particle tracking in the post-threshold hydraulic conditions

6.3.7 Standard Modelling Protocol

In the detailed CFD manhole simulation study, sensitivity studies have been carried out for grid density, spatial discretisation scheme, turbulence model and solute transport model. The conclusions of the parametric studies are highlighted below:

- A grid independent model has been developed in the grid refinement study and then used in the subsequent parametric tests. However, it is important to note that the number of cells in the domain required for the grid independent solution in the scale manhole models does not necessarily mean that a grid independent solution would be obtained when the same number of cells is applied in a larger scale model. This is because the gradient of the variables, such as velocity, pressure and turbulence quantities, in the domain of a larger scale model would be different.
- The parametric study of discretisation scheme has examined a number of combinations of the spatial discretisation schemes. The results from the study suggest that the four combinations of the second order accurate schemes produce highly comparable flow field results for the scale manhole. However, in terms of computational stability, *PRESTO* appeared to be superior over *second order* for solving the pressure terms; *QUICK* and *second order upwind*, which are the discretisation schemes for momentum and turbulence terms, performed similarly. *QUICK* and *PRESTO* discretisation schemes are recommended for manhole simulations.
- Two RANS turbulence models have been investigated in the parametric study of turbulence model. The RNG $k-\epsilon$ turbulence model assumes isotropy of turbulent viscosity and the

RSM calculates Reynolds stresses using the exact transport equations. However, the comparisons of the flow fields made by the two models suggest that their predictions are similar. The extra computational expense required by the RSM does not lead to improved predictions and the model was proved to be less computationally stable. For this reason, the RNG k - ϵ turbulence model is the recommended turbulence model for manhole simulations. The flow field simulated by the recommended model show reasonable agreement with the PIV measurement data, although there are some discrepancies in the pre-threshold flow field prediction that the predicted jet is less skewed (stronger) in comparison to the measured time average flow field data.

- The particle tracking technique and species model have been examined in the sensitivity study of solute transport model. The two transport models show highly comparable predictions when the same flow field was used for prediction. Considering the computational time, the species model simulations required longer time to run in comparison to particle tracking for the scale manhole models. The particle tracking approach is therefore recommended for solute transport predictions. The particle tracking results were compared to the laboratory tracer measurements and the comparisons present excellent agreement.

A standard modelling protocol is proposed based on the findings in the sensitivity studies (Table 6.10). The modelling protocol employs a single phase model to replicate the hydraulic and solute transport characteristics in the manhole. There is undoubtedly some uncertainty in the model accuracy as the effects of the free surface are not considered and could be significant when the surcharge depth is low. Nevertheless, the proposed modelling protocol should be sufficient for engineering applications, representing an appropriate compromise between the accuracy of the solution and simulation time.

Set-up Parameter	Setting/Value
Meshing strategy	Version 2 in Section 6.2.1.1.1.2
Spatial discretisation scheme	
<i>Pressure</i>	<i>PRESTO</i>
<i>Momentum, turbulence terms</i>	<i>QUICK</i>
<i>Velocity-pressure coupling</i>	<i>SIMPLEC</i>
Turbulence model	RNG <i>k-ε</i> turbulence model
Solute transport model	Uncoupled particle tracking with stochastic modelling
Scale time constant	0.15
Number of injection	60,000

Table 6.10 – Standard modelling protocol for manhole simulations

6.4 Conclusion

This chapter has discussed the feasibility study and detailed study for manhole simulations. In the feasibility study, the prototype model was investigated and a meshing strategy for circular manholes was proposed. The preliminary indications in the study suggest that a single phase CFD model could be employed to replicate the hydraulic and solute transport characteristics in surcharged manholes.

The detailed study considered the scale manhole model and examined the set-up parameters that might affect the flow field and solute transport predictions. The parameters examined were the arrangement of grid, discretisation scheme, turbulence model and solute transport model. A standard modelling protocol for manhole simulations was developed using the findings of the parametric studies.

The modelling protocol is subsequently used to create larger scale manhole models for studying the effects of scale on the hydraulic and solute transport characteristics. Details of the study are covered in the following chapter.

7 Analysis of Scale Effects

7.1 Introduction

This chapter describes the generation of three differently scaled CFD manhole models; and the investigation of the scale effects on the hydraulic and solute transport characteristics using the CFD numerical model results. Methodologies for scaling the hydraulic and solute transport characteristics of surcharged manholes are also proposed.

The investigation of the effects of scale using a CFD-based approach was motivated by the findings of the laboratory-based analysis for the scale effects in Chapter 4. The laboratory-based study adopted two approaches to analysing the impact of physical scale on the solute transport characteristics between the small scale manhole and the prototype. The first method was based on the comparisons of the derived advection dispersion equation (ADE) and aggregated dead zone (ADZ) model parameters between the two manhole models, with the aid of dimensional analysis to non-dimensionalise the model coefficients. The second technique compared the normalised cumulative temporal concentration profiles (CTCPs), i.e. the downstream responses corresponding to non-instantaneous upstream injections, between the two manhole structures. However, the laboratory-based study shows that neither approach could be used to quantify the effects of scale on the solute transport processes. This is because both techniques are sensitive to inconsistencies in the shape of the upstream profiles. It is also concluded that to study the scale effects in surcharged manholes would require comparison of downstream responses to instantaneous upstream injections, i.e. retention time distributions (RTDs) or cumulative retention time distributions (CRTDs). One way of generating instantaneous responses for the manholes could be by means of the CFD approach.

CFD numerical models also calculate the flow properties (velocity and pressure) within the structures. This provides additional opportunities to examine the effects of scale on the flow structure as well as energy loss in manholes.

Numerical models for the three differently scaled manholes were created following the standard modelling protocol developed in Chapter 6. Section 7.2 describes the configurations of the manholes considered in this study and the methodology used to create the CFD manhole models. Section 7.3 presents the results of the flow field, energy loss and solute transport predictions for the manhole models; the assessment of the scale effects on these processes is also highlighted in Section 7.3. Section 7.4 suggests the scaling methodologies for manholes and the study is concluded in Section 7.5.

7.2 Generation of the Three Manhole Models

7.2.1 Manhole Dimensions and Flow Conditions

Three differently scaled manholes of the same manhole configuration (manhole ID to pipe ID ratio) were generated for this present study. They are the prototype manhole (800 mm ID); the small scale manhole (218 mm ID) considered in the laboratory tracer and flow visualisation experiments; and a large scale manhole with an ID of 1,200 mm. The size of the large scale model was chosen based on realistic dimensions of a manhole in the UK urban drainage network which provides access for cleaning and inspection by personnel (BS EN 476:1998). The dimensions of the three manholes are detailed in Table 7.1.

In each of the manholes, five surcharge ratios and two flowrates were examined, giving thirty manhole simulations in total. The five surcharge ratios considered are comparable in each of the manholes (Table 7.1), comprising three surcharge conditions (surcharge ratios smaller than 2.5), in the pre-threshold hydraulic regime, and two post-threshold surcharge conditions (see Section 4.4). The discharge conditions examined are different in the three models. In the prototype, discharges of 4 l/s and 8 l/s were studied because these conditions had been covered in the laboratory tracer experiments carried out by Guymer *et al.* (2005) and validation of the particle tracking predictions is possible if this is needed. The two discharges were then scaled using Froudian similarity (Equation 4.8 and Equation 4.9) to give the discharges to be examined in the large scale manhole. However, the flowrates investigated in the small scale manhole model were not determined from the principles of scaling. This is because one of the Froude scaled discharges, for the scale manhole would have produced a flow condition in the transitional turbulent regime ($Q = 0.16$ l/s; $Re < 10,000$). In this case, the assumption made in the Froudian scaling, which ignore Reynolds number effects, would become invalid. Two discharges covered in the laboratory tracer tests (Chapter 3) were considered. They are 0.35 l/s and 0.50 l/s, giving a Froude scaled discharge with respect to the prototype of 9.06 l/s and 12.90 l/s. A discharge of 0.35 l/s was chosen because the models have been validated with this flowrate in Chapter 6.

Configurations and Flow Conditions	Prototype Model	Small Scale Model	Large Scale Model
Manhole diameter (mm)	800	218	1,200
Pipe diameter (mm)	88	24	132
Distance of the model inlet and outlet to the manhole centreline (mm)	1,350	368	2,025
Discharge (l/s)	4; 8	0.35; 0.50	11; 22
Reynolds number (-)	49,892; 99,784	16,053; 22,867	91,468; 182,937
Froude scaled discharge with respect to the prototype (l/s)	-----	9.06; 12.90	3.99; 7.98
Surcharge ratios (-)	1.25; 1.70; 2.05; 2.50; 3.34	1.25; 1.67; 2.08; 2.50; 3.33	1.25; 1.67; 2.08; 2.50; 3.33

Table 7.1 – Summary of the manhole configurations and flow conditions considered during the study

7.2.2 Model Set-up Parameters

The numerical models for the three differently scaled manholes were created according to the standard modelling protocol developed in Chapter 6. The manholes were simulated using a single phase modelling approach, with the fixed lid approximation to simplify the free surface. The version 2 meshing strategy in Section 6.2.1.1.2 was adopted to mesh the model domains; and the fluid and boundary conditions were defined as in Section 6.2.1.1.2. For the flow field solver, consideration was given to the RNG k - ϵ turbulence model in association with the non-equilibrium wall functions. The flow field solution was solved using the second order accurate spatial discretisation schemes, shown in Table 6.10. The solute transport predictions were made using the uncoupled particle tracking approach in conjunction with the stochastic modelling to account for the effects of turbulence in the flow. Details of the particle tracking model set-up can be found in Table 6.10.

In the manhole simulations, the double precision solver (64 bits) of Fluent 6.2 was adopted. The use of this approach was to obtain the most precise results for the flow field and solute transport predictions (personal communication with Fluent engineer).

Grid refinement studies were repeated in the three manhole models based on the higher flowrate conditions. The higher discharge models were chosen because they would require a higher density mesh in order to achieve a grid independent solution than lower discharge models due to the larger gradient of the variables in the domain. A typical mesh setting defined for the three differently sized manholes to obtain a nearly grid independence solution is given in Table 7.2. Concern may be expressed that the average cell size for the nearly grid independence solution

between the three manhole models is not identical, with greater size in larger scale models. The truncation error caused by spatial discretisation scheme may be different as the second order accurate schemes are a function of the square of cell size. However, due to the limitations of the computational resources, it was not possible to further refine the mesh of the prototype and the large scale model so as to obtain equivalent truncation error (cell size) as in the scale manhole model. Nevertheless, the cell size in these three models is small that the difference in the truncation errors should be insignificant.

Manhole Diameter (mm)	Model Volume (mm ³)	Total Number of Cells	Average Cell Volume (mm ³)	Average Cell Size (mm)
218	4,059,643	464,280	8.74	2.06
800	203,296,500	1,085,040	187.36	5.72
1,200	685,850,300	1,304,202	525.88	8.07

Table 7.2 – Typical mesh setting for the three manhole models considered in the study (These configurations were based on the models with a surcharge ratio of 3.33)

7.2.3 Wall Roughness

In the preliminary and detailed CFD manhole simulations reported in Chapter 6, the roughness effects of the wall-bounded flows were specified using the suggested values for the roughness height and roughness constant given by Grimm (2004). Grimm (2004) calculated the roughness height value using theoretical head loss data estimated by the Darcy-Weisbach and Colebrook-White equations (Chadwick and Morfett, 1998). However, the theoretical head loss data might deviate from the actual head loss; and therefore the derived roughness might not be the best description for smooth pipes/surfaces.

The wall roughness parameters for the manhole simulations were estimated using a separate CFD straight pipe model and the energy loss data measured for the 24 mm ID straight pipe (Section 3.5.1.1). To simplify the calibration process, only the roughness height value was adjusted and the roughness constant remained unchanged during the calibration. The laboratory pressure measurements were taken under fully developed flow conditions. Therefore, a straight pipe with the ‘periodic’ boundary condition and a length of 10 diameters (IDs) was adopted to simulate the same hydraulic conditions. Details of the model setup can be found in Section 6.2.1.4. During the calibration, four roughness height values, which are 2×10^{-5} m, 4×10^{-5} m, 6×10^{-5} m and 8×10^{-5} m, and a range of flowrates between 0.25 l/s and 0.50 l/s were considered. Note that the straight pipe model generated a grid independent solution.

The results of the energy loss predictions made by the four parameter values are compared with the measured data in Figure 7.1. The error bars of the observed data represent 5 % deviations of

the head loss measurements. It may be noticed that when the discharge is smaller than 0.35 l/s, all head loss predictions made by the four parameter values match the measured data very well. However, when the discharge is greater than 0.35 l/s, the results for the roughness values of 6×10^{-5} m and 8×10^{-5} m appear to deviate from the measurements and the deviation increases with discharge. For the other two values (2×10^{-5} m and 4×10^{-5} m), the predicted head loss is in excellent agreement with the experimental data. Of the two, the larger value appears to fit the data marginally better. A value of 4×10^{-5} m was adopted in the further manhole simulations. Note that the change in the roughness height value from 8×10^{-5} m to 4×10^{-5} m should introduce a negligible effect on the flow field within the manhole chamber.

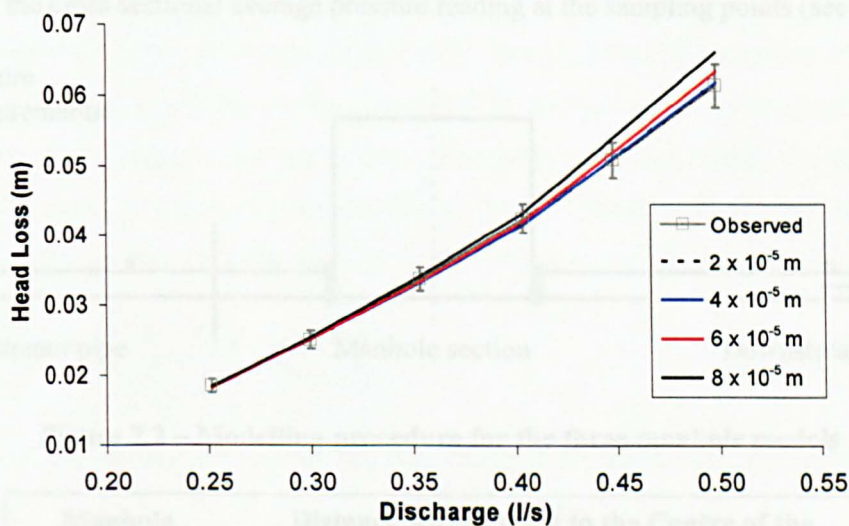


Figure 7.1 – Calibration of the wall roughness parameter using the measured straight pipe energy loss data

7.2.4 Methodology for Pressure Data Collection in CFD

Estimation of the head loss due to surcharged manholes using CFD followed the method and arrangement used in the laboratory experiments (Chapter 3). In the physical experiments of the small scale manhole, the pressure measurement points were set at 500 mm, 750 mm and 1,000 mm (or $20.83D_p$, $31.25D_p$ and $41.67D_p$) upstream and downstream from the centre of the manhole. However, the corresponding numerical models replicated only the experimental section of the manhole rig from the upstream fluorometer to the downstream fluorometer (Section 3.2.2.1 and Section 6.3.2), i.e. 368 mm (or $15.33D_p$) upstream and downstream. The pipe sections where the pressure readings were recorded were not included in the model. In order to obtain comparable pressure readings between the numerical models and the experiments, two extra straight pipes were modelled in each of the thirty manhole simulations. The two straight pipes have an ID same as the manhole upstream pipe and a length of

approximately 31 times pipe ID. The modelling procedure for the three differently sized manholes was revised:

1. Create two straight pipes and a manhole section as illustrated in Figure 7.2;
2. Input a fully developed flow profile into the upstream pipe and then transfer the outlet profile from this pipe to the manhole model after the completion of the simulation;
3. Use the outlet profile from the manhole model (after the completion of the simulation) to setup the inlet boundary condition of the downstream pipe and then calculate the flow field of the downstream pipe;
4. Extract the cross sectional average pressure reading at the sampling points (see Table 7.3).

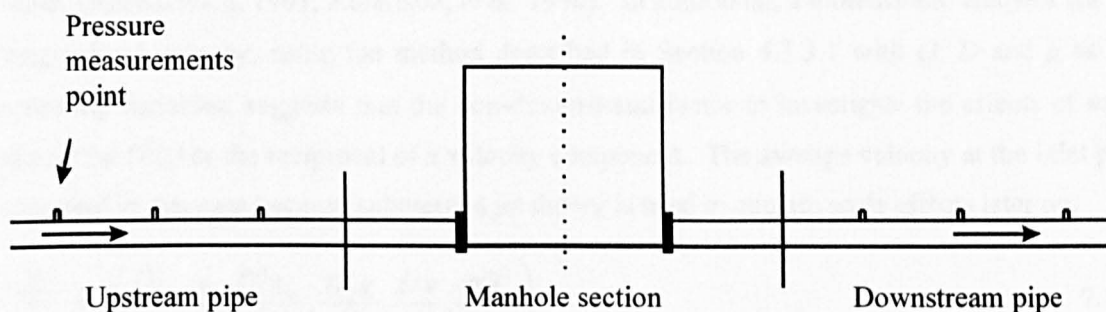


Figure 7.2 – Modelling procedure for the three manhole models

Manhole Diameter (mm)	Distance with respect to the Centre of the Manhole (mm)
218	500 ($20.83D_p$), 750 ($31.25D_p$), 1,000 ($41.67 D_p$)
800	1,835 ($20.85D_p$), 2,752 ($31.27D_p$), 3,669 ($41.69D_p$)
1,200	2,752 ($20.85D_p$), 4,128 ($31.27D_p$), 5,504 ($41.70D_p$)

Table 7.3 – Pressure sampling positions in the three manholes considered in the study
(D_p – diameter of the manhole upstream pipe)

7.3 Comparisons of Hydraulic and Solute Transport Results

7.3.1 Flow Field Results

This sub-section examines the effects of surcharge, discharge and geometrical scale of the manholes on the flow field results. To enable direct comparison of the flow field between different discharges and manholes to be made, the results are presented in a normalised form (longitudinal velocity normalised with respect to the average velocity at the inlet pipe). For presentation purposes, only the velocity results for the vertical plane and horizontal plane at the centreline of the pipe (CVP and CHP in Figure 5.2) are shown. Note that this dimensionless form of the longitudinal velocity is commonly used to study jet flows of different physical scales (Abramovich, 1963; Albertson, *et al.* 1950). In addition, a dimensional analysis for the longitudinal velocity, using the method described in Section 4.3.3.1 with Q , D and ρ as the repeating variables, suggests that the non-dimensional factor to investigate the effects of scale should be D^2/Q or the reciprocal of a velocity component. The average velocity at the inlet pipe was used in this case because submerged jet theory is used to explain scale effects later on.

$$\frac{uD^2}{Q} = f\left(\frac{D_p}{D}, \frac{s}{D}, \frac{D^4 \tau_w}{\rho Q^2}, \frac{D^5 g}{Q^2}, \frac{Dv}{Q}, \frac{\rho Q^2}{D^3 \sigma}\right) \quad 7.1$$

If the governing parameter for the flow is Froude number, Equation 7.1 can be simplified as:

$$\frac{uD^2}{Q} = f\left(\frac{D_p}{D}, \frac{s}{D}, \frac{D^5 g}{Q^2}\right) \quad 7.2$$

7.3.1.1 The Effect of Surcharge on Flow Fields

Figure 7.3 and Figure 7.4 show the variations of the flow fields with the five surcharge ratios in the small scale manhole at a discharge of 0.35 l/s. At the surcharge ratios of 1.25 and 1.67 (pre-threshold), the flow field within the chamber can be generally described as a skewed jet in association with circulations in the dead zone. However, careful examination of the two flow fields (Figure 7.3a and b; Figure 7.4a and b) suggests that the degree of skewness of the jet and the magnitude of the velocity of the circulations appear to decrease with increasing surcharge ratio.

At the surcharge ratio of 2.05, a change in the hydraulic characteristics to the post-threshold flow field is evident in Figure 7.3c and Figure 7.4c. The asymmetrical flow field is now replaced with a straight through jet flow in conjunction with nearly symmetrical circulations

about the pipe centreline. For higher surcharge ratios, the general flow pattern barely changes with increasing surcharge (Figure 7.3c-e and Figure 7.4c-e).

Compared with the tracer results presented in Chapter 4, it is evident that the hydraulic transition has prematurely occurred in the numerical models. The tracer data for the small scale manhole suggests that the threshold depth should be at a surcharge ratio between 2.05 and 2.50, while this has occurred before/at the surcharge ratio of 2.05 in the model. Explanation of the premature hydraulic transition is offered in the following sub-section.

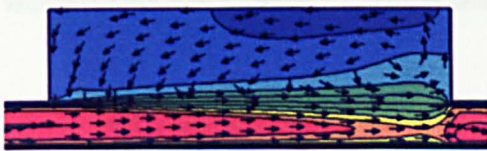
The results of the variations of the flow field with surcharge ratio at the higher discharge conditions ($Q = 0.50$ l/s) of the small scale manhole provided the same conclusion as the results above. The same conclusion also applied to the flow field results of the other two manhole models (figures not provided).



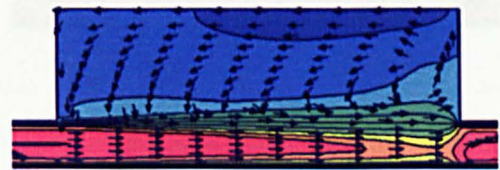
(a) – Surcharge ratio = 1.25



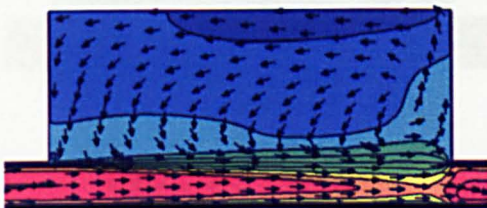
(b) – Surcharge ratio = 1.67



(c) – Surcharge ratio = 2.08



(d) – Surcharge ratio = 2.50



(e) – Surcharge ratio = 3.33

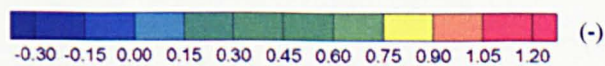


Figure 7.3 – Comparisons of the flow field on the CVP for the small scale model (Discharge = 0.35 l/s, contours coloured by normalised longitudinal velocity)

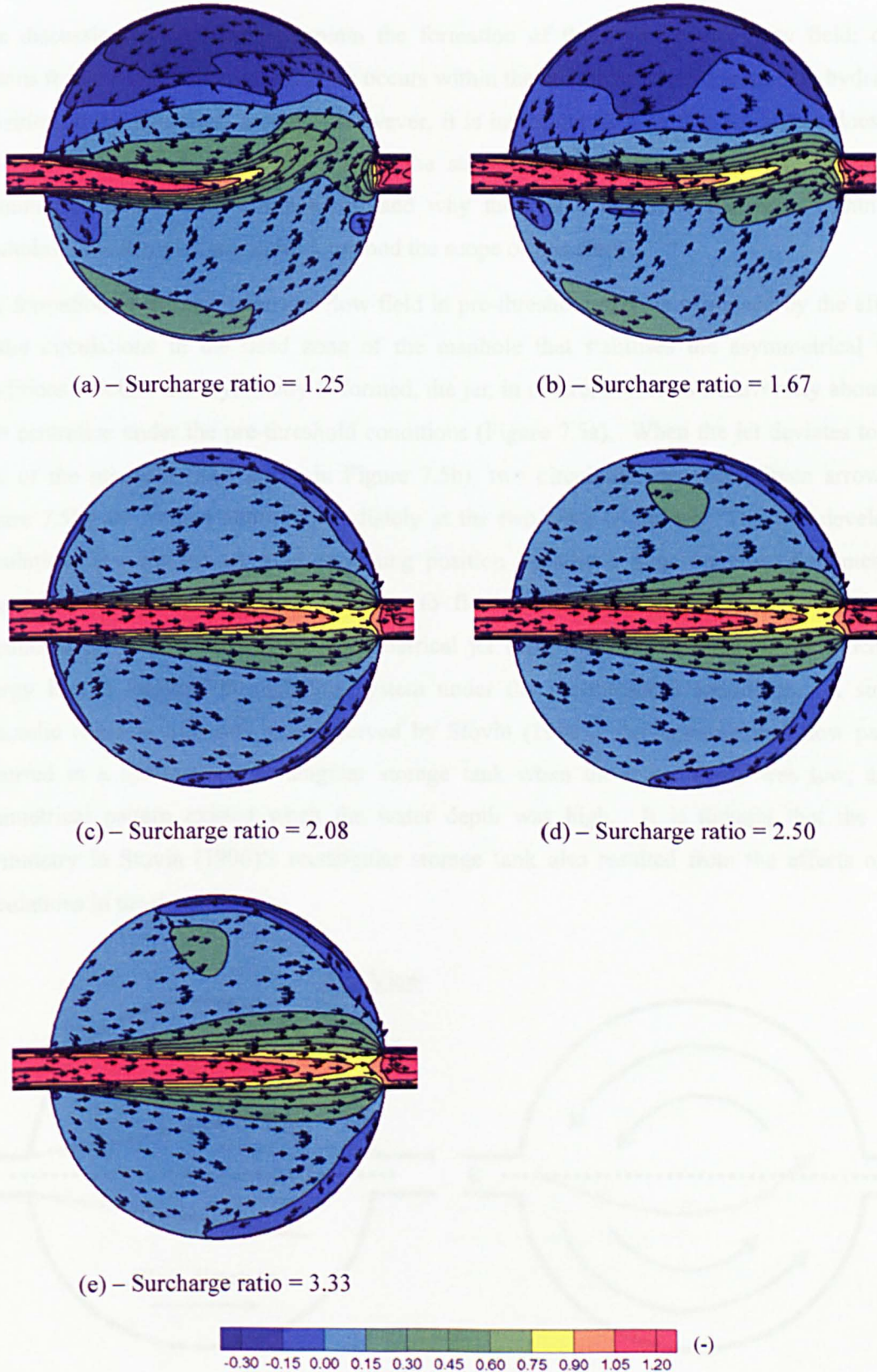


Figure 7.4 – Comparisons of the flow field on the CHP for the small scale model (Discharge = 0.35 l/s, contours coloured by normalised longitudinal velocity)

7.3.1.1 Discussion

This discussion is intended to explain the formation of the asymmetrical flow field; offer reasons for how the hydraulic transition occurs within the manholes and the premature hydraulic transition in the numerical models. However, it is important to state that the author does not have an answer to the question of why the stable flow field in this type of situation is asymmetrical rather than symmetrical; and why there is a hydraulic transition within the manholes. These topics are, indeed, beyond the scope of this study.

The formation of the asymmetrical flow field in pre-threshold may be explained by the effects of the circulations in the dead zone of the manhole that stabilises the asymmetrical flow conditions. Before the asymmetry is formed, the jet, in nature, oscillates transversely about the pipe centreline under the pre-threshold conditions (Figure 7.5a). When the jet deviates to one side of the manhole (Red arrow in Figure 7.5b), two circulation currents (Green arrows in Figure 7.5b) are formed almost immediately at the two sides of the jet. The two developed circulations prevent the jet from switching position because a large amount of momentum (energy) is needed from the jet in order to flow against the circulation and reverse the circulation direction. This stable asymmetrical jet form may be the situation in which the energy loss is minimal through this system under the pre-threshold conditions. A similar hydraulic characteristic was also observed by Stovin (1996). An asymmetrical flow pattern occurred in a symmetrical rectangular storage tank when the water depth was low; and a symmetrical pattern existed when the water depth was high. It is thought that the flow asymmetry in Stovin (1996)'s rectangular storage tank also resulted from the effects of the circulations in the dead zone.

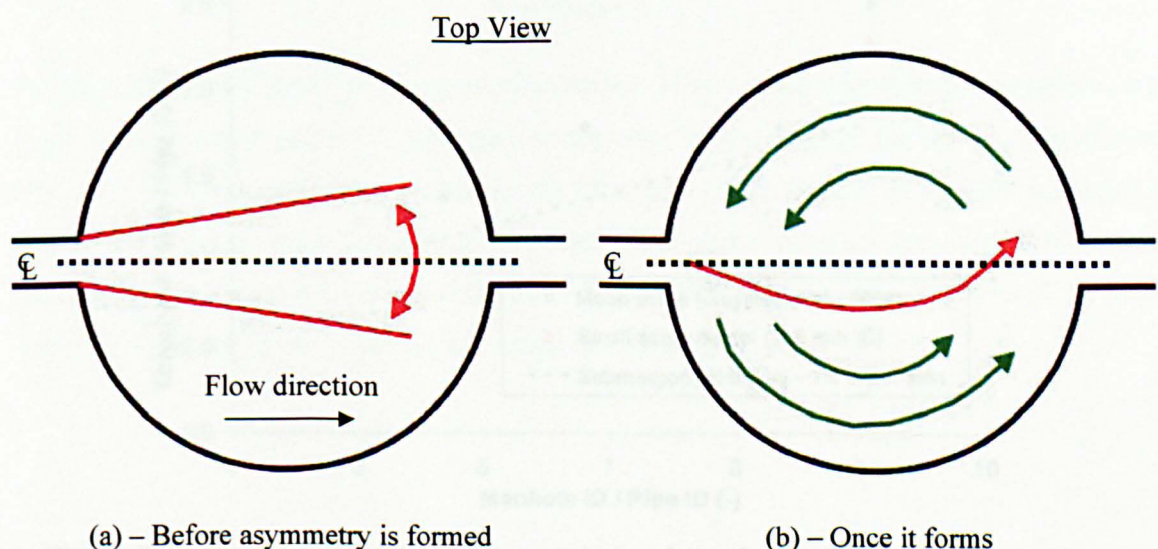


Figure 7.5 – Illustration of the formation of the asymmetrical flow field in pre-threshold

It is thought that the velocity (strength) of the circulation determines the degree of the jet deviation within the manhole. When surcharge depth increases, the increase in surcharge volume leads to a reduction in the average velocity of the horizontal circulation because a fixed amount of jet momentum is transferred to a larger volume of slowly flowing water. As the velocity of the horizontal circulation reduces, the circulation may not be able to stabilise the skewed position of the jet and the skewed jet may gradually return to the pipe centreline position.

Pre-threshold, the incoming jet appears to spread vertically throughout the surcharge depth, but it becomes suppressed in post-threshold. This hydraulic characteristic may be explained by submerged jet theory, developed by Albertson *et al.* (1950) (also see Section 2.5.3). When the surcharge is low ($< \text{manhole ID}/5$), the diffusion region interacts with the free surface. The interaction causes vigorous free surface oscillations and additional turbulence leading to more vertical mixing. Above the threshold depth, the diffusion region is completely kept within the storage volume and this promotes the formation of a submerged jet as observed in post-threshold flow field. Guymer *et al.* (2005) suggested that the threshold depth may be correlated to the rate of expansion of the diffusion region. Their study observed that the threshold depth varied as a function of the manhole ID to pipe ID (D/D_p) ratio and that the value of the threshold depth may be approximately predicted by reference to submerged jet theory (Figure 7.6). However, using the jet theory alone under-predicted the threshold depth in the four manholes with different D/D_p ratios that they considered. Applying the same theory to the small scale manhole also under-estimates the measured threshold value, between surcharge ratios of 2.0 and 2.5 (Figure 7.6).

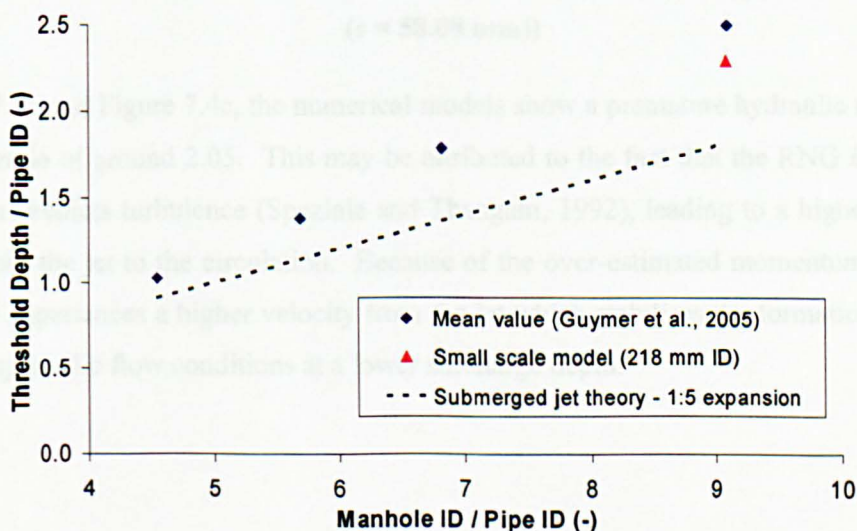
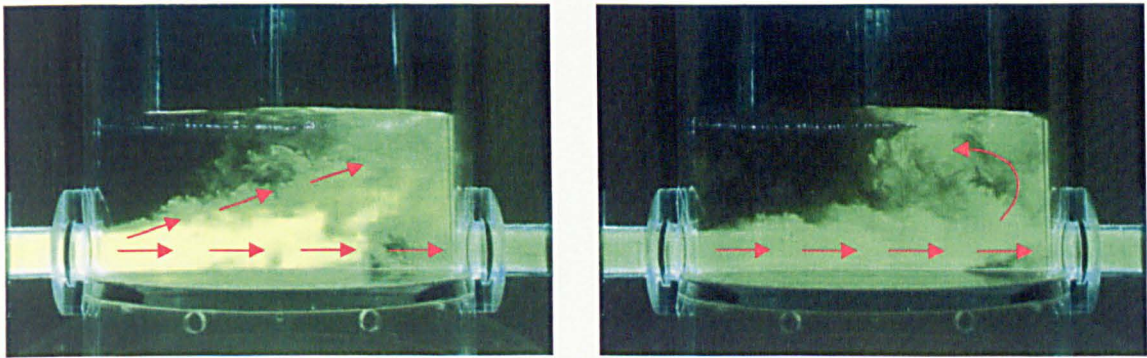


Figure 7.6 – Comparisons of laboratory measured surcharge threshold and surcharge threshold predicted by submerged jet theory

There are two possible explanations for the under-estimation of the threshold level using submerged jet theory. Firstly, it is thought that the level determined from the jet theory would only suggest the minimum surcharge depth for the development of a submerged jet. Additional forces introduced by the vertical circulation and/or other forces, such as hydrostatic pressure, are required to stabilise the hydraulic transition. For example, in the transition zone ($S = 2.42$), the flow field randomly oscillates between the two hydraulic regimes (Figure 7.7). The hydraulic transition was only completed once the surcharge depth had been clear from the transitional zone. Secondly, there may be a different expansion ratio for a confined jet (the jet observed in this type of manhole) as submerged jet theory was developed for a free jet with infinite boundary conditions. The change of hydraulic regime from pre-threshold to post-threshold at high surcharge levels may be because the flow in the manhole always tends to minimise energy loss by itself. Note that energy loss in the post-threshold conditions is much smaller than that in pre-threshold.



(a) – Pre-threshold flow field

(b) – Post-threshold flow field

Figure 7.7 – Flow field in the transitional zone (Small scale model; $Q = 0.38$ l/s; $S = 2.42$ ($s = 58.08$ mm))

In Figure 7.3c and Figure 7.4c, the numerical models show a premature hydraulic transition at a surcharge ratio of around 2.05. This may be attributed to the fact that the RNG $k-\epsilon$ turbulence model over-predicts turbulence (Speziale and Thangam, 1992), leading to a higher momentum transfer from the jet to the circulation. Because of the over-estimated momentum transfer, the circulation experiences a higher velocity from the jet which stabilises the formation of the post-threshold hydraulic flow conditions at a lower surcharge depth.

7.3.1.2 The Effect of Flowrate on Flow Fields

Figure 7.8 and Figure 7.9 present the comparisons of the flow fields for the large scale manhole at two different discharge conditions. The large scale model results are shown because the difference in the discharge is the greatest among the three manhole models.

The results show that after the normalisation of the velocity, the flow fields within the manhole in the two flowrate conditions display high comparability in terms of flow pattern and velocity magnitude. Detailed comparisons of the flow field between the two models suggest that the strength (velocity) of the jet appears to increase with discharge. At all three scales considered, high comparability between flow fields was observed for configurations with the same surcharge depth, irrespective of discharge. Further discussion of the discharge effects is presented in Section 7.3.1.3.1.

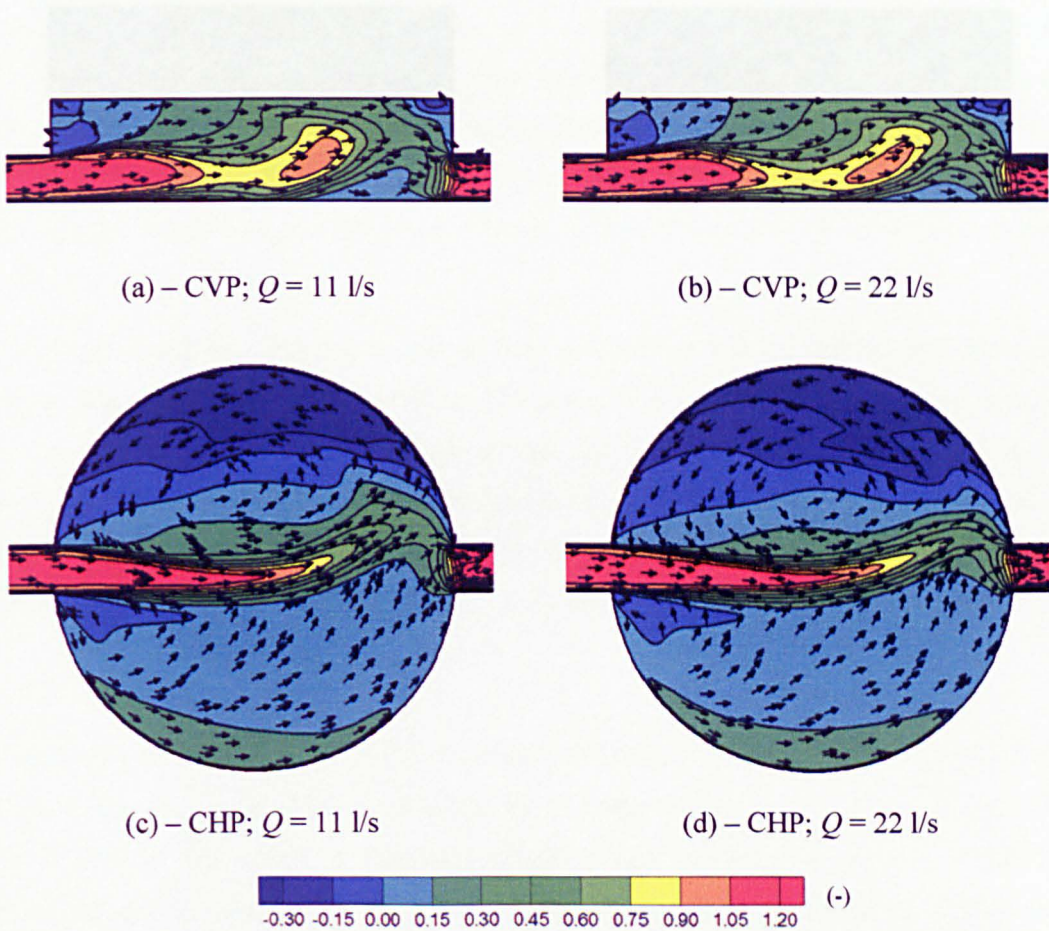


Figure 7.8 – Comparisons of the pre-threshold flow field on the CVP and CHP for the large scale model ($Q = 11$ and 22 l/s, contours coloured by normalised longitudinal velocity)

7.2.2.3 The Effect of Seafloor Flow Fields

Contours of the flow field in a geometrical scale under the pre- and post-threshold conditions are shown in Figure 7.10 and Figure 7.11. For presentation purposes, only one reference case is provided (i.e. $Q = 11 \text{ l/s}$) and the same is used in the following.

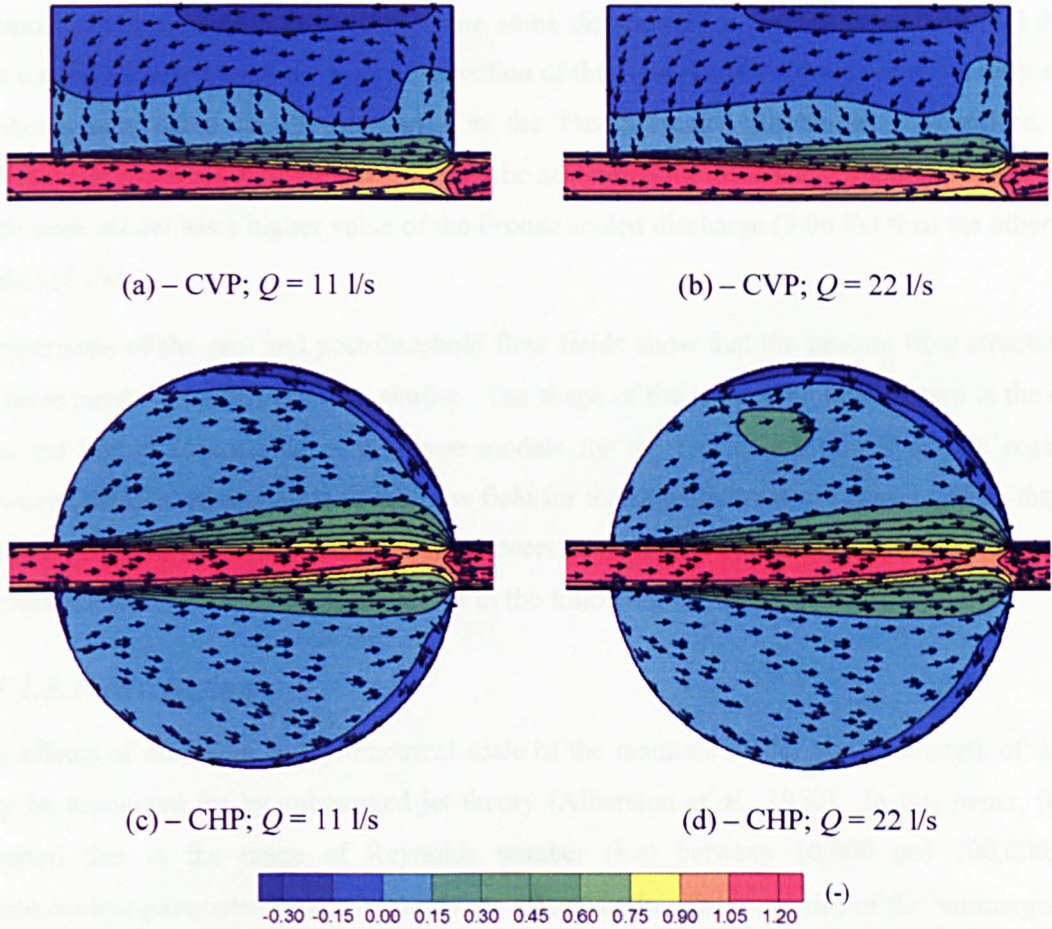


Figure 7.9 – Comparisons of the post-threshold flow field on the CVP and CHP for the large scale model ($Q = 11$ and 22 l/s , contours coloured by normalised longitudinal velocity)

7.3.1.3 The Effect of Scale on Flow Fields

Variations of the flow field with geometrical scale under the pre- and post-threshold hydraulic conditions are shown in Figure 7.10 and Figure 7.11. For presentation purposes, only one surcharge ratio in pre-threshold ($S = 1.25$) and one case in post-threshold ($S = 3.33$) are presented. The surcharge ratios chosen are some distance from the predicted threshold depth where the hydraulic transition occurs. Selection of the flow fields for the three differently sized manholes was based on the similarity in the Froude scaled discharges. Therefore, any difference between the flow field results may be accounted for the effects of scale. Note that the small scale model has a higher value of the Froude scaled discharge (9.06 l/s) than the other two models (8 l/s).

Comparisons of the pre- and post-threshold flow fields show that the general flow structure in the three manhole models are very similar. The shape of the jet and the flow pattern in the dead zone are highly comparable in the three models for the two contrasting hydraulic regimes. However, detailed examination of the flow field for the same hydraulic regime suggests that the strength of the jet, i.e. the jet velocity, appears to increase by a very small amount as the physical scale increases. This is explained in the following sub-section.

7.3.1.3.1 Discussion

The effects of discharge and geometrical scale of the manhole model on the strength of the jet may be accounted for by submerged jet theory (Albertson *et al.*, 1950). In this paper, it was reported that in the range of Reynolds number (Re) between 10,000 and 200,000, the dimensionless parameter induces a moderate effect on the characteristics of the submerged jet. The length of the core increased with Reynolds number; for example the length increased from approximately 5 times the nozzle diameter for a Re of 10,000 to approximately 7 times the nozzle diameter for a Re of 200,000. The relationship is linear. This physical phenomenon explains why at higher discharge conditions or in a larger scale manhole (higher Re , see Table 7.1) the results show a stronger jet within the manhole.

With reference to the scaling methodologies developed for manholes in Section 4.3.3.1, the fact that Re effects are ignored in the adoption of Froudian similarity may introduce scale effects. The effects of scale on the energy loss and solute transport characteristics are studied in the following sections.

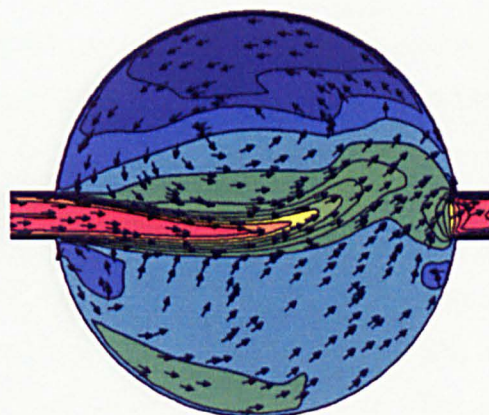


(a) – Small scale manhole ($Q = 0.35$ l/s;
Froude scaled $Q = 9.06$ l/s)

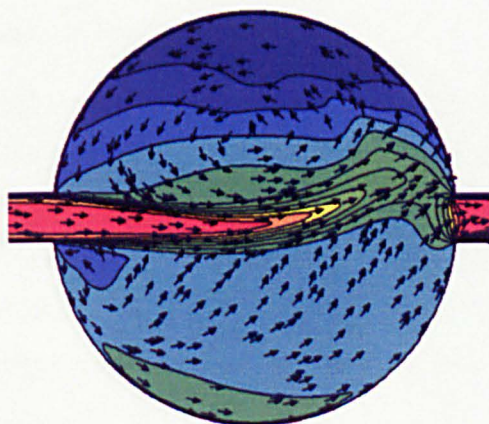
(b) – Prototype ($Q = 8$ l/s)



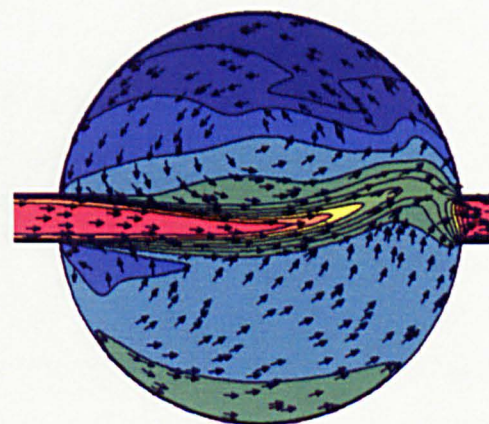
(c) – Large scale manhole ($Q = 22$ l/s;
Froude scaled $Q = 7.98$ l/s)



(d) – Small scale manhole ($Q = 0.35$ l/s;
Froude scaled $Q = 9.06$ l/s)



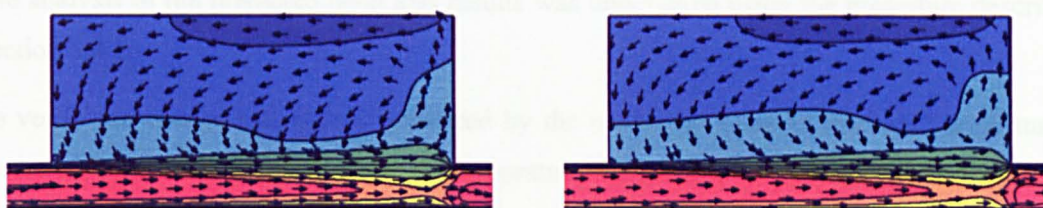
(e) – Prototype ($Q = 8$ l/s)



(e) – Large scale manhole ($Q = 22$ l/s;
Froude scaled $Q = 7.98$ l/s)

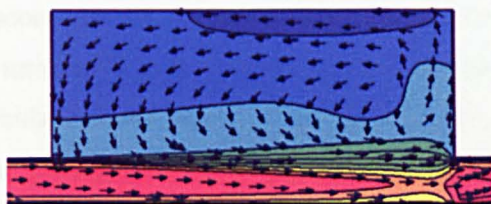


Figure 7.10 – Comparisons of the pre-threshold flow field on the CVP and CHP for the three manhole models ($S = 1.25$, contours coloured by normalised longitudinal velocity)

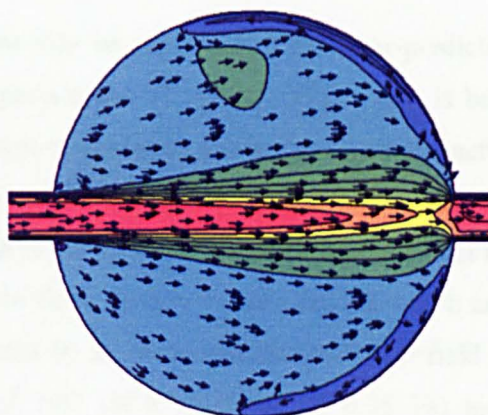


(a) – Small scale manhole ($Q = 0.35$ l/s;
Froude scaled $Q = 9.06$ l/s)

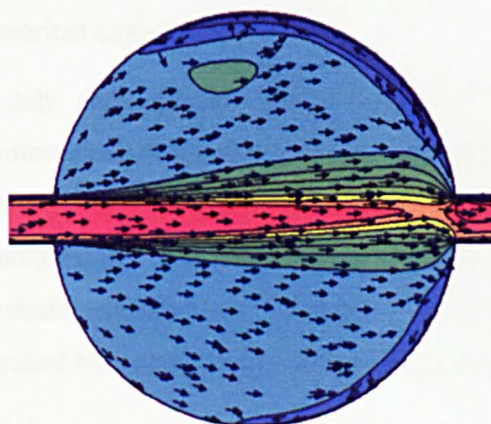
(b) – Prototype ($Q = 8$ l/s)



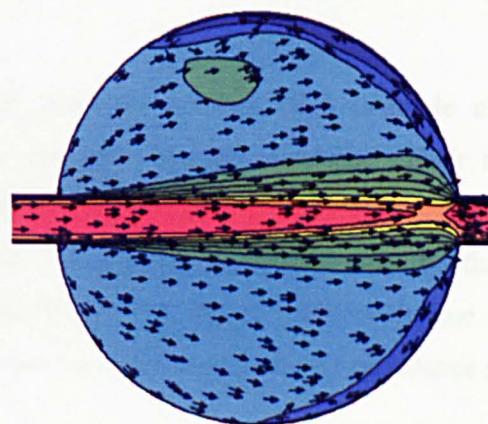
(c) – Large scale manhole ($Q = 22$ l/s;
Froude scaled $Q = 7.98$ l/s)



(d) – Small scale manhole ($Q = 0.35$ l/s;
Froude scaled $Q = 9.06$ l/s)



(e) – Prototype ($Q = 8$ l/s)



(e) – Large scale manhole ($Q = 22$ l/s;
Froude scaled $Q = 7.98$ l/s)

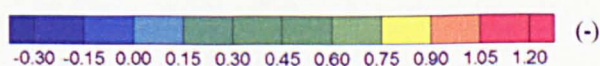


Figure 7.11 – Comparisons of the post-threshold flow field on the CVP and CHP for the three manhole models ($S = 3.33$, contours coloured by normalised longitudinal velocity)

7.3.2 Energy Loss Results

The analysis of the predicted head loss results was undertaken using the procedure described in Section 3.4.1.

To verify the energy loss results predicted by the numerical models, the small scale manhole predicted data is compared with the laboratory measurements presented in Figure 3.16. Comparison of the two sets of data suggests that the CFD data appears to be consistently higher than the measured results by approximately 20 - 30 % (Figure 7.12). There are exceptions at the surcharge ratios of around 1.67 (at a discharge of 0.35 l/s) and 2.05 (at discharges of 0.35 l/s and 0.50 l/s) where the CFD data is lower than the laboratory measurements.

The over-estimation of the energy loss coefficient may be explained by the over-prediction of turbulence by the RNG $k-\varepsilon$ turbulence model (Speziale and Thangam, 1992). This is because the turbulent kinetic energy generated in a flow system gradually dissipates due to the action of viscous stresses leading to energy loss (Versteeg and Malalasekera, 1995). The major sources of turbulence in the manhole system can be found at the turbulent jet; flow impingement by the circulations; the vena contracta at the outlet pipe in close vicinity to the manhole outlet; and the wall boundary. All of these areas might be affected by an over-estimated turbulent field in the model. The anomaly at the surcharge ratio of 1.67 (at a discharge of 0.35 l/s) may be attributable to the flow field prediction that suggested a less skewed jet, leading to a lower degree of energy loss in the system; while at the points corresponding to a surcharge ratio of 2.05, the under-prediction is due to the premature hydraulic transition predicted by the numerical models.

Asztely and Lyngfelt (1996) generated 'halved' three-dimensional CFD manhole models (symmetrical about the CVP) to predict energy loss in a benched manhole. Their results showed excellent agreement with the experimental data published by Lindvall (1984), with approximately 5 % deviations. The reasons for the excellent agreement may be that the manhole modelled was benched and therefore the jet did not spread transversely due to the physical boundary, which reduced the prediction errors associated with the $k-\varepsilon$ turbulence model.

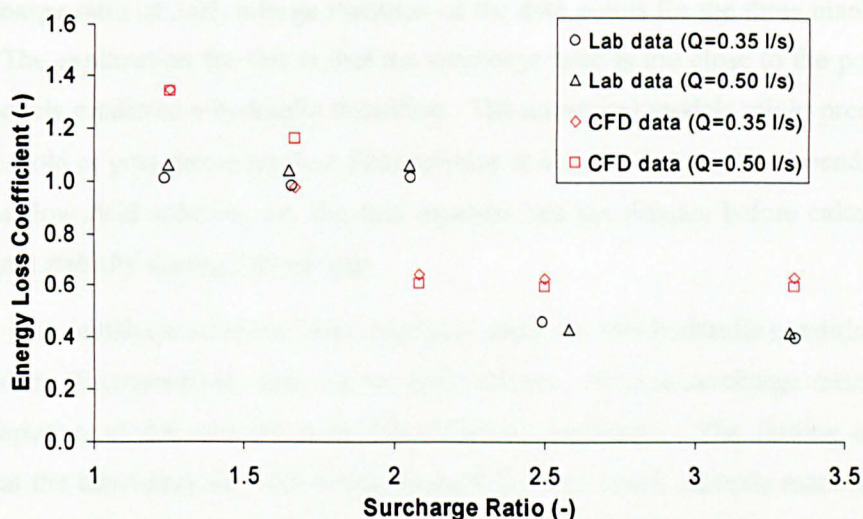


Figure 7.12 – Comparison of the energy loss coefficients for the small scale manhole measured in the laboratory experiment and predicted by CFD

The dimensional analysis for energy loss coefficient, K_L , suggests that the coefficient for two geometrically similar models will be identical if dynamic similarity, such as Reynolds number or Froude number, between the models is valid. Therefore, any difference in the coefficient, K_L , between different scale models could be accounted for the effects of scale.

$$K_L = f\left(\frac{D_p}{D}, \frac{s}{D}, \frac{D^4 \tau_w}{\rho Q^2}, \frac{D^5 g}{Q^2}, \frac{Dv}{Q}, \frac{\rho Q^2}{D^3 \sigma}\right) \quad 7.3$$

If the governing parameter for the flow is Froude number, Equation 7.3 can be simplified as:

$$K_L = f\left(\frac{D_p}{D}, \frac{s}{D}, \frac{D^5 g}{Q^2}\right) \quad 7.4$$

Variations of energy loss coefficient predicted by the three manhole models with surcharge ratio are shown in Figure 7.13. The results show a transition in the coefficient at a surcharge ratio of around 2.05. Before the transition, the dimensionless coefficient stays at values above 1.0 and appears to be an inverse function of surcharge ratio. The coefficients drop to approximately half of the pre-threshold values after the hydraulic transition, yielding values of nearly 0.6. The coefficient stays constant with regard to surcharge. The higher energy loss in pre-threshold may be explained by the jet asymmetry that promotes a higher momentum transfer from the jet to the storage water than a straight through jet (Asztely and Lyngfelt, 1996). In addition, the trajectory of the jet does not direct towards the outlet but to one side of the manhole wall, forming an impingement. Energy loss is expected in the process of the flow impingement.

At the surcharge ratio of 2.05, a large variation of the data points for the three manholes can be observed. The explanation for this is that the surcharge ratio is too close to the point at which the CFD models predicted a hydraulic transition. The numerical models might predict either of the pre-threshold or post-threshold flow field solution at this surcharge ratio depending upon the initial guess flow field solution, i.e. the data inputted into the domain before calculations; and computational stability during calculations.

The energy loss coefficients for the three manholes under the two hydraulic conditions appear to be independent of geometrical scale, i.e. no scale effects. At each surcharge ratio, there is no systemic variation of the variable with Froude scaled discharge. The finding of this study suggests that the laboratory derived energy loss coefficients based on scale manhole models in previous research should be applicable to full scale structures in urban drainage systems.

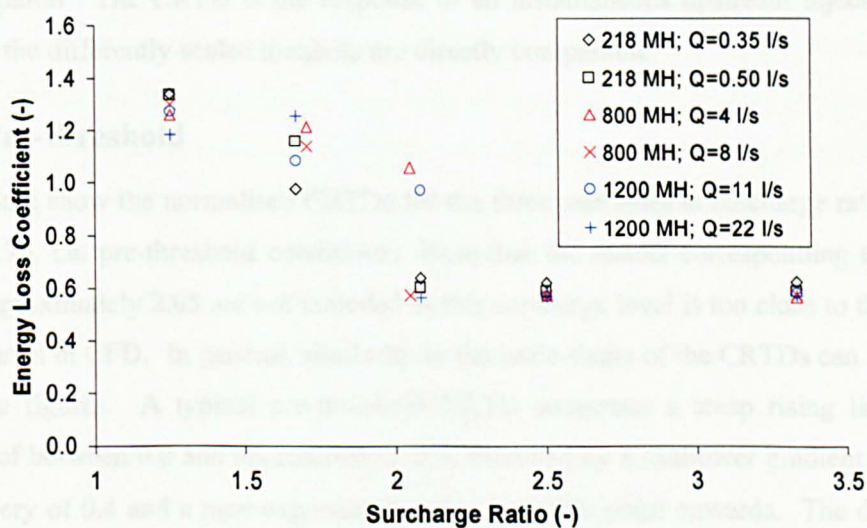


Figure 7.13 – Variations of predicted energy loss coefficient with surcharge ratio for the three differently sized manholes

7.3.3 Solute Transport Predictions

In Chapter 4, cumulative temporal concentration profiles (CTCPs), which are the response to a non-instantaneous upstream distribution, obtained from the laboratory were adopted for the study of the scale effects. Promising results are shown when CTCPs were normalised with respect to the volumetric travel time. The normalised distributions for each manhole collapse onto a single curve for each of the two hydraulic regimes, and the normalised profiles for the two differently scaled manholes also appear to be similar in terms of profile shape. However, detailed examination of the scale effects was not made using the CTCPs in the laboratory-based analysis. This was because the CTCPs for the two manholes are not directly comparable due to inconsistencies in the shape of the upstream concentration distributions. This sub-section continues the study in Chapter 4 but uses cumulative retention time distributions (CRTDs) for the investigation. The CRTD is the response to an instantaneous upstream injection and the CRTDs for the differently scaled manhole are directly comparable.

7.3.3.1 Pre-threshold

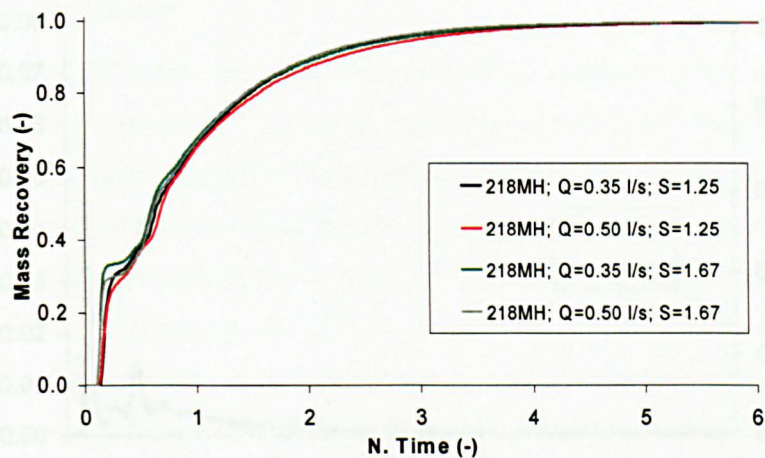
Figure 7.14a-c show the normalised CRTDs for the three manholes at surcharge ratios between 1.25 and 1.70, i.e. pre-threshold conditions. Note that the results corresponding to surcharge ratios of approximately 2.05 are not included as this surcharge level is too close to the threshold surcharge level in CFD. In general, similarity in the basic shape of the CRTDs can be observed in the three figures. A typical pre-threshold CRTD comprises a steep rising limb at mass recoveries of between 0.0 and approximately 0.3, followed by a shallower gradient limb until a mass recovery of 0.4 and a near-exponential curve from this point onwards. The discontinuity of the CRTD at mass recoveries of between 0.3 and 0.4 indicates the trough between the first and secondary peak on the RTD (Figure 7.15).

Comparisons of the pre-threshold CRTDs for each of the manholes suggest that the temporal normalisation process may account for the effects of both discharge and surcharge. The CRTDs appear to collapse onto a single curve, although there are some variations at mass recoveries between 0.2 and approximately 0.4. The variations may be attributable to the difference in the degree of deviation of the skewed jet in the manhole and therefore different travel times in the circulations.

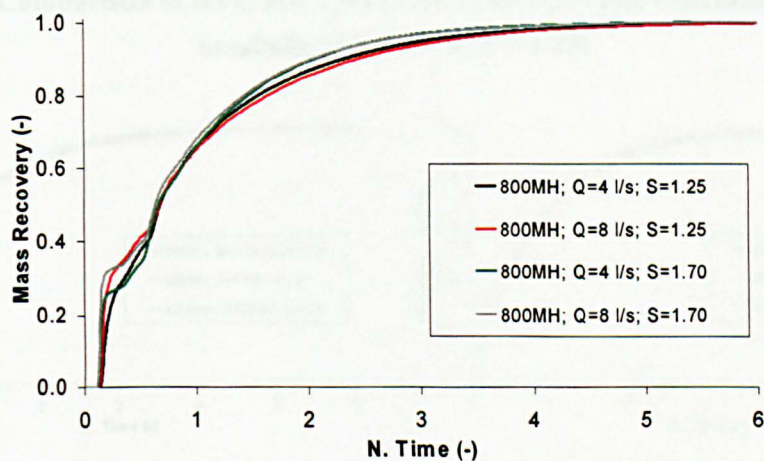
To examine the effects of scale on the mixing characteristics, the cumulative distributions for the three manholes are plotted against normalised time (with respect to the volumetric travel time) in Figure 7.16. The distributions selected for the comparisons are the numerical model results at similar Froude scaled discharges (~ 8 l/s). The distributions corresponding to the two surcharge ratios ($S = 1.25$ and $S = 1.70$) in the pre-threshold regime are considered in the present

study. The comparisons of the CRTDs show a high degree of similarity and suggest that a single curve may be used to characterise the mixing process in each of the pre-threshold surcharge ratio cases.

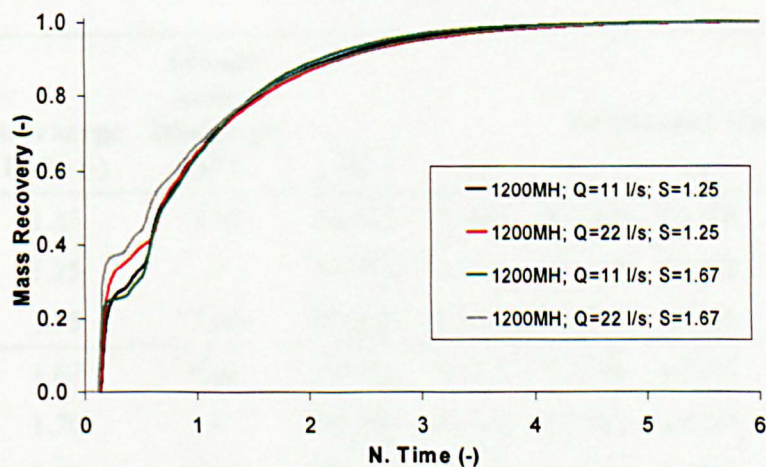
Table 7.4 summarises the normalised percentile travel times (with respect to volumetric travel time) for the two pre-threshold surcharge cases to highlight the difference between the normalised CRTDs. Normalised percentile travel time indicates the normalised time at which a certain percentage of the solute has travelled through the system. In this study, five percentile travel times, which are t_{10} , t_{30} , t_{50} , t_{70} and t_{90} , were determined from the normalised CRTDs. t_{10} , t_{50} , and t_{90} are the parameters usually used to determine the hydraulic performance of a system (Adamsson, 2004; Persson, 2000); t_{30} and t_{70} were chosen as they mark the sudden change in gradient in the CRTDs and are used in a new technique for modelling longitudinal dispersion introduced in Section 7.3.3.3. The results show that in each of the surcharge cases, the normalised percentile travel times for the three differently scaled manholes deviate about the mean within 10 % and the largest variation of the parameter is at t_{90} . It may be noticed that the parameter values appear to reduce as surcharge ratio increases. This may indicate that for very precise description of the mixing characteristics in pre-threshold requires separate mixing curves for different surcharge conditions, though the variations between the distributions within the same regime are indeed small.



(a) – Small scale manhole



(b) – Prototype manhole



(c) – Large scale manhole

Figure 7.14 – Comparisons of the pre-threshold CRTDs for the three manholes

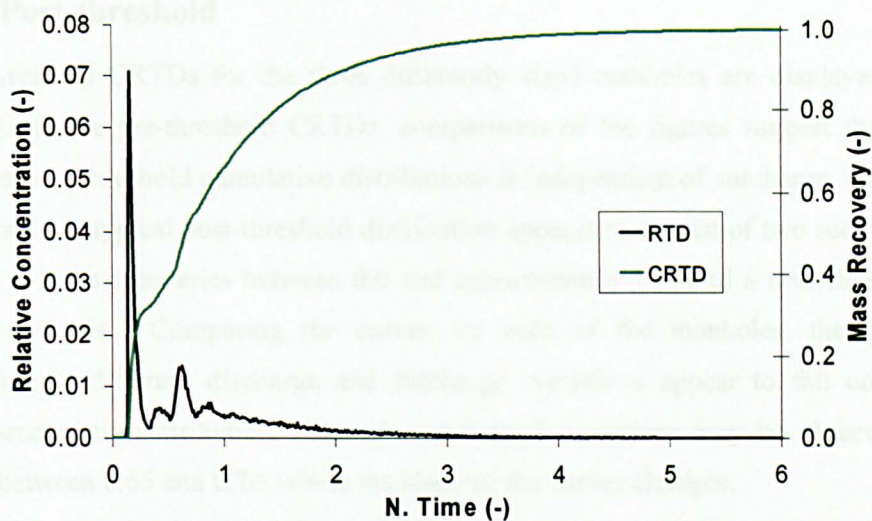
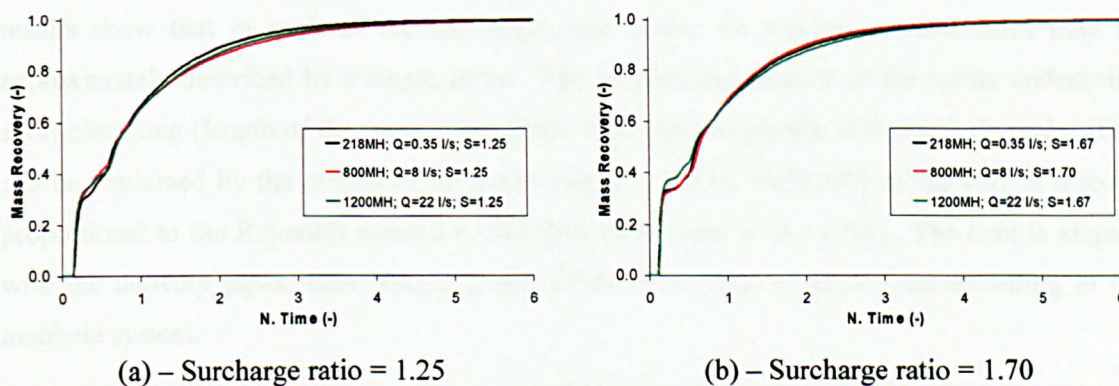


Figure 7.15 – Comparison of RTD and CRTD for a pre-threshold distribution (Small scale manhole; $Q = 0.35$ l/s; $S = 1.25$)



(a) – Surcharge ratio = 1.25

(b) – Surcharge ratio = 1.70

Figure 7.16 – Effects of scale on the pre-threshold CRTDs

Manhole Diameter (mm)	Surcharge Ratio (-)	Froude Scaled Discharge (l/s)	Re	Normalised Time (-)				
				t_{10}	t_{30}	t_{50}	t_{70}	t_{90}
218	1.25	9.06	16,053	0.1602	0.2590	0.6558	1.1168	2.1123
800	1.25	8	99,784	0.1536	0.2333	0.6753	1.1680	2.4290
1,200	1.25	7.98	182,937	0.1535	0.2233	0.6811	1.1621	2.2965
218	1.67	9.06	16,053	0.1247	0.1596	0.6055	1.0739	2.1121
800	1.70	8	99,784	0.1253	0.1742	0.6367	1.0602	2.0247
1,200	1.67	7.98	182,937	0.1267	0.1595	0.5792	1.1041	2.2709

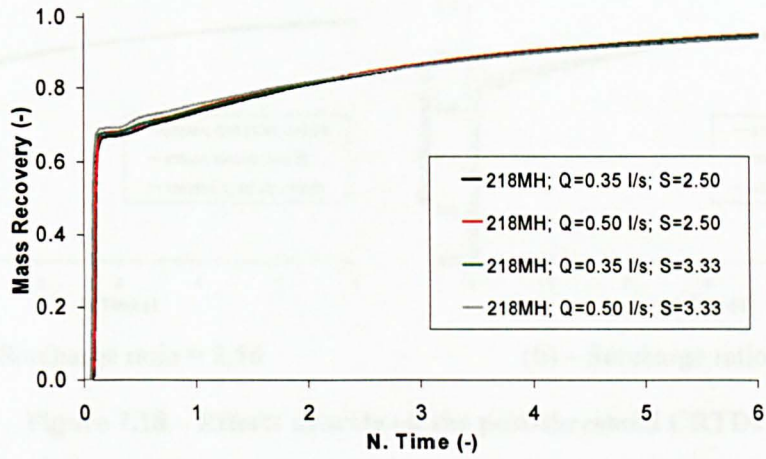
Table 7.4 – Summary of the normalised percentile travel time for the two pre-threshold surcharge studies

7.3.3.2 Post-threshold

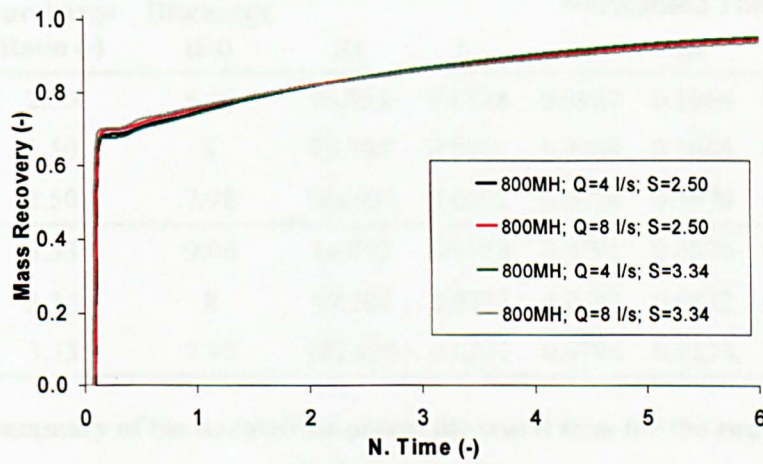
The post-threshold CRTDs for the three differently sized manholes are displayed in Figure 7.17a-c. As in the pre-threshold CRTDs, comparisons of the figures suggest that the basic shape of the post-threshold cumulative distributions is independent of surcharge, discharge and manhole scale. A typical post-threshold distribution appears to consist of two sections: a steep rising limb at mass recoveries between 0.0 and approximately 0.7; and a near-linear tail from this point onwards. Comparing the curves for each of the manholes, the distributions corresponding to different discharge and surcharge conditions appear to fall onto a single mixing characteristic distribution, although some small variations may be observed at mass recoveries between 0.65 and 0.70, where the slope of the curves changes.

Figure 7.18 shows the scale effects on the post-threshold CRTDs. Similar to the pre-threshold study, consideration of the distributions for the comparisons is given to the model results at similar Froude scaled discharges (~ 8 l/s) and two surcharge ratios ($S = 2.50$ and $S = 3.33$). The results show that in each of the surcharge ratio cases, the mixing characteristics may be approximately described by a single curve. The proportional amount of the solute undergoing short-circuiting (length of the steep rising limb) increases marginally with manhole scale. This can be explained by the effects of Reynolds number, in that the length of the core is directly proportional to the Reynolds number of the flow (Albertson *et al.*, 1950). The core is aligned with the delivery pipes; thus, longer length of the core leads to more short-circuiting in the manhole system.

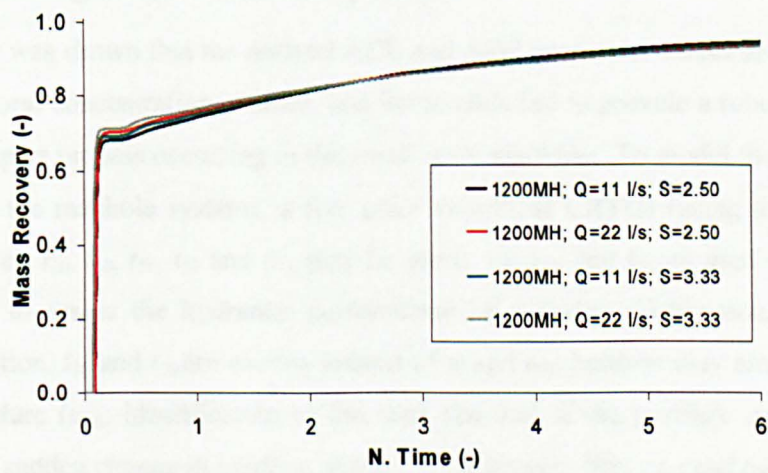
As in the pre-threshold study, the five normalised percentile travel times were extracted from the post-threshold CRTDs and are tabulated in Table 7.5 to highlight the effects of scale. Comparisons of the parameter values for each surcharge ratio suggest that there are small variations (approximately 5 % about the mean) of the parameter values between the three manhole model results. This is with the exception of t_{70} where significant variations among the three model results can be observed. The large variations of the t_{70} value are stemmed from the fact that t_{70} is too close to the point at which the sudden change in gradient in the CRTDs occurs and that the numerical models obtain different points (mass recoveries) for the change. Comparing the parameter values between the two surcharge ratio models, higher parameter values, except t_{90} , are obtained for the lower surcharge ratio models. This indicates that separate characteristic curves may be required for highly precise description of the CRTDs at different surcharge conditions. It was intended to develop scaling laws for the pre- and post-threshold CRTDs to account for the effects of scale on the parameter values. However, the work proved unsuccessful as the Reynolds number effects are different at different percentile travel times. For example, in Table 7.5, t_{30} increases with Reynolds number, while the opposite is true for t_{70} .



(a) – Small scale manhole



(b) – Prototype manhole



(c) - Large scale manhole

Figure 7.17 – Comparisons of the post-threshold CRTDs for the three manholes

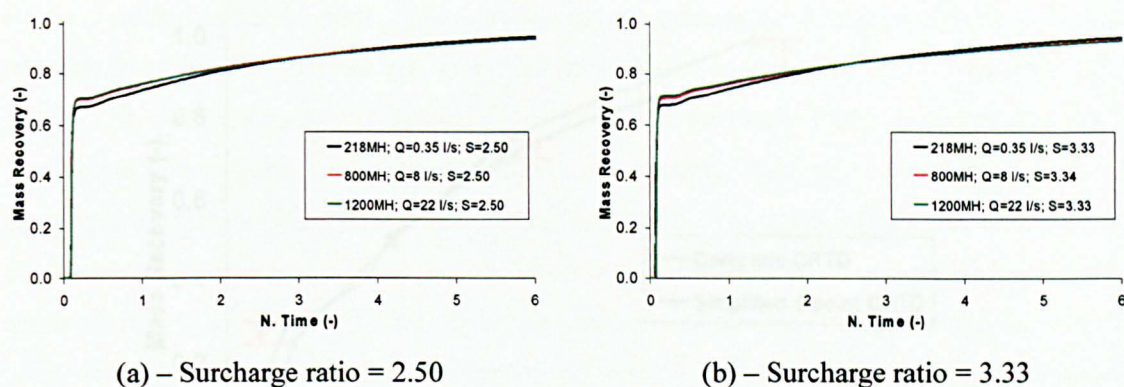


Figure 7.18 – Effects of scale on the post-threshold CRTDs

Manhole Diameter (mm)	Surcharge Ratio (-)	Froude Scaled Discharge (l/s)	Re	Normalised Time (-)				
				t_{10}	t_{30}	t_{50}	t_{70}	t_{90}
218	2.50	9.06	16,053	0.0878	0.0967	0.1069	0.5955	3.9716
800	2.50	8	99,784	0.0894	0.0969	0.1066	0.3347	4.0351
1,200	2.50	7.98	182,937	0.0902	0.0974	0.1070	0.1861	4.1864
218	3.33	9.06	16,053	0.0718	0.0791	0.0874	0.4816	3.9756
800	3.34	8	99,784	0.0732	0.0793	0.0872	0.1547	4.3604
1,200	3.33	7.98	182,937	0.0737	0.0796	0.0873	0.1248	4.3488

Table 7.5 – Summary of the normalised percentile travel time for the two post-threshold surcharge studies

7.3.3.3 Modelling Longitudinal Dispersion

In Chapter 4, it was shown that the derived ADE and ADZ parameter values are sensitive to the upstream temporal concentration profiles, and the models fail to provide a robust description of the solute transport process occurring in the small scale manhole. To model the solute transport process within the manhole systems, a five point simplified CRTDs (using the CRTD results presented above), t_{10} , t_{30} , t_{50} , t_{70} and t_{90} , may be used. t_{10} , t_{50} , and t_{90} are used because they are routinely used to assess the hydraulic performance of a system (Adamsson, 2004; Persson, 2000). In addition, t_{10} and t_{90} are chosen instead of t_0 and t_{100} because they are less sensitive to analysis procedure (e.g. identification of the start and end of the profile). t_{30} and t_{70} are the points where a sudden change in gradient in the CRTD occurs. Since t_{10} and t_{90} are the new start and end points of the profile, the simplified CRTD is redistributed between t_{10} and t_{90} to obtain mass balance (Figure 7.19). Note that this modelling methodology has been presented in Stovin *et al.* (2007).

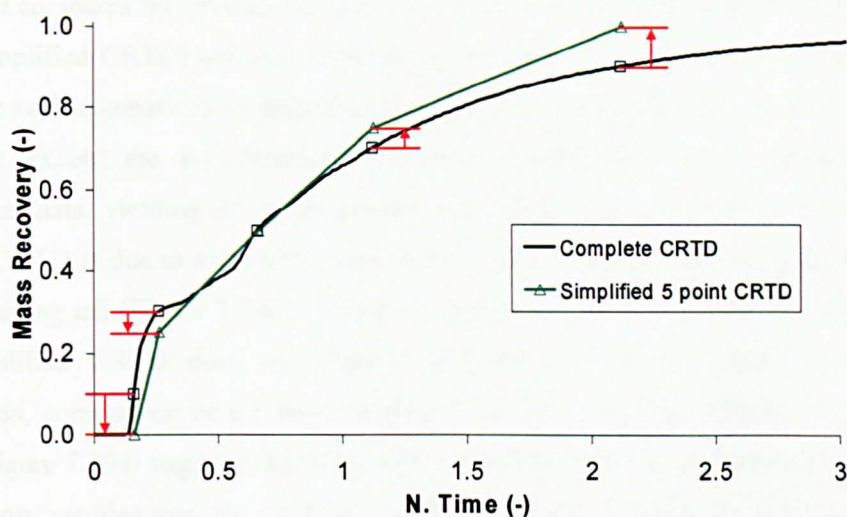


Figure 7.19 – Derivation of simplified 5 point CRTD

A preliminary study has been undertaken to apply the simplified CRTD approach to modelling longitudinal dispersion in the small scale and prototype manholes. These two manholes were considered because the predictions can be verified against laboratory measurements. In the study, it was assumed that the solute transport process for this type of manhole (manhole ID to pipe ID ratio) could be generalised by just two normalised CRTDs, one for each of the two identified hydraulic regimes. This assumption was made based on the findings of the above study that the effects of discharge, surcharge and manhole scale on CRTDs may be accounted for by temporal normalisation. A characteristic mixing curve for each of the hydraulic regimes was obtained by averaging the results of different surcharge ratios, discharges and manhole scales corresponding to the same hydraulic condition (Table 7.4 and Table 7.5). Note that the results corresponding to the surcharge ratio of 2.05 were not included in the derivation of the two mixing curves.

To determine a specific CRTD for a particular hydraulic condition (surcharge and discharge) and manhole scale, the five normalised percentile travel times (Table 7.6) were multiplied by the volumetric travel time. The CRTD was then converted into a RTD which can be used to generate a downstream response to any upstream input by means of superposition.

The simplified CRTD approach was studied using four different sets of laboratory tracer data, which are one pre- and post-threshold conditions for the small scale manhole and the prototype model. To highlight the findings of the study in Chapter 4 that the laboratory derived ADE and ADZ parameters for the surcharged manholes (small scale and prototype manholes) are not scalable, ADE and ADZ predictions were also made for these four sets of profiles but using the model parameters derived from the other scale manhole. These model parameters were scaled using the scaling methodologies developed in Section 4.3.3.1.

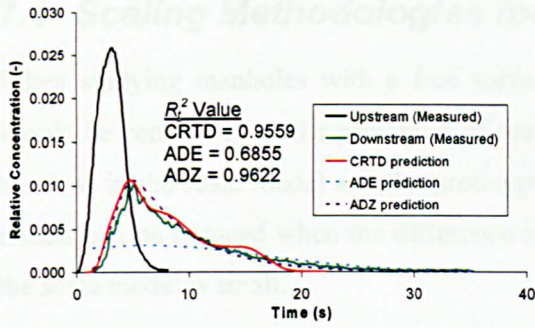
Figure 7.20 compares the predictions made using the three modelling approaches (ADE, ADZ and the simplified CRTD) and the measured tracer data. A goodness of fit parameter, R_r^2 , is provided in each comparison to determine the quality of the predictions. In general, the CRTD predictions, except the post-threshold prototype results, show good agreement with the experimental data, yielding R_r^2 values greater than 0.90. The poorer fit in the post-threshold prototype CRTD is due to a delayed rising limb; a slightly suppressed and delayed peak; and a deviated trailing tail (Figure 7.20d). These deviations may be attributed to the fact that the five point simplified CRTD does not exactly describe the mixing process in the manhole. Nevertheless, comparison of the three predictions (ADE, ADZ and CRTD) to the laboratory profiles (Figure 7.20d) suggests that the CRTD prediction provides much closer agreement with the laboratory profiles than the ADE and ADZ predictions. In fact, the CRTD approach also appears to be superior to the ADE and ADZ models (with scaled parameters) in the other three cases (Figure 7.20a-c). There may be exception in Figure 7.20a that the ADZ prediction is marginally better than the CRTD prediction. However, both predictions are, indeed, very good. In general, the ADE and ADZ routed profiles have poor fits to the recorded data, with R_r^2 values smaller than 0.81.

It is important to note that the preliminary analysis is intended to highlight the feasibility to use simplified CRTDs for modelling longitudinal dispersion in manholes. There is clearly scope for sensitivity analysis to select the number of points and refine the selection of points adopted to define a simplified CRTD; or for a more precise description of the mixing process, the full CRTD should be used. However, further development of the CRTD modelling approach is beyond the scope of this research.

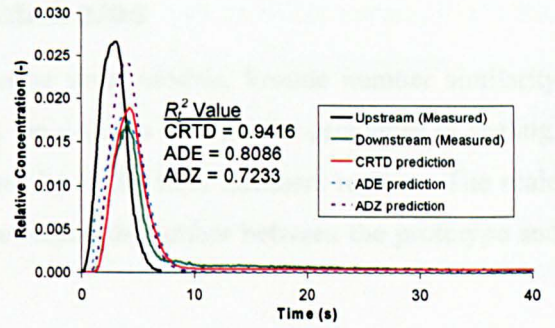
It is suggested that two curves, together with a prediction of threshold surcharge depth (Figure 7.6, also see Section 7.3.1.1.1), would provide a complete scale independent model of this one manhole configuration's solute transport characteristics.

Hydraulic Regime	Normalised Time				
	t_0	t_{25}	t_{50}	t_{75}	t_{100}
Pre-threshold	0.1407	0.2015	0.6389	1.1142	2.2076
Post-threshold	0.0810	0.0882	0.0971	0.3129	4.1463

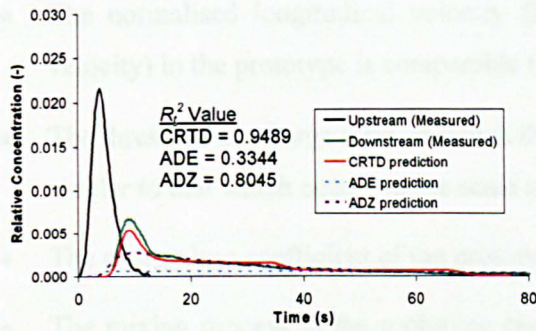
Table 7.6 –The two simplified CRTDs for manholes with a manhole ID to pipe ID ratio of 9.08



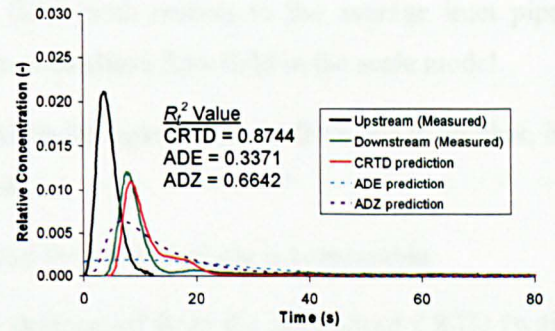
(a) – Small scale manhole; $Q = 0.35$ l/s;
 $S = 1.25$



(b) – Small scale manhole; $Q = 0.35$ l/s;
 $S = 3.33$



(c) – Prototype manhole; $Q = 4$ l/s; $S = 1.36$



(d) – Prototype manhole; $Q = 4$ l/s; $S = 3.41$

Figure 7.20 – Comparisons of the measured profiles and the predicted profiles made by the ADE, ADZ and the simplified CRTD approaches

7.4 Scaling Methodologies for Manholes

When studying manholes with a free surface using scale models, Froude number similarity should be considered as the principles of scaling. In order to validate the principles of scaling, the flow in the scale model and the prototype must be in the fully turbulent regime. The scale effects can be reduced when the difference in the Reynolds number between the prototype and the scale model is small.

To obtain the information of the hydraulic and solute transport processes in the prototype manhole from a Froude scaled manhole model, the following principles can be used:

- The normalised longitudinal velocity flow field (with respect to the average inlet pipe velocity) in the prototype is comparable to the normalised flow field in the scale model.
- The threshold surcharge ratio, at which the hydraulic regime changes from one to another, is similar to that which occurs in the scale model.
- The energy loss coefficient of the prototype and the scale manhole is comparable.
- The mixing process in the prototype can be determined from the normalised CRTD (with respect to the volumetric travel time of the scale model) for the scale model.

7.5 Conclusion

Three differently sized manhole models have been generated using the CFD approach for the investigation of scale effects on flow field, energy loss and solute transport processes. Generation of the numerical models was based on the standard modelling protocol for manhole simulations developed in Chapter 6.

The effects of surcharge, discharge and geometrical scale for manholes on the flow field were studied. The study shows that the degree of jet deviation in the flow field under the pre-threshold conditions is a function of surcharge conditions; a lower degree of deviation is observed with increasing surcharge ratio and the jet deviation disappears when the surcharge ratio rises above the threshold level. Post-threshold, the general flow field appears to be independent of surcharge. In most of the cases, the numerical models predicted a hydraulic transition before/at the surcharge ratio of 2.05. Comparing this numerical prediction to the laboratory tracer results in Chapter 4 confirm that the models obtain a premature hydraulic transition. The effects of discharge and geometrical scale do not impose a significant impact on the flow structure. However, the length of the jet seems to increase slightly with Reynolds number.

A new modelling procedure was adopted to collect head loss data from the numerical models. Comparisons of the head loss data to the laboratory data (the small scale model) suggest that the predicted results are consistently higher than the measured data and this could be related to the over-prediction of turbulence by the RNG $k-\varepsilon$ turbulence model. The energy loss coefficients for the three manhole models show no evidence of the scale effects. This implies that the laboratory derived energy loss coefficients in previous manhole research should be applicable to full scale structures in urban drainage systems.

Cumulative retention time distributions (CRTDs) were used to study the effects of scale on the solute transport characteristics in the three manholes. The study suggests that normalised the time axis of the CRTDs with respect to the volumetric travel time may account for the effects of surcharge, discharge and geometrical scale. Two normalised CRTDs may be used to approximate the solute transport process in this particular type of manhole (manhole ID to pipe ID ratio). Careful examination of the CRTDs for the three manhole models suggests that the effects of scale exist but are not significant.

A simplified CRTD model was proposed to model longitudinal dispersion in this type of manhole. Two characteristic mixing curves, one for pre-threshold and one for post-threshold, were determined from the solute transport results presented in Section 7.3.3.1 and Section 7.3.3.2. An assessment of the modelling approach was made by comparing the predicted profiles to the laboratory tracer data. Preliminary results suggest that the predictions made by the simplified CRTD model provide good agreement with the laboratory measurements. The study also suggests that the simplified CRTD approach is superior to the ADE and ADZ model (with scaled model parameters). Two curves in associated with a prediction of threshold surcharge depth, may provide a complete scale independent model of this manhole configuration's (manhole ID to pipe ID ratio) solute transport characteristics.

Methodologies for scaling the hydraulic and solute transport characteristics in surcharge manholes have been developed through the study of the effects of scale.

8 Conclusions and Suggestions for Further Work

8.1 Conclusions of the Thesis

The aim of the study is to derive generic scaling methodologies to describe the impact of physical scale on the hydraulic and mixing processes occurring within surcharged manholes. A scale model of an 800 mm ID manhole (the prototype) studied by Guymer *et al.* (2005) was constructed in the laboratory. Tracer experiments were conducted in the scale model and the results were compared to the results of the prototype models. The study identified a threshold surcharge ratio in the scale model, comparable to that of the prototype, separating two hydraulic regimes, pre- and post-threshold. However, the laboratory-derived ADE and ADZ model parameters for manholes were not found to be scalable because they were found to be sensitive to the shape of the upstream concentration distribution. This finding also implies that the ADE and ADZ models are not appropriate tools to model solute transport within surcharged manholes or other urban drainage structures.

A more robust approach, based on the cumulative retention time distribution (CRTD), to describing the mixing process in surcharged manholes is proposed. Comparisons of the CRTDs show that two basic forms of the curve, one for each hydraulic regime, exist. The form of the curve in each case is independent of surcharge, discharge or physical scale. The two curves, together with a prediction of threshold surcharge depth, provide a complete scale independent model of this one manhole configuration's solute transport characteristics.

Rigorous parametric studies of CFD model set-up parameters and detailed model validation were conducted on the CFD scale manhole model (218 mm ID manhole). The model validation was achieved using a new set of flow data collected in the laboratory. The flow visualisation data, based on five planes (three vertical and two horizontal) of LIF recordings and PIV measurements, is novel in manhole research, and it provides new insights into the internal hydraulic and solute transport characteristics of surcharged manholes. One outcome of the CFD model validation study is a standard modelling protocol for manhole simulations. This standard modelling protocol is applicable to the simulation of manholes with different configurations, such as step manholes, manholes with pipe direction change, or different benching options.

Methodologies for scaling the hydraulic and solute transport characteristics within surcharged manholes have been proposed. The principles of scaling (Froudian scaling) have been shown to be valid, with negligible scale effects on the flow field, energy loss coefficient or mixing process over a practical range of Reynolds numbers. The threshold surcharge depth scales as a

geometric variable. The energy loss coefficient is a dimensionless parameter which has been shown to be scale independent, meaning that laboratory-derived energy loss coefficients from previous manhole research are applicable to full scale structures. For mixing characteristics, the normalised CRTDs provide scale independent models of the system's mixing characteristics.

Detailed conclusions have been presented at the end of each chapter. The following section focuses on the key outcomes of the thesis. Suggestions for further work are outlined in Section 8.3.

8.2 Key Outcomes of the Thesis

8.2.1 Laboratory-Based Analysis

8.2.1.1 Scale Manhole Model

- A 1:3.67 physical scale model of an 800 mm ID manhole (the prototype) has been constructed and experiments have been undertaken to examine its hydraulic and solute transport characteristics. The 800 mm ID manhole was chosen because Guymer *et al.* (2005) identified a threshold surcharge level in this manhole at which the solute transport characteristics clearly indicated a sharp transition between pre- and post-threshold conditions. The solute transport process behaved differently under pre- and post-threshold conditions and this formed an interesting test for the physical scale model.
- Energy loss at this type of manhole (manhole ID to pipe ID ratio) has not been previously studied. Comparison of the energy loss results was made with the study of Arao and Kusuda (1999) and both sets of data clearly showed a sharp transition in the energy loss coefficient. However, the surcharge conditions at which the transition occurred differ between the two datasets. This was because the configuration (manhole ID to pipe ID ratio) of the two manholes is not identical.
- The advection dispersion equation (ADE) and aggregated dead zone (ADZ) models, in association with the optimisation procedure, were adopted to analyse the temporal concentration profiles collected for the scale manhole. The optimisation procedure for the ADZ model was slightly modified to improve the precision of the predictions. A threshold surcharge level is evident in the model parameter results and the threshold surcharge ratio is comparable to that of the prototype. However, there is an issue regarding the physical meaning of the derived model parameters, e.g. optimised predictions in some cases indicated a negative ADZ read time delay.

8.2.1.2 Examination of Scale Effects

- The impact of physical scale on the mixing process was analysed using two different techniques: the comparisons of the ADE and ADZ derived parameters and the cumulative temporal concentration profiles (CTCPs) between the two manhole models.
- The ADE and ADZ results for the scale manhole and the prototype models were non-dimensionalised using dimensional analysis to enable comparisons to be made. However, the comparisons reveal large discrepancies in the two experimental datasets. It is believed

that this was attributable to inconsistencies in the shape of the upstream distributions between the two datasets.

- A sensitivity study was performed to assess the sensitivity of the ADE and ADZ model coefficients to the shape of the upstream temporal concentration profile. The study highlights that the model parameters for the manhole are sensitive to the shape of the upstream profile, and that the results presented can only be strictly applicable in situations where the upstream profiles match those for which the parameters were originally derived. The explanation for the sensitivity is that the ADE and ADZ models fail to fully describe the solute transport process occurring in the manhole, leading to some degree of deviations of the predictions from the measured profiles ($R_r^2 < 1$). The sensitivity issue would disappear only when the solute transport process could be exactly described by the solute transport models ($R_r^2 = 1$). The finding of this sensitivity study suggests that the ADE and ADZ models are not appropriate for modelling solute transport in surcharged manholes and in other urban drainage structures.
- Cumulative temporal concentration profiles (CTCPs) were adopted as a tool to examine the effects of surcharge, discharge and geometrical scale in surcharged manholes. Two basic forms of CTCPs, one for each of the two hydraulic regimes are identified, and these are shown to be independent of surcharge, discharge and manhole scale. Pre-threshold, the shape of the curve is indicative of instantaneous mixing; post-threshold, the shape of the distribution shows that the flow regime comprises a short-circuiting flow, affecting approximately 65 % of the incoming flow, and a dead zone.
- The scale effects were studied using normalised CTCPs (with respect to the volumetric travel time). The results suggest that the temporal normalisation may account for the effects of discharge and surcharge. The normalised CTCPs for each manhole collapse onto a single curve for each of the two hydraulic regimes. Comparisons of the normalised curves of the two manholes also show similarity in terms of profile shape. This suggests that the solute transport characteristics of the surcharge manholes may be summarised by just two CTCPs, one for pre-threshold and one for post-threshold. However, the CTCPs for the two manhole models are not directly comparable because of the difference in the shape of the upstream distributions.

8.2.2 CFD-Based Analysis

8.2.2.1 Collection of Validation Data

- Flow visualisation experiments were carried out in the scale manhole model for the collection of flow field validation data. Two techniques were adopted in the study: laser induced fluorescence (LIF) and particle image velocimetry (PIV). The LIF technique provided qualitative visualisation of the flow structure and general interpretation of the solute mixing process throughout the manhole. Quantitative flow measurements were generated using the PIV measurement technique. In the study, five flow planes and two surcharged conditions were considered. The comprehensive picture of the flow field in surcharged manholes generated through these experiments is novel in manhole research.
- The PIV analysis provided velocity and turbulence information from the recorded images. Comparisons were undertaken to confirm the validity of the velocity measurements. However, the turbulence data was found to be unreliable, in that the time average turbulence results varied between repeat tests. The turbulence data was not used for CFD validation.
- Tracer data for the validation of the CFD solute transport predictions was collected in the dye tracing experiments.

8.2.2.2 CFD Model Validation

- A feasibility study and a detailed study of CFD manhole simulations were undertaken. In the feasibility study, the 800 mm ID manhole was modelled and two meshing techniques were developed for circular manholes. The models meshed with different techniques were assessed. Both model results indicate that a hydraulic transition occurs in the structure when the surcharge conditions change from one hydraulic regime to another. Comparisons of the simulated and measured traces were used to determine which mesh produced the better predictions.
- Four parametric tests (grid density, spatial discretisation scheme, turbulence model and solute transport model) were considered in the detailed study of CFD manhole simulations. The manhole modelled was the 218 mm ID manhole. A mesh density in the manhole models (average cell size ~ 2 mm) that provided a nearly grid independent solution was identified in the grid density study and adopted in the subsequent parametric tests. The best combination of the spatial discretisation schemes, in terms of numerical stability and accuracy, was established in the sensitivity study of spatial discretisation scheme. In general, the second order accurate schemes considered in this study produced highly

comparable results but with different convergence performance. *PRESTO* for pressure term and *QUICK* for other terms were recommended.

- Two turbulence models (RNG k - ϵ and RSM turbulence models) were investigated in the parametric test of turbulence model. Comparisons of the predicted results and the PIV evaluated data suggest that the predictions made by the two turbulence models are comparable and both simulation results show reasonable agreement with the experimental data. Careful examination of the two model results suggests that the RNG k - ϵ turbulence model is slightly superior to the RSM. In addition, the RNG model appeared to be more stable during calculations. Therefore, the RNG k - ϵ turbulence model was recommended.
- The parametric study of solute transport model investigated the particle tracking and species models. In general, the predictions made by the two models are highly comparable but the simulation time for the species model was considerably higher than the particle tracking model. For this reason, particle tracking was recommended. The particle tracking results were validated against the measured tracer profiles and the comparisons reveal good agreement between the computed and measured data.
- It is interesting to note that the CFD models provide insights into the flow field (e.g. through transverse view-planes, particle tracks) which add to and complement the explanatory information provided by laboratory-based visualisation techniques alone.
- A standard modelling protocol was developed using the conclusions of each of the parametric tests considered in the study. This is summarised in Section 6.3.7. The standard modelling protocol should be applicable to the simulation of manholes with different configurations, such as step manholes, manholes with pipe direction change or different benching options.

8.2.2.3 Examination of Scale Effects

- Three virtual versions of the same manhole at different scale were generated using the standard modelling protocol developed in the study. In each of the manholes, five surcharge conditions and two flowrates were studied, yielding thirty simulation cases in total. The effects of scale on the flow field, energy loss and solute transport characteristics were examined.
- The flow field results appear to be independent of physical scale, although the length of the jet increases slightly with Reynolds number. The flow field predictions also suggest that the hydraulic transition occurs at a lower surcharge ratio than expected. This is believed to be caused by the over-prediction of turbulence by the RNG k - ϵ turbulence model.

- No evidence of scale effects is observed in the energy loss results for the three differently sized manholes.
- The effects of scale on the solute transport characteristics were studied by comparing cumulative retention time distributions (CRTDs) for the three manhole models. The study suggests that normalised CRTDs with respect to the volumetric travel time may account for the effects of surcharge, discharge and geometrical scale. Two approximated curves, one for each of the hydraulic regimes, may be used to generalise the mixing characteristics in this type of manhole (manhole ID to pipe ID ratio). Scale effects are observed. However, the degree of the effects is small. The scale effects are caused by the effects of Reynolds number on the jet characteristics in the manhole. The Reynolds number effects on CRTD were found to be different at different percentile travel times, e.g. t_{30} and t_{70} . It was not possible to use a simple equation to generalise the effects of Reynolds number on CRTD.
- Scaling methodologies for the hydraulic and solute transport processes in surcharged manholes have been established based on the findings of the study and have been presented in Section 7.4.
- A simplified 5 point CRTD model was used to predict longitudinal dispersion in manholes. Using the simplified CRTD model in association with the two characteristic mixing curves developed for manholes with a manhole ID to pipe ID ratio of 9.03, a reasonable representation of the solute transport process was produced. The simplified CRTD predictions were then compared to the ADE and ADZ predictions made by scaled model parameters. The simplified CRTD approach shows superiority over the two other approaches. Further research is needed to verify the simplified 5 point CRTD model.

8.3 Suggestions for Further Work

A number of topics that could be considered for further investigation are outlined below:

- Due to limited availability of time, it was not possible to repeat the experimental tracer tests in the scale manhole model and prototype using either a pulse (real instantaneous injection) or step experiment (continuous injection) and study the effects of scale using a laboratory-based analysis. It would be beneficial to use the laboratory-based analysis to confirm the conclusion obtained from the CFD-based study of scale effects.
- Re-analysis of the two manhole laboratory traces using higher order solute transport models, such as the ADE transient storage model and the two or more cells ADZ models, to examine the effects of scale on their mixing parameters.

- The simplified CRTD model in association with the two derived mixing characteristics for this type of manhole may be used for solute transport predictions. However, further research should be performed to verify the selection of the normalised percentile travel times for describing the CRTDs and a wider range of surcharge ratios and discharges should be modelled to define a more representative characteristic mixing curve for the two hydraulic regimes.
- When more advanced computational resources becomes available, the manhole simulations should be repeated using two phase modelling to account for the effects of the free surface. The results could be used to assess the effects of the fixed lid assumption on the flow field and solute transport predictions. In additional, LES or a coupled LES/RANS modelling approach (Turnbull, 2003) should be considered.
- Steady state conditions were considered throughout the laboratory- and CFD-based studies. Further study should examine the unsteady flow effects on the hydraulic and solute transport characteristics in manhole structures.
- Determination of concentration within the manhole structure using the LIF technique could provide additional insights in the mixing characteristics. However, due to limited availability of the high speed camera, it was not possible to carry out a complete study for the ten test cases. Further work should consider repeating the LIF experiments for the ten test cases. The collected data would also provide validation data for the solute transport modelling using the species model. The suggested methods to improve the parallel dye concentration measurement technique should be considered.
- During the PIV study, only one set of PIV data was analysed for each of the ten studies. Further work should be conducted to analyse all the three repeat data for the determination of turbulence quantities.
- Use of CFD model to generate characteristic CRTDs for broader range of sewer ancillary structures (manholes, tanks etc)

References

- Abramovich, G.N. (1963). *The Theory of Turbulent Jets*. The Massachusetts Institute of Technology, USA.
- Adamsson, A., Stovin, V. and Bergdahl, L. (2003). 'Bed Shear Stress Boundary Condition for Storage Tank Sedimentation'. *Journal of Environmental Engineering*, Vol. 129, No. 7, pp. 651-658.
- Adamsson, A. (2004). *Three-Dimensional Simulation and Physical Modelling of Flows in Detention Tanks*. PhD Thesis, Chalmers University of Technology, Sweden.
- Adeniji-Fashola, A. and Chen, C.P. (1990). 'Modelling of Confined Turbulent Fluid-Particle Flows Using Eulerian and Lagrangian Schemes'. *International Journal of Heat and Mass Transfer*, Vol. 33, No. 4, pp. 691-701.
- Adrian, R.J. (1986). 'Multipoint Optical Measurements of Simultaneous Vectors in Unsteady Flow – A Review'. *International Journal of Heat and Fluid Flow*, Vol. 7, pp. 127-145.
- Ahyerre, M., Chebbo, G., Tassin, B. and Gaume, E. (1998). 'Storm Water Quality Modelling, An Ambitious Objective?'. *Water and Science Technology*, Vol. 37, No. 1, pp.205-213.
- Albertson, M.L., Dai, Y.B., Jensen, R.A. and Rouse, H. (1950). 'Diffusion of Submerged Jet'. *ASCE Transactions*, Vol. 115, pp. 639-697.
- Arao, S. and Kusuda, T. (1999). 'Effects of Pipe Bending Angle on Energy Losses at Two-Way Circular Drop Manholes'. *Proceedings of the 8th International Conference on Urban Storm Drainage*, Sydney, Australia, pp. 2163-2168.
- Arcoumanis, C., McGuirk, J.J. and Palma, J.M.L.M. (1990). 'On the Use of Fluorescent Dyes for Concentration Measurements in Water Flows'. *Experiments in Fluids*, Vol. 10, pp. 177-180.
- Archer, B., Bettess, F. and Colyer, P.J. (1978). 'Head Losses and Air Entrainment at Surcharged Manholes', *Report Number IT 185*, HR Wallingford, UK.
- Armfield (1990). *Instruction Manual Water Level Follower*, UK.

-
- ASCE Manuals and Reports on Engineering Practice No. 97 (2000). *Hydraulic Modelling: Concepts and Practice*, ASCE, USA..
- Asztely, M. and Lyngfelt, S. (1996). 'Three-Dimensional Numerical Modelling of Energy Losses in a Manhole'. *Proceedings of the 7th International Conference on Urban Storm Drainage*, Hannover, Germany, pp. 647-652.
- Awbi, H. (2003). *Ventilation of Buildings*, Spon Press, London, UK.
- Barth, T.J. and Jespersen, D. (1989). 'The Design and Appliation of Upwind Schemes on Unstructured Meshes'. *Technical Report AIAA-89-0366*, AIAA 27th Aerospace Sciences Meeting, Reno, Nevada.
- Baxter, L.L. and Smith P.J. (1993). 'Turbulent Dispersion of Particles: The STP Model'. *Energy & Fuels*, Vol. 7, pp. 852-859.
- Beer T. and Young P.C. (1983). 'Longitudinal Dispersion in Natural Streams '. *Journal of Environmental Engineering*, Vol. 109, No. 5, pp. 1049-1067.
- Bo Pedersen, F. and Mark, O. (1990). 'Head Losses in Storm Sewer Manholes, Submerged Jet Theory'. *Journal of Hydraulic Division ASCE*, Vol. 116, No. 11, pp. 1317-1328.
- Boxall, J.B. (2000). *Dispersion of Solutes in Sinuous Open Channel Flows*. PhD thesis, The University of Sheffield, UK.
- Boxall, J.B., Shepherd W. Guymer I. and Fox K. (2003). 'Changes in Water Quality Parameters due to In-sewer Processes'. *Water Science and Technology*, Vol. 47, No. 7-8, pp. 343-350.
- BS 5911. *Pre-cast Concrete Pipes and Fittings for Drainage and Sewerage. Part 200: 1989 Unreinforced and Reinforced Manholes and Soakaways of Circular Cross-Section*.
- BS 8301:1985. *Code of Practice For Building Drainage*.
- BS EN 476:1997. *General Requirements for Component Used in Discharge Pipes, Drains and Sewers for Gravity Systems*.
- BS EN 752-3:1997. *Drain and Sewer Systems Outside Building. Part 3; Planning*.
- BS EN 24006:1993. *Measurement of Fluid Flow in Closed Conduits. Vocabulary and Symbols*.
- BS EN 60825-1:1994. *Safety of Laser Products. Equipment Classification, Requirements and User's Guide*.
-

-
- BS EN ISO 5167-1:2003. *Measurement of Fluid Flow by Means of Pressure Differential Devices Inserted in Circular Cross-Section Conduits Running Full. General Principles and Requirements.*
- Butler, D. and Davies, J.W. (2000). *Urban Drainage*, 2nd edition, E & FN Spon, London, UK.
- Buxton, A.P. (2003). *The Development of a Computational Methodology for the Prediction of the Sediment Retention Performance of Invert Traps in Combined Sewer Systems.* PhD thesis, The University of Sheffield, UK
- Chadwick, A. and Morfett, J. (1999). *Hydraulics in Civil and Environmental Engineering*, 3rd edition, E & FN Spon, London, UK.
- Chen, D. and Jirka, G.H. (1999). 'LIF Study of Plane Jet Bounded in Shallow Water Layer'. *Journal of Hydraulic Engineering*, Vol. 125, No.8, pp. 817-826.
- Coherent. *Operator's Manual: The Coherent Innova 70 Series Ion Laser.* Coherent Inc., USA.
- Crimaldi, J.P. and Koseff, J.R. (2001). 'High-resolution Measurements of the Spatial and Temporal Scalar Structure of a Turbulent Plume'. *Experiments in Fluids*, Vol. 31, pp. 90-102.
- Daly, B.J. and Harlow, F.H. (1970). 'Transport Equations of Turbulence'. *Physics of Fluids*, Vol. 13, pp. 2634-2649.
- Danckwerts, P.V (1958). 'Continuous Flow Systems'. *Chemical Engineering Science*, Vol. 2, No. 1, pp. 1-13.
- Danish Hydraulic Institute (DHI) (2000). *MOUSETRAP User Manual, Version 2000*, DHI.
- Danish Hydraulic Institute (DHI) (2008). *MOUSE Technical Reference Manual, Version 2008*, DHI.
- Day, T.J. (1975). 'Longitudinal Dispersion in Natural Streams'. *Water Resources Research*, Vol. 11, No. 6, pp. 909-918.
- De Martino, F., Gissoni, C. and Hager, W.H. (2002). 'Drop in Combined Sewer Manhole for Supercritical Flow'. *Journal of Irrigation and Drainage Engineering*, Vol. 128, No. 6, pp. 397-400.
- Del Giudice, G. and Hager, W.H. (2001). 'Supercritical Flow in 45° Junction Manhole'. *Journal of Irrigation and Drainage Engineering*, Vol. 127, No.2, pp. 100-108.
-

-
- Dennis, P.M. (2000). *Longitudinal Dispersion due to Surcharged Manholes*. PhD thesis, The University of Sheffield, UK.
- Douglas, J.F., Gasiorek, J.M. and Swaffield, J.A. (1985). *Fluid Mechanics*, Second Edition, Longman Scientific and Technical, UK.
- Dutton, R.J. (2004). *Modelling Transient Storage Processes*. PhD thesis, The University of Sheffield, UK.
- Egarr D.A., Faram M. G., Phipps D.A. and Syred N. (2005). 'Computational Fluid Dynamic Prediction of the Residence Time Distribution of a Prototype Hydrodynamic Vortex Separator Operating with a Base Flow Component'. *Journal of Process Mechanical Engineering*, Vol. 219, Part E, pp. 53-67.
- Elder, J.W. (1959). 'The Dispersion of Marked Fluid in Turbulent Shear Flow'. *Journal of Fluid Mechanics*, Vol. 5, pp. 544-560.
- Fischer, H.B. (1966). 'A Note on the One-Dimensional Dispersion Model', *Air and Water Pollution: An International Journal*, Vol. 10, pp. 443-452.
- Fluent (2003). *Modelling Guide*, Fluent, Europe, Sheffield, UK.
- Fluent (2005). *Fluent 6 User's Guide*, Fluent Europe, Sheffield, UK.
- Fogler, H.G. (1992). *Elements of Chemical Reaction Engineering*, Prentice-Hall, New Jersey, USA.
- Gargano, R. and Hager W.H. (2002). 'Supercritical Flow across Sewer Manholes'. *Journal of Hydraulic Engineering*, Vol. 128, No. 11, pp. 1014-1017.
- Giudice G.D. and Hager W.H. (2001). 'Supercritical Flow in 45° Junction Manhole'. *Journal of Irrigation and Drainage Engineering*, Vol. 127, No. 2, pp. 100-108.
- Goldman, I.B. and Marchello, J.M. (1969). 'Turbulent Schmidt Numbers'. *International Journal of Heat and Mass Transfer*, Vol. 12, pp. 797-802.
- Goldstein, S. (1938). *Modern Developments in Fluid Mechanics*, Oxford: Clarendon Press.
- Gosman, A.D. and Ioannides, E. (1981). 'Aspects of Computer Simulation of Liquid-Fuelled Combustors'. *AIAA 19th Aerospace Sciences Meeting*, 1981, St. Louis, Missouri.
-

-
- Gray, C., Greated, C.A., McCluskey, D.R. and Easson, W.J. (1991). 'An Analysis of the Scanning Beam PIV Illumination System'. *Measurement Science and Technology*, Vol. 2, No. 8, pp. 717-724.
- Green, H.M., Beven, K.J., Buckley, K. and Young, P.C. (1994). 'Pollution Prediction with Uncertainty'. *Mixing and Transport in the Environment*, edited by Beven, K. J., Chatwin, P. and Millbank, J., pp. 113-137, John Wiley, New York, USA.
- Grimm, J.P. (2004). *An Evaluation of Alternative Methodologies for the Numerical Simulation of Solute Transport*. PhD thesis, The University of Sheffield, UK.
- Guymer, I. and O'Brien, R. (1995). 'The Effects of Surcharged Manholes on the Travel Time and Dispersion of Solutes in Sewer Systems'. *Water Science and Technology*, Vol. 31, No. 7, pp. 51-59.
- Guymer, I. and Harry, A. (1996). 'Use of Laser Induced Fluorescence and Video Imaging Techniques in an Investigation of Mixing across the Dead Zone/Flow Zone Boundary'. *IMechE.*, pp. 419-428.
- Guymer, I., O'Brien, R., and Harrison C. (1996). 'Representation of Solute Transport and Mixing within a Surcharged Benched Manhole Using an Aggregated Dead Zone (ADZ) Technique'. *Water Science and Technology*, Vol. 34, No. 3-4, pp. 95-101.
- Guymer, I., O'Brien, R., Mark, O. and Dennis, P.M. (1998). 'Investigation of Fine Sediment Mixing within Free-flowing and Surcharged Manholes'. *Water Science and Technology*, Vol. 37, No. 1, pp. 215-222.
- Guymer, I. and O'Brien, R. (2000). 'Longitudinal Dispersion Due To Surcharged Manhole'. *Journal of Hydraulic Engineering, A.S.C.E.*, Vol. 126, No. 2, pp. 137-149.
- Guymer, I., Dennis, P. M., O'Brien, R. and Saiyudthong, C. (2005). 'Diameter and Surge Effects on Solute Transport across Surge Manholes'. *Journal of Hydraulic Engineering*, Vol. 131, No. 4, pp. 312-321.
- Guymer, I., and Dutton, R. (2007). 'Application of Transient Storage modelling to Solute Transport Across a Surcharged Manhole'. *Water Science and Technology*, Vol. 55, No. 4, pp. 65-73.
- Hammer, M.J. (2003). *Water and Wastewater Technology*. 5th edition, Prentice-Hall, New Jersey, USA.
-

-
- Hanjalic, K. (1970). *Two-Dimensional Asymmetric Turbulent Flow in Ducts*, PhD thesis, University of London, UK.
- Hanjalic, K. and Jakirlic, S. (2002). 'Second-Moment Turbulence Closure Modelling'. *Closure Strategies for Turbulent and Transitional Flows*, Launder, B and Sandham, N., Cambridge University Press, UK.
- Hart, D.R. (1995). 'Parameter-estimation and Stochastic Interpretation of the Transient Storage Model for Solute Transport in Streams'. *Water Resources Research*, Vol. 31, No. 2, pp. 323-328.
- Harwood, R. (1999). *Modelling Combined Sewer Overflow Chambers using Computational Fluid Dynamics*. PhD Thesis, The University of Sheffield, UK.
- Herath, S.K., Jayasuriya, L.N.N. and Hussey, C.J. (1999). 'Modelling Wastewater Quality in Sewerage Systems'. *Proceedings of the 8th International Conference on Urban Storm Drainage*, Sydney, Australia, The Australian Institution of Engineers, pp. 179-186.
- Hinze, O. (1959). *Turbulence*, McGraw Hill, New York, USA.
- Hinze, O. (1975). *Turbulence - Second Edition*, McGraw Hill, New York, USA.
- Howarth, D.A., and Saul, A. J. (1984). 'Energy Loss Coefficients at Manholes'. *Proceedings of the 3rd International Conference on Urban Storm Drainage*, Goteberg, Sweden, Vol. 1, pp. 127-136.
- Howarth, D.A. (1985). *The Hydraulic Performance of Scale Model Storm Sewer Junctions*, PhD Thesis, University of Manchester, UK.
- Jain, S. (1995). *Three-Dimensional Simulation of Turbulent Particle Dispersion*. PhD thesis, University of Utah, USA.
- Johnston, A.J. and Volker, R.E. (1990). 'Head Losses at Junction Boxes'. *Journal of Hydraulic Engineering*, Vol. 116, No. 3, pp. 326-341.
- Kilpatrick, F. A. & Wilson, J. F. (1982). *Measurement of Time of Travel in Streams by Dye Tracing*, Techniques of Water-Resources Investigations of the United States Geological Survey, USA.
-

- Kim, B.K., Jackman, A.P. and Triska, F.J. (1992). 'Modelling Biotic Uptake by Periphyton and Transient hyporheic Storage of Nitrate in a Natural Stream'. *Water Resources Research.*, Vol. 28, No. 10, pp. 2743-2752.
- Kim, S.E. and Choudhury, D. (1995). 'A Near Wall Treatment Using Wall Functions Sensitised to Pressure Gradient'. *ASME FED, Separated and Complex Flows*, Vol. 217, pp. 273-280.
- Kluck, J. (1997). *The Design of Optimally Function Storm Water Settling Tanks*, PhD Thesis, DUT, Delft, The Netherlands.
- Koeltzsch, K. (2000). 'The Height Dependence of the Turbulent Schmidt Number within the Boundary Layer'. *Atmospheric Environment*, Vol. 34, pp. 1147-1151.
- Kolmogorov, A.N. (1991). 'Dissipation of Energy in the Locally Isotropic Turbulence'. *Proceedings of the Royal Society of London, Series A: Mathematical and Physical Sciences*, Vol. 434, pp. 15-17.
- Koochesfahani, M.M. and Dimotakis, P.E. (1985). 'Laser-Induced Fluorescence Measurements of Mixed Fluid Concentration in a Liquid Plane Shear Layer'. *American Institute of Aeronautics and Astronautics Journal*, Vol. 23, pp. 1700-1707.
- Kusuda, T. and Arao, S. (1996). 'Energy Losses at Circular Drop Manholes'. *Proceedings of the 7th International Conference on Urban Storm Drainage*, Hannover, Germany, pp. 85-90.
- Kusuda, T., Arao, S. and Moriyama, K. (1993). 'Energy Losses at Junction and Transient Flow in Sewer Networks'. *Proceedings of the 6th on Urban Storm Drainage*, pp. 121-127.
- Kychakoff, G., Howe, R.D., Hanson, R.K. and McDaniel, J.C. (1982). 'Quantitative Visualisation of Combustion Species in a Plane'. *Applied Optics*, Vol. 21, No. 18, pp. 3225-3227.
- Lakowicz, J.R. (2006). *Principle of Fluorescence Spectroscopy*, Third Edition, Springer, New York, USA.
- LaVision, 2006. *DaVis FlowMaster Software Manual for DaVis 7.1*, LaVision GmbH, Gottingen, Germany.

- Lau, S.D., Stovin, V., Guymer, I. & Saul, A. (2004). 'Prediction of Storm Tank Performance using Computational Fluid Dynamics'. *4th International Symposium on Environmental Hydraulics and 14th Congress of Asia and Pacific Division, International Association of Hydraulic Engineering and Research*, pp. 15-18 December 2004, Hong Kong, China.
- Lau, S.D., Stovin, V.R. and Guymer, I. (2007). 'The prediction of solute transport in surcharged manholes using CFD'. *Water Science and Technology*, Vol. 55, No. 4, pp. 57-64.
- Lau, S.D., Stovin, V.R. and Guymer, I. (2008). 'Scaling the Solute Transport Characteristics of a Surcharged Manholes'. *Urban Water*, Vol. 5, No. 1, pp. 33-43.
- Lauder, B.E. and Spalding, D.B. (1974). 'The Numerical Computation of Turbulence Flow'. *Computer Methods in Applied Mechanics and Engineering*, Vol. 3, pp. 269-289.
- Lauder, B.E., Reece, G.J. and Rodi, W. (1975). 'Progress in the Development of a Reynolds-Stress Turbulence Closure'. *Journal of Fluid Mechanics*, Vol. 68, pp. 537-566.
- Lauder, B.E. (1976). *Heat and Mass Transport*. In: Bradshaw, P., Topics in Applied Physics, Vol. 12, Turbulence, Springer, Berlin, Germany.
- Lauterborn, W. & Vogel, A. (1984). 'Modern Optical Techniques in Fluid Mechanics'. *Annual Review of Fluid Mechanics*, Vol. 16, pp. 223.
- Leonard, B.P. (1979). 'A Stable and Accurate Convective Modelling Procedure Based on Quadratic Upstream Interpolation', *Computer Methods in Applied Mechanics and Engineering*, Vol. 19, pp. 59-98.
- Lees, M.J., Camacho, L.A. and Chapra, S. (2000). 'On the Relationship of Transient Storage and Aggregated Dead Zone Models of Longitudinal Solute Transport in Streams'. *Water Resources Research*, Vol. 36, No.1, pp. 213-224.
- Levenspiel, O. (1972). *Chemical Reaction Engineering*, John Wiley and Sons, Inc., Hoboken, USA.
- Li, S.G., Ruan, F. and Mclaughlin, D. (1992). 'A Space-time Accurate Method for Solving Solute Transport Problems', *Water Resources Research*, Vol. 28, No. 9, pp. 2297-2306.
- Lindvall, G. (1984). 'Head Losses at Surcharged Manholes with a Main Pipe and a 90 Degree Lateral'. *Proceedings of the 3rd International Conference on Urban Storm Drainage, Goteberg, Sweden*, Vol. 1, pp. 137-146.
-

-
- Litchford, R.J. and Jeng, S.M. (1991). 'Efficient Statistical Transport Model for Turbulent Particle Dispersion in Sprays'. *American Institute of Aeronautics and Astronautics Journal*, Vol. 29, pp. 1443-1451.
- Mark, O., Appelgren C. and Kosir, M. (1996). 'Water Quality Modelling for the Ljubljana Master Plan'. *7th International Conference on Urban Storm Drainage*, Hannover, Germany, pp. 1109-1114.
- Mark, O., Wennberg, C., Van Kalken, T., Rabbi, F. & Albinsson, B. (1998). 'Risk Analyses for Sewer Systems based on Numerical Modelling and GIS'. *Safety Science*, Vol. 30, pp. 99-106.
- Mark, O., Di, X. Li, L. and Guymmer, I. (submitted in 2006). 'An Analytical Model for Solute Mixing in Surcharged Manholes'. *Journal of Hydraulic Engineering*.
- Marsalek, J. (1984). 'Head Losses at Sewer Junction Manholes'. *Journal of Hydraulic Engineering*, Vol. 110, No. 8, pp. 1150-1154.
- Marsalek, J. and Greck, B.J. (1988). 'Head Losses at Manhole with a 90° Bend'. *Journal of Civil Engineering*, Vol. 15, pp. 851-858.
- Martino, F.D., Gisonni, C. and Hager, W. (2002). 'Drop in Combined Sewer Manhole for Supercritical Flow'. *Journal of Irrigation and Drainage Engineering*, Vol. 128, No. 6, pp. 397-400.
- Melling, A. (1997). 'Tracer Particles and Seeding for Particle Image Velocimetry'. *Measurement Science and Technology*, Vol. 8, No. 12, pp. 1406-1416.
- Meynart, R. (1983). 'Instantaneous Velocity Field Measurements in Unsteady Gas Flow by Speckle Velocimetry'. *Applied Optics*, Vol. 22, No. 4, pp. 535-540.
- Morsi, S.A. and Alexander, A.J. (1972). 'An Investigation of Particle Trajectories in Two-Phase Flow Systems'. *Journal of Fluid Mechanics*, Vol. 55, No. 2, pp. 193-208.
- Naib, S.K.A. (1992). *Jet Mechanics and Hydraulic Structures – Theory, Analysis and Design*. University of East London, UK.
- O'Brien, R. (2000). *Dispersion due to Surcharged Manholes*. PhD Thesis, The University of Sheffield, UK.
- Optical Flow Systems (1994). *Instructions for Use Scanning Beam Illumination System*, Optical Flow Systems Ltd., UK.
-

- Patankar, S.V. and Spalding D. B. (1980). 'A Calculation Procedure for Heat, Mass and Momentum Transfer in Three-dimensional Parabolic Flows'. *International Journal of Heat and Mass Transfer*, Vol. 15, p.1787.
- Patankar, S.V. (1980). *Numerical Heat Transfer and Fluid Flow*, Hemisphere Publishing corporation, Taylor & Francis Group, New York, USA.
- Pedersen, F.B. (1977). 'Prediction of Longitudinal Dispersion in Natural Streams'. *Series Paper No. 14*, Institute of Hydrodynamic and Hydraulic Engineering., University of Denmark, Lyngby, Denmark.
- Personal Communication with Fluent Engineer – Gerasimov, A. (Sept, 2006).
- Persson, J., Somes, N.L.G. and Wong, T.H.F. (1999). 'Hydraulics Efficiency of Constructed Wetlands and Ponds'. *Water Science and Technology*, Vol. 40, No. 3, pp. 291-300.
- Persson, J. (2000). 'The Hydraulics Performance of Ponds of Various Layouts'. *Urban Water*, Vol. 2, No. 3, pp. 243-250.
- Purnama, A. (1988). 'The Effect of Dead Zones on Longitudinal Dispersion in Streams'. *Journal of Fluid Mechanics*, Vol. 186, pp. 351-377.
- Quarini, G., Innes, H., Smith, M. and Wise, D. (1996). 'Hydrodynamic Modelling of Sedimentation Tanks'. *Proceeding of Institute of Mechanical Engineers.*, Vol. 210, pp. 83-91.
- Raffel, M., Willert, C. and Kompenhans, J. (1998). *Particle Image Velocimetry: A Practical Guide*, Springer, New York, USA.
- Rayer, Q.G. (2001). 'Computational Fluid Dynamics Guidelines for Best Working Practice'. *NAFEMS International Journal of CFD Case Studies*, Vol. 3, pp. 109-142.
- Reddy, S., Russell, J., Narasimhan, R. and Burns, C. (1999). 'Improving Clearwell Design Using Computational Fluid Dynamics'. In: *Preparing for the 21st Century. Proceeding of the 26th Annual Water Resources Planning and Management Conference*, Tempe, Arizona, June 6-9, 1999 by E.M Wilson (Edition), ASCE.
- Reed, E.C. (1983). *Design and Analysis of Urban Storm Drainage: the Wallingford Procedure*. Hydraulic Research Limited, Wallingford, UK.
- Rodi, W. (1993). *Turbulence Models and Their Application in Hydraulics – A State of the Art Review, Third Edition*. IAHR, Rotterdam, Netherland.
-

-
- Runkel, R.L. and Chapra, S.C. (1993). 'An Efficient Numerical Solution of Transient Storage Equations for Solute Transport in Small Streams'. *Water Resources Research*, Vol. 29, No. 1, pp. 211-215.
- Runkel, R.L., Bencala, K.E., Broshears, R.E. and Chapra, S.C. (1996a). 'Reactive Solute Transport in Streams, 1, Development of an Equilibrium-based Model'. *Water Resources Research*, Vol. 32, No. 2, pp. 409-418.
- Runkel, R.L., McKnight, D.M., Bencala, K.E. and Chapra, S.C. (1996b). 'Reactive Solute Transport in Streams, 2, Simulation of a pH Modification Experiment'. *Water Resources Research*, Vol. 32, No. 2, pp. 419-430.
- Runkel, R.L. (1998). 'One Dimensional Transport with Inflow and Outflow (OTIS): A Solute Transport model for Streams and Rivers', *US Geological Survey Water Resources Investigation Report 98-4018*, US Geological Survey, Denver, Colorado, USA.
- Rutherford, J.C. (1994). *River Mixing*. John Wiley & Sons.
- Saiyudthong, C. (2004). *Effect of Changes in Pipe Direction across Manholes on Dispersion*. PhD thesis, The University of Sheffield, UK.
- Salter, H.E., Ta, C.T. and Williams, S.C., (2000). 'Three-Dimensional Computational Fluid Dynamic Modelling of a Facultative Lagoon'. *Water Science and Technology*, Vol. 42, No. 10-11, pp. 335-342.
- Sangster, W.M., Wood, H.W. Smerdon, E.T. and Bossy, H.G. (1958). 'Pressure Changes at Storm Drain Junctions'. *Bulletin No. 41*, Engineering Experimental Station, University of Missouri, Columbia, USA.
- Schlicke, T. (2001). *Breaking Waves and the Dispersion of Surface Films*. PhD thesis, The University of Edinburgh, UK.
- Schmid, B.H. (1995). 'On the Transient Storage Equations for Longitudinal Solute Transport in Open Channels: Temporal Moments Accounting for the Effects of First-Order Decay'. *Journal of Hydraulic Research*, Vol. 33, pp. 595-607.
- Shaw, C.T. (1992). *Using Computational Fluid Dynamics*, Prentice Hall International Ltd., UK.
- Shih, T.H., Liou, W.W., Shabbi, A. and Zhu, J. (1995). 'A New k- ϵ Eddy Viscosity Model for High Reynolds Number Turbulent Flows – Model Development and Validation'. *Computational Fluid*, Vol. 24, No. 3, pp. 227-238.
-

-
- Shilton, A., (2000). 'Potential Application of Computational Fluid Dynamics to Pond Design', *Water Science and Technology*, Vol. 42, No. 10-11, pp. 327-334.
- Shiono, K. and Feng, T. (2003). 'Turbulence Measurements of Dye Concentration and Effects of Secondary Flow on Distribution in Open Channel Flows'. *Journal of Hydraulic Engineering*, Vol. 129, No.5, pp. 373-384.
- Shirodkar, J.S., Coimbra, C.F.M. and Queiroz McQuay, M. (1996). 'Fundamental Aspects of Modelling Turbulent Particle Dispersion in Dilute Flows'. *Progress in Energy Combustion Science*, Vol. 22, pp. 363-399.
- Smart, P.L. and Laidlaw, I.M.S. (1977). 'An Evaluation of Some Fluorescent Dyes for Water Tracing'. *Water Resources Research*, Vol. 13, No. 1, pp. 15-33.
- Solis, S.S. (2006). *Influence of Channel Planform and Shape on Solute Mixing*. PhD thesis, The University of Sheffield, UK.
- Speziale, C.G., Sarkar, S. and Gatski, T.B. (1991). 'Modelling the Pressure-Strain Correlation of Turbulence: An Invariant Dynamical Systems Approach'. *Journal of Fluid Mechanics*, Vol. 227, pp. 245-272.
- Speziale, C.G. and Thangam, S. (1992). 'Analysis of an RNG Based Turbulence Model for Separated Flows'. *International Journal of Engineering Science*, Vol. 30, No. 10, pp. 1379-1388.
- Stefan, H.G. and Demetracopoulos, A.C. (1981). 'Cells-In-Series Simulation of Riverine Transport'. *Journal of Hydraulic Division ASCE*, Vol. 107, No. HY6, pp. 675-697.
- Stovin, V.R. (1996). *The Prediction of Sediment Deposition in Storage Chambers based on Laboratory Observations and Numerical Simulation*. PhD Thesis, The University of Sheffield, UK.
- Stovin, V.R. and Saul, A.J. (1998). 'A Computational Fluid Dynamics (CFD) Particle Tracking Approach to Efficiency Prediction'. *Water Science and Technology*, Vol. 37, No. 1, pp. 285-293.
- Stovin, V.R., Saul, A.J., Drinkwater, A. and Clifforde, I. (1999). 'Field Testing CFD-Based Predictions of Storage Chamber Gross Solids Separation Efficiency'. *Water Science and Technology*, Vol. 39, No. 9, pp. 161-168.
- Stovin, V.R., Grimm, J.P., Buxton, A.P. and Tait, S.J. (2002). 'Parametric Studies on CFD Models of Sewerage Structures'. *Global Solutions for Urban Drainage*, pp. 1-15.
-

-
- Stovin, V.R., Guymer, I. and Lau, S.D. (2007). 'Modelling Longitudinal Dispersion – An Upstream Temporal Concentration Profile-Independent Approach'. *The 5th International Symposium on Environmental Hydraulics*, Dec 4-7, Arizona, USA.
- Stovin, V.R., Grimm, J.P. and Lau, S.D. (in press). 'Solute Transport Modelling for Urban Drainage Structures'. *ASCE Journal of Hydraulic Engineering*.
- Ta, C.T. and Brignal, W.J. (1998). 'Application of Computational Fluid Dynamics Technique to Storage Reservoir Studies'. *Water Science and Technology*, Vol. 37, No. 2, pp. 219-226.
- Ta, C.T. (1999). 'Computational Fluid Dynamic Model of Storm Tank'. *Proceedings of the 8th International Conference on Urban Storm Drainage*, Sydney, Australia, The Australian Institution of Engineers, pp. 1279-1286.
- Taylor G. (1921). 'Diffusion by Continuous Movement'. *Proc. London Math. Soc. Series A*, Vol.20, No. 1, pp. 186-203.
- Taylor G. (1953). 'Dispersion of Soluble Matter in Solvent Flowing Slowly Through A Tube'. *Proc. Roy. Soc. Series A*, Vol.219, pp. 186-203.
- Taylor G. (1954). 'The Dispersion of Matter in Turbulent Flow Through A Pipe'. *Proc. Roy. Soc. Series A*, Vol. 223, pp. 446-468.
- Thackston, E.L. and Schnelle, K.B. (1970). 'Predicting Effects of Dead Zones on Stream Mixing'. *Journal of Environmental Engineering*, Vol. 96, pp. 319-331.
- Thackston, E.L., Shields, F.D. and Schroeder, P.R. (1987). 'Residence Time Distributions of Shallow Basins'. *Journal of Environmental Engineering*, Vol. 113, No. 6, pp. 1319-1332.
- Thornton, R.C. and Saul, A.J. (1986). 'Some Quality Characteristics of Combined Sewer Flows'. *Public Health Engineer*, Vol. 3, No. 14, pp. 35-38.
- Tritthart, M. and Gutknecht, D. (2007). 'Three-Dimensional Simulation of Free-Surface Flows Using Polyhedral Finite Volumes'. *Engineering Applications of Computational Fluid Mechanics*, Vol. 1, No. 1, pp. 1-14.
- Tyack, J.N. and Fenner, R.A. (1999). 'Computational Fluid Dynamics Modelling of Velocity Profiles within a Hydrodynamic Separator'. *Water Science and Technology*, Vol. 39, No. 9, pp. 169-176.
-

-
- Turner Designs (1990). *Model 10 Fluorometer User's Manual*, Sunnyvale, UK.
- Valentine, E. W. & Wood, I. R. (1977). 'Longitudinal Dispersion with Dead Zones'. *Journal of the hydraulics division, ASCE*, Vol. 109, No. HY9., pp. 975-990.
- Verbanck, M.A., Ashley, R. M. and Bachoc, A. (1994). 'International Workshop on the Origin, Occurrence and Behaviour of Sediments in Sewer Systems: Summary of Conclusions'. *Water Research*, Vol. 28, No.1, pp. 187-194.
- Versteeg, H.K. and Malalasekera, W. (1995). *An Introduction to Computational Fluid Dynamics – The Finite Volume method*, Pearson Education Limit, Essex, UK.
- Wagner, B.J. and Harvey, J.W. 'Experimental Design for Estimating Parameters of Rate-limited Mass Transfer: Analysis of Stream Tracer Studies'. *Water Resources Research*, Vol. 33, No. 7, pp. 1731-1741.
- Walker, D.A. (1987). 'A Fluorescence Technique for Measurement of Concentration in Mixing Liquids'. *Journal of Physics E: Scientific Instruments*, Vol. 20, No. 2, pp. 217-224.
- Wallis, S.G., Young, P.C. and Beven, K.J. (1989). 'Experimental Investigation of The Aggregated Dead Zone Model for Longitudinal Solute Transport in Stream Channels'. *Proceedings of the Institution of Civil Engineers, Part2*, PAPER 9335.
- Webster, D.R., Rahman, S. and Dasi, L.P. (2003). 'Laser-Induced Fluorescence Measurements of a Turbulent Plume'. *Journal of Engineering Mechanics*, Vol. 129, No. 10, pp. 1130-1137.
- Wiener, N. (1949). *Extrapolation, Interpolation, and Smoothing of Stationary Time Series*, MIT Press, USA.
- Wilson, J.F, Cobb, E.D. and Kilpatrick, F.A. (1986). *Fluorometric Procedures for Dye Tracing, Techniques of Water-Resources Investigations of the United States Geological Survey*, USA.
- Wood, M.G., Greenfield, P.F., Howes, T., Johns, M.R. and Keller, J. (1995). 'Computational Fluid Dynamic Modelling of Wastewater Ponds to Improve Design'. *Water Science and Technology*, Vol. 31, No. 12, pp 111-118.
- Wood, M.G., Howes, T., Keller, J. and Johns, M.R., (1998). 'Two Dimensional Computational Fluid Dynamic Models for Waste Stabilisation Ponds'. *Water Resources*, Vol. 32, No. 3, pp. 958-963.
-

-
- Woolley, L. (1988). *Drainage Details*, 2nd edition, E & FN Spon.
- Yagi, S. (1984). 'Mass Exchange of a Cavity Shear Layer and its Effects on Longitudinal Dispersion in Open Channel Flows with Dead Zones'. *Proceedings, Fourth Congress Asian and Pacific Division, LAHR, Chiang-Mai, Thailand*, pp. 887-889.
- Yakhot, V. and Orszag, S.A. (1986). 'Renormalization Group Analysis of Turbulence: Basic Theory'. *Journal of Scientific Computing*, Vol. 1, No. 1, pp. 3-51.
- Yakhot, V., Orszag, S.A., Thangam, S., Gatski, T.B. and Speziale, C.G. (1992). 'Development of Turbulence Models for Shear Flows by a Double Expansion Technique'. *Physics of Fluids A*, Vol. 4, No. 7, pp. 1510-1520.
- Young, P.C. (1980). 'An Instrument Variable Method for Model Order Identification'. *Automatica*, Vol. 16, pp. 281-294.
- Young, P.C. (1984). *Recursive Estimation and Time Series Analysis*, Springer-Verlag, New York, USA.
- Young, P.C. (1985). 'The Instrumental Variable Method: A Practical Approach on Identification and System Parameter Estimation', presented at 7th IFAC/IFORS Symposium on System Parameter Estimation, *International Federation of Automatic Control*, York, UK.
- Young, P.C. and Wallis, S.G. (1986). 'The Aggregated Dead Zone (ADZ) Model for Dispersion in River', *International Conference on Water Quality Modelling in the Inland Natural Environment*, Bournemouth, England, 10-13, June 1986.
- Young, P.C. (1992). 'Parallel Processes in Hydrology and Water Quality: A Unified Time-Series Approach', *Water and Environmental Journal*, Vol. 6, No. 6, pp. 598-612.
- Younis, B.A., Gatski, T.B. and Speziale, C.G. (1996). 'Assessment of the SSG Pressure-Strain Model in Free Turbulent Jets with and without Swirl'. *Journal of Fluid Engineering*, Vol. 118, pp. 800-809.

Appendixes

A. Raw Fluorometric Data

This appendix provides the raw fluorometric data of the profiles presented in Figure 3.18 – Figure 3.20; Figure 4.5 and Figure 4.6; Figure 4.30 and Figure 4.31. Note that the fluorometric data in Figure 4.31A corresponding to the prototype traces are not the raw measurements. Relative concentration is presented as the original concentration is not known. Table 1A displays the statistics of the upstream profiles in Figure 4.30A and Figure 4.31A.

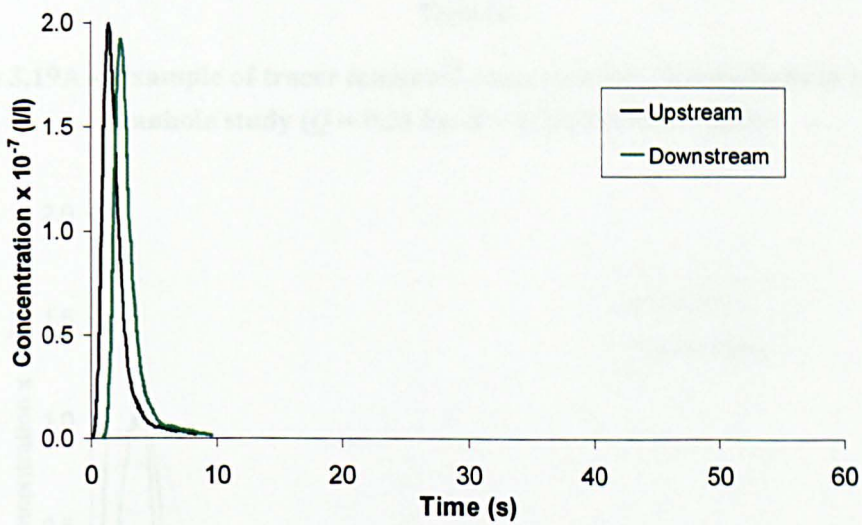


Figure 3.18A – Example of tracer temporal concentration distributions in the straight pipe study ($Q = 0.35$ l/s)

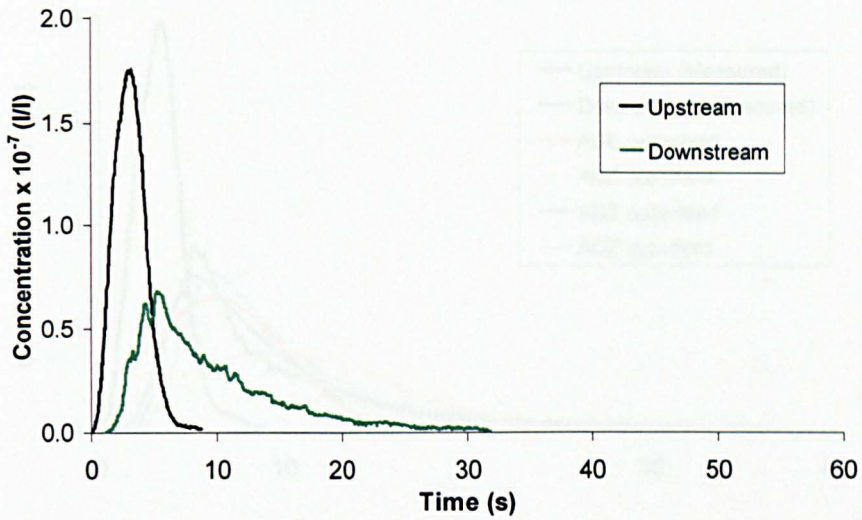


Figure 3.19A – Example of tracer temporal concentration distributions in the scale manhole study ($Q = 0.35$ l/s; $S = 1.25$; Pre-threshold)

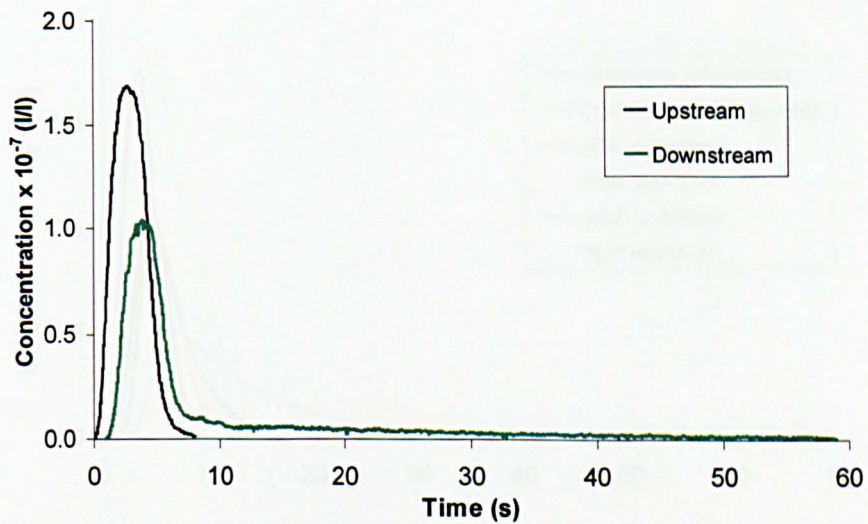


Figure 3.20A – Example of tracer temporal concentration distributions in the scale manhole study ($Q = 0.35$ l/s; $S = 3.33$; Post-threshold)

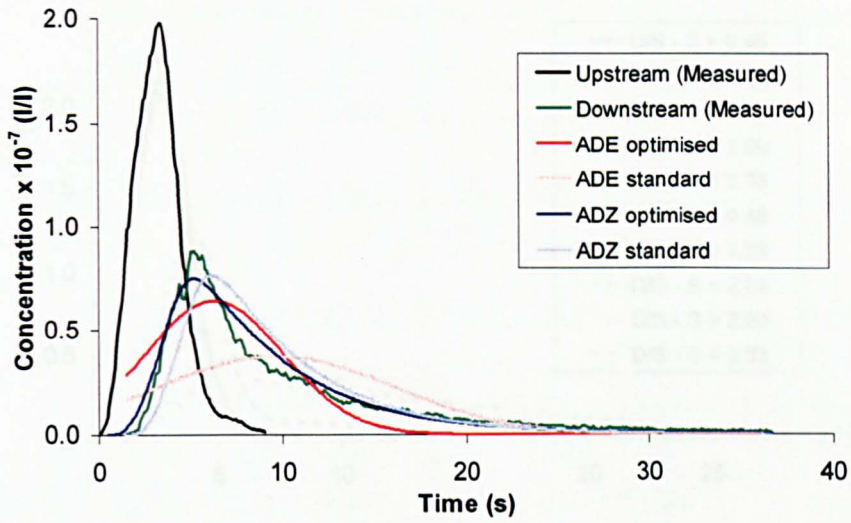


Figure 4.5A – Measured downstream temporal concentration profile ($Q = 0.25$ l/s; $S = 0.417$; Pre-threshold) with ADE and ADZ predictions for the scale manhole

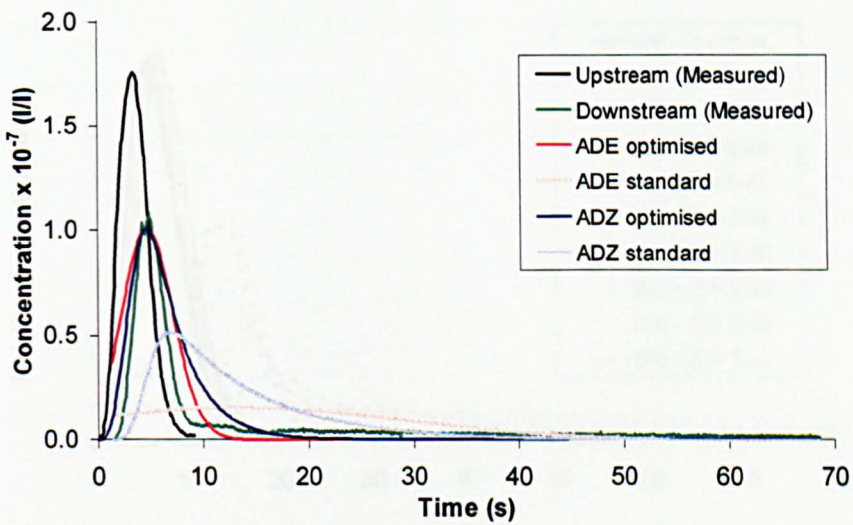


Figure 4.6A – Measured downstream temporal concentration profile ($Q = 0.25$ l/s; $S = 4.167$; Post-threshold) with ADE and ADZ predictions for the scale manhole

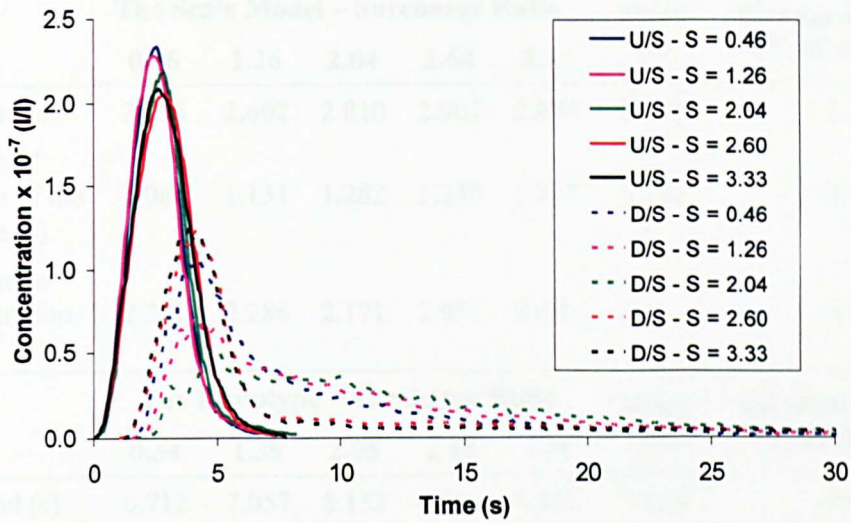


Figure 4.30A – Effects of variations in surcharge on downstream temporal concentration distributions: The scale model operated at 0.3 l/s

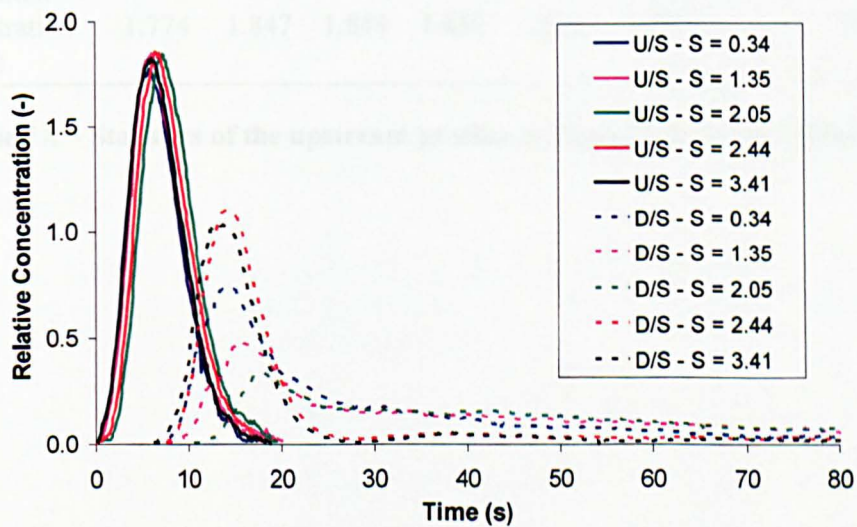


Figure 4.31A – Effects of variations in surcharge on downstream temporal concentration distributions: The prototype operated at 2 l/s (after Guymer *et al.*, 2005)

	The Scale Model – Surcharge Ratio					Mean (s)	Standard Deviation (% of the Mean)
	0.46	1.26	2.04	2.60	3.33		
Centroid (s)	2.616	2.602	2.810	2.907	2.894	2.766	5.349
Standard Deviation of the Profile (s)	1.066	1.131	1.282	1.249	1.377	1.221	10.109
Maximum Concentration (x 10 ⁻⁷ l/l)	2.337	2.286	2.171	2.051	2.083	1	5.686
	The Prototype – Surcharge Ratio					Mean (s)	Standard Deviation (% of the Mean)
	0.34	1.35	2.05	2.44	3.41		
Centroid (s)	6.712	7.057	8.153	7.584	6.891	7.279	8.063
Standard Deviation of the Profile (s)	8.020	9.263	8.950	8.196	8.502	8.586	6.026
Maximum Concentration (-)	1.774	1.847	1.844	1.859	1.828	1.830	1.815

Table 1A – Statistics of the upstream profiles in Figure 4.30A and Figure 4.31A

B. List of Publications

The published papers can be found in the CD attached in this thesis.

Publications – Journal

1. Lau S. D., Stovin V. & Guymer I. (2008). Scaling the Solute Transport Characteristics of Surcharged Manholes. *Urban Water*, Vol. 5, No. 1, pp.33.
2. Lau S. D., Stovin V. & Guymer I. (2007). The Prediction of Solute Transport in Surcharged Manholes using CFD. *Water Science and Technology*, Vol. 55, No. 4, pp. 57.

Publications – Conference

1. Stovin V., Guymer I., Nawasra J., Dunkley P. & Lau D. (2007). Insights into Flow Field Interactions within Surcharged Manholes. *The 5th International Symposium on Environmental Hydraulics*, 4-7 December 2007, Tempe, Arizona, USA.
2. Stovin V., Guymer I. and Lau D. (2007). Modelling Longitudinal Dispersion – An Upstream Temporal Concentration Profile-Independent Approach. *The 5th International Symposium on Environmental Hydraulics*, 4-7 December 2007, Tempe, Arizona, USA.
3. Nawasra J., Lau S., Stovin V., Guymer I. & Bryanston-Cross P. J. (2007). Characterising Flow within a Manhole under Different Surge Heights using Particle Image Velocimetry. *Hydraulic Measurements & Experimental Methods 2007*, 10-13 September 2007, New York, USA.
4. Lau S. D., Stovin V. & Guymer I. (2006). Scaling the Solute Transport Characteristics of Surcharged Manholes. *Proceedings 2nd International IWA Conference on Sewer Operation and Maintenance*, 26-28 October 2006, Vienna, Austria.
5. Lau, S. D., Stovin, V. and Guymer, I. (2006). The Prediction of Solute Transport in Surcharged Manholes using CFD. *Proc. 7th Int. Conf. on Urban Drainage Modelling and 4th Int. Conf. on Water Sensitive Urban Design*, 2-7 April 2006, Melbourne, Australia, Vol. 1, 51-58.
6. Lau S. D., Stovin V., Guymer I. & Saul A. (2004). Prediction of Storm Tank Performance using Computational Fluid Dynamics. *4th International Symposium on Environmental Hydraulics and 14th Congress of Asia and Pacific Division, International Association of Hydraulic Engineering and Research*, 15-18 December 2004, Hong Kong, China.